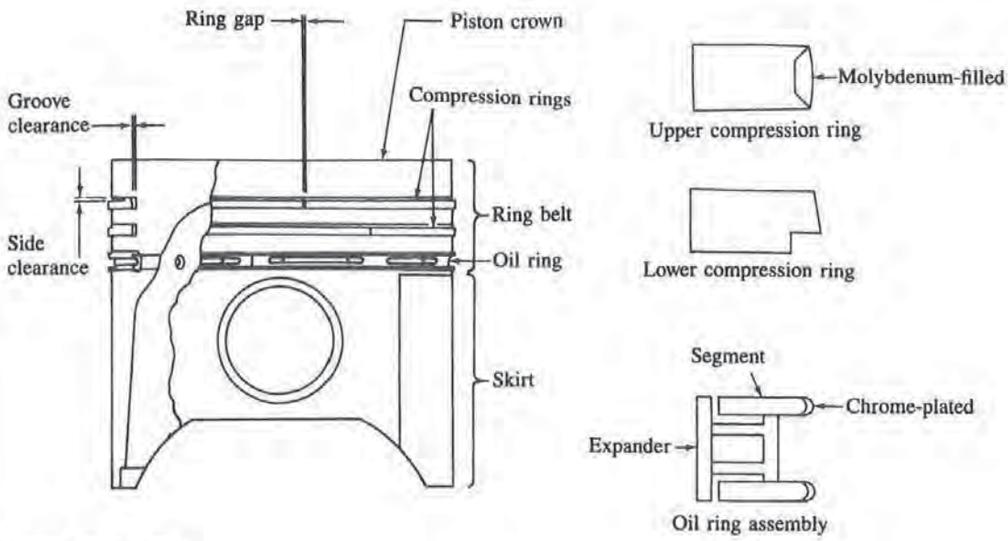


FIGURE 13-17
Construction and nomenclature of typical piston and ring assembly.[10]

13.6.3 Piston Assembly Friction

The construction and nomenclature of a typical piston and ring assembly is shown in Fig. 13-17. The piston skirt is a load-bearing surface which keeps the piston properly aligned within the cylinder bore. The piston lands and skirt carry the side load which is present when the connecting rod is at an angle to the cylinder axis. The rings control the lubrication between these surfaces and the liner. Two types of rings—compression and oil rings—perform the following tasks: (1) seal the clearance between the piston and cylinder to retain gas pressure and minimize blowby; (2) meter adequate lubricant to the cylinder surface to sustain high thrust and gas force loads at high surface speed and at the same time control oil consumption to acceptable limits; and (3) control piston temperatures by assisting in heat transfer to the cylinder walls and coolant. Automobile engines normally use three rings, though two-ring designs exist. Larger diesel engines may use four rings.

Many designs of compression ring are employed,[13] the differences between them being in the cross-sectional shapes (and hence relative flexibility) and in their use of wear-resistant surface treatments. Top compression rings are usually made of cast iron. The axial profiles are chosen to facilitate hydrodynamic lubrication. Common shapes are a rectangular cross section with inner and outer edges chamfered to prevent sticking in the groove, or with a barrel-shaped working surface which can accommodate the rotation of the piston which occurs with short piston skirts. Wear-resistant coatings (either a hard chromium-plated overlay or a molybdenum-filled inlay) are usually applied to the outer ring surface. The second compression ring serves principally to reduce the pressure drop across the top ring. Since the operating environment is less arduous, the

PETITIONER'S EXHIBIT 1002
US PATENT NO. 6,581,565

second ring can be made more flexible to give better oil control. The objective is to compensate for the torsional deflection of the ring under load so that top-edge contact with the cylinder liner is avoided. Top-edge contact tends to pump oil toward the combustion chamber, detracting from the performance of the oil control ring. Bottom-edge contact provides an oil scraping action on the downstroke. The oil control ring meters and distributes the oil directed onto the cylinder liner by the crankshaft system, returning excess oil to the crankcase sump. It must exert sufficient pressure against the cylinder, possess suitably shaped wiping edges (usually two thin steel rings), and provide adequate oil drainage. Slotted or composite rings are normally used.[14]

The tension in all the piston rings holds them out against the cylinder wall and hence contributes to friction. The gas pressure behind the compression rings increases this radial force. The gas pressures behind the second ring are substantially lower than behind the first ring. The gas pressures behind the rings are a function of speed and load. An approximate rule for estimating ring friction is that each compression ring contributes about 7 kPa (1 lb/in^2) mep.[5] Oil rings, due to their substantially higher ring tension, operate under boundary lubrication; they contribute about twice the friction of each compression ring.[15]

The piston assembly is the dominant source of engine rubbing friction. The components that contribute to friction are: compression rings, oil control rings, piston skirt, and piston pin. The forces acting on the piston assembly include: static ring tension (which depends on ring design and materials); the gas pressure forces (which depend on engine load); the inertia forces (which are related to component mass and engine speed). The major design factors which influence piston assembly friction are the following: ring width, ring face profile, ring tension, ring gap (which governs inter-ring gas pressure), liner temperature, ring-land width and clearances, skirt geometry, skirt-bore clearance.[3]

Piston assembly friction is dominated by the ring friction. The forces acting on a typical compression ring, lubricated by a thin oil film, are shown in Fig. 13-18. The analysis of this hydrodynamic contact is complex because the forces acting on the ring vary with time and slight changes in ring face geometry can have large effects on the computed results. Cylinder pressure p_c normally acts on the top and back of the ring. The inter-ring gas pressure p_{ir} (which depends on cylinder pressure and the geometry of the lands, ring grooves, and ring, especially the ring gap), acts on the oil film and bottom part of the ring. The character of the gas flow into and out of the inter-ring regions and its effect on ring motion were discussed in Sec. 8.6. Late in the expansion stroke, pressure reversals can occur which may cause the ring to move to the upper surface of the groove or to flutter in between. Ring tension acts to force the ring against the liner. The pressure in the lubricating oil film is generated as shown by the surface A-B in Fig. 13-18 as the ring moves downward. It is believed that the film cavitates between B and C so the pressure decreases to a low value and then increases to p_c. When the direction of motion is reversed, C-B becomes the pressure-generating surface.

Models for the ring and oil film behavior have been developed. For the practical case where the oil film thickness h is much less than the ring width, the

PETITIONER'S EXHIBIT 1002
US PATENT NO. 6,581,565

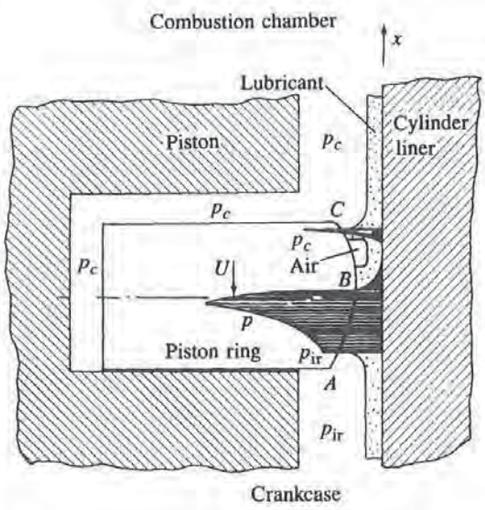


FIGURE 13-18
Schematic of pressure distribution in the lubricating oil film and around a compression ring during expansion stroke. Pressure profile in the oil film indicated by horizontal shading.[3]

Navier-Stokes equation for the liquid film motion reduces to a Reynolds equation of the form:

$$\frac{\partial}{\partial x}\left(h^3 \frac{\partial p}{\partial x}\right) = 6U\mu \frac{\partial h}{\partial x} + 12\mu \frac{\partial h}{\partial t} \tag{13.14}$$

where h is the local film thickness, μ the liquid viscosity, and U the relative velocity between the two surfaces. This equation, along with the appropriate force balances on the ring, can then be solved for the coupled film and ring behavior (e.g., see Ref. 15).

Measured oil film thicknesses in an operating direct-injection diesel engine are shown in Fig. 13-19. A capacitance technique with electrodes embedded in the top compression ring was used to make the measurements.[16] At top-center during combustion, the thickness is a minimum (≈ 1 μm); it then increases as gas loading on the rings decreases and piston velocity increases during the expansion stroke to a value an order of magnitude higher. Higher engine load results in higher gas loading on the rings. It also results in higher lubricant temperatures and lower viscosity, which reduce the film thickness during intake, compression, and exhaust. This large change in film thickness over one cycle is the reason the ring friction regime changes from boundary lubrication to thick-film hydrodynamic lubrication. When the oil film thickness drops below about 1 μm, asperity contact will begin.†

An analysis of the side thrust between the piston and cylinder wall helps explain piston design trends. A force balance on the crank/connecting rod mechanism of Fig. 2-1 leads to the following. An axial force balance relates the piston

† The critical film thickness depends on both the cylinder liner and ring surface finish.

PETITIONER'S EXHIBIT 1002
US PATENT NO. 6,581,565

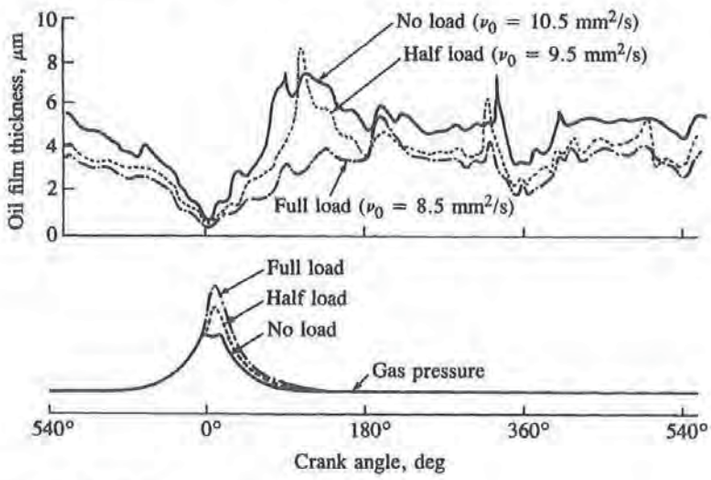


FIGURE 13-19
Measured oil film thickness between top ring and cylinder liner of a DI diesel engine, operated at 1300 rev/min. Bore = 139.7 mm, stroke = 152.4 mm. ν_0 is estimated oil viscosity. Reprinted by permission of the Society of Tribologists and Lubrication Engineers (STLE), formerly the American Society of Lubrication Engineers (ASLE).[16]

mass m and acceleration to the net axial force:

$$m\frac{dS_p}{dt} = -F_r\cos\phi + \frac{\pi B^2}{4}p \mp F_f \tag{13.15}$$

where ϕ is the angle between the cylinder axis and connecting rod, and p is the cylinder *gauge* pressure. A transverse force balance gives

$$F_t = F_r\sin\phi = \left(-m\frac{dS_p}{dt} + \frac{\pi B^2}{4}p \mp F_f\right)\tan\phi \tag{13.16}$$

Here F_r is the force in the connecting rod (positive when in compression) and F_f is the friction force on the piston assembly (− when piston is moving toward the crank; + when piston moves away from the crank). dS_p/dt is the piston acceleration obtained by differentiating the equation for piston velocity [Eq. (2.11)]:

$$\frac{dS_p}{dt} = \frac{d^2s}{dt^2} = \pi^2 N\bar{S}_p\left[\cos\theta + \frac{R^2\cos 2\theta + \sin^4\theta}{(R^2 - \sin^2\theta)^{3/2}}\right] \tag{13.17}$$

The side thrust F_t given by Eq. (13.16) is transmitted to the liner via the rings and piston skirt. It changes direction as the piston passes through top- and bottom-center positions. Since the friction force changes sign at these locations and the gas pressure during expansion is greater than during compression, the side thrust during expansion is greater.

The piston skirt carries part of this side thrust so it contributes to piston assembly friction. The large contact area between the skirt and liner, relative to

PETITIONER'S EXHIBIT 1002
US PATENT NO. 6,581,565

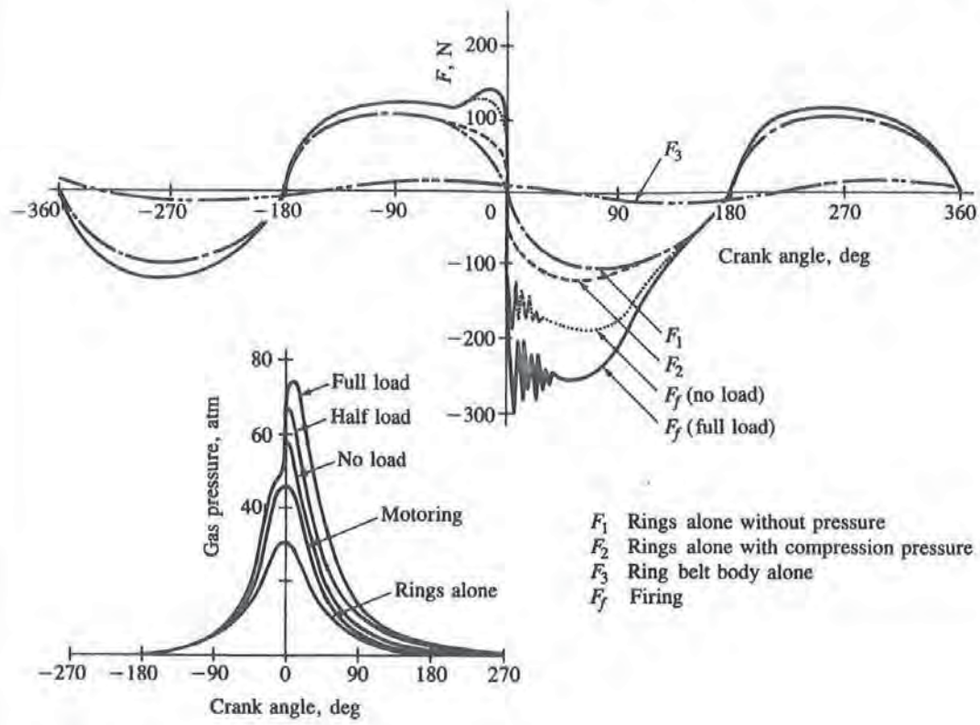


FIGURE 13-20
Measured frictional force on cylinder liner of 137 mm bore and 135 mm stroke single-cylinder DI diesel engine. 1200 rev/min, coolant temperature 80°C, cylinder liner inside temperature 97°C.[18]

the ring contact area, results in lighter loading (force/area) and promotes hydrodynamic lubrication. Piston skirt areas have been reduced substantially in recent years to reduce piston mass (which reduces side thrust) and contact area. An additional reduction in side thrust, leading to reduced skirt friction, has been achieved with the use of an offset wrist-pin. By offsetting the pin axis by 1 to 2 mm without changing its vertical location, the crank angle at which the piston traverses the bore and "slaps" the other side of the cylinder is advanced so it occurs before combustion has increased the cylinder gas pressure significantly.[17]

Direct measurements of the friction force associated with the piston assembly have been made. The most common technique involves the use of a special engine where the axial force on the cylinder liner is measured directly with a load transducer (e.g., Ref 18). Figure 13-20 shows the friction forces measured in such an engine (a DI diesel engine) through the engine's operating cycle. Friction forces are highest just before and after top-center at the end of the compression stroke. The high values at the start of the expansion stroke under firing conditions are caused by the piston slap impulse and the high side-thrust force as well as the combustion gas pressure loading on the rings.

Bishop[12] has developed correlations for piston and ring friction in the following categories: boundary condition friction (primarily between the rings and

PETITIONER'S EXHIBIT 1002
US PATENT NO. 6,581,565

the cylinder wall due to ring tension, and gas pressure behind the compression rings) and viscous ring and piston friction. He argued that boundary condition friction was primarily due to breakdown of the oil film between the rings and cylinder wall over part of the piston travel. Assuming that the transition to boundary lubrication occurred at a critical speed, he showed that fmep due to boundary friction was proportional to stroke/bore^2, i.e.:

$$(\text{fmep})_{\text{boundary}} \propto \text{loading} \times \frac{L}{B^2} \tag{13.18}$$

The ring loading has two components. The component due to ring tension is essentially constant. The component due to gas pressure behind the rings will depend on load. Bishop assumed it to be proportional to inlet manifold pressure. The viscous piston friction—friction between the piston and rings and cylinder wall under hydrodynamic lubrication conditions—was correlated by

$$(\text{fmep})_{\text{hydrodyn}} \propto \frac{\bar{S}_p A_{p,\,\text{eff}}}{LB^2} \tag{13.19}$$

where $A_{p,\,\text{eff}}$ is the effective area of the piston skirt in contact with the cylinder liner.

The relative importance of the boundary lubrication piston and ring friction, and viscous piston and ring friction over the load and speed range, is as follows. The viscous friction component increases in importance with increasing speed. The boundary lubrication friction component increases with increasing load as the cylinder gas pressures increase.

13.6.4 Crankshaft Bearing Friction

Crankshaft friction contributions come from journal bearings (connecting rod, main and accessory or balance shaft bearings) and their associated seals. A schematic of a journal bearing operating under hydrodynamic lubrication is shown in Fig. 13-21. Large loads can be carried by journal bearings with low energy losses under normal operating conditions, due to the complete separation of the two surfaces in relative motion by the lubricant film. Loads on crankshaft journal bearings vary in magnitude and direction because they result primarily from the inertial loads of the piston/connecting rod mechanism and the cylinder gas loads [see Eq. (13.15)]. Typical loads and the resulting journal eccentricity diagram for a connecting rod bearing are shown in Fig. 13-22. From the journal eccentricity diagram the minimum oil film thickness is determined. This quantity, the minimum separation distance between the journal and bearing surfaces, is a critical bearing design parameter. If the film thickness is too low, asperities will break through the oil film and substantially increase the friction and wear. Journal bearings are usually designed to provide minimum film thicknesses of about 2 μm.

PETITIONER'S EXHIBIT 1002
US PATENT NO. 6,581,565

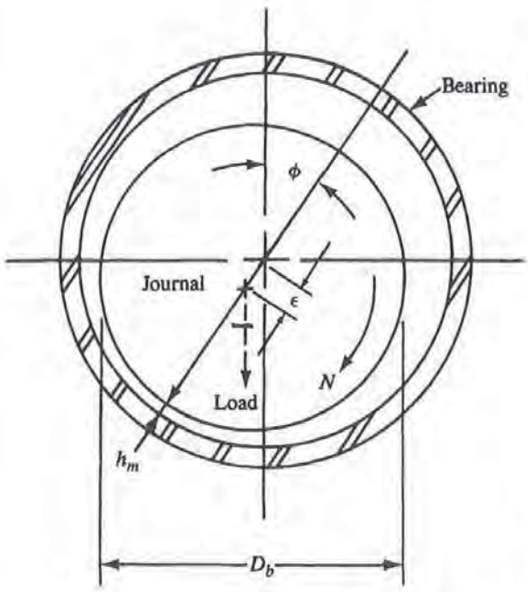


FIGURE 13-21
Schematic of hydrodynamically lubricated journal bearing.[3]

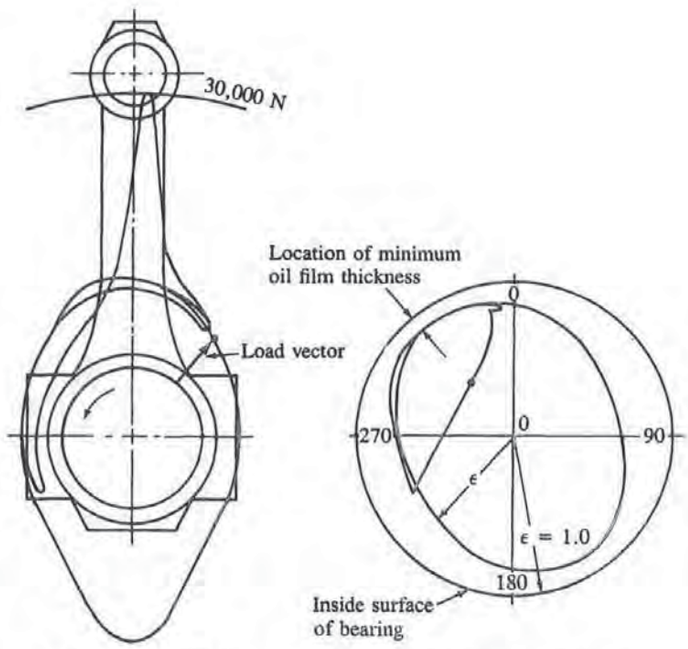


FIGURE 13-22
Typical engine journal bearing load and eccentricity diagrams.[3]

PETITIONER'S EXHIBIT 1002
US PATENT NO. 6,581,565

The friction force F_f in the bearing is given approximately by the product of the bearing area, the oil viscosity, and the mean velocity gradient in the oil:

$$F_f \approx (\pi D_b L_b)\mu\left(\frac{\pi D_b N}{\bar{h}}\right) = \frac{\pi^2 \mu D_b^2 L_b N}{\bar{h}} \tag{13.20}$$

where D_b and L_b are the bearing diameter and length, $\bar{h}$ is the mean radial clearance, and N is the shaft rotational speed. A more sophisticated analysis of the friction in a hydrodynamically lubricated bearing yields the relation[19]

$$F_f = \frac{\pi^2 \mu D_b^2 L_b N}{(1-\varepsilon^2)^{1/2}\bar{h}} + \frac{\bar{h}\varepsilon W}{D_b}\sin\phi \tag{13.21}$$

where ε is the eccentricity ratio $(\bar{h} - h_m)/\bar{h}$ and h_m is the minimum clearance. The first term closely matches the approximation given in Eq. (13.20). The factor $1/(1-\varepsilon^2)^{1/2}$ and the second term correct for the offset of the journal center relative to the bearing center: W is the bearing load and ϕ the attitude angle. To first order, with hydrodynamic lubrication the friction power does not depend significantly on the bearing load. If σ is the loading per unit projected area of the bearing $[W/(L_b D_b)]$, then the coefficient of friction f is given by

$$f = \frac{F_f}{W} \approx \frac{\pi^2 \mu D_b^2 L_b N}{\sigma L_b D_b \bar{h}} = \frac{\pi^2 D_b}{\bar{h}}\frac{\mu N}{\sigma} \tag{13.22}$$

For a given bearing, or series of geometrically similar bearings, the friction coefficient is proportional to $\mu N/\sigma$. However, at low values of $\mu N/\sigma$ the hydrodynamic pressure in an actual bearing will be insufficient to support the shaft load and the oil film becomes incomplete. The friction coefficient increases rapidly as mixed lubrication then occurs.

Bishop[12] summed the friction power loss in all crankshaft and con rod journal bearings and divided by the displaced volume per unit time to obtain the following correlation for bearing friction mep (in kilopascals):

$$\text{fmep (bearings)} = 41.4\left(\frac{B}{L}\right)\left(\frac{N}{1000}\right)K \tag{13.23}$$

where

$$K = \frac{D_{mb}^2 L_{mb} + D_{rb}^2 L_{rb}/m + D_{as}^2 L_{as}}{B^3} \tag{13.24}$$

In Eq. (13.24), D_{mb} is the main bearing diameter, L_{mb} the total main bearing length ÷ number of cylinders, D_{rb} the rod bearing diameter, L_{rb} the rod bearing length, m the number of pistons per rod bearing, D_{as} the accessory shaft bearing diameter, L_{as} the total length of all accessory shaft bearings ÷ number of cylinders, and all dimensions are in millimeters. The similarity between engines is such that $K \approx 0.14$ for spark-ignition engines and $K \approx 0.29$ for diesel engines.

PETITIONER'S EXHIBIT 1002
US PATENT NO. 6,581,565

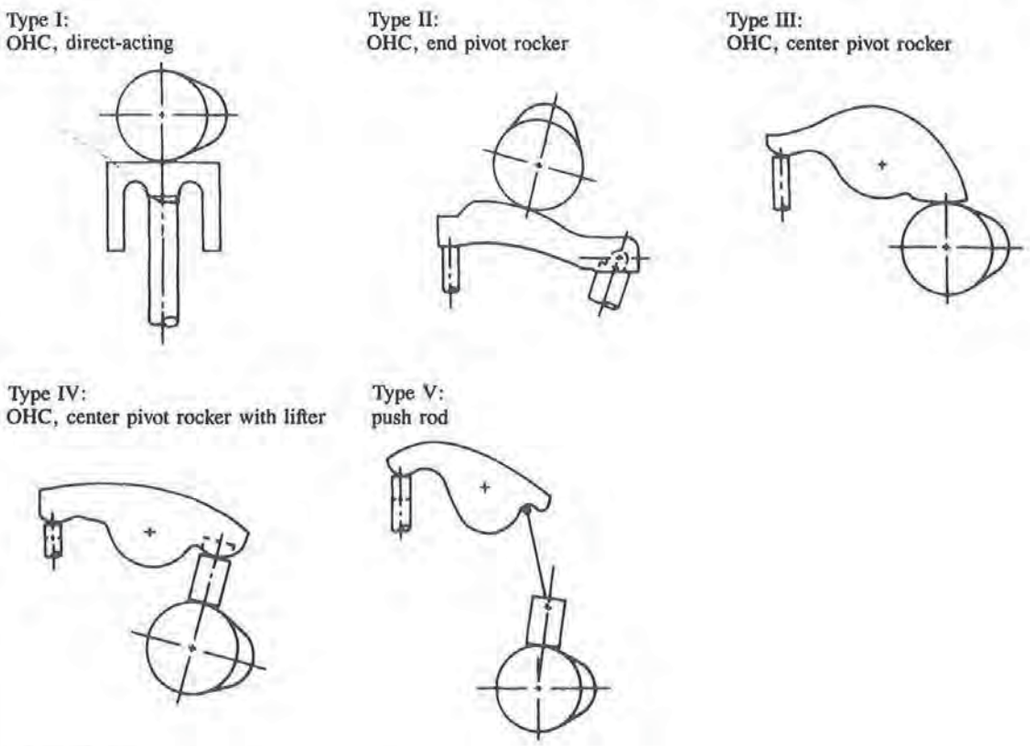


FIGURE 13-23
Different valve train configurations.[21]

The front and rear main bearing seals[20] also contribute to crankshaft assembly friction. At 1500 rev/min they are responsible for about 20 percent of the friction attributable to the crankshaft.[10]

13.6.5 Valve Train Friction

The valve train carries high loads over the entire speed range of the engine. Loads acting on the valve train at lower speeds are due primarily to the spring forces, while at higher speeds the inertia forces of the component masses dominate. Valve train designs can be classified by type of configuration, as indicated in Fig. 13-23. Large valves and high rated speeds generally increase spring and inertia loads and friction. Friction differences between these systems are difficult to quantify. For example, measurements of valve train friction mean effective pressure for several of these valve train types showed significant variations (± 30 percent): see Fig. 13-24*a*.[10,21] However, when the data were adjusted to a common spring load, Fig. 13-24*b*, the low-speed friction mep values converged and the high-speed fmep differences were reduced.[10]

The total valve train friction can be broken down by critical contact regions: camshaft journal bearings, rocker arm/fulcrum and cam/tappet interface.

PETITIONER'S EXHIBIT 1002
US PATENT NO. 6,581,565

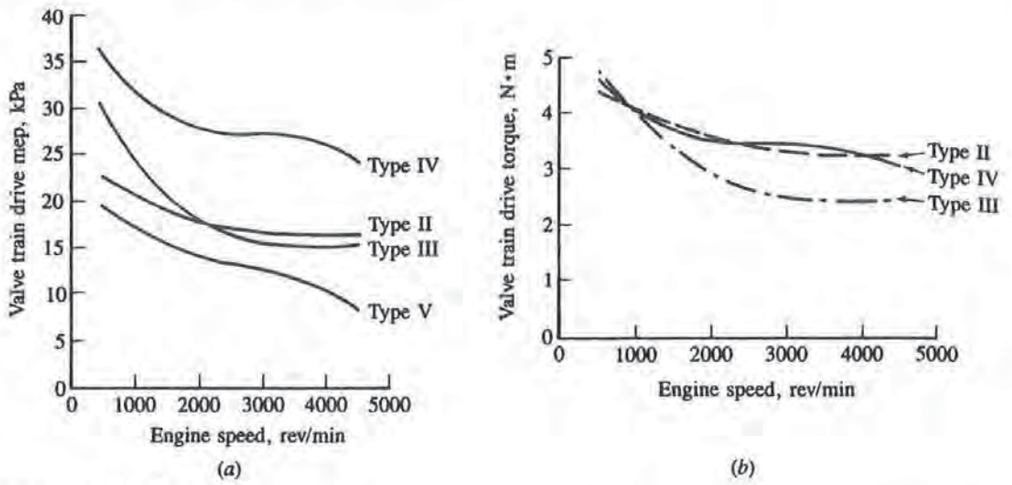


FIGURE 13-24
(*a*) Total valve train friction mean effective pressure as a function of speed for four engines with different valve configurations (see Fig. 13-23). (*b*) Valve train friction torque for three of these engines after adjusting to common valve spring load.[10]

The shape of the valve train mep versus speed curve indicates that the predominant regime of lubrication in the valve train at lower engine speeds is boundary lubrication. The cam/lifter interface usually contributes the largest friction loss due to the very high loads and small contact areas.[22]

Effective methods of reducing valve train friction are: (1) spring load and valve mass reduction; (2) use of tappet roller cam followers; (3) use of rocker arm fulcrum needle bearings. One such low-friction valve train design is shown in Fig. 13-25.[22] The roller cam-followers provide the largest benefit especially at lower speeds: reductions of order 50 percent in valve train friction can be achieved.

Bishop[12] developed a correlation for valve train friction from design data on valve spring loads and valve weights, and experimental data from dynamometer tests of push rod engines. He shows that

$$\text{fmep (valve train)} = \frac{C[1 - 0.133(N/1000)]n_{iv} D_{iv}^{1.75}}{B^2 L} \tag{13.25}$$

where n_{iv} is the number of inlet valves per cylinder, D_{iv} is the inlet valve head diameter, and B and L are bore and stroke. This relation does not include camshaft bearing friction, which is included in Eq. (13.23). The functional form of Eq. (13.25) is an acceptable fit to more modern engine data. Bishop's value for C (1.2×10^4 with fmep in kilopascals, N in revolutions per minute, and dimensions in millimeters) gives valve train fmep values (which exclude camshaft bearing losses) about two-thirds the total valve train friction of current production engines. This is consistent with the data in Fig. 13-24.

PETITIONER'S EXHIBIT 1002
US PATENT NO. 6,581,565

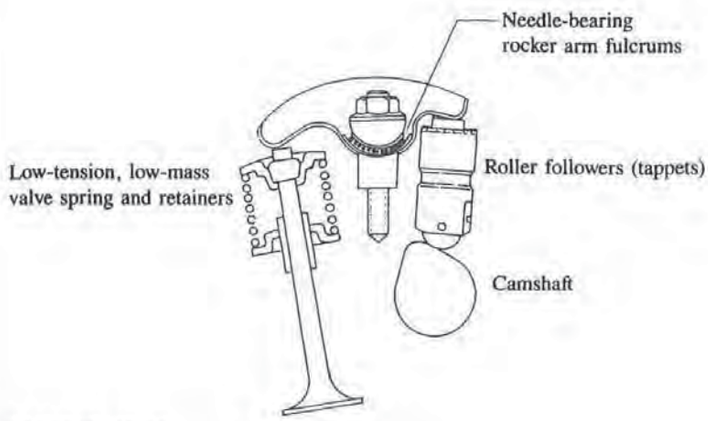


FIGURE 13-25
Low friction valve train.[22]

13.7 ACCESSORY POWER REQUIREMENTS

The coolant water pump and oil pump are built-in accessories, essential to engine operation, and are normally considered part of the basic engine.[2] A fully equipped engine usually includes additional accessories—a fan and generator; in automobile use it often includes a power-steering pump, an air conditioner, and an air pump for emission control. The power delivered by the fully equipped engine (the net power) is lower than the power delivered by the basic engine due to the power requirements of these additional accessories.

The friction mean effective pressures associated with driving the water pump and alternator, and oil pump are shown in Fig. 13-14*a*. Together they comprise about 20 percent of the total (motored) engine friction. The water pump is typically less than about 7 kPa at 1500 rev/min;[10] the oil pump 4 to 10 kPa at this speed;[10] the alternator requires 7 to 10 kPa.[23] These numbers vary significantly with component design details. The generator power depends on the electrical load to be met and the generator blower design. A requirement of about two-thirds of the peak is indicated for average generator power.[23]

The power requirements for a fan, generator, and power-steering pump typical of a 5.7-liter engine are shown in Fig. 13-26. The fan requirements are the largest and with a direct drive increase with the cube of the speed. Alternative couplings such as a viscous drive reduce the fan speed at high engine speed and thereby reduce its power significantly. The power-steering pump is only required to provide high pressures intermittently. Here only the fluid pumping losses are charged against the engine.

Air-conditioning is standard on a majority of U.S. cars; additional power is required for the air-conditioning compressor. Also, since the compressed refrigerant is condensed in a second radiator, a larger-than-standard fan is required to pull additional air through the combined radiator systems. An air pump which pumps air into the engine exhaust ports may be part of an SI engine emission

PETITIONER'S EXHIBIT 1002
US PATENT NO. 6,581,565

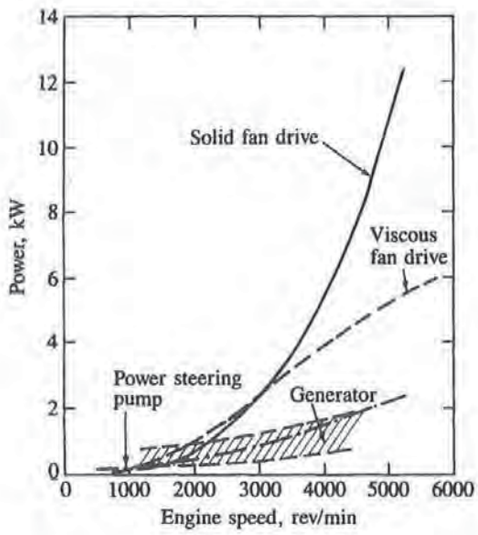


FIGURE 13-26
Power requirements for engine fan, generator, and power-steering pump typical of 5.7-liter eight-cylinder engine.[23, 24]

control system (see Sec. 11.6). Its power requirements ($\sim$1 kW at normal engine speeds) must then be added to the accessory friction requirements.

13.8 LUBRICATION

The lubricant and the lubricating system perform the following functions:[25]

1. Reduce the frictional resistance of the engine to a minimum to ensure maximum mechanical efficiency.
2. Protect the engine against wear.
3. Contribute to cooling the piston and regions of the engine where friction work is dissipated.
4. Remove all injurious impurities from lubricated regions.
5. Hold gas and oil leakage (especially in the ring region) at an acceptable minimum level.

13.8.1 Lubrication System

The principle moving parts of an engine are positively lubricated by introducing a supply of oil from a pressurized system. An example of a lubrication system (for an air-cooled diesel engine) is shown in Fig. 13-27. The oil pump draws oil from the engine sump and delivers it through a control valve to the oil cooler. The oil then passes through the filter to the main oil gallery. From the main oil gallery it is branched to the main, the big end, and the camshaft bearings. Oil is also ducted to the injection pump. Through a passage in the camshaft bearing the oil flows to the tappet bridges. As the oil passages of tappets and tappet bridges line up during tappet motion, rocker arms and valve stems are pulse-lubricated

PETITIONER'S EXHIBIT 1002
US PATENT NO. 6,581,565

1 Sump
2 Suction pipe
3 Lube oil pump
4 Oil pressure control valve
5 Pressure pipe
6 Bypass pipe or alternative
7 Cooling coil or, alternatively:
8 Block-type oil cooler
9 Oil filter
10 Safety valve
11 Main oil gallery
12 Main bearing
13 Big end bearing
14 Camshaft bearing
15 Tappet (with timing groove to pulse-lubricate rocker arm)
16 Push rod (hollow, used as rocker arm oil feed pipe)
17 Rocker arm bearing
18 Metering plug (to control valve lubrication)
19 Push rod duct (used as cylinder-head-to-crankcase oil return pipe)
20 Splash hole to lubricate timing gears
21 Piston cooling nozzle
22 Oil pressure gauge adaptor
23 Oil pressure gauge

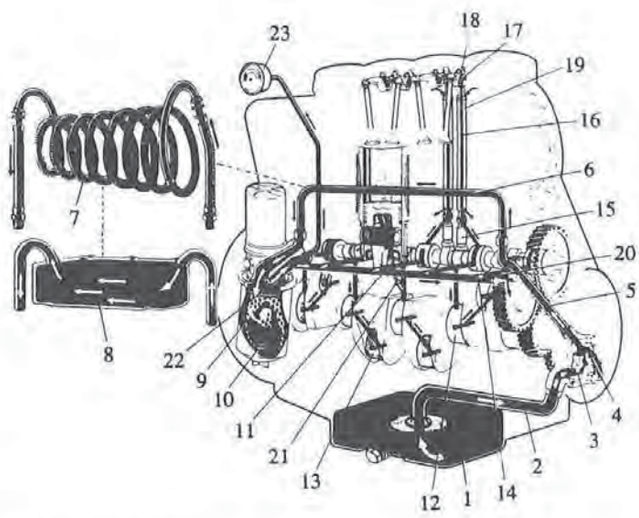


FIGURE 13-27
Lubrication system layout for air-cooled DI diesel engine. (*Courtesy Klöckner-Humboldt-Deutz AG.*)

through the tappets and pushrods. For cooling pistons and lubricating cylinders, oil is thrown against the underside of the piston through nozzles connected to the main bearings. Spring-loaded ball valves incorporated in the nozzles interrupt the jet cooling at low engine speeds to insure that the oil pressure remains above a safe level. The gears of the main timing train are splash-lubricated. The oil is returned from the injection pump and rocker chamber cover to the sump.

13.8.2 Lubricant Requirements

Table 13.1 lists the qualities required of engine oils to perform the main lubrication system functions. These qualities can be summarized under the following headings.[25]

OXIDATION STABILITY. The temperature of the oil and engine parts it contacts, the presence of oxygen, the nature of the metal surfaces and debris, and the products of the fuel combustion, all influence the oxidation of the hydrocarbon components in lubricating oil. High temperatures are the primary factor, and the top piston ring groove and the crankcase are the critical regions. The temperature of the top ring groove can easily reach 250°C. The lubricating oil when subject to these conditions must not, through oxidation, contribute to deposit formation, even after long periods of running. These deposits would eventually

PETITIONER'S EXHIBIT 1002
US PATENT NO. 6,581,565

TABLE 13.1
Functions and qualities required of engine oils

Main functions required	Where and when	Qualities required
Reduce frictional resistance	During cold-starting	Low enough viscosity to provide good pumping and avoid undue cranking resistance
	Between con-rod/ crankshaft bearings, and journals	Minimum viscosity without risk of metal-to-metal contact under the varying conditions of temperature, speed, and load
	Between pistons, rings, and cylinders	Sufficiently high viscosity at high temperatures; good lubrication property outside the hydrodynamic condition, especially at top-center
		Antiseizure properties, especially during the run-in period
Protect against corrosion and wear	During shut-down or when running at low temperature	Must protect metallic surfaces against corrosive action of fuel decomposition products (water, SO_2, HBr, HCl, etc.)
		Must resist degradation (resist oxidation, have good thermal stability)
	In normal running	Must counteract action of fuel and lubricant decomposition products at high temperatures, especially on non-ferrous metals
		By intervention in the friction mechanism must reduce the consequences of unavoidable metal-to-metal contact
		Must resist deposit formations which would affect lubrication (detergency or dispersive action)
		Must contribute to the elimination of dust and other contaminants (dispersive action)
Assist sealing	In the ring zone, especially at TC	Must have sufficient viscosity at high temperatures and low volatility
		Must limit ring and liner wear
		Must not contribute to formation of deposits in ring grooves and must prevent such formation
Contribute to cooling	Chiefly of pistons, rings, and con-rod bearings	Must have good thermal stability and oxidation resistance
		Must have low volatility
		Viscosity must not be too high
Facilitate the elimination of undesirable products	During oil drains to eliminate atmospheric dust, soot from diesel engines, Pb salts, wear debris, organic products from burned fuel and lubricants, and other contaminants which promote deposits or accelerate wear	Must be able to maintain in fine suspension all solid material (dispersivity) whatever the temperature and physical and chemical conditions (water)
		Must be able to solubilize certain organic compounds, particularly heavy oxidation products

Source: From Schilling.[25]

PETITIONER'S EXHIBIT 1002
US PATENT NO. 6,581,565

lead to ring sticking which results in excessive blowby. At high temperatures, deposits are related to the oxidized fraction of the oil.

The oil temperature in the crankcase is 120 to 130°C, or higher. Oil maintained at this temperature should neither form any acid products capable of attacking the bearing alloys nor form insoluble products which form deposits. Good-quality mineral oils cannot withstand these temperatures, so antioxidant and anticorrosive additives are used to control these problems. While antioxidants help to reduce deposit formation, detergent/dispersant additives are required to maintain any insoluble materials formed through oxidation in suspension.

DETERGENCY/DISPERSION. Except for deposits formed in the combustion chamber, deposits in the oil are controlled by its detergency. The amount of deposits formed depends on the fuel used, the quality of combustion, the temperature of the lubricating oil and coolant, and on the effectiveness of gas sealing at the piston rings. The detergency property is given to straight mineral oils by additives; the function of the detergent additive is to reduce the amount of deposits formed and make their removal easier.

At low temperatures, deposits are mainly byproducts of fuel combustion, and the detergency function is to keep them in suspension or solution in the oil. At high temperatures, deposits come from the oxidized fractions of the oil. The detergency function here is both to keep these products in suspension and to inhibit the reactions that lead to the formation of varnishes and lacquers. In addition, in diesel engines, the detergency helps in neutralizing the acidic reaction products from the sulfur compounds in the fuel.

WEAR REDUCTION. Wear is due to the individual and combined effects of corrosion, adhesion (i.e., metal-to-metal contact), and abrasion.

Corrosive attack by acidic products of combustion is one of the chief causes of cylinder and ring wear. The effect is worst at low cylinder wall temperatures. In diesel engines, the sulfur in the fuel increases the corrosive wear. Corrosive wear is effectively prevented by the use of detergent oils which neutralize the corrosive acids as they form, and by designing the cooling system to give appropriate metal temperatures.

Adhesive wear affects certain parts of the engine. In the upper cylinder, metal-to-metal contact between piston, rings, and cylinder walls takes place each time the engine is started (most significant during cold-starts) because there is insufficient oil in the top portion of the engine. Oils with antiwear additives and low viscosity at low temperatures provide a partial remedy. Adhesive wear also occurs on components such as cams, tappets, drive gears, rocker arm ends, and valve stems.

Abrasion results from the presence of atmospheric dust, and metallic debris from corrosive and adhesive wear, in the lubricating oil. Efficient air filtration is therefore most important (see Ref. 26 for a discussion of air filters). Elimination of

PETITIONER'S EXHIBIT 1002
US PATENT NO. 6,581,565

abrasive particle impurities from the oil system by filtration and periodic oil change is essential.

VISCOSITY. For low resistance to cranking and ease of starting, and rapid distribution of the oil while the engine is cold, a low oil viscosity at low ambient temperatures is required. When the engine (and oil) is fully warmed up, viscosity in the proper range is important for adequate sealing of the piston, acceptable oil consumption, and low friction losses. The viscosity of the oil at both low and normal engine temperatures (a spread of some 200 K) is, therefore, important. The viscosity of lubricating oils decreases with increasing temperature. The *pour point*, *viscosity*, and *viscosity index* are used to characterize the behavior of a lubricating oil for these aspects of engine operation.

The *pour point* is determined by cooling a sample of oil in a test jar until, when the jar is rotated from the vertical to the horizontal, no perceptible movement of the oil will occur within 5 s; 5°F above this temperature is the pour point.

The viscosity of lubricating oils is determined by measuring the time required for a specified volume of oil to flow through a capillary tube or orifice, contained in a constant temperature water bath. The *kinematic viscosity*, ν ($\nu = \mu/\rho$), is determined by this method. Use of a Saybolt tube with an orifice of specified diameter is the standard U.S. measurement practice. The viscosity is then given by the time t (in seconds) required to flow 60 cm^3 of oil, and is expressed as Saybolt universal seconds, SUS. Approximate conversion to centistokes (1 centistoke = 10^{-6} m^2/s) can be obtained via

$$\nu = at - \frac{b}{t}$$

where for $115 > t > 34$ s, $a = 0.224$ and $b = 185$; for $215 > t > 115$ s, $a = 0.223$ and $b = 155$; and for $t > 215$ s, $a = 0.2158$ and $b = 0$.[27]

The viscosity of lubricating oils decreases with increasing temperature. Since engine oils must operate over a range of temperatures, a measure of the rate of decrease is important. The *viscosity index*, an empirical number indicating the effect of temperature changes on viscosity, is used for this purpose;[28] a low viscosity index indicates a relatively large change of viscosity with temperature. To increase the viscosity index, lubricating oils incorporate additives called "viscosity-index improvers." These are high molecular weight compounds (molecular weight $\approx 10^3$ to 10^4) whose primary function is to reduce the viscosity variation with temperature.

The lubricating oil classification used most extensively is the SAE classification.[29] It depends solely on the viscosity of the oil. The seven different classification numbers 5W, 10W, 20W, 20, 30, 40, and 50 correspond to viscosity ranges; increasing numbers correspond to increasing viscosity, as shown in Fig. 13-28. SAE numbers followed by W (abbreviation for winter) refer to oils for use in cold climates, and viscosity is determined at −18°C (0°F). SAE numbers without W are applied to engine oils commonly used under warmer conditions;

PETITIONER'S EXHIBIT 1002
US PATENT NO. 6,581,565

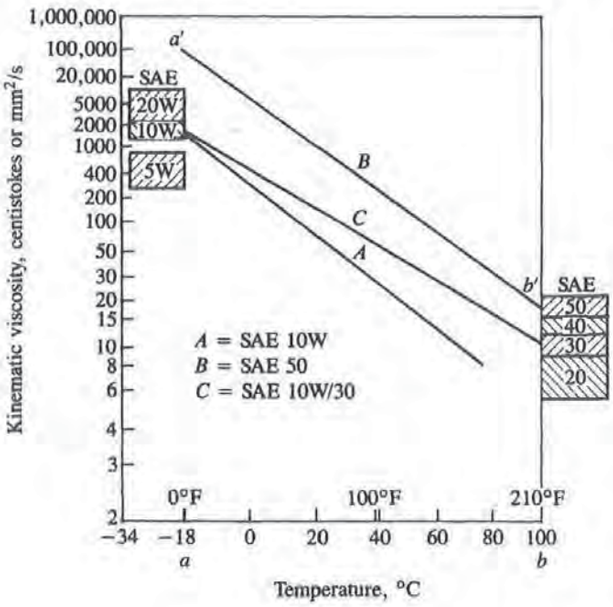


FIGURE 13-28
Viscosity versus temperature curves illustrating SAE lubricating oil classification.[25]

they are based on viscosity at 99°C (210°F). Multigrade oils (for example, 10W-40) satisfy service requirements at low as well as high temperatures in terms of the SAE classification. The first number indicates the viscosity at −18°C; the second number at 99°C. Examples are shown in Fig. 13-28. Multigrade oils have a higher viscosity index than single-grade oils, which make them more attractive for engine use.

PROBLEMS

13.1. (*a*) Show how friction mean effective pressure for a four-stroke cycle engine can be obtained from the brake power P_b, engine speed N, displaced volume V_d, and $\int p\,dV$ over the compression and expansion strokes ($= W_{c,ig}$).

(*b*) How is pumping mean effective pressure related to $\int p\,dV$ over the compression and expansion strokes and $\int p\,dV$ over the full four-stroke cycle?

(*c*) Find the brake power, total friction power, total friction imep, and pumping imep for a four-stroke cycle SI engine operating at 1800 rev/min with a measured brake torque of 32 N · m, a gross imep of 933 kPa, and a net imep of 922 kPa. $V_d = 0.496$ dm^3.

13.2. Three categories of friction are described in Sec. 13.3: boundary friction, hydrodynamic (or fully lubricated) friction, and turbulent dissipation. By means of Eq. (13.6), estimate the relative proportion of total friction work per cycle in each category for a four-cylinder automobile spark-ignition engine operating at 3000 rev/min.

13.3. For four-stroke cycle naturally aspirated multicylinder spark-ignition and diesel automobile engines at full load and one-third full load, at mid speed (2000 rev/min), give approximate estimates of the percentages of total friction mep in these three categories: pumping mep, rubbing friction mep, and accessory friction mep. State explicitly how you develop these estimates and what you include as accessories.

PETITIONER'S EXHIBIT 1002
US PATENT NO. 6,581,565

13.4. All of the friction measurement procedures except the difference between brake and gross indicated power or mep measured directly assume that motored engine friction and firing engine friction are closely comparable. This is not an accurate assumption for the pumping component. Summarize the differences between the gas exchange processes under motoring and firing conditions for a spark-ignition engine at a fixed part-load throttle setting that will result in the pumping work being significantly different under these two conditions.

13.5. On separate accurately proportioned sketches of the piston, cylinder, connecting rod, and crank mechanism (similar to Fig. 2-1), during the intake stroke (at 120° ATC), compression stroke (at 60° BTC), expansion stroke (at 60° ATC), and exhaust stroke (at 120° BTC), draw an arrow for each of the forces acting on the piston (pressure forces, force from connecting rod, friction force, inertia force). Mark clearly the *positive* direction of each force. Express each force in terms of cylinder pressure p_c, crankcase pressure p_{cc}, friction force F_f, piston area A_p, effective piston (and part of connecting rod) mass m_p, piston acceleration a, connecting rod force F_{cr}.

13.6. (*a*) For the DI diesel engine for the friction force data in Fig. 13-20, estimate the maximum pressure force on the piston (under full-load conditions) and the approximate magnitude of the inertia force [mass of piston plus part of the connecting rod (7 kg) × $\bar{S}_p$ × $(N/4)$]. Compare these forces with the piston friction force at time of peak pressure.

(*b*) Figure 13-6 shows the variation in friction force acting on the piston of a DI diesel engine under no-load and full-load firing conditions. Carefully sketch the shape (indicating direction and rough magnitude) of the cylinder pressure force on the piston, the piston velocity, and the piston acceleration, as functions of crank angle on the same graph as these friction forces. Use these graphs to explain the variation of piston friction force throughout the four strokes of the cycle.

13.7. (*a*) Show by dimensional analysis of the variables that govern the friction in a journal bearing (friction force F_f, oil viscosity μ, bearing diameter D_b, length L_b, mean clearance $\bar{h}$, shaft rotational speed N) that

$$\frac{F_f}{\mu D_b^2 N} = f\left(\frac{L_b}{D_b}, \frac{\bar{h}}{D_b}\right)$$

What additional physical assumptions are then required to obtain an equation of the form of (13.20)?

(*b*) Under what conditions can Eq. (13.23), an empirically developed relation for engine bearing fmep, be obtained from Eq. (13.20)?

13.8. Explain whether each of the following components of engine friction would be expected to depend on (1) crankshaft rotational speed N, (2) mean piston speed $\bar{S}_p$, (3) or both of these variables. Crankshaft journal bearings, connecting rod bearings, valve train, piston rings, piston skirt, water pump, fan, valve flow loss (resistance to flow through the inlet and exhaust valves).

REFERENCES

1. Ball, W. F., Jackson, N. S., Pilley, A. D., and Porter, B. C.: "The Friction of a 1.6 Litre Automotive Engine-Gasoline and Diesel," SAE paper 860418, 1986.
2. SAE Test Code J816b.

PETITIONER'S EXHIBIT 1002
US PATENT NO. 6,581,565

3. Rosenberg, R. C.: "General Friction Considerations for Engine Design," SAE paper 821576, 1982.
4. Schilling, A.: *Automobile Engine Lubrication*, Scientific Publication, 1972.
5. Millington, B. W., and Hartles, E. R.: "Frictional Losses in Diesel Engines," paper 680590, *SAE Trans.*, vol. 77, 1968.
6. Barnes-Moss, H. W.: "A Designer's Viewpoint," in *Passenger Car Engines, Conference Proceedings*, pp. 133–147, Institution of Mechanical Engineers, London, 1975.
7. Lancaster, D. R., Krieger, R. B., and Lienesch, J. H.: "Measurement and Analysis of Engine Pressure Data," paper 750026, *SAE Trans.*, vol. 84, 1975.
8. Gish, R. E., McCullough, J. D., Retzloff, J. B., and Mueller, H. T.: "Determination of True Engine Friction," *SAE Trans.*, vol. 66, pp. 649–661, 1958.
9. Brown, W. L.: "The Caterpillar IMEP Meter and Engine Friction," paper 730150, *SAE Trans.*, vol. 82, 1973.
10. Kovach, J. T., Tsakiris, E. A., and Wong, L. T.: "Engine Friction Reduction for Improved Fuel Economy," SAE paper 820085, 1982.
11. Cleveland, A. E., and Bishop, I. N.: "Several Possible Paths to Improved Part-Load Economy of Spark-Ignition Engines," SAE paper 150A, 1960.
12. Bishop, I. N.: "Effect of Design Variables on Friction and Economy," *SAE Trans.*, vol. 73, pp. 334–358, 1965.
13. *Piston Rings*, Mobil Technical Bulletin.
14. Nunney, M. J.: *The Automotive Engine*, Newnes-Butterworths, London, 1974.
15. Furuhama, S., Takiguchi, M., and Tomizawa, K.: "Effect of Piston and Piston Ring Designs on the Piston Friction Forces in Diesel Engines," SAE paper 810977, *SAE Trans.*, vol. 90, 1981.
16. Furuhama, S., Ashi, C., and Hiruma, M.: "Measurement of Piston Ring Oil Film Thickness in an Operating Engine," ASLE preprint 82-LC-6C-1, 1982.
17. McGeehan, J. A.: "A Literature Review of the Effects of Piston and Ring Friction and Lubricating Oil Viscosity on Fuel Economy," SAE paper 780673, *SAE Trans.*, vol. 87, 1978.
18. Furuhama, S., and Takiguchi, M.: "Measurement of Piston Frictional Force in Actual Operating Diesel Engine," SAE paper 790855, *SAE Trans.*, vol. 88, 1979.
19. Cameron, A.: *The Principles of Lubrication*, Wiley, New York, 1966.
20. McGeehan, J. A.: "A Survey of the Mechanical Design Factors Affecting Engine Oil Consumption," SAE paper 790864, *SAE Trans.*, vol. 88, 1979.
21. Armstrong, W. B., and Buuck, B. A.: "Valve Gear Energy Consumption: Effect of Design and Operational Parameters," SAE paper 810787, 1981.
22. Staron, J. T., and Willermet, P. A.: "An Analysis of Valve Train Friction in Terms of Lubrication Principles," SAE paper 830165, *SAE Trans.*, vol. 92, 1983.
23. Burke, C. E., Nagler, L. H., Campbell, E. C., Lundstrom, L. C., Zierer, W. E., Welch, H. L., Kosier, T. D., and McConnell, W. A.: "Where Does All the Power Go," *SAE Trans.*, vol. 65, pp. 713–737, 1957.
24. Dean, J. W., and Casebeer, H. M.: "Chrysler 340 Cu In. V-8 Engine Produces 275 HP at 5000 RPM," SAE paper 680019, 1968.
25. Schilling, A.: *Motor Oils and Engine Lubrication*, Scientific Publications, 1968.
26. Annand, W. J., and Roe, G. E.: *Gas Flow in the Internal Combustion Engine*, Haessner Publishing, 1974.
27. ASTM Standards, Part 17, Petroleum Products.
28. ASTM D2270-64.
29. SAE J300a.

PETITIONER'S EXHIBIT 1002
US PATENT NO. 6,581,565

CHAPTER 14

MODELING REAL ENGINE FLOW AND COMBUSTION PROCESSES

14.1 PURPOSE AND CLASSIFICATION OF MODELS

In engineering, modeling a process has come to mean developing and using the appropriate combination of assumptions and equations that permit critical features of the process to be analyzed. The modeling of engine processes continues to develop as our basic understanding of the physics and chemistry of the phenomena of interest steadily expands and as the capability of computers to solve complex equations continues to increase. Modeling activities can make major contributions to engine engineering at different levels of generality or detail, corresponding to different stages of model development, by:

1. Developing a more complete understanding of the process under study from the discipline of formulating the model;
2. Identifying key controlling variables to provide guidelines for more rational and therefore less costly experimental development efforts;
3. Predicting engine behavior over a wide range of design and operating variables to screen concepts prior to major hardware programs, to determine

PETITIONER'S EXHIBIT 1002
US PATENT NO. 6,581,565

trends and tradeoffs, and, if the model is sufficiently accurate, to optimize design and control;

4. Providing a rational basis for design innovation.

Each of these contributions is valuable. Whether a model is ready to pass from one stage to the next depends on the accuracy with which it represents the actual process, the extent to which it has been tested and validated, and the time and effort required to use the model for extensive sets of calculations and to interpret the results.

This chapter reviews the types of models and their primary components that are being developed and used to describe engine operating and emissions characteristics. These models describe the thermodynamic, fluid-flow, heat-transfer, combustion, and pollutant-formation phenomena that govern these performance aspects of engines. Many of the building blocks for these models have been described in the previous chapters. The purpose here is to show how fluid dynamics, heat-transfer, thermodynamics, and kinetics fundamentals can be combined at various levels of sophistication and complexity to predict, with varying degrees of completeness, internal combustion engine combustion and emissions processes, and hence engine operating characteristics.

For the processes that govern engine performance and emissions, two basic types of models have been developed. These can be categorized as *thermodynamic* or *fluid dynamic* in nature, depending on whether the equations which give the model its predominant structure are based on energy conservation or on a full analysis of the fluid motion. Other labels given to thermodynamic energy-conservation-based models are: zero-dimensional (since in the absence of any flow modeling, geometric features of the fluid motion cannot be predicted), phenomenological (since additional detail beyond the energy conservation equations is added for each phenomenon in turn), and quasi-dimensional (where specific geometric features, e.g., the spark-ignition engine flame or the diesel fuel spray shapes, are added to the basic thermodynamic approach). Fluid-dynamic-based models are often called multidimensional models due to their inherent ability to provide detailed geometric information on the flow field based on solution of the governing flow equations.

Some general observations about models of engine processes provide a context for the details that follow. The processes themselves are extremely complex. While much is known about these processes, they are not adequately understood at a fundamental level. At present, it is not possible to construct models that predict engine operation from the basic governing equations alone. Thus the objectives of any model development effort should be clearly defined, and the structure and detailed content of the model should be appropriate to these objectives. It is impractical to construct models that attempt to describe *all* important aspects of engine operation: more limited objectives are appropriate.

Due to this complexity of engine processes and our inadequate understanding at a fundamental level, most engine models are incomplete. Empirical relations and *ad hoc* approximations are often needed to bridge gaps in our

PETITIONER'S EXHIBIT 1002
US PATENT NO. 6,581,565

understanding of critical phenomena. Hence, since models will continue to develop greater completeness and generality, the emphasis in this chapter is on the basic relationships used in engine process models rather than the current status of these models.

Finally, an important issue in any overall engine model is balance in complexity and detail amongst the process submodels. A model is no more accurate than its weakest link. Thus critical phenomena should be described at comparable levels of sophistication.

14.2 GOVERNING EQUATIONS FOR OPEN THERMODYNAMIC SYSTEM

It is often required to model a region of the engine as an open thermodynamic system. Examples are the cylinder volume and the intake and exhaust manifolds (or portions of these volumes). Such a model is appropriate when the gas inside the open system boundary can be assumed uniform in composition and state at each point in time, and when that state and composition vary with time due to heat transfer, work transfer and mass flow across the boundary, and boundary displacement. Such an open system is illustrated in Fig. 14-1. The important equations are mass and energy conservation. These equations for an open system, with time or crank angle as the independent variable, are the building blocks for thermodynamic-based models.

14.2.1 Conservation of Mass

The rate of change of the total mass m of an open system is equal to the sum of the mass flows into and out of the system:

$$\dot{m} = \sum_j \dot{m}_j \tag{14.1}$$

Mass flows into the system are taken as positive; mass flows out are taken as negative. For conservation of the fuel chemical elements, it is convenient to use the fuel fraction f, which is defined as m_f/m, where m_f denotes the mass of fuel (or

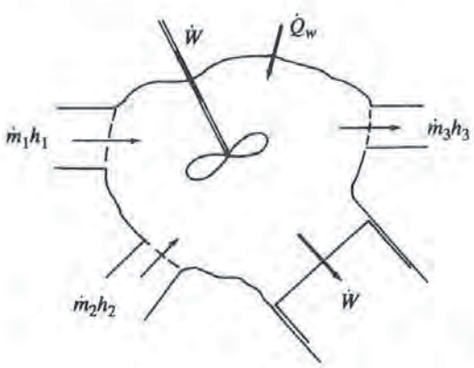


FIGURE 14-1
Open thermodynamic system.

PETITIONER'S EXHIBIT 1002
US PATENT NO. 6,581,565

fuel elements in the combustion products) in the open system:

$$\dot{m}_f = \frac{d}{dt}(mf) = \sum_j \dot{m}_{f,j} = \sum_j \dot{m}_j f_j \tag{14.2}$$

Differentiation of Eq. (14.2) leads to an equation for the rate of change of fuel fraction:

$$\dot{f} = \sum_j \left(\frac{\dot{m}_j}{m}\right)(f_j - f) \tag{14.3}$$

The fuel/air equivalence ratio ϕ is related to f via $\phi = f/[(F/A)_s(1-f)]$. Hence the rate of change of equivalence ratio of the material in the open system is

$$\dot{\phi} = \frac{1}{(F/A)_s}\frac{\dot{f}}{(1-f)^2} \tag{14.4}$$

14.2.2 Conservation of Energy

The first law of thermodynamics for the open system in Fig. 14-1 can be written:

$$\dot{E} = \dot{Q}_w - \dot{W} + \sum_j \dot{m}_j h_j \tag{14.5}$$

$\dot{Q}_w$ is the total heat-transfer rate into the system, across the system boundary, and equals the sum of the heat-transfer rates across each part of the boundary, $\sum_i \dot{Q}_{w,i}$. $\dot{W}$ is the work-transfer rate out of the system across the boundary; where the piston is displaced, the work-transfer rate equals $p\dot{V}$. Because all energies and enthalpies are expressed relative to the same datum (see Sec. 4.5.3), it is not necessary to include the heat released by combustion in Eq. (14-5); this is already accounted for in the energy and enthalpy terms.

The goal is to define the rate of change of state of the open system in terms of $\dot{T}$ and $\dot{p}$. Two approaches are commonly used, depending on whether the thermodynamic property routines provide values for internal energy u or enthalpy h. Thus $\dot{E}$ in Eq. (14.5) can be expressed as

$$\dot{E} = \frac{d}{dt}(mu) \qquad \text{or} \qquad \dot{E} = \frac{d}{dt}(mh) - \frac{d}{dt}(pV) \tag{14.6a, b}$$

It is assumed that the system can be characterized by T, p, and ϕ; thus

$$u = u(T, p, \phi) \qquad h = h(T, p, \phi) \qquad \rho = \rho(T, p, \phi) \tag{14.7}$$

and the rate of change of u, h, and ρ can be written in the form

$$\dot{\alpha} = \left(\frac{\partial \alpha}{\partial T}\right)\dot{T} + \left(\frac{\partial \alpha}{\partial p}\right)\dot{p} + \left(\frac{\partial \alpha}{\partial \phi}\right)\dot{\phi} \tag{14.8}$$

PETITIONER'S EXHIBIT 1002
US PATENT NO. 6,581,565

where α is u, h, or ρ. Using the ideal gas law in its two forms, $p = \rho RT$ and $pV = mRT$, and Eq. (14.8) for $\dot{\rho}$, an equation for $\dot{p}$ can be derived:

$$\dot{p} = \frac{\rho}{\partial\rho/\partial p}\left(-\frac{\dot{V}}{V} - \frac{1}{\rho}\frac{\partial\rho}{\partial T}\dot{T} - \frac{1}{\rho}\frac{\partial\rho}{\partial\phi}\dot{\phi} + \frac{\dot{m}}{m}\right) \tag{14.9}$$

Returning now to the energy conservation equation, expressing $\dot{E}$ in terms of $\dot{u}$ or $\dot{h}$, and $\dot{u}$ or $\dot{h}$ in terms of partial derivatives with respect to T, p, and ϕ, and substituting for $\dot{p}$ with Eq. (14.9), one can obtain equations for $\dot{T}$:

$$\dot{T} = \left[B - \frac{p}{D}\frac{\partial u}{\partial p}\left(\frac{\dot{m}}{m} - \frac{\dot{V}}{V} + \frac{\partial R}{\partial\phi}\frac{\dot{\phi}}{R}\right) - \frac{\partial u}{\partial\phi}\dot{\phi}\right] \Big/ \left(\frac{\partial u}{\partial T} + \frac{C}{D}\frac{p}{T}\frac{\partial u}{\partial p}\right) \tag{14.10}$$

where

$$B = -RT\frac{\dot{V}}{V} + \frac{1}{m}\left(\dot{Q}_w + \sum_j \dot{m}_j h_j - \dot{m}u\right)$$

$$C = 1 + \frac{T}{R}\frac{\partial R}{\partial T}$$

$$D = 1 - \frac{p}{R}\frac{\partial R}{\partial p}$$

(see Ref. 1, for example). From Ref. 2,

$$\dot{T} = \frac{B'}{A'}\left[\frac{\dot{m}}{m}\left(1 - \frac{h}{B'}\right) - \frac{\dot{V}}{V} - \frac{C'}{B'}\dot{\phi} + \frac{1}{B'm}\left(\sum_j \dot{m}_j h_j - \dot{Q}_w\right)\right] \tag{14.11}$$

where

$$A' = \frac{\partial h}{\partial T} + \frac{\partial\rho/\partial T}{\partial\rho/\partial p}\left(\frac{1}{\rho} - \frac{\partial h}{\partial p}\right)$$

$$B' = \frac{1 - \rho(\partial h/\partial p)}{\partial\rho/\partial p}$$

$$C' = \frac{\partial h}{\partial\phi} + \frac{\partial\rho/\partial\phi}{\partial\rho/\partial p}\left(\frac{1}{\rho} - \frac{\partial h}{\partial p}\right)$$

Equations (14.1), (14.3), (14.4), (14.9), and (14.10) or (14.11) can now be solved to obtain the state of the open system as a function of time. $\dot{V}$ is obtained from Eq. (2.6), and the thermodynamic properties and their derivatives from the models described in Chap. 4.

Often, for specific applications, the above equations can be simplified substantially. For the intake and exhaust systems (or sections of these systems such as the manifold or plenum, etc.), $\dot{V}$ is zero and effects of dissociation (the terms $\partial u/\partial p$, $\partial h/\partial p$, and $\partial R/\partial p$) can usually be neglected. For the cylinder during compression, dissociation can usually be neglected, also. Application of these equations during combustion must be related to the combustion model used. For the single-zone model often used in diesel engine simulations (see Sec. 10.4) the whole

PETITIONER'S EXHIBIT 1002
US PATENT NO. 6,581,565

of the combustion chamber is treated as one system. For the two-zone model used for spark-ignition engine simulations, the unburned mixture zone and the burned mixture zone are each treated as separate open systems, with volumes V_u and V_b, respectively, where $V_u + V_b = V$. If a thermal boundary-layer region is included (see Sec. 12.6.5) an additional open system must be defined.

14.3 INTAKE AND EXHAUST FLOW MODELS

14.3.1 Background

The behavior of the intake and exhaust systems are important because these systems govern the air flow into the engine's cylinders. Inducting the maximum air flow at full load at any given speed and retaining that mass within the engine's cylinders is a primary design goal. The higher the air flow, the larger the amount of fuel that can be burned and the greater the power produced. The important parameters are volumetric efficiency (for four-stroke cycle engines) or scavenging and trapping efficiencies (for two-stroke cycle engines), along with equal air flows to each engine cylinder (see Secs. 6.2, 6.6, and 7.6.2).

The objectives of any manifold model have an important bearing on its complexity and structure. If the goal is to provide the input or boundary conditions to a detailed model of in-cylinder processes, then sophisticated intake and exhaust system models are not necessarily required. If the manifold flows are the primary focus, then models that adequately describe the unsteady gas-flow phenomena which occur are normally required. Then simple models for the in-cylinder phenomena usually suffice to connect the intake and exhaust processes. The valves and ports, which together provide the major restriction to the intake and exhaust flow, largely decouple the manifolds from the cylinders.

Three types of models for calculating details of intake and exhaust flows have been developed and used:

1. Quasi-steady models for flows through the restrictions which the valve and port (and other components) provide
2. Filling and emptying models, which account for the finite volume of critical manifold components
3. Gas dynamic models which describe the spatial variations in flow and pressure throughout the manifolds

Each of these types of models can be useful for analyzing engine behavior. The appropriate choice depends on objectives, and the time and effort available. Each will now be reviewed.

14.3.2 Quasi-Steady Flow Models

Here the manifolds are considered as a series of interconnected components, which each constitute a significant flow restriction: e.g., air cleaner, throttle, port,

PETITIONER'S EXHIBIT 1002
US PATENT NO. 6,581,565

and valve for the intake system. The flow restriction each of these components represents is defined by their geometry and discharge coefficient, usually determined empirically under steady-state conditions. The gas flow rate through each component is computed using steady one-dimensional flow equations [see App. C, Eqs. (C.8) and (C.9)]: the actual flow is assumed to be quasi steady. These components are connected by the gas flow passing through them and the pressure ratios across them; mass accumulation between components is neglected.

Quasi-steady models are often used to calculate the flow into and out of the cylinder through the inlet and exhaust valves (see Secs. 6.3 and 6.5 and Fig. 6-20). If the pressure variation with time upstream of the valve is known or is small, as usually occurs with large plenums and short manifold pipe lengths, such methods are accurate enough to be useful. This approach has been used extensively with engine cycle simulations which predict engine performance characteristics from a thermodynamics-based analysis, to calculate the mass flow rates into and out of the cylinder (see Sec. 14.4). Such methods are not able to predict the variation of volumetric efficiency with engine speed, however, because many of the phenomena which govern this variation are omitted from this modelling approach (see Sec. 6.2 and Fig. 6-9).

14.3.3 Filling and Emptying Methods

In "filling and emptying" models, the manifolds (or sections of manifolds) are represented by finite volumes where the mass of gas can increase or decrease with time. Such models can range from treating the whole intake or exhaust system as a single volume to dividing these systems into many sections, with flow restrictions such as the air cleaner, throttle valve, or inlet valve at the beginning, in between volumes, or at the end. Each volume is then treated as a control volume (an open system of fixed volume) which contains gas at a uniform state. The mass and energy conservation equations developed in Sec. 14.2 [Eqs. (14.1), (14.3), (14.9), and (14.10) or (14.11)], coupled with information on the mass flow rates into and out of each volume [e.g., determined by the equations for flow through a restriction, Eqs. (C.8) and (C.9)] are used to define the gas state in each control volume. For intake and exhaust flows these equations can be simplified since the volumes are fixed ($\dot{V} = 0$), gas composition can be assumed frozen ($\partial u/\partial p$, $\partial h/\partial p$, and $\partial R/\partial p$ are then zero), unless backflow occurs or recycled exhaust is used for emission control changes in fuel fraction are not significant, and for intake systems it may be acceptable to omit heat transfer to the walls ($\dot{Q}_w$). Such methods characterize the contents of the manifold (or a region thereof) with a single gas temperature, pressure, and composition. These vary periodically with time as each cylinder in turn draws on the intake system and discharges to the exhaust system. Also, under transient conditions when engine load and/or speed change with time, manifold conditions will vary until the new engine steady-state conditions are established. Watson and Janota[3] discuss the application of filling and emptying models to manifolds in more detail. Such models can characterize these time-varying phenomena, spatially averaged over each mani-

PETITIONER'S EXHIBIT 1002
US PATENT NO. 6,581,565

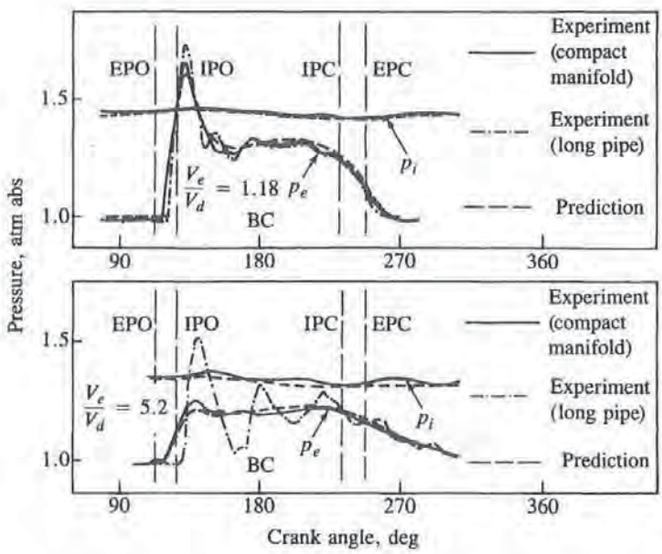


FIGURE 14-2
Comparison of intake and exhaust manifold pressures, p_i and p_e, predicted by filling and emptying model, with experimental data. Single-cylinder two-stroke loop-scavenged direct-injection diesel engine. Different ratios of exhaust system volume V_e to displaced volume V_d, and exhaust manifold shapes.[4]

EPO Exhaust port opens
IPO Inlet port opens
IPC Inlet port closes
EPC Exhaust port closes

fold region corresponding to each volume analyzed: however, they cannot describe the spatial variation of pressure (and other gas properties) due to unsteady gas dynamics in the manifolds.

A simple application of a filling and emptying model to the intake manifold of a spark-ignition engine was described in Sec. 7.6.2. The manifold was analyzed as a single control volume with the throttle plate controlling mass flow into the manifold and the engine cylinders controlling mass flow out. An equation for the rate of change of manifold pressure [Eq. (7.22)] was derived and used to explain how the air flow past the throttle varied as the throttle open angle was increased, as would occur at the start of a vehicle acceleration at part-throttle conditions (see Fig. 7-24).

A second example will illustrate the conditions under which filling and emptying models give sufficiently accurate predictions to be useful.[4] It concerns a single-cylinder two-stroke cycle loop-scavenged direct-injection diesel engine. The engine was modeled as three open systems (the intake system, the cylinder, the exhaust system) connected by flow restrictions. Various exhaust manifold volumes and shapes were examined, using nozzles at the manifold exit to simulate the exhaust-driven turbine. The in-cylinder models were calibrated to match the measured engine performance. Figure 14-2 shows the predicted and measured pressure variation at the exhaust system exit for two exhaust system volumes (V_e). With the compact manifold the measured and predicted pressures were in good agreement. With the larger exhaust system shown in the figure ($V_e/V_d = 5.2$) and the compact manifold, good agreement is again obtained. Only with the larger volume and long pipe exhaust system is there evidence in the measured pressure variation of substantial unsteady gas dynamic effects. For small manifolds, and manifolds that are compact in shape, filling and emptying models can be a useful predictive tool.

PETITIONER'S EXHIBIT 1002
US PATENT NO. 6,581,565

14.3.4 Gas Dynamic Models

Many induction and exhaust system design variables determine overall performance. These variables include the length and cross-sectional area of both primary and secondary runners, the volume and location of the plenums or junctions which join the various runners, the entrance or exit angles of the runners at a junction, the number of engine cylinders and their dimensions, intake and exhaust port and valve design, and valve lift and timing (see Secs. 6.2, 6.3, 6.7, and 7.6). Most of this geometric detail is beyond the level which can be incorporated into the models discussed above. Coupled with the pulsating nature of the flow into and out of each cylinder, these details create significant gas dynamic effects on intake and exhaust flows which require a more complete modeling approach.

Gas dynamic models have been in use for a number of years to study engine gas exchange processes. These models use the mass, momentum, and energy conservation equations for the unsteady compressible flow in the intake and exhaust. Normally, the one-dimensional unsteady flow equations are used.† These models often use a thermodynamic analysis of the in-cylinder processes to link the intake and exhaust flows. In the past, the method of characteristics was used to solve the gas dynamic equations. Finite difference techniques are used in more recent intake and exhaust flow models. The basic equations and assumptions of these models will now be reviewed.[5, 6]

UNSTEADY FLOW EQUATIONS. Consider the flow through the control volume within a straight duct shown in Fig. 14-3. It is assumed that the area change over the length dx of the control volume is small so the flow is essentially one-

† Two- and three-dimensional effects can be important and can be modeled with multidimensional flow models described in Sec. 14.5.

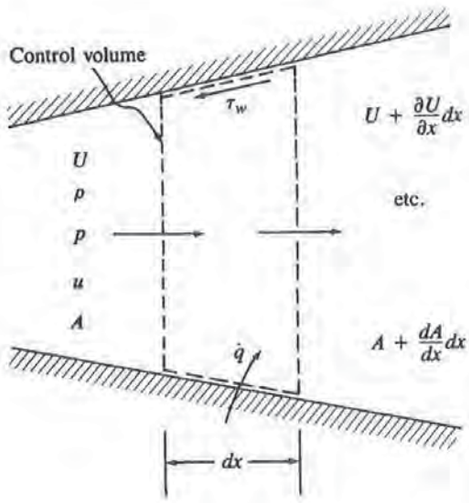


FIGURE 14-3
Control volume for unsteady one-dimensional flow analysis.

PETITIONER'S EXHIBIT 1002
US PATENT NO. 6,581,565

dimensional. Mass conservation requires that the rate of change of mass within the control volume equals the net flow into the control volume: i.e.,

$$\frac{\partial}{\partial t}(\rho A\, dx) = \rho AU - \left[\rho AU + \frac{\partial}{\partial x}(\rho AU)\, dx\right] \tag{14.12}$$

Retaining only first-order quantities, this equation simplifies to

$$\frac{\partial \rho}{\partial t} + \frac{\partial}{\partial x}(\rho U) + \frac{\rho U}{A}\frac{dA}{dx} = 0 \tag{14.13}$$

The momentum conservation equation states that the net pressure forces plus the wall shear force acting on the control volume surface equal the rate of change of momentum within the control volume plus the net flow of momentum out of the control volume. The net forces and momentum changes are given by:

Pressure forces:

$$pA - \left(p + \frac{\partial p}{\partial x}\, dx\right)\left(A + \frac{dA}{dx}\, dx\right) + p\frac{dA}{dx}\, dx = -A\frac{\partial p}{\partial x}\, dx$$

Shear forces:

$$-\tau_w \pi D\, dx = -\xi \frac{\rho U^2}{2} \pi D\, dx$$

where D is the equivalent diameter $(4A/\pi)^{1/2}$ and ξ is the friction coefficient given by $\tau_w/(\frac{1}{2}\rho U^2)$.

The rate of change of momentum within the control volume is

$$\frac{\partial}{\partial t}(U\rho A\, dx)$$

and the net efflux of momentum across the control volume surface is

$$\left(\rho + \frac{\partial \rho}{\partial x}\, dx\right)\left(U + \frac{\partial U}{\partial x}\, dx\right)^2\left(A + \frac{dA}{dx}\, dx\right) - \rho U^2 A = \frac{\partial}{\partial x}(\rho U^2 A)\, dx$$

Combining these terms into the momentum equation yields

$$-A\frac{\partial p}{\partial x}\, dx - \xi \frac{\rho U^2}{2} \pi D\, dx = \frac{\partial}{\partial t}(\rho UA\, dx) + \frac{\partial}{\partial x}(\rho U^2 A)\, dx \tag{14.14}$$

This can be rearranged and combined with the mass conservation equation (14.13) to give

$$\frac{\partial U}{\partial t} + U\frac{\partial U}{\partial x} + \frac{1}{\rho}\frac{\partial p}{\partial x} + 2\xi\frac{U^2}{D} = 0 \tag{14.15}$$

ENERGY CONSERVATION. The first law of thermodynamics for a control volume states that the energy within the control volume changes due to heat and shear work transfers across the control volume surface and due to a net efflux of

PETITIONER'S EXHIBIT 1002
US PATENT NO. 6,581,565

stagnation enthalpy resulting from flow across the control volume surface. The stagnation enthalpy h_0 is

$$h_0 = h + \frac{U^2}{2} = u + \frac{p}{\rho} + \frac{U^2}{2}$$

where u is the specific internal energy of the fluid (often approximated by $c_v T$). The shear work transfer across the control volume surface is zero.

The heat-transfer rate $\dot{Q}_w$ is given by

$$\delta\dot{Q}_w = \dot{q}\rho A \; dx$$

where $\dot{q}$ is the heat transfer per unit mass of fluid per unit time into the control volume.

The rate of change of energy within the control volume is

$$\frac{\partial E}{\partial t} = \frac{\partial}{\partial t}\left[(\rho A \; dx)\left(u + \frac{U^2}{2}\right)\right]$$

The net efflux of stagnation enthalpy is

$$\frac{\partial}{\partial x}\left[(\rho U A)\left(u + \frac{p}{\rho} + \frac{U^2}{2}\right)\right] dx$$

Hence, the equation for energy conservation becomes

$$\frac{\partial}{\partial t}\left[(\rho A \; dx)\left(u + \frac{p}{\rho} + \frac{U^2}{2}\right)\right] + \frac{\partial}{\partial x}\left[(\rho U A)\left(u + \frac{p}{\rho} + \frac{U^2}{2}\right)\right] dx - \dot{q}\rho A \; dx = 0 \tag{14.16}$$

Additional simplifications are possible. Expanding Eq. (14.16) and using the mass and momentum conservation equations yields

$$\frac{\partial u}{\partial t} + U\frac{\partial u}{\partial x} = \dot{q} + 2\xi\frac{U^3}{D} - \frac{p}{\rho A}\frac{\partial (UA)}{\partial x} \tag{14.17}$$

If u can be represented by $c_v T$ and $R/c_v = \gamma - 1$ is constant, Eq. (14.17) can be rearranged and simplified to give

$$\frac{\partial p}{\partial t} + U\frac{\partial p}{\partial x} - a^2\left(\frac{\partial \rho}{\partial t} + U\frac{\partial \rho}{\partial x}\right) - (\gamma - 1)\rho\left(\dot{q} + 2\xi\frac{U^3}{D}\right) = 0 \tag{14.18}$$

where the sound speed a for an ideal gas is given by

$$a^2 = \left(\frac{\partial p}{\partial \rho}\right)_s = \gamma\frac{p}{\rho} \tag{14.19}$$

If friction and heat-transfer effects are small enough to be neglected, Eqs. (14.15) and (14.18) can be considerably simplified. In the absence of these effects the flow is *isentropic*; it has uniform entropy which is constant with time and is often called *homentropic* flow.[6] If the duct area can be neglected then the continuity equation, (14.13), can be simplified also.

PETITIONER'S EXHIBIT 1002
US PATENT NO. 6,581,565

These one-dimensional unsteady flow equations have been used for a number of years to study the flow in the intake and exhaust systems of spark-ignition and diesel engines, both naturally aspirated and turbocharged. Two types of methods have been used to solve these equations: (1) the method of characteristics and (2) finite difference procedures. The characteristic methods have a numerical accuracy that is first order in space and time, and require a large number of computational points if resolution of short-wavelength variations is important. Finite difference techniques can be made higher order and prove to be more efficient:[7, 8] this approach is now preferred. Methods for treating the boundary conditions will also be described.

METHOD OF CHARACTERISTICS. The method of characteristics is a well-established mathematical technique for solving hyperbolic partial differential equations. With this technique, the partial differential equations are transformed into ordinary differential equations that apply along so-called characteristic lines. Pressure waves are the physical phenomenon of practical interest in the unsteady intake flow, and these propagate relative to the flowing gas at the local sound speed. In this particular application, the one-dimensional unsteady flow equations, (14.13) and (14.15), are rearranged so that they contain only the local fluid velocity U and local sound speed a.

Since the absolute velocity of small amplitude sound waves is $U + a$ in the direction of flow and $U - a$ opposite to the flow direction, the lines of slope $U \pm a$ are the *position* characteristics of the propagating pressure waves which define the position x of the pressure wave at time t. *Compatability conditions* accompanying the position characteristics relate U to a. The compatability relationships are expressed in terms of variables (called Riemann invariants) which are constant along the position characteristics for constant-area homentropic flow, though they vary if these restrictions do not apply. Thus, the solution of the mass and momentum conservation equations for this one-dimensional unsteady flow is reduced to the solution of a set of ordinary differential equations.

The equations are usually solved numerically using a rectangular grid in the x and t directions. The intake or exhaust system is divided into individual pipe sections which are connected at junctions. A mesh is assigned to each section of pipe between junctions. From the initial values of the variables at each mesh point at time $t = 0$, the values of the Riemann variables at each mesh point at subsequent time steps are then determined. Gas pressure, density, and temperature can then be calculated from the energy conservation equation and the ideal gas law. Additional details of the method are given by Benson *et al.*[5, 6]

FINITE DIFFERENCE METHODS. Finite difference methods for solving the one-dimensional unsteady flow equations in intake and exhaust manifolds are proving more efficient and flexible than the method of characteristics. The conservation equations, (14.13), (14.14), and (14.16), can be rearranged and written in

PETITIONER'S EXHIBIT 1002
US PATENT NO. 6,581,565

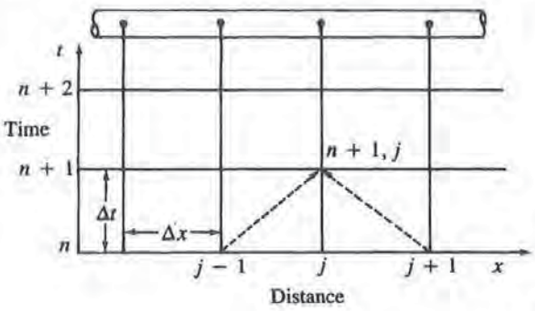


FIGURE 14-4
Mesh in time-distance plane for application of one-step Lax-Wendroff method to intake or exhaust pipe.

matrix form as

$$\frac{\partial}{\partial t}\begin{pmatrix}\rho\\ \rho U\\ \rho u\end{pmatrix}+\frac{\partial}{\partial x}\begin{pmatrix}\rho U\\ \rho U^2+p\\ pU+\rho Uu\end{pmatrix}=\begin{pmatrix}-\rho U\dfrac{dA}{dx}\\ -\rho\dfrac{U^2}{A}\dfrac{dA}{dx}-\rho\dfrac{2\xi U|U|}{D}\\ -\dfrac{4h_c(T-T_w)}{D\rho}-\dfrac{1}{A}\dfrac{dA}{dx}\left(\dfrac{1}{2}\rho U^3+\dfrac{\gamma}{\gamma-1}Up\right)\end{pmatrix} \tag{14.20}$$

The fluid viscous shear is small relative to friction at the wall in the momentum equation, and heat conduction and viscous dissipation prove negligible relative to convective heat transfer at the wall in the energy conservation equation. These equations have the vector form:

$$\frac{\partial F}{\partial t}+\frac{\partial G}{\partial x}=H \tag{14.21}$$

where G and H are functions of F only. Several finite difference methods have been used to solve Eq. (14.21) (see Refs. 7, 8, and 9). The one-step Lax-Wendroff method will be illustrated.[8] Equation (14.21) can be developed into a Taylor series with respect to time, and the time and space derivatives approximated by central differences around the mesh point, shown in Fig. 14-4, as

$$F_j^{n+1}=F_j^n-\frac{1}{2}\frac{\Delta t}{\Delta x}(G_{j+1}^n-G_{j-1}^n)+\Delta tH_j^n$$
$$+\frac{1}{4}\left(\frac{\Delta t}{\Delta x}\right)^2[(G'^n_{j+1}+G'^n_j)(G^n_{j+1}-G^n_j)-(G'^n_j+G'^n_{j-1})(G^n_j-G^n_{j-1})] \tag{14.22}$$

where $G'=\partial G/\partial F$. This equation is first-order accurate, unless H is small. For stability in the integration process, the time step and mesh size must satisfy the requirement that

$$C=(|U|+a)\frac{\Delta t}{\Delta x}<1 \tag{14.23}$$

where C is the Courant number.

PETITIONER'S EXHIBIT 1002
US PATENT NO. 6,581,565

TABLE 14.1
Boundary conditions for unsteady one-dimensional finite element analysis[9]

Pipe ends		
Out-flow	Mass	$\rho_1 U_1 A_1 = \rho_2 U_2 A_2$
	Energy	$c_p T_1 + \frac{U_1^2}{2} = c_p T_2 + \frac{U_2^2}{2}$
	Isobaric	$p_2 = p_3$
In-flow	Mass	$\rho_1 U_1 A_1 = \rho_2 U_2 A_2$
	Energy	$c_p T_3 = c_p T_2 + \frac{U_2^2}{2} = c_p T_1 + \frac{U_1^2}{2}$
	Isentropic	$p_2/\rho_2^\gamma = p_3/\rho_3^\gamma$
Pipe junctions		
	Mass	$V \frac{\partial \rho}{\partial t} = \sum_i \rho_i U_i A_i$
	Energy	$\rho V \frac{\partial u}{\partial t} = \sum_i (\rho_i U_i A_i)\left(c_p T_i + \frac{U_i^2}{2}\right)$
	Pressure	$p_1 - \Delta p_1 = p_2 + \Delta p_2 = p_3 + \Delta p_3 = \cdots$ $\Delta p_i / p_i = C_i (U_i / a_i)^2$

These finite difference solution methods usually require the introduction of some form of dissipation or damping to prevent instabilities and large nonphysical oscillations from occurring with nonlinear problems with large gradients (e.g., a shock wave in the exhaust system). Amplification of the physical viscosity and the addition of artificial viscosity, damping, and smoothing terms to Eq. (14.22) are frequently used techniques.[8, 9]

The boundary conditions at pipe ends and junctions are obtained from the appropriate conservation equations and pressure relations, as illustrated in Table 14.1. Out-flows and in-flows obviously conserve mass and energy. For the flow out through a restriction, there is no pressure recovery downstream: for flow in through a restriction, the flow upstream of the restriction is isentropic. For pipe junctions, the conservation equations are applied to the control volume contained within the dashed line in the sketch in the table. The pressure boundary conditions are most easily estimated by modifying the simple constant-pressure assumption with pressure losses at each pipe exit or entry, calculated from experimentally determined loss coefficients (see Fig. 6-5).[9]

Calculations of intake and exhaust flows using these techniques predict the variations in intake and exhaust manifold pressure with crank angle (as shown, for example, in Fig. 6-7), in single and multicylinder engines, with acceptable accuracy.[7, 9] Measured volumetric efficiency variations with engine speed, manifold design, and valve dimensions and timing are adequately predicted also. Figure 14-5*a* shows the instantaneous exhaust and intake mass flow rates for cylinder number 1 of a four-cylinder spark-ignition engine at wide-open throttle at 1500 rev/min. Note how gas dynamic effects distort the exhaust flow. Note also the "reverse" flows into the cylinder past the exhaust valve and out of the

PETITIONER'S EXHIBIT 1002
US PATENT NO. 6,581,565

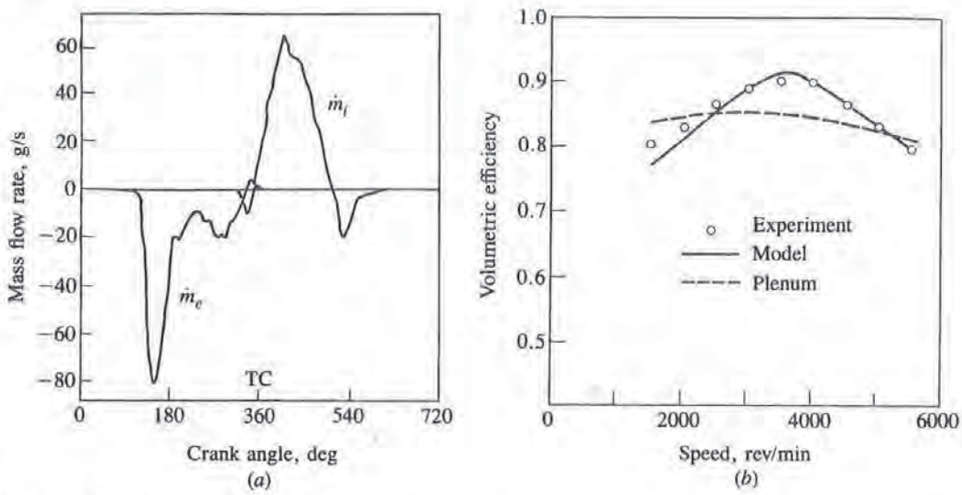


FIGURE 14-5
(*a*) Predicted mass flow rate through the exhaust valve $\dot{m}_e$ and through the intake valve $\dot{m}_i$ in cylinder 1, four-cylinder four-stroke-cycle spark-ignition engine at wide-open throttle and 1500 rev/min. Flows into cylinder are positive; flows out are negative. (*b*) Predicted and measured volumetric efficiency at wide-open throttle for four-cylinder spark-ignition engine. Solid line: one-dimensional unsteady flow model. Dashed line: quasi-steady flow calculation based on infinite plenums for manifolds.[7]

cylinder past the intake valve at the end of the exhaust process, and the larger reverse flow at the end of the intake process at this low engine speed. Figure 14-5*b* shows the volumetric efficiency for this engine based on these predicted mass flow rates, as a function of speed. Experimental values and values predicted with quasi-steady flow equations and infinite plenums for manifolds are also shown. These results clearly demonstrate the important role that intake and exhaust system gas dynamics play in determining both the engine speed at which peak breathing efficiency occurs and the air charging characteristics over the full engine speed range.[7]

14.4 THERMODYNAMIC-BASED IN-CYLINDER MODELS

14.4.1 Background and Overall Model Structure

If the mass transfer into and out of the cylinder during intake and exhaust, the heat transfer between the in-cylinder gases and the cylinder head, piston, and cylinder liner, and the rate of charge burning (or energy release from the fuel) are all known, the energy and mass conservation equations permit the cylinder pressure and the work transfer to the piston to be calculated. Engine models of this type have been developed and used extensively to predict engine operating characteristics (indicated power, mean effective pressure, specific fuel consumption, etc.) and to define the gas state for emission calculations. These models effectively follow the changing thermodynamic and chemical state of the working fluid through the engine's intake, compression, combustion, expansion, and exhaust processes; they are often called engine *cycle simulations.*

PETITIONER'S EXHIBIT 1002
US PATENT NO. 6,581,565

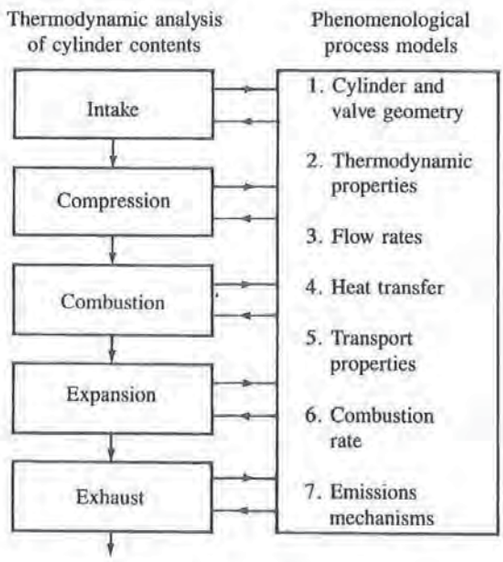


FIGURE 14-6
Logic structure of thermodynamic-based simulations of internal combustion engine operating cycle.

The starting point for these cycle simulations is the first law of thermodynamics for an open system, developed in Sec. 14.2. This is applied to the cylinder volume for the intake, compression, combustion, expansion, and exhaust processes that in sequence make up the engine's operating cycle. The structure of this type of engine simulation is indicated in Fig. 14-6. Then, during each process, submodels are used to describe geometric features of the cylinder and valves or ports, the thermodynamic properties of the unburned and burned gases, the mass and energy transfers across the system boundary, and the combustion process.

During intake and compression, the cylinder volume is modeled as a single open system. Application of the conservation equations in the form of Eqs. (14.1), (14.3), and (14.10) or (14.11) for the intake and then the compression process gives[2]

Intake:

$$\dot{m} = \dot{m}_i - \dot{m}_e \tag{14.24}$$

$$\dot{f} = \frac{\dot{m}_i}{m}(f_i - f) - \frac{\dot{m}_e}{m}(f_e - f) \tag{14.25}$$

$$\dot{T} = \frac{B}{A}\left[\frac{\dot{m}}{m}\left(1 - \frac{h}{B}\right) - \frac{\dot{V}}{V} - \frac{C}{B}\dot{\phi} + \frac{1}{Bm}(\dot{m}_i h_i - \dot{m}_e h_e - \dot{Q}_w)\right] \tag{14.26}$$

where m is the mass of gas in the cylinder, $\dot{m}_i$ and $\dot{m}_e$ are the mass flow rates through the inlet valve and the exhaust valve, and f is the fuel fraction m_f/m. The subscripts i and e denote properties of the flow through the intake and exhaust valves, respectively. The thermodynamic properties for these flows are the values upstream of the valves and therefore depend on whether the flow is into or out of the cylinder.

PETITIONER'S EXHIBIT 1002
US PATENT NO. 6,581,565

Compression:

$$\dot{m} = 0 \qquad \dot{f} = 0 \tag{14.27a, b}$$

$$\dot{T} = \frac{B}{A}\left(-\frac{\dot{V}}{V} - \frac{\dot{Q}_w}{Bm}\right) \tag{14.28}$$

The pressure is then determined from Eq. (14.9).

During intake and compression, the working fluid composition is frozen. The composition and thermodynamic properties can be determined using the models described in Secs. 4.2 and 4.7. Mass flows across open valves are usually calculated using one-dimensional compressible flow equations for flow through a restriction (see App. C and Secs. 6.3.2 and 14.3.2) or filling and emptying models (Sec. 14.3.3). The more accurate unsteady gas dynamic intake (and exhaust) flow models described in Sec. 14.3.4 are sometimes used to calculate the mass flow into the engine cylinder in complete engine cycle simulations when the variation in engine flow rate with speed is especially important:[10] the disadvantage is much increased computing time. Heat transfer during intake and compression is calculated using one of the Nusselt-Reynolds number relations for turbulent convective heat transfer described in Sec. 12.4.5. The transport properties, viscosity, and thermal conductivity used in these correlations can be obtained from relations such as Eqs. (4.52) to (4.55).

During combustion which starts with the spark discharge in spark-ignition engines and with spontaneous ignition of the developing fuel-air jets in compression-ignition engines, the actual processes to be modeled become much more complex. Many approaches to predicting the burning or chemical energy release rate have been used successfully to meet different simulation objectives. The simplest approach has been to use a one-zone model where a single thermodynamic system represents the entire combustion chamber contents and the energy release rate is defined by empirically based functions specified as part of the simulation input. At the other extreme, quasi-geometric models of turbulent premixed flames are used with a two-zone analysis of the combustion chamber contents—an unburned and a burned gas region—in more sophisticated simulations of spark-ignition engines. In compression-ignition engines, multiple-zone models of the developing fuel-air jets have been used to provide more detailed predictions of the combustion process and nonuniform cylinder composition and state. These combustion models will be reviewed in the following sections (14.4.2 and 14.4.3) and the appropriate conservation equations for the *combustion process* will be developed there. In diesels, radiation heat transfer becomes important during the combustion process (see Sec. 12.5).

The *expansion process* is either treated as a continuation of the combustion process or, once combustion is over, can use the form of the mass, fuel, and energy conservation equations which hold during compression [Eqs. (14.27) and (14.28)]. The exhaust process conservation equations for a one-zone open-system model of the cylinder contents are[2]

PETITIONER'S EXHIBIT 1002
US PATENT NO. 6,581,565

Exhaust:

$$\dot{m} = -\dot{m}_e \qquad \dot{f} = -\frac{\dot{m}_e}{m}(f_e - f) \tag{14.29a, b}$$

$$\dot{T} = \frac{B}{A}\left[-\frac{\dot{m}_e}{m}\left(1 - \frac{h}{B}\right) - \frac{\dot{V}}{V} - \frac{C}{B}\dot{\phi} + \frac{1}{Bm}(-\dot{m}_e h_e - \dot{Q}_w)\right] \tag{14.30}$$

where h_e, the enthalpy of the flow through the exhaust valve, is the cylinder average enthalpy for flow *out* of the cylinder and the exhaust system gas enthalpy if reverse flow occurs.

The engine operating cycle should end with the working fluid at the same state that it started out. For the first calculations of the sequence of processes in Fig. 14-6, property values defining the initial state of the fluid in the cylinder were assumed. If the values of these properties at the end of the first cycle differ from the assumed values, the cycle calculation is repeated with the appropriate new initial values until the discrepancy is sufficiently small. Convergence with these cycle simulations occurs within a few iterations.

The working fluid state is now defined throughout the operating cycle. The work transfer to the piston per cycle

$$W_c = \oint p\, dV \tag{14.31}$$

can now be obtained. From W_c, the masses of fuel and air inducted, m_f and m_a, and engine speed N, all the engine *indicated* performance parameters can be calculated: power, torque, mean effective pressure, specific fuel consumption, fuel-conversion efficiency; as well as volumetric efficiency, residual gas fraction, total heat transfer, etc. With a friction model, the indicated quantities can be converted to brake quantities.

The more sophisticated of these thermodynamic-based engine cycle simulations define the working fluid state throughout the cycle in sufficient detail for useful predictions of engine emissions to be made. The discussion in Chap. 11 of emission-formation mechanisms indicates that our understanding of how some of these pollutants form (e.g., NO_x, CO) is reasonably complete, and can be modeled accurately. The formation processes of the other pollutants (unburned hydrocarbons and particulates) are not adequately understood, though modeling activities are continuing to contribute to that understanding. The key features of models for predicting engine emissions were discussed in Chap. 11.

Cycle simulations and combustion models which have been developed for spark-ignition engines, where the fuel, air, residual gas mixture is essentially uniformly mixed, are discussed in Sec. 14.4.2. Compression-ignition engine simulations and combustion models are then discussed in Sec. 14.4.3. The special features required for prechamber engine models are reviewed in Sec. 14.4.4. Finally, thermodynamic-based models for more complex engine systems—multicylinder, turbocharged, and turbocompounded engines—are discussed in Sec. 14.4.5.

PETITIONER'S EXHIBIT 1002
US PATENT NO. 6,581,565

14.4.2 Spark-Ignition Engine Models

These models have usually followed the conceptual structure indicated in Fig. 14-6. Our focus here is on the combustion submodels that have been developed and used successfully. Features of the spark-ignition engine combustion process that permit major simplifying assumptions for thermodynamic modeling are: (1) the fuel, air, residual gas charge is essentially uniformly premixed; (2) the volume occupied by the reaction zone where the fuel-air oxidation process actually occurs is normally small compared with the clearance volume—the flame is a thin reaction sheet even though it becomes highly wrinkled and convoluted by the turbulent flow as it develops (see Sec. 9.3); thus (3) for thermodynamic analysis, the contents of the combustion chamber during combustion can be analyzed as two zones—an unburned and a burned zone.

Useful combustion chamber design information can be generated with simple geometric models of the flame. In the absence of strong swirl, the surface which defines the leading edge of the flame can be approximated by a portion of the surface of a sphere. Thus the mean burned gas front can also be approximated by a sphere. Then, for a given combustion chamber shape and assumed flame center location (e.g., the spark plug), the spherical burning area A_b [see Eq. (9.40)], the burned gas volume V_b [see Eq. (9.39)], and the combustion chamber surface "wetted" by the burned gases can be calculated for a given flame radius r_b and piston position (defined by crank angle) from purely geometric considerations.† The practical importance of such "model" calculations is that (1) the mass burning rate for a given burning speed S_b (which depends on local turbulence and mixture composition) is proportional to the spherical burning area A_b as given by Eq. (9.44); (2) the heat transfer occurs largely between the burned gases and the walls and is proportional to the chamber surface area wetted by the burned gases $A_{b,w}$ [see Eq. (12.21)]. Using the fact that the density ratio across the flame ρ_u/ρ_b is approximately constant and equal to 4, the unburned and burned gas volumes V_u and V_b can be related to the unburned and burned mass fractions $(1 - x_b)$ and x_b, respectively.

Examples of the results of such flame geometry calculations are shown in Figs. 14-7 and 14-8.[11] Figure 14-7*a* shows spherical flame areas A_b as a function of flame radius r_b for two different chambers and two plug locations and the TC piston position. The much larger flame area and shorter flame travel length of the central plug location are obvious. Such area data can be plotted as a function of burned gas volume V_b, as shown in Fig. 14-7*b*, so that comparisons of $A_b(r_b)$ for different chambers at the same mass fraction burned can be made. The advantage of a more compact chamber with higher central clearance height is apparent. Figure 14-8 shows that burned-gas-wetted wall area on the cylinder head, cylin-

† Note that the center of this sphere may be convected away from the spark plug location, especially if some swirl is present. However, only strong swirling and squish flows produce major distortions to the flame surface shape.

PETITIONER'S EXHIBIT 1002
US PATENT NO. 6,581,565

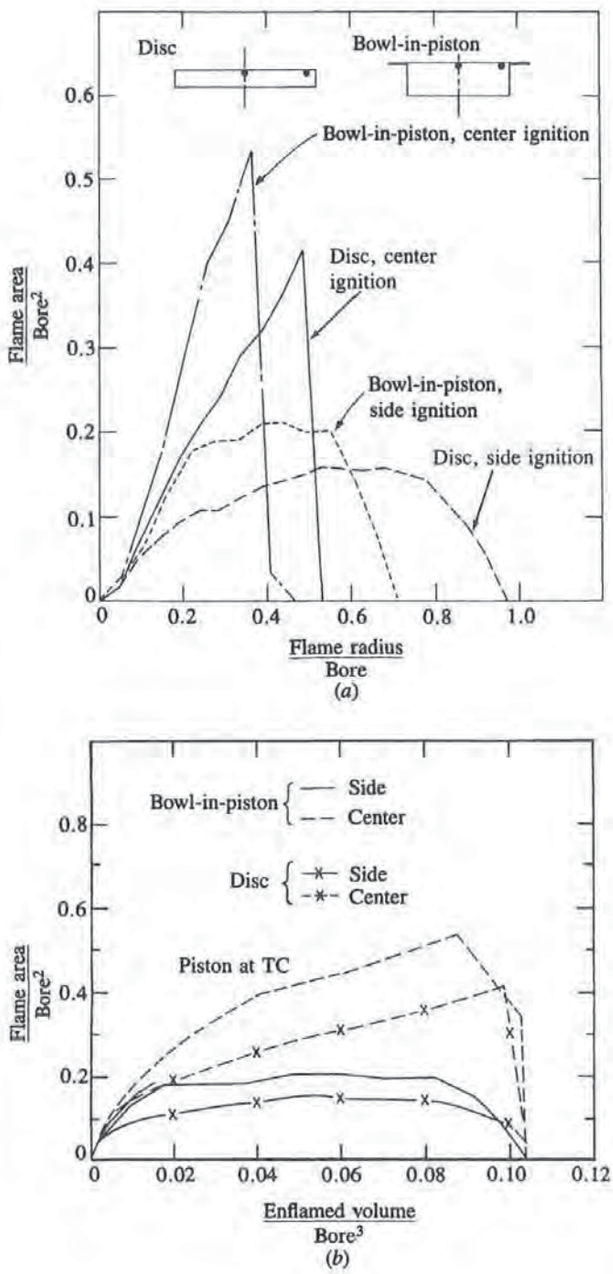


FIGURE 14-7
Calculated spark-ignition engine spherical flame surface area: (*a*) as a function of flame radius for different combustion chamber shapes and spark plug locations and (*b*) as a function of enflamed volume. Piston in top center position.[11]

der wall, and piston as a function of flame radius and crank angle for an open chamber with central ignition. The cylinder head and piston are the dominant areas early in the expansion stroke when the burned gas temperatures and heat fluxes are highest.

Mass fraction burned versus crank angle profiles determined from a first law analysis of cylinder pressure data, as shown in Figs. 9-2, 9-5, and 9-8, have an essentially universal dimensionless shape, as indicated in Fig. 9-13. Much useful

PETITIONER'S EXHIBIT 1002
US PATENT NO. 6,581,565

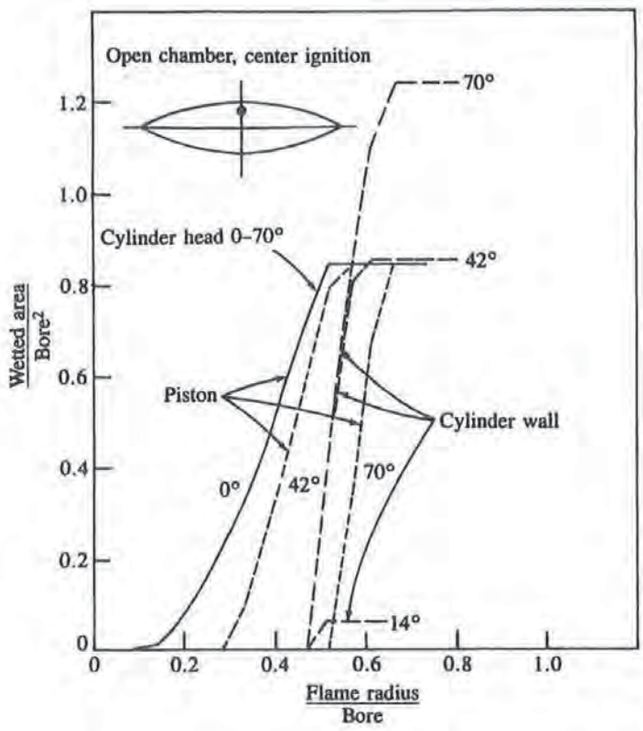


FIGURE 14-8
Calculated burned-gas-wetted wall area as a function of radius based on spherical flame model of an open-chamber SI engine with center plug location, for piston locations of 0°, 42°, and 70°.[11]

analysis has been done with engine simulations where this universal combustion profile has been used as a calculation input. The S-shaped mass fraction burned profile is often represented by the Wiebe function:

$$x_b = 1 - \exp\left[-a\left(\frac{\theta - \theta_0}{\Delta\theta}\right)^{m+1}\right] \tag{14.32}$$

where θ is the crank angle, θ_0 is the start of combustion, $\Delta\theta$ is the total combustion duration ($x_b = 0$ to $x_b \approx 1$), and a and m are adjustable parameters which fix the shape of the curve. Actual mass fraction burned curves have been fitted with $a = 5$ and $m = 2$.[12]

The conservation equations for an open system [Eqs. (14.1) and (14.10) or (14.11)] are now applied to the unburned gas zone ahead of the flame and to the burned zone behind the flame, in turn (see Fig. 9-4). For premixed engines, $\dot{f}$ and $\dot{\phi}$ are zero. During combustion, $\dot{m}$ and $\dot{m}_j$ in Eq. (14.10) or Eq. (14.11) are the mass flow rate across the flame sheet. This is $-\dot{m}_b$ for the unburned zone system and $+\dot{m}_b$ for the burned zone system; $\dot{m}_b$ is given by $m\dot{x}_b$, with $\dot{x}_b$ obtained by differentiating Eq. (14.32).

To calculate the effect of heat transfer on the burned gas state more accurately, the burned gas zone in Fig. 9-4 can be modeled in two parts: an adiabatic core and a boundary-layer region. The intent here is to account for the fact that heat loss to the walls primarily cools the burned gas adjacent to the wall, and only indirectly affects the core gas through the change in pressure that results

PETITIONER'S EXHIBIT 1002
US PATENT NO. 6,581,565

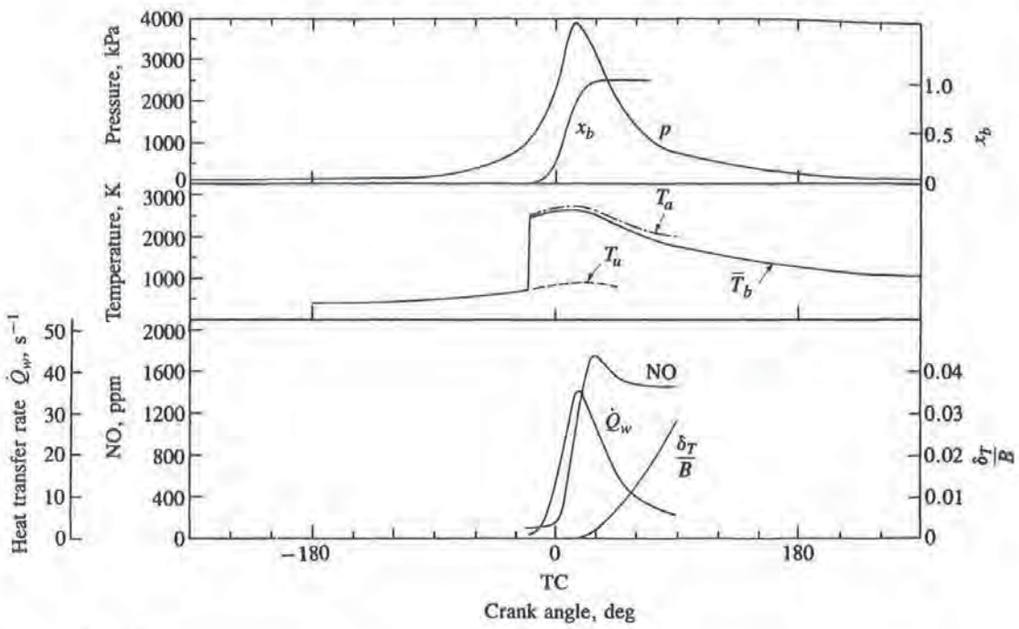


FIGURE 14-9
Cylinder pressure p, mass fraction burned x_b, unburned and burned gas temperatures (T_u = unburned, T_a = adiabatic burned core, $\bar{T}_b$ = mean burned gas temperatures), heat-transfer rate $\dot{Q}_w$ (normalized by fuel flow rate × heating value), thermal boundary-layer thickness δ_T, and mean nitric oxide concentration in the burned gases, through a four-stroke engine operating cycle, predicted by thermodynamic-based cycle simulation. 5.7-dm^3 displacement eight-cylinder engine operating at wide-open throttle, 2500 rev/min, with equivalence ratio = 1.1. Gross indicated mean effective pressure is 918 kPa and specific fuel consumption is 254 g/kW · h.[13]

from heat loss. The open-system conservation equations, (14-1) and (14.10) or (14.11), are now applied to the core and boundary-layer region separately. The boundary-layer region covers that portion of the combustion chamber wall wetted by the burned gases, as shown in Fig. 9-4, and is of thickness δ_T, which increases with time. The temperature of the boundary-layer zone (assumed uniform) is usually taken to be the mean of the wall temperature and burned gas core temperature. Equation (14.10) or Eq. (14.11) is used to relate the enthalpy flux due to the mass flow across the inner edge of the boundary layer (which has an enthalpy equal to the core gas enthalpy), the heat transfer to the wall, the changing energy within the boundary-layer system due to its increasing mass and changing state, and the work transfer due to its changing volume.

An example of predictions of cylinder pressure, unburned and burned gas temperatures, heat-transfer rate, and boundary-layer thickness, based on an assumed 50° total burn duration for a 5.7-dm^3 eight-cylinder engine at wide-open throttle and 2500 rev/min is shown in Fig. 14-9.[13] Appropriately based predictions of overall engine performance parameters made with this type of thermodynamic model agree well with engine data. Figure 14-10 shows predictions of indicated specific fuel consumption and exhaust gas temperature as a function of

PETITIONER'S EXHIBIT 1002
US PATENT NO. 6,581,565

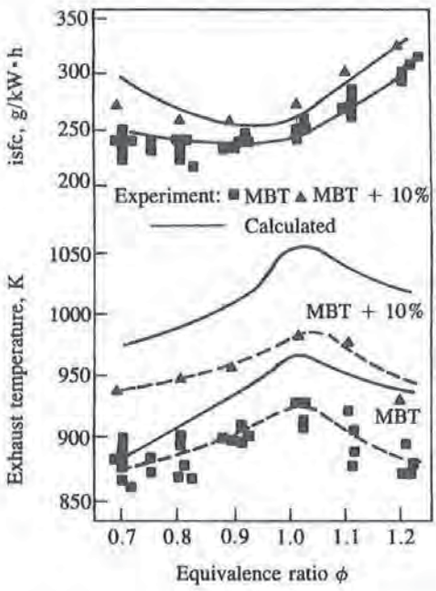


FIGURE 14-10
Predicted and measured indicated specific fuel consumption and exhaust temperature as a function of the fuel/air equivalence ratio for a spark-ignition engine operated at 1250 rev/min and imep of 379 kPa. MBT: maximum brake torque timing. MBT + 10%: combustion timing retarded to give 10 percent fuel consumption penalty.[14]

the fuel/air equivalence ratio at fixed load and speed. The isfc predictions and data agree well (except for very lean mixtures with retarded timing where cycle-by-cycle combustion variations are sufficiently large so predictions based on the average cycle lose accuracy); the predicted curves for exhaust temperature show the same trends as the experimental data. However, they are higher due to underestimation of the heat losses during the exhaust process.[14]

The output from such thermodynamic-based cycle simulations has replaced the fuel-air cycle as a predictor of effects of major variables on engine performance and efficiency. An instructive example of the value of such predictions is shown in Fig. 14-11, where fuel consumption at constant equivalence ratio, load, and speed has been computed as a function of total burn duration and heat loss to the chamber walls: increasing burn duration and heat loss both worsen fuel consumption.[15] Such data can be used to assess the efficiency improvements that should result from reduced heat transfer (e.g., reduced chamber surface area) and increased burn rate. Obviously the dependence of burn rate on engine design and operating parameters has not been modeled; the burn rate profile was a calculation input. Such models are most useful either (1) when the burn rate profile is *not critical* to the problem under study or (2) when predictions for a *range* of assumed burn rate profiles provide the required information.

So far we have discussed engine cycle simulations where details of the combustion process have been specified as input. The same thermodynamic-based simulation structure can be used in conjunction with a combustion model which *predicts* the rate of fuel burning. Various combustion models have been proposed and used for this purpose. Some of these are empirically based; some are based on the highly wrinkled, thin reaction-sheet flame model described in Sec. 9.3. All

PETITIONER'S EXHIBIT 1002
US PATENT NO. 6,581,565

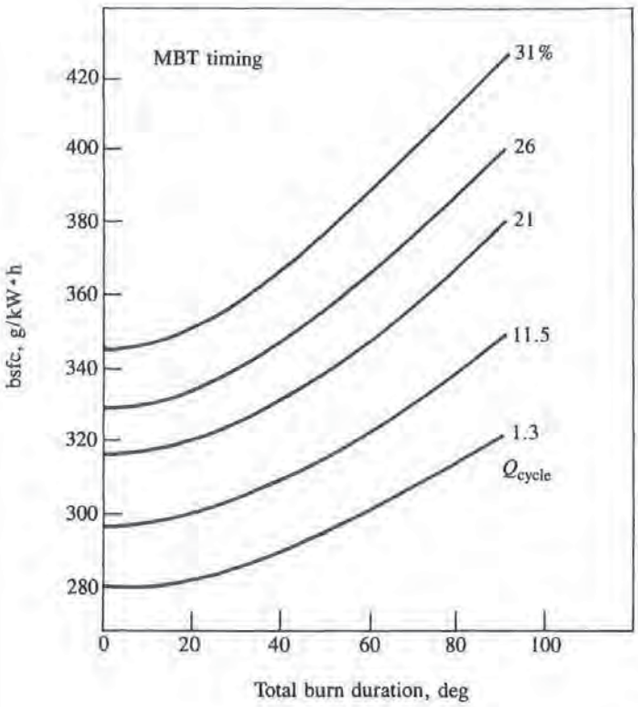


FIGURE 14-11
Predicted brake specific fuel consumption as a function of heat transfer per cycle to the combustion chamber walls (as a percent of the fuel's heating value) and total burn duration [$\Delta\theta$ in Eq. (14.32)]. 1250 rev/min, 262 kPa bmep, fuel/air equivalence ratio = 0.91, maximum brake torque spark timing.[15]

these models assume that the overall flame shape approximates a portion of a sphere centered at or near the spark plug. Empirical flame models have difficulty appropriately describing the three phases of the combustion process—flame development, rapid burning, and termination—with sufficient generality to be widely useful. One such model, based on the experimental data shown in Fig. 9-30, has been used successfully to evaluate different combustion chambers.[16, 17] The burning speed S_b [defined by Eq. (9.44)] is related empirically to the laminar flame speed S_L (see Sec. 9.3.3), the local rms velocity fluctuation u'_T [see Eq. (8.22)] under motored engine conditions, the firing and motored cylinder pressure at the same crank angle, and spark advance. While a good fit to the data in Fig. 9-30 for engine flames during their turbulent rapid-burning phase was obtained, during the flame development period a correction factor was required to fit the data.

Spark-ignition engine combustion models with a more fundamental framework have been developed and used. Based on coupled analysis of flame front location and cylinder pressure data, Keck and coworkers[18–20] have derived the following burning law:

$$\frac{dm_b}{dt} = \rho_u A_f S_L + \frac{\mu}{\tau_b} \tag{14.33}$$

$$\frac{d\mu}{dt} = \rho_u A_f u_T (1 - e^{-t/\tau_b}) - \frac{\mu}{\tau_b} \tag{14.34}$$

PETITIONER'S EXHIBIT 1002
US PATENT NO. 6,581,565

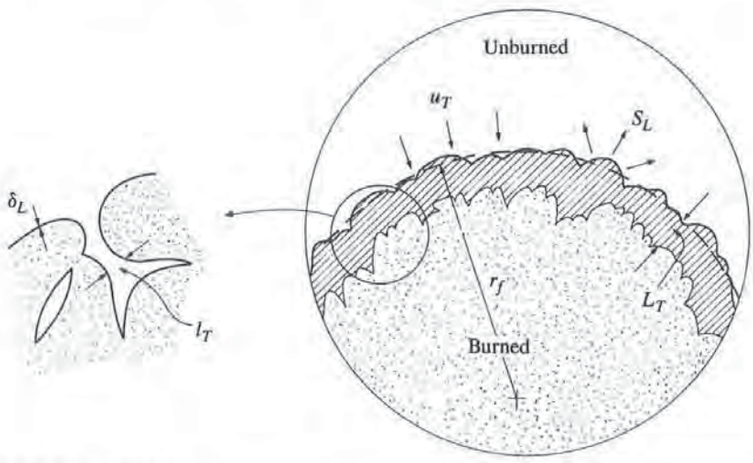


FIGURE 14-12
Schematic of turbulent premixed spark-ignition engine flame, illustrating the physical basis for burning law of Eqs. (14.33) to (14.35). The approximately spherical front of the "thick" turbulent flame (dashed line) diffuses outward at the laminar flame speed S_L. Fresh mixture also crosses this front at a characteristic velocity u_T due to turbulent convection. Schematic on left shows detailed flame structure: δ_L is a reaction-sheet thickness, l_T is characteristic scale of wrinkles in the sheet.

where

$$\mu = m_e - m_b = \rho_u(V_f - V_b) = \rho_u l_T(A_L - A_f) \tag{14.35}$$

is a parametric mass (interpreted as the mass entrained within the flame region that has yet to burn), u_T a characteristic speed, and $\tau_b = l_T/S_L$ is a characteristic burning time. l_T, A_L, V_f, A_f, V_b are defined in Sec. 9.3.4.

Figure 14-12 illustrates the physical basis for this model. The first term in Eq. (14.33) represents the laminar (diffusive) propagation forward of the approximately spherical front of the "thick" turbulent flame; the second term represents the burning of mixture already entrained within this flame front. In Eq. (14.34), which describes the rate of change of *unburned* mixture mass μ within the flame zone, the first term represents the turbulent convection of unburned mixture across the spherical front of the flame and the second term represents the mass rate of burning of entrained but not yet burned mixture which is contained within the "wrinkles" and "islands," which the distorting and stretching of the thin reaction sheet by the turbulent flow produces. This has been called an "entrainment" or "eddy-burning" model for the above reasons. The exponential term in brackets in Eq. (14.34) allows for the fact that the flame sheet initially is spherical and laminarlike: it requires a time of about τ_b to develop into a turbulent flame.

The behavior of Eqs. (14.33) and (14.34) in four important limits is:

1. For a quiescent mixture, $u_T \to 0$ or $l_T \to \infty$,

$$S_b \to S_L \tag{14.36a}$$

PETITIONER'S EXHIBIT 1002
US PATENT NO. 6,581,565

2. Initially, as $t \to 0$,

$$S_b \to S_L \tag{14.36b}$$

3. Quasi-steady state, $d\mu/dt \approx 0$,

$$S_b \approx u_T + S_L \tag{14.36c}$$

4. Final burning stage after the flame front reaches the wall, $t \geq t_w$ (when $A_f \to 0$),

$$\frac{\dot{m}_b}{\dot{m}_b(t_w)} = e^{-(t-t_w)/\tau_b} \tag{14.36d}$$

To apply Eqs. (14.33) and (14.34), the quantities u_T and τ_b (or $l_T = \tau_b S_L$) must be evaluated. Two approaches have been taken: (1) use of empirical correlations for these variables, derived from engine flame data (such as that described in Sec. 9.3.4); (2) use of more fundamental models to predict these quantities.

Keck has derived the following correlations for u_T and l_T, based on the application of Eqs. (14.33) and (14.34) to several sets of engine combustion data:

$$u_T = 0.08\bar{u}_i\left(\frac{\rho_u}{\rho_i}\right)^{1/2} \tag{14.37}$$

$$l_T = 0.8L_{iv}\left(\frac{\rho_i}{\rho_u}\right)^{3/4} \tag{14.38}$$

u_T was found to be proportional to $\sqrt{\rho_u}$ (at time of spark) and to correlate well with mean inlet gas speed $\bar{u}_i = \eta_v(A_p/A_{iv})\bar{S}_p$, where η_v is volumetric efficiency, A_p is piston area, A_{iv} is the maximum open area of the inlet valve, $\bar{S}_p$ is mean piston speed. l_T appears to scale with valve lift, L_{iv}; it decreases with increasing density at a rate proportional to $\rho_u^{-3/4}$. While u_T and l_T are not constant during the combustion process, their variation is modest.[18]

A quantitative comparison of predicted and measured flame radius as a function of time is shown in Fig. 14-13 for hydrogen and propane fuel-air mixtures which exhibit widely different behavior:[18] the figure indicates both the behavior and validity of the model. Predicted burned gas expansion speeds u_b [see Eq. (9.43)] are shown in Fig. 14-13*a* as a function of burned gas radius; the parameters u_T and l_T were chosen to fit the propane data. Figure 14-13*b* shows that the measured flame front radii, r_f, are in good agreement with the predicted flame and burned gas radii, r_f and r_b, for these two fuels. The initial expansion speed of hydrogen is about 10 times that of propane. Since $r_f \approx r_b$ for early times, $S_b \approx S_L$ and this ratio is expected. As r_b become large, $(r_f - r_b) \to u_T\tau_b$, which is several times smaller for hydrogen mixtures than for propane mixtures.

An adaption of this approach developed by Tabaczynski and coworkers[21, 22] is based on the following model of turbulent flame propagation. The vorticity in the turbulent flow field is concentrated in vortex sheets which are

PETITIONER'S EXHIBIT 1002
US PATENT NO. 6,581,565

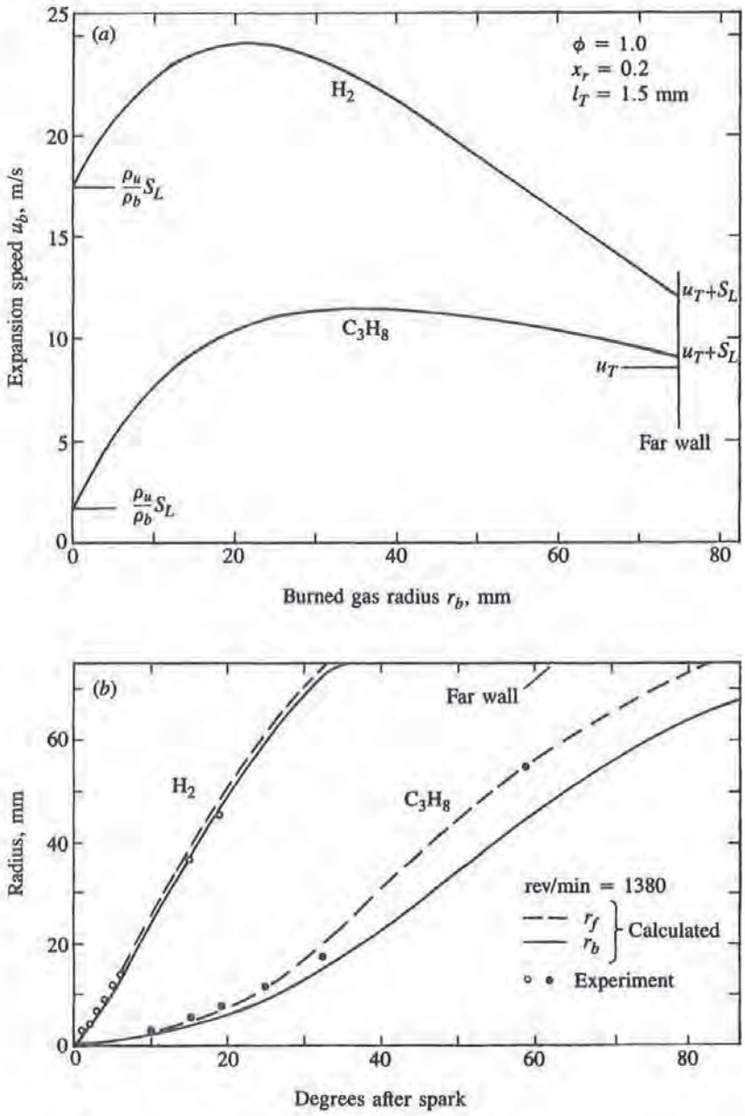


FIGURE 14-13
(*a*) Calculated burned gas expansion speed u_b for stoichiometric hydrogen-air and propane-air mixtures as a function of burned gas radius r_b. (*b*) Comparison of experimentally measured (points) and calculated (dashed curve) flame radii r_f for these mixtures as a function of crank angle. Also shown (solid curve) is the burned gas radius r_b.[18]

of a size comparable to the Kolmogorov scale l_K [see Eq. (8-11)]. These vortex sheets are assumed to have a characteristic spacing which is of the order of the Taylor microscale l_M, which is a function of the integral length scale l_I and the turbulent Reynolds number as indicated by Eq. (8.15). From these turbulence assumptions it is argued that ignition sites propagate along the vortex sheets with a velocity $u' + S_L$, where u' is the local turbulence intensity. The propagation of the reaction front between the vortex sheets is assumed to be a laminar process.

PETITIONER'S EXHIBIT 1002
US PATENT NO. 6,581,565

Thus, in Eqs. (14.33) and (14.34), u_T and τ_b are given by

$$u_T \approx u' \qquad \text{and} \qquad \tau_b = \frac{l_T}{S_L} \approx \frac{l_M}{S_L} \tag{14.39}$$

where l_M, the microscale, is determined from the integral scale and the turbulent Reynolds number via Eq. (8.15), assuming that the turbulence is homogeneous and isentropic. The task therefore becomes one of evaluating u' and l_I.

One approach used is to relate the turbulence intensity at the start of the combustion process to the mean intake flow velocity through the valve: e.g.,[23]

$$u'_0 = \frac{C\bar{S}_p B^2}{L_{\text{iv}} D_{\text{iv}}} \tag{14.40}$$

where $\bar{S}_p$ is the mean piston speed, B the bore, and L_{iv} and D_{iv} the lift and diameter of the inlet valve. It is assumed that the integral length scale at the start of combustion, $l_{I,0}$, is proportional to a characteristic flow dimension, usually the clearance height h. Then, during combustion, the unburned portion of the charge is assumed to undergo isentropic compression sufficiently rapidly that the angular momentum of the "eddies" is conserved and the length scale follows the eddy size, i.e., a simple rapid distortion process occurs:

$$u' = u'_0\left(\frac{\rho}{\rho_0}\right)^{1/3} \qquad l_I = l_{I,0}\left(\frac{\rho_0}{\rho}\right)^{1/3} \tag{14.41}$$

This model predicts an increase in turbulence intensity and decrease in length scale with compression, which is only partly confirmed by experiment.

A more sophisticated approach is to describe the dynamic behavior of the turbulence with one or more rate equations for the key turbulence parameters: k the turbulent kinetic energy and ε the dissipation rate of k. Turbulence is generated, diffused, and dissipated by the flow field, so the rate of change of turbulent kinetic energy k can be written:

$$\frac{dk}{dt} = P_k + D_k - \rho\varepsilon \tag{14.42}$$

where the term P_k represents the volumetric production of turbulence and the diffusion term D_k can be modeled as a gradient diffusion with an effective turbulent viscosity which dominates the laminar diffusion process. In this application, Eq. (14.42) is integrated over the combustion chamber (or a region of the chamber) to provide spatially averaged turbulence predictions. Then the diffusion terms become boundary fluxes: e.g., the transport of kinetic energy across the combustion chamber boundary due to flow through the inlet or exhaust valve. The dissipation rate ε is related to the integral length scale via

$$\varepsilon = \frac{C_D k^{3/2}}{l_I} \qquad C_D = 0.09 \tag{14.43}$$

l_I can be taken as proportional to the clearance height ($l_I \approx 0.22\ h$), or an additional rate equation for a second turbulence parameter, the dissipation rate ε, can

PETITIONER'S EXHIBIT 1002
US PATENT NO. 6,581,565

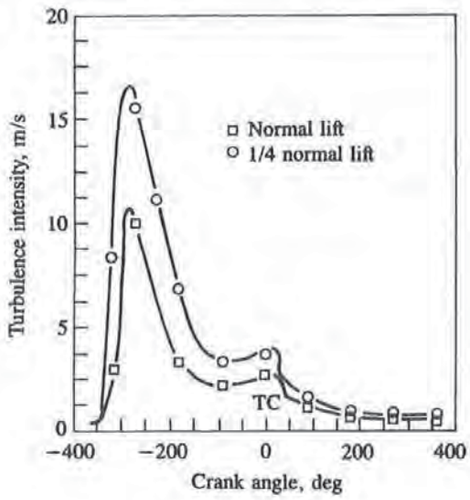


FIGURE 14-14
Predicted turbulence intensity u' as a function of crank angle and valve lift in engine operating at 1500 rev/min, 414 kPa imep, with a compression ratio of 10.[27]

be used. In the more complete of these $k - \varepsilon$ turbulence models,[24] the ε equation is similar to the k equation with production, diffusion, and dissipation terms. These $k - \varepsilon$ turbulence models are discussed more fully in Sec. 14.5.2.

The application of this turbulence model to the spark-ignition engine combustion chamber becomes complicated and the reader is referred to references for the details.[25–28] Considerable success with predicting trends in mass burning rate has been achieved with this type of model. Design variables examined include: swirl, squish, valve lift, bore/stroke ratio. The advantage of such models is that they are straightforward computationally so that extensive parametric sets of calculations are feasible. The major disadvantage is the *ad hoc* nature of the turbulence and flame models which involve plausible but arbitrary assumptions. Sample predictions are shown in Figs. 14-14 and 14-15.[27, 28] Figure 14-14 shows the variation in turbulence intensity u' in an engine with a disc-shaped combustion chamber, throughout the operating cycle. A normal valve-lift profile and

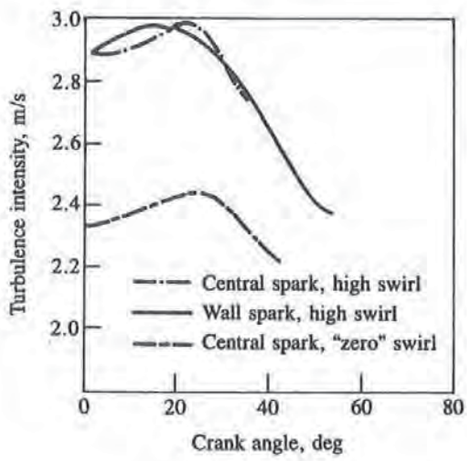


FIGURE 14-15
Predicted turbulence intensity during combustion for high and "zero" swirl levels for central and cylinder wall spark plug locations. Same engine and operating conditions as in Fig. 14-14.[28]

PETITIONER'S EXHIBIT 1002
US PATENT NO. 6,581,565

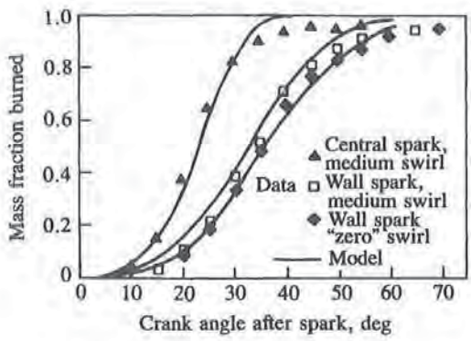


FIGURE 14-16
Comparisons of predicted and measured mass fraction burned versus crank angle profiles for same swirl levels and plug locations as Fig. 14-15.[28]

reduced maximum valve-lift profile (one-quarter normal) are shown. The high levels of turbulence generated during the first half of the intake process decay substantially before the latter stages of the compression stroke produce some amplification. Reduced valve lift produces higher levels of turbulence intensity at combustion, as is well known.[29] Figure 14-15 shows the predicted turbulence behavior during combustion for a disc-shaped chamber for different swirl levels and plug locations. Swirl is shown to increase the turbulence intensity. Comparison of predicted and measured mass fraction burned profiles versus crank angle for different swirl levels and plug locations are shown in Fig. 14-16. The large flame area effects (shown here in the two limiting plug locations: side wall and center) and significant though lesser effect of swirl are correctly modeled. Such models are useful for relating changes in spark-ignition engine design and operating variables to changes in engine performance, via predictions of changes in flame development and propagation.

The above type of combustion model has been used to obtain explicit relations for the flame development and rapid burning angles as functions of engine design and operating variables.[30] The equation for the mass burning rate, (14.33), was effectively integrated over the relevant portion of the total combustion process; the turbulent characteristic velocity was assumed proportional to $\bar{S}_p$, the mean piston speed. The flame development angle was found to vary as

$$\Delta\theta_d = C(\bar{S}_p \nu)^{1/3}\left(\frac{h}{S_L}\right)^{2/3} \tag{14.44}$$

where ν is the kinematic viscosity ($\nu = \mu/\rho$) and h is the clearance height at ignition. C is a constant which depends on engine geometry and is determined by matching Eq. (14.44) with engine data. The rapid burn angle (here taken as the crank angle between $x_b = 0.01$ and 1.0) is given by

$$\Delta\theta_b = C'\left(\frac{B}{h^*}\right)\left(\frac{\rho_i}{\rho_u^*}\right)^{10/9}(\bar{S}_p \nu^*)^{1/3}\left(\frac{h_i}{S_L^*}\right)^{2/3} \tag{14.45}$$

where C' is a constant which depends on engine geometry, B is the bore, the subscript i denotes the value at ignition, and the superscript $*$ denotes the value

PETITIONER'S EXHIBIT 1002
US PATENT NO. 6,581,565

at cylinder conditions where $x_b = 0.5$. These expressions show reasonable agreement with observed trends in $\Delta\theta_d$ and $\Delta\theta_b$.

14.4.3 Direct-Injection Engine Models

In direct-injection compression-ignition and stratified-charge engines, the liquid fuel is injected into the cylinder as one or several jets just prior to ignition. In large direct-injection compression-ignition engines, the air flow is essentially quiescent. However, in medium and smaller size DI engines, the air flow is usually swirling about the cylinder axis at up to 10 times the crankshaft rotational speed; this air-flow pattern increases the rate of entrainment of air into the fuel jet to increase the fuel-air mixing rate. Thus modeling of the ignition and combustion processes for direct-injection types of engines is much more complex than for premixed-charge spark-ignition engines. The unsteady liquid-fuel jet phenomena—atomization, liquid jet and droplet motion, fuel vaporization, air entrainment, fuel-air mixing, and the ignition chemistry—all play a role in the heat-release process (see Chap. 10). It is not yet possible to model all these phenomena from a fundamental basis, even with the most sophisticated fluid-dynamic-based codes now available (see Sec. 14.5), since many of these processes are not yet adequately understood. However, models at various levels of detail and empiricism have been developed and have proven useful in direct-injection diesel and stratified-charge engine analysis. This section reviews the important features of single-zone heat-release models and phenomenological jet-based combustion models. Their relative simplicity and modest computer time requirements make them especially useful for diesel cycle simulation and more complex engine system studies.

Single-zone models assume that the cylinder contents can be adequately described by property values representing the average state, and use one or more algebraic formulas to define the heat-release rate. The functional forms of these formulas are chosen to match experimentally observed heat-release profiles (see Sec. 10.4.2). Coefficients in these formulas, which may vary with engine design details and operating conditions, are determined empirically by fitting with data. The phenomenological description of diesel combustion developed by Lyn (see Sec. 10.3) comprises three primary phases: the ignition delay period, the premixed fuel-burning phase, and the mixing-controlled fuel-burning phase. Ignition delay correlations are reviewed in Sec. 10.6.6. Here models for the second and third phases, when the major heat release occurs, are summarized (see Ref. 31 for a more extensive review). The attraction of the one-zone heat-release approach is its simplicity: however, since it cannot fully describe the complex phenomena which comprise the compression-ignition engine combustion process, substantial empirical input must be used. Several one-zone heat-release models have been proposed and used (e.g., Refs. 32 to 34). These use simple equations to describe the rate of release of the fuel's energy, sometimes modeled on the presumed controlling physical or chemical process and always calibrated by comparison with data.

PETITIONER'S EXHIBIT 1002
US PATENT NO. 6,581,565

One extensively used model of this type developed by Watson *et al.*[35] is especially appropriate for use in total diesel system simulations where the combustion process details are not the primary focus. It is based on Lyn's description of compression-ignition combustion—a rapid premixed burning phase followed by a slower mixing controlled burning phase. The fraction of the injected fuel that burns in each of these phases is empirically linked to the duration of the ignition delay. One algebraic function is used to describe the premixed heat-release phase and a second function to describe the mixing-controlled heat-release phase. These two functions are weighted with a phase proportionality factor, β, which is largely a function of the ignition delay. Thus:

$$\frac{m_{f,b}(t')}{m_{f,0}} = \beta f_1 + (1 - \beta) f_2 \tag{14.46}$$

where $m_{f,b}$ is the mass of fuel burned, $m_{f,0}$ is the total fuel mass injected per cycle per cylinder, and t' is time from ignition non-dimensionalized by total time allowed for combustion $[=(t - t_{ign})/\Delta t_{comb}]$.† The premixed-burning function is

$$f_1 = 1 - (1 - t'^{K_1})^{K_2} \tag{14.47}$$

and the mixing-controlled function is

$$f_2 = 1 - \exp(-K_3 t'^{K_4}) \tag{14.48}$$

where K_1, K_2, K_3, and K_4 are empirical coefficients. The proportionality factor β is given by

$$\beta = 1 - \frac{a\phi^b}{\tau_{id}^c} \tag{14.49}$$

where ϕ is the overall fuel/air equivalence ratio and a, b, and c are empirical constants.

Correlation with data from a typical turbocharged truck engine gave the following values for K_1 to K_4:

$$\begin{aligned} K_1 &= 2 + 1.25 \times 10^{-8}(\tau_{id} N)^{2.4} \\ K_2 &= 5000 \\ K_3 &= \frac{14.2}{\phi^{0.644}} \\ K_4 &= 0.79 K_3^{0.25} \end{aligned} \tag{14.50}$$

where τ_{id}, the ignition delay, is in milliseconds and N, engine speed, is in revolutions per minute. It also gave these ranges for a, b, c:[35]

$$0.8 < a < 0.95; \qquad 0.25 < b < 0.45; \qquad 0.25 < c < 0.5$$

† The combustion duration at Δt_{comb} is an arbitrary period within which combustion must be completed. A value of 125° was used above.

PETITIONER'S EXHIBIT 1002
US PATENT NO. 6,581,565

Such single-zone heat-release models are useful because of their simplicity. They obviously cannot relate engine design and operating variables explicitly to the details of the combustion process. Experience indicates that those models with only one function are not usually able to fit experimentally determined heat-release profiles with sufficient accuracy. All single-zone heat-release models should be checked against experimentally derived heat-release profiles, and recalibrated if necessary, before being used for predictions.

Many thermodynamic-based direct-injection engine simulations incorporate an explicit model for each fuel spray which attempts to describe how the spray develops with time. The spray starts out as a liquid fuel jet which then vaporizes, entrains air and (later) burned gases. Mixture preparation can be limited by the availability of either fuel vapor or air, the former limited by droplet evaporation and the latter by air entrainment. While there is evidence in the literature to support both of these phenomena as rate-limiting, more recent studies[36] show that most (70 to 95 percent) of the injected fuel is in the vapor phase at the start of combustion, whereas only 10 to 35 percent of the vaporized fuel is mixed to within the combustion limits (equivalence ratio between 0.3 and 3). This suggests that the combustion process in typical heavy-duty direct-injection compression-ignition engines is mixing controlled rather than vaporization controlled.

While spray geometry is an essential aspect of the fuel-air mixing process, it may not be necessary to model the precise details of the actual configuration. For the purpose of heat-release and emission analysis, it suffices in many phenomenological models to calculate the evolution of the fuel mass, composition, volume, and temperature of critical regions of the spray based on a generic spray geometry. Alternate approaches attempt to provide a detailed structure for the fuel spray to improve the modeling of air entrainment, effects of swirl/spray interaction, and heat transfer. The more commonly used approaches are illustrated in Fig. 14-17.

The schematic in Fig. 14-17*a* illustrates the simplest approach: it is assumed that the growth and motion of the spray or jet within the chamber can be analyzed as a quasi-steady one-dimensional turbulent gaseous jet.[38–40] The intent here is to describe the position of the jet within the combustion chamber and the overall jet size as a function of time. Entrainment of air into the jet is assumed to take place at each point along the jet surface at a rate proportional to the velocity difference between the jet and surrounding air at that point. Two empirical entrainment coefficients[41] are used for the proportionality constants for the relative motion in the jet axial and transverse directions. Conservation equations for fuel mass and total mass, and momentum (in two or three orthogonal directions) are used to determine the jet trajectory and size. The jet slows down due to air entrainment. Deflection of the jet results from the entrainment of air with a momentum component normal to the jet axis, and from drag forces due to the normal component of air flow past the jet. This approach does not define the velocity and concentration profiles across the jet: it only calculates the mean values at any jet axial position. Experimentally determined radial profiles for

PETITIONER'S EXHIBIT 1002
US PATENT NO. 6,581,565

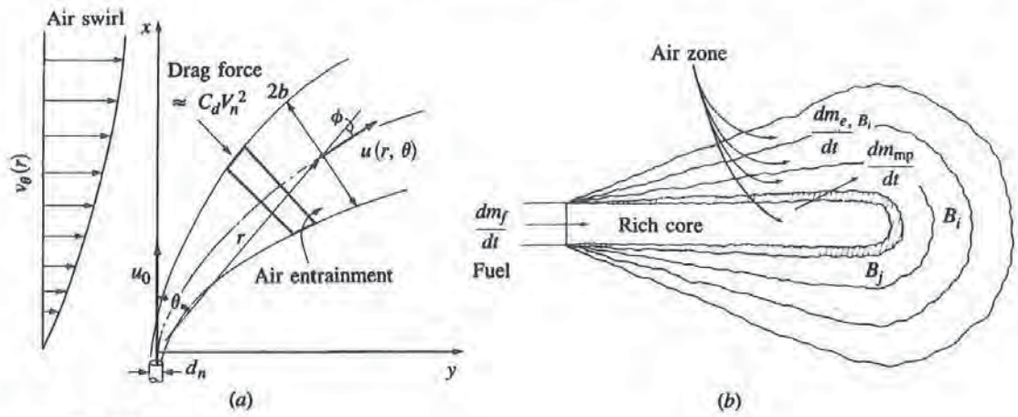


FIGURE 14-17
(*a*) Schematic of one-dimensional quasi-steady fuel spray model used to define spray centerline trajectory and width as radially outward-moving spray interacts with swirling air flow. (*b*) Schematic of multizone model for fuel spray which, based on empirically calculated spray motion and assumed concentration distributions in the spray, successfully evolves discrete combustion zones (each containing a fixed fraction of the fuel) as fuel is injected, vaporized, and mixed with air. (dm_f/dt) = rate of fuel injection into rich core; (dm_{mp}/dt) = rate of preparation of mixture for burning; ($dm_{e,B_i}/dt$) = rate of entrainment of air into zone B_i.[37]

axisymmetric turbulent jets[42] are often assumed to apply. Although the fuel spray is initially pure liquid, the liquid fuel drops soon become a small fraction of the jet volume due to vaporization and air entrainment. Downstream of the initial liquid breakup region, the velocity of the small drops relative to the vaporized fuel and air is small, so the spray acts as a gas jet. Adding a combustion model to this quasi-steady gaseous jet model for fuel-air mixing is an additional major step.

A comparison between this type of gas jet model and an experimental engine spray is shown in Fig. 14-18. A single fuel jet was injected into a disc-shaped chamber in the location shown, and schlieren photography used to observe the spray trajectory. Good agreement was obtained for the spray centerline: note the significant effect of swirl. Reasonable agreement was also obtained between predicted and measured spray boundaries.

Figure 14-17*b* shows a multizone model for each fuel spray which has been used extensively for engine performance and emissions studies in quiescent DI diesels.[37,43] The spray is modeled as a gas jet, with penetration, trajectory and spreading rate determined from empirical equations based on axisymmetric turbulent jet data. These equations describe the approximate spray geometry. The fuel-air distribution within the spray is determined by using a normal distribution across the spray cross section and a hyperbolic profile along the axis of the spray. Progressively evolving, discrete combustion zones, each containing a fixed fraction of the total fuel mass, are then superimposed on the geometrically defined fuel-air distribution. Outer zones are diluted with air and inner zones are added as fuel vaporizes and mixes, as injection and combustion proceeds. The model implicitly assumes that combustion does not affect the mixing rates. With careful

PETITIONER'S EXHIBIT 1002
US PATENT NO. 6,581,565

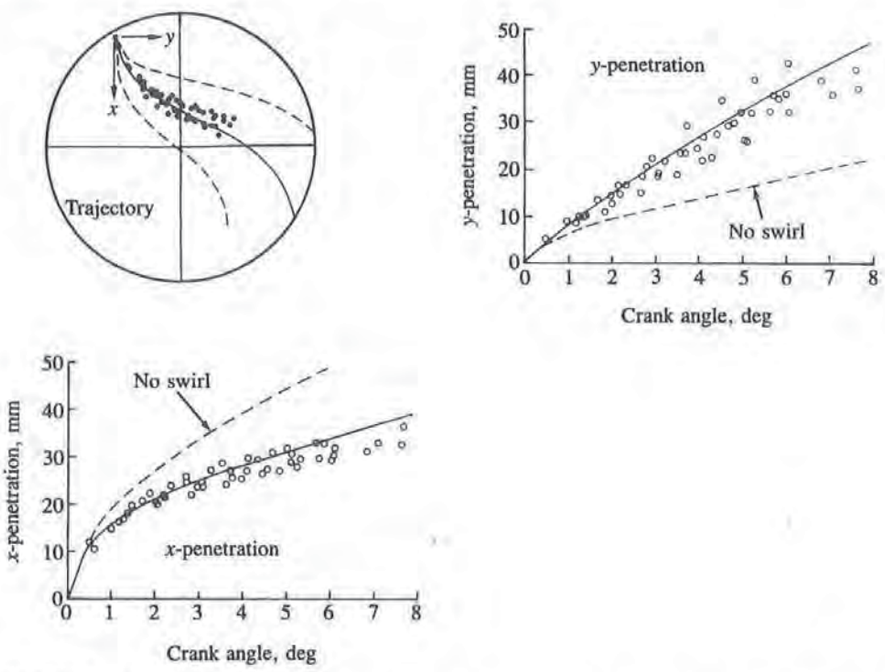


FIGURE 14-18
Spray trajectory and width calculated using one-dimensional quasi-steady spray model of type illustrated in Fig. 14-17*a*, compared with experimental data taken in special visualization direct-injection stratified-charge engine.[39]

adjustment of calibrating constants, this model describes engine performance variations with reasonable accuracy as major design and operating variables change.

More detailed geometric models of the fuel-air mixing and combustion processes in engine sprays have been developed (e.g., Ref. 44). The intent is to follow the spray development in a swirling air flow and the spray interaction with the combustion chamber wall. Figure 14-19 illustrates the approach. The liquid fuel which enters the chamber through the injector nozzle is divided into many small equal mass "elements." The spray motion is defined by an experimentally based correlation. Air entrainment is calculated from momentum conservation and the spray velocity decrease predicted by this correlation. The processes which occur within each element are also illustrated in Fig, 14-19. The fuel drops evaporate and fuel vapor mixes with entrained air. When ignition occurs combustible mixture prepared before ignition burns rapidly: it is assumed to burn at the stoichiometric composition. The continuation of the burning process then depends on the composition of the element: it may be limited by either the rate of production of fuel vapor by evaporation or the availability of air by the rate of entrainment (paths *A* and *B* in Fig. 14-19).

The growth of the spray is determined from the air entrainment into each element and the combustion-produced expansion of each element, as indicated in Fig. 14-20. When impingement on the wall occurs, the spray is assumed to spread

PETITIONER'S EXHIBIT 1002
US PATENT NO. 6,581,565

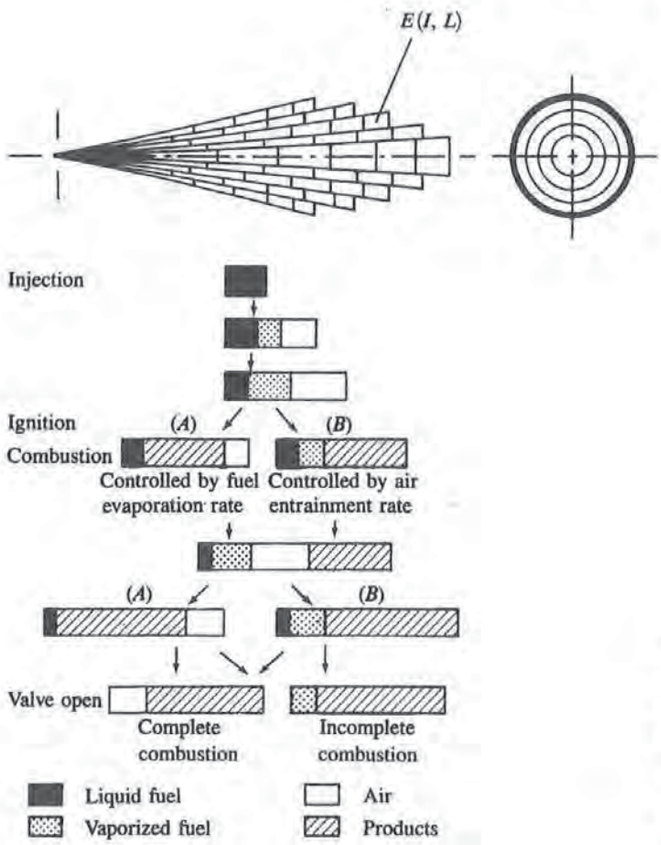


FIGURE 14-19
Schematic of spray model with many small packages, each with the same fuel mass, and of the processes that occur within each package, developed and used by Hiroyasu *et al.*[44]

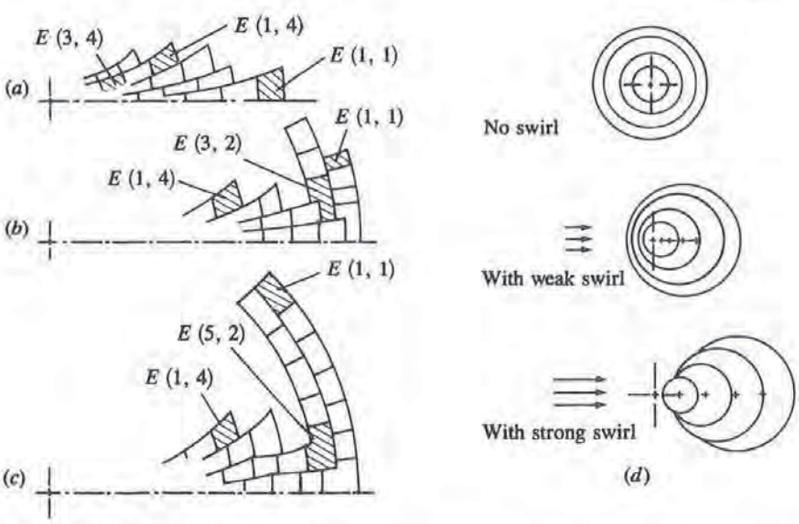


FIGURE 14-20
Method used with model of Fig. 14-19 to compute spray and flame configuration: (*a*) prior to impingement of spray on wall—shaded elements indicate combustion; (*b*) and (*c*) show spray behavior following impingement on the cylindrical bowl wall of the DI diesel combustion chamber; (*d*) shows effect of swirl on spray and flame configuration.[44]

PETITIONER'S EXHIBIT 1002
US PATENT NO. 6,581,565

along the wall with a constant thickness as shown in Fig. 14-20. When the periphery of the spray reaches that of a neighboring spray the sideways growth of the spray is then prevented and the thickness of the elements along the wall increases. Swirl effects are calculated from tangential momentum considerations. Each annular cone ring element is shifted sideways by the swirl as indicated in Fig. 14-20.

The heat-release rate in the combustion chamber is obtained by summing up the heat release in each element. Nitric oxide and soot formation calculations are based on the time histories of temperature, vaporized fuel, air and combustion products in each element. The overall structure of this particular complete diesel engine performance and emissions model is indicated in Fig. 14-21: it is typical of the type of compression-ignition engine simulation used to study engine performance and emissions. Figure 14-22 shows an example of the output from the above model. The injection rate diagram, the assumed Sauter mean drop size of the spray, and the air swirl determine the spray development which leads to the heat-release rate predictions. This determines the cylinder pressure profile. Predicted engine performance results show reasonable but not precise agreement with experimental data. That is not surprising given the complexity of the phenomena being modeled. A review of these types of jet models is given by Hiroyasu.[46]

14.4.4 Prechamber Engine Models

Small high-speed compression-ignition engines use an auxiliary combustion chamber, or prechamber, to achieve adequate fuel-air mixing rates. The prechamber is connected to the main combustion chamber above the piston via a nozzle, passageway, or one or more orifices (see Secs. 1.8, 8.5, and 10.2.2). Auxiliary chambers are sometimes used in spark-ignition engines, also. The plasma and flame-jet ignition systems described in Sec. 9.5.3 enclose the spark plug in a cavity or small prechamber which connects to the main chamber via one or more orifices. The function of the prechamber is to increase the initial growth rate of the flame. Combustion in the main chamber is initiated by one or more flame jets emanating from the prechamber created by the ignition process and subsequent energy release within the prechamber. If the mixture within the prechamber is richer than in the main chamber (due to fuel injection or a separate prechamber intake valve—see Sec. 1.9) these are called stratified-charge engines.

The additional phenomena which these prechambers introduce beyond those already present in conventional chamber engines are: (1) gas flows through the nozzle or orifice between the main chamber and prechamber due to piston motion; (2) gas flows between these chambers due to the combustion-generated pressure rise; (3) heat is transferred to the nozzle or passageway walls due to these flows. The first of these phenomena results in nonuniform composition and temperature distributions between the main and prechamber due to gas displacement primarily during compression, and determines the nature of the flow field within the prechamber toward the end of compression just prior to combustion.

PETITIONER'S EXHIBIT 1002
US PATENT NO. 6,581,565

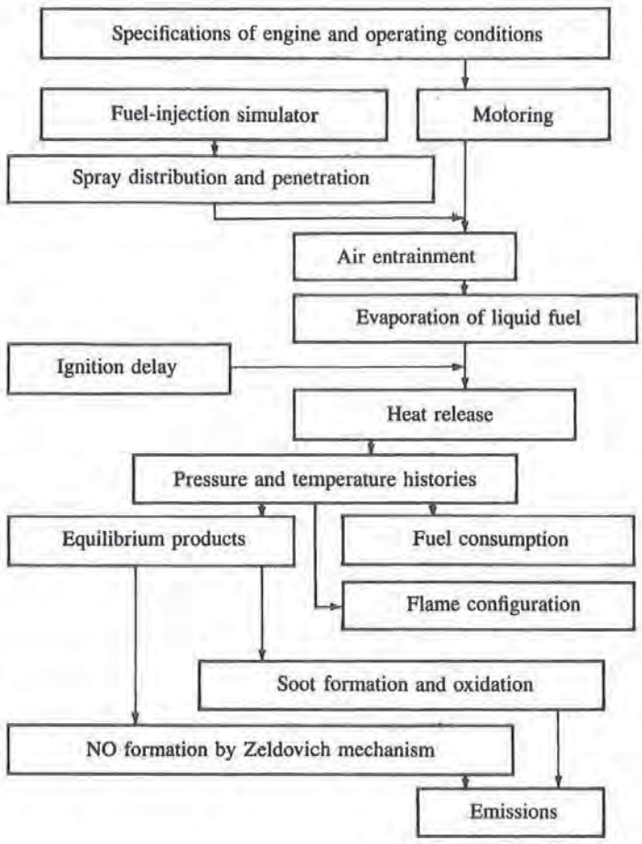


FIGURE 14-21
Structure of thermodynamic-based DI diesel simulation for predicting engine performance and emissions. Simulation incorporates spray model of type illustrated in Figs. 14-19 and 14-20.[45]

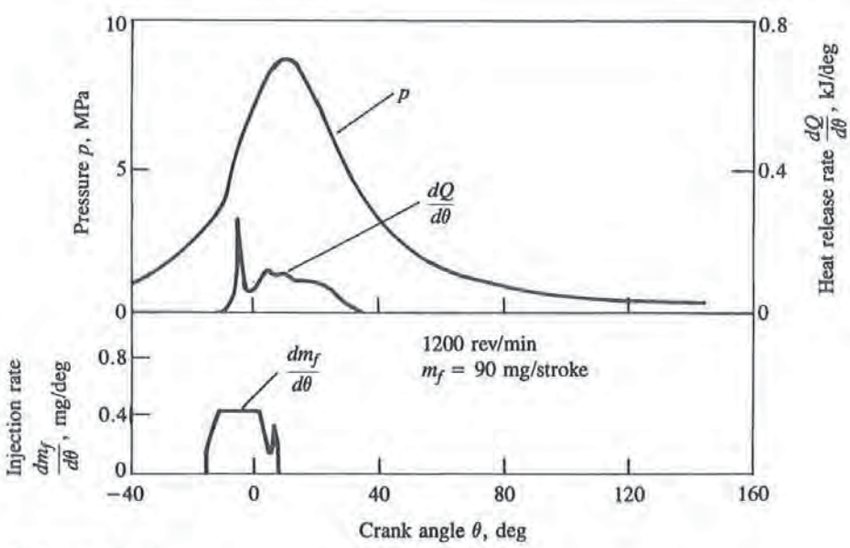


FIGURE 14-22
Fuel-injection rate, heat-release rate profile, and cylinder pressure predicted with thermodynamic-based DI diesel simulation with spray and combustion model of type shown in Fig. 14-21.[45]

PETITIONER'S EXHIBIT 1002
US PATENT NO. 6,581,565

The second phenomena controls the rate of energy release in the main chamber. The heat losses in the passageway and to the additional chamber surface area of the prechamber designs relative to conventional open chambers result in decreased engine performance and efficiency. Thus the prechamber concept adds additional complexity to the engine processes that must be modeled to predict engine behavior.

The following variables are important to prechamber engine performance and emissions characteristics, in addition to the design and operating variables which govern single-chamber engine behavior: prechamber geometry—size, shape, flow area and shape of connecting passageway(s); prechamber location in relation to main chamber geometry; geometry and timing of any auxiliary prechamber valve; fuel metering strategy in prechamber compression-ignition or stratified-charge engine. Thermodynamic-based models have been developed and used to examine the overall impact of these variables (see Ref. 47). Computational fluid dynamic models (see Sec. 14.5 and Fig. 8-26) have also been used to examine specific prechamber engine flow and combustion processes.

Useful predictions of fuel, air, and residual gas distributions and the corresponding temperature within the prechamber and main chamber can be obtained with simple gas displacement models. Only during combustion is the pressure difference across the nozzle or orifice sufficiently large in magnitude for its modeling to be essential; the assumption of uniform pressure during compression, the critical process for determining conditions just prior to combustion, introduces little error into calculations of the flows between the chambers. Section 8.5 develops the appropriate equations for these piston-motion driven gas displacements. Use of the conservation equations for an open system, for total mass, fuel mass, residual gas, and energy given in Sec. 14.2, for the main chamber and the prechamber, then give the mean composition and temperature variation in each chamber as a function of time due to this flow. Figure 8-25 illustrates the mean composition variation in the prechamber that results during the compression stroke of a three-valve stratified-charge engine.

During combustion, the pressure difference across the connecting passageway or orifice is the driving force for the flow between chambers. Since combustion starts in the prechamber, the initial flow is into the main chamber; later, as the heat release in the main chamber becomes dominant, the flow may reverse direction and be into the prechamber. In thermodynamic-based models, the equations for one-dimensional quasi-steady ideal gas flow through a restriction given in App. C are used to relate these flows to the pressure difference between the two chambers. Open-system conservation equations are again used to calculate mean properties in each chamber.

Combustion models used are either empirically based [e.g., using specified heat-release or mass burning rates such as Eq. (14.32)[48]] or are developed from direct-injection compression-ignition engine models with spray evaporation, fuel-air mixing, and ignition delay processes explicitly included.[49] Because of the complexity of these processes in the prechamber engine geometry, substantial simplifying assumptions and empiricism must be used.

PETITIONER'S EXHIBIT 1002
US PATENT NO. 6,581,565

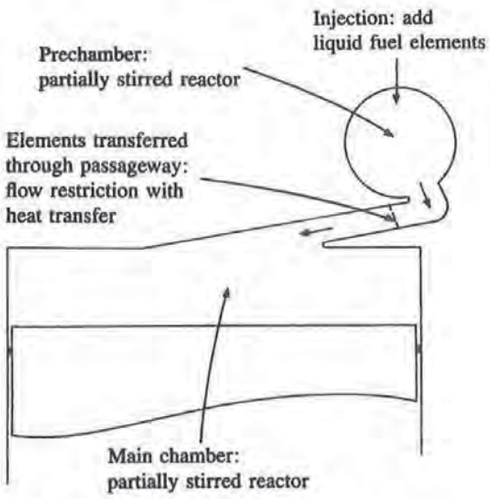
Heat transfer to the passageway and chamber walls is affected by the flows between the chambers: high velocities within the passageway result in high heat-transfer rates to the passageway walls, and the vigorous flows set by the passageway exit flow entering the prechamber or the main chamber increase heat-transfer rates to the walls of these chambers. The standard engine heat-transfer correlations which relate the heat-transfer coefficient to mean flow field variables via Nusselt-Reynolds number relationships (see Sec. 12.4) are normally used to describe these heat-transfer processes. The length scales are chosen to match the prechamber or main chamber or passageway dimensions. The characteristic velocities in these relationships are equated with velocities which are representative of the flow in each of these regions at the relevant time in the engine operating cycle.[50, 51]

The utility of the more sophisticated of these prechamber engine performance and emissions models is illustrated by the sample results shown in Fig. 14-23. This simulation of the indirect-injection compression-ignition engine's flow and combustion processes describes, through the use of stochastic mixing models, the development of the fuel/air ratio distribution and fuel-energy release distribution, and hence the development of the gas pressure and gas temperature distribution, within the prechamber and main chambers of the engine. With the (nonuniform) gas composition and state defined, the models for NO formation described in Sec. 11.2.1 was used to predict NO_x emissions. The approaches used to describe the evolution of the prechamber, main chamber, and passageway contents are summarized in Fig. 14-23*a*.

The cylinder contents were divided up into a large number of elements. Pairs of elements are selected at random to undergo "turbulent mixing" interactions at a frequency related to the turbulence in each region. Rate processes—evaporation, ignition, NO formation, etc.—proceed within each element between these mixing interactions. Figure 14-23*b* shows sample results. At about TC, after some of the injected fuel has evaporated and the ignition delay is over, combustion starts in the prechamber and the prechamber pressure p_p rises above the main chamber pressure p_m. This forces air, fuel, and burned gases to flow from the prechamber into the main chamber; fuel and rich products can now mix with air and burn in the main chamber. NO starts to form in each mass element, once it burns, at a rate dependent on each element's composition and state. Most of the NO forms within the prechamber and then flows into the main chamber as the expansion process proceeds. The attractive feature of this type of emission calculation is that the kinetically controlled NO formation calculations are based directly on local gas composition and temperature in a manner that approximately simulates the mean and turbulent nonuniformities in these variables. Predictions of engine operation and emissions showed good agreement with data.[52]

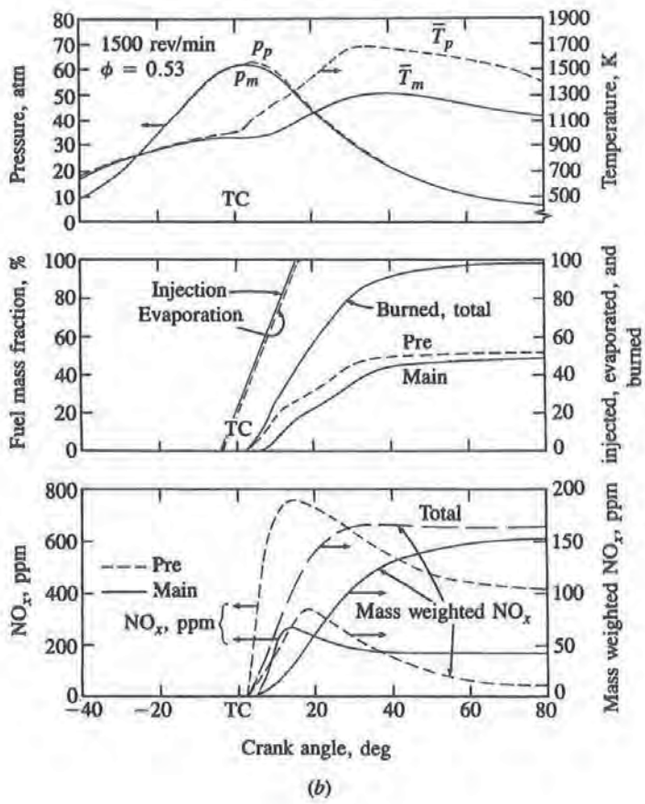
Fluid-dynamic-based models have been used to study fluid flow, combustion, and pressure wave phenomena in prechamber engines. Section 14.5 reviews this type of engine model. Additional details of these applications can be found in Refs. 53 and 54.

PETITIONER'S EXHIBIT 1002
US PATENT NO. 6,581,565



Partially stirred reactors contain many equal mass elements. These elements may be air (plus residual), liquid fuel, unburned mixture (fuel vapor, air, burned gas), and burned mixture

(*a*)



(*b*)

FIGURE 14-23
(*a*) Schematic of IDI diesel engine illustrating how stochastic mixing models are applied to prechamber, main chamber, and passageway to simulate turbulent mixing processes and pressure-driven flows. (*b*) Example of simulation predictions through the engine's operating cycle. Shown are prechamber and main chamber pressures, prechamber and main chamber average gas temperatures; fuel mass injected, evaporated, and burned in prechamber and main chamber, average NO concentration in each chamber (and total) in ppm by volume and mass weighted ppm (mass in chamber × NO concentration in chamber/total mass in cylinder).[52]

PETITIONER'S EXHIBIT 1002
US PATENT NO. 6,581,565

14.4.5 Multicylinder and Complex Engine System Models

The models discussed in the previous parts of Sec. 14.4 focus on the processes occurring within *each* cylinder of an internal combustion engine. Most engines are multicylinder engines and the individual cylinders interact via the intake and exhaust manifolds. Also, many engine systems are more complex: internal combustion engines can be supercharged, turbocharged, or turbocompounded, and the manifolds then connect to the atmosphere via compressors or turbines (see Fig. 6-37 and Sec. 6.8). Thermodynamic-based simulations of the relevant engine processes, constructed from the types of model components already described, prove extremely useful for examining the behavior of these more complex engine systems. By describing the mass and energy flows between individual components and cylinders of such systems throughout the engine's operating cycle, the total system preformance can be predicted. Such models have been used to examine steady-state engine operation at constant load and speed (where time-varying conditions in the manifolds due to individual cylinder filling and emptying events affect multicylinder engine behavior), and how the total system responds to changes in load and speed during engine transients.

The block diagram of a turbocharged and turbocompounded diesel engine system in Fig. 14-24 illustrates the interactions between the system components. By describing the mass and energy flows between components and the heat and work transfers within each component, total system behavior can be studied. In such engine simulations, the reciprocator cylinders, the intake manifold, and the various sections of the exhaust system are treated as connected open systems. The flows into and out of these volumes are usually analyzed using the quasi-steady emptying and filling approach described in Sec. 14.3.3, using the open-system conservation equations of Sec. 14.2. The reciprocator cycle is treated as a sequence of processes within each cylinder: intake, compression, combustion (including expansion), and exhaust. These are modeled using the approaches described previously in Secs. 14.4.1 to 14.4.4. Heat transfer has, of course, an important effect on the in-cylinder processes. It also is important in the exhaust system since the performance of the turbocharger turbine and of any compounded turbine depends on the gas state at the turbine inlet. The performance of the turbomachinery components is normally defined by maps that interrelate efficiency, pressure ratio, mass flow rate, and shaft speed for each component (see Secs. 6.8.2 to 6.8.4). Special provisions are usually required in the logic of the turbomachinery map interpolation routines to avoid problems with the compressor surge and turbine choking operating limits of these devices.

When the reciprocator is coupled with turbomachinery its manifolds no longer connect directly with the atmosphere: matching procedures are required to ensure that the pressure levels and mass flow rates of the compressor and turbines match with those of the engine. The following matching process is typical of those used for turbocharged engines (one compressor and one turbine only). At a given time, the values of the variables describing the state of the

PETITIONER'S EXHIBIT 1002
US PATENT NO. 6,581,565

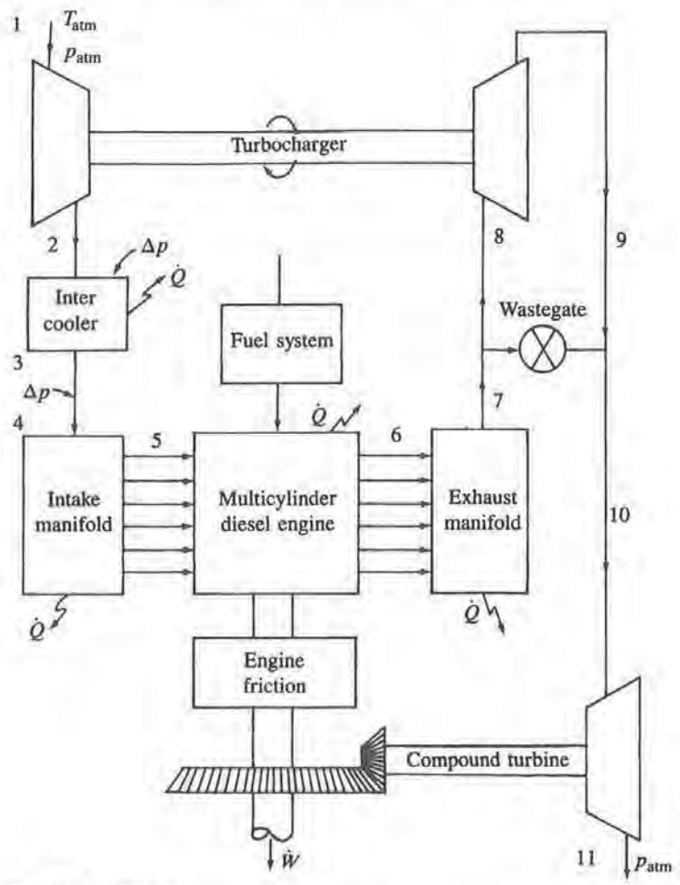


FIGURE 14-24
Block diagram of turbocharged turbocompounded diesel engine system.

various system components are known (from integration of the system governing equations over the previous time step). These include the intake and exhaust manifold pressures and the turbocharger rotor speed. The compressor inlet pressure is atmospheric pressure less the intake air-filter pressure drop. The turbine exit pressure is atmospheric plus the muffler pressure drop. By relating the compressor discharge pressure to the intake manifold pressure and the turbine inlet pressure to the exhaust manifold pressure (through suitable pressure drops) the pressure ratio across each machine is determined. Hence, the compressor and turbine maps can be entered using the calculated pressure ratios, and the rotor speed (same for both turbomachines) as inputs. The output from the map interpolation routines determines the mass flow rate and efficiency of each component for the next time step. From these the power required to drive the compressor ($-\dot{W}_C$) and to drive the turbine ($\dot{W}_T$) are determined from Eqs. (6.42) and (6.48), respectively. Any excess power (or power deficiency) will result in a change of

PETITIONER'S EXHIBIT 1002
US PATENT NO. 6,581,565

rotor speed according to the turbocharger dynamics equation

$$\dot{W}_C + \dot{W}_T = I_{TC}\,\omega\,\frac{d\omega}{dt} + B\omega^2 \tag{14.51}$$

where I_{TC} is the rotational inertia of the turbocharger, ω is angular velocity, and B is the rotational damping. The values of the other state variables for the next time step are determined from the solution of the mass and energy conservation equations for each open system, with the compressor and turbine mass flows taken from the output of the turbomachinery map interpolation routines.

This approach can be used to establish the steady-state engine operating characteristics from an assumed initial set of state variables. (Of course, due to the pulsating nature of the flows into and out of the cylinders, these state variables will vary in a periodic fashion throughout the engine cycle at a fixed engine load and speed.) This approach can also be used to follow transient engine behavior as load or speed is varied from such a steady-state condition.[35] The additional inputs required are the fuel pump delivery characteristics as a function of fuel pump rack position and speed, with the latter evaluated from an appropriate model for dynamic behavior of the governor.[55] From the brake torque of the engine (determined by subtracting friction torque from the indicated torque), the torque required by the load T_L, the inertia of the engine and load I_E and I_L, the dynamic response of the engine and load to changing fuel rate or engine speed can be obtained from

$$T_B - T_L = (I_E + I_L)\,\frac{d\omega}{dt} \tag{14.52}$$

An example of the output from this type of engine model is shown in Fig. 14-25. The response of a turbocharged DI diesel engine to an increase in load from 0 to 95 percent of full load is shown. The predictions come from a model of the type shown in Fig. 14-24, and engine details correspond to the experimental configuration.[55] The simulation follows the data through the engine transient with reasonable accuracy. Note that with the assumed constant governor setting, during this transient the equivalence ratio of the trapped mixture rises to close to stoichiometric because the increase in air flow lags the increase in fuel flow. This would result in excessive smoke emissions. Such models prove extremely useful for exploring the effect of changes in engine system design on transient response.[56]

For two-staged turbocharged or turbocompounded systems the engine-turbocharger matching process is more complicated. The division of the pressure ratio between the exhaust manifold and atmosphere between the two turbines in Fig. 14-24 is not known a priori. Nor, with two compressors, is the intake pressure ratio distribution known. Iterative procedures based on an assumed mass flow rate are used to determine the pressure level between the two turbines such that mass flow and pressure continuity through the exhaust system is satisfied (e.g., Ref. 2).

PETITIONER'S EXHIBIT 1002
US PATENT NO. 6,581,565

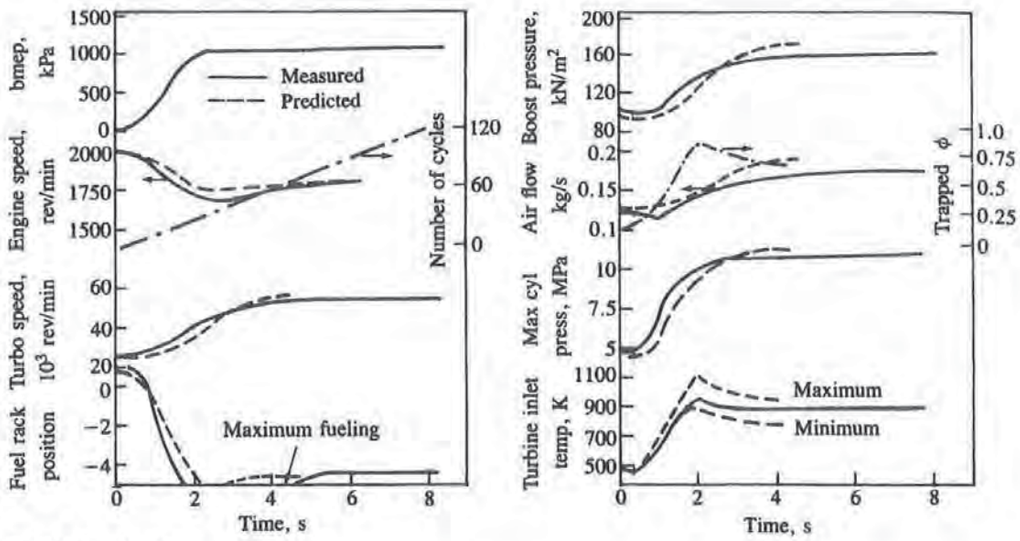


FIGURE 14-25
Predicted (---) and measured (—) response of a turbocharged direct-injection diesel engine to an increase in load.[55]

14.4.6 Second Law Analysis of Engine Processes

The first-law-based methods for evaluating power plant performances do not explicitly identify those processes within the engine system that cause unrecoverable degradation of the thermodynamic state of the working fluid. However, second-law-based analysis methods do provide the capability to identify and quantify this unrecoverable state degradation. Thus, cause and effect relationships which relate these losses to individual engine processes can be determined. The first law analysis approaches summarized in this section (14.4) are based on the fact that energy is conserved in every device and process. Thus, they take account of the conversion of energy from one form to another: e.g., chemical, thermal, mechanical. Although energy is conserved, second law analysis indicates that various forms of energy have differing levels of ability to do useful mechanical work. This ability to perform useful mechanical work is defined as *availability*.

The availability of a system at a given state is defined as the amount of useful work that could be obtained from the combination of the system and its surrounding atmosphere, as the system goes through reversible processes to equilibrate with the atmosphere. It is a property of the system and the environment with which the system interacts, and its value depends on both the state of the system and the properties of the atmosphere. Availability is not a conserved property; availability is destroyed by irreversibilities in any process the system undergoes. When availability destruction occurs, the potential for the system to do useful mechanical work is permanently decreased. Thus to make a proper evaluation of the processes occurring within an engine system both energy and availability must be considered concurrently.

The basis for an availability analysis of realistic models of internal com-

PETITIONER'S EXHIBIT 1002
US PATENT NO. 6,581,565

TABLE 14.2
Available energy equations for various processes

Mechanism	Equation
Work transfer	$dA_W = dW$
Heat transfer	$dA_Q = dQ(1 - T_0/T)$
Gas transfer	$dA_g = dm_g[(h - h_0) - T_0(s - s_0)]$
Liquid fuel transfer†	$dA_f = dm_f(1.0338Q_{LHV})$
Control volume storage	$dA_{CV} = d\{m_{CV}[(u - u_0) - T_0(s - s_0) + p_0(v - v_0)]\}$

† The availability of the fuel is 1.0338 times its lower heating value; see Sec. 5.7.

bustion engine processes has already been developed in Sec. 5.7. The change in availability of any system undergoing any process where work, heat, and mass transfers across the system boundary occur (see Fig. 5.13) can be written:

$$\Delta A = A_{in} - A_{out} - A_{destroyed} \tag{14.53}$$

where A_{in} and A_{out} represent the availability transfers into and out of the system across the boundary. Since availability is not a conserved quantity, this equation can only be used to solve for the availability destruction term, $A_{destroyed}$. Table 14.2 summarizes the equations for the availability change of the system and the availability transfers associated with work, heat and mass transfer across the system boundary, developed in Sec. 5.7.

This availability balance is applied to the internal combustion engine operating cycle as follows. A first-law-based cycle analysis of the type described above in this section (14.4) is used to define the variation in working fluid thermodynamic state, and the work, heat, and mass transfers that occur in each of the processes that make up the total engine cycle. Integration of the availability balance over the duration of each process then defines the magnitude of the availability destruction that occurs during that process.

To illustrate this procedure, consider the operating cycle of a 10-liter six-cylinder turbocharged and aftercooled direct-injection four-stroke cycle compression-ignition engine, operating at its rated power and speed of 224 kW and 2100 rev/min. The variations in temperature, energy, and entropy are determined with a first-law-based analysis. Figure 14-26 shows the T-s diagram for the working fluid as it goes through the sequence of processes from air inlet from the atmosphere (state 1) to exhaust gas exit to the atmosphere (state 10).[57] The incoming air is compressed (with some irreversibility) in the turbocompressor to state 2 and cooled with an aftercooler to state 3. The air at state 3 is drawn into the cylinder and mixed (irreversibly) with residual gases until, at the end of the intake, the cylinder gases are represented by state 4. That mixture is subsequently compressed (with modest heat loss) to state 5. Fuel addition commences close to state 5; subsequent burning increases the combustion chamber pressure and temperature along the line 5-6. At 6 the heat release, heat transfer, and volume change rate are such that the maximum cylinder pressure is reached (a few degrees after TC). From 6 to 7 combustion continues to completion, the burned

PETITIONER'S EXHIBIT 1002
US PATENT NO. 6,581,565

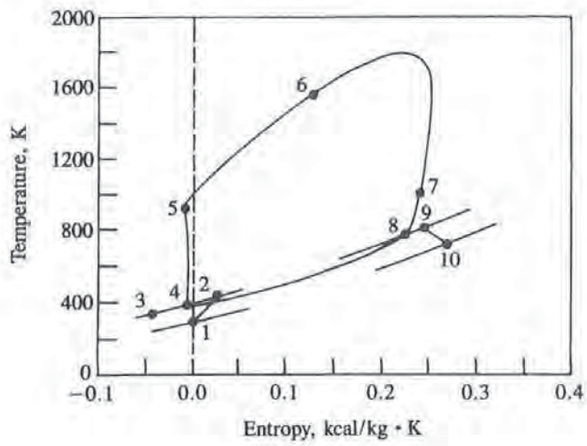


FIGURE 14-26
T-s diagram for the working fluid as it goes through the sequence of processes from air inlet to exhaust in turbocharged aftercooled DI compression-ignition engine. The 10-liter six-cylinder engine is operated at its rated power (224 kW) and speed (2100 rev/min). The text relates processes to numbered end states.[57]

gases continue to expand, doing work on the piston and losing heat to the walls. At state 7 the exhaust valve opens initiating a rapid pressure equilibration with the exhaust manifold to a pressure corresponding to point 8. Gases are expelled from the cylinder to the exhaust manifold. After the intake valve opens, cylinder residual gases are mixed with incoming air at state 3 to yield gases at state 4 to complete the in-cylinder cycle. The exhaust gases that have been expelled from the cylinder experience additional thermodynamic losses and can be represented by state 9. These gases then pass through the turbocharger turbine to state 10 to provide the work to drive the compressor.

A first law and second law analysis of a naturally aspirated diesel engine are compared in Table 14.3. Also shown is a second law analysis of a turbocharged version of the naturally aspirated diesel. These results illustrate the value of defining the losses in availability that occur in each process.

Consider the first and second law analysis results for the naturally aspirated engine. While 25.1 percent of the fuel energy leaves the combustion chamber in the form of heat transfer, the availability transfer corresponds to 21.4 percent of the fuel's availability. It is this latter number that indicates the maximum amount of the heat transfer that can be converted to work. The table shows that 34.6 percent of the fuel energy is carried out of the engine in the exhaust gases. However, the second law analysis shows that the exhaust contains only 20.4 percent of the available energy of the fuel. The ratio of these quantities shows that only about 60 percent of the exhaust energy can be converted to work using ideal thermodynamic devices.† The exhaust gas leaves the system in a high-temperature, ambient pressure state and therefore has high entropy (relative to the p_0, T_0 reference state). This, via the gas-transfer equation in Table 14.2, reduces the available energy of the exhaust gas stream.

† Of course, real thermodynamic devices will produce less work than ideal devices.

PETITIONER'S EXHIBIT 1002
US PATENT NO. 6,581,565

TABLE 14.3
Comparison of first and second law analysis for six-cylinder 14-liter naturally aspirated and turbocharged diesel engine at 2100 rev/min[58]

	Naturally aspirated		Turbocharged
	First law, % fuel energy	Second law, % fuel availability	
Indicated work†	40.3	39.1	43.9
Combustion loss	—	15.9	19.2
Cylinder heat transfer	25.1	21.4	17.6
Internal valve throttling	—	0.7	0.7
Exhaust valve throttling	—	2.5	2.3
Loss in compressor	—	—	1.4
Loss in turbine	—	—	0.8
Exhaust to ambient	34.6	20.4	14.1
Total	100.0	100.0	100.0
Brake power, kW	185	185	220

† Note that the indicated work for the second law balance is a lower percentage than for the first law. This occurs because the availability of the fuel is 1.0317 times the fuel's heating value.

The quantity referred to as combustion loss in Table 14.3 is determined from an availability balance for the combustion chamber over the duration of the combustion period. The "availability destroyed" term in Eq. (14.53) then represents the deviation of the actual combustion process from a completely reversible process. The second law analysis shows that the availability loss associated with the combustion irreversibilities is 15.9 percent of the fuel's availability. This loss depends on the overall equivalence ratio at which the engine is operating, as indicated in Fig. 5-17. Combustion of leaner air/fuel ratios would give a higher fractional availability loss due to mixing of the fuel combustion products with increased amounts of excess air and the lower bulk temperature.

Overall, the most important point emerging from this comparison is that the work-producing potential of the heat loss to the combustion chamber walls and the exhaust mass flow out of the engine is not as large as the magnitude of the energy transferred: some of these energy transfers, even with ideal thermodynamic work-producing devices, must ultimately be rejected to the environment as heat.

A comparison of the second and third columns in Table 14.3, both obtained with a combined first and second law analysis, illustrates how turbocharging improves the performance of a naturally aspirated engine. The brake fuel conversion efficiency of the turbocharged engine is considerably improved—from 33.9 to 39.2 percent. The table indicates that through turbocharging, the availability transfers associated with the heat loss and exhaust gas flow are reduced from 41.8

PETITIONER'S EXHIBIT 1002
US PATENT NO. 6,581,565

to 31.7 percent (a difference of 10.1 percentage points), while the combustion and added turbomachinery availability losses increase from 15.9 to 21.4 percent (a difference of 5.5 percentage points). By turbocharging, advantage has been taken of the following changes. While the leaner air/fuel ratio operation of the turbocharged engine increases the combustion availability losses due to the use of a greater portion of the chemical energy of the fuel to mix with and heat excess air, the lower burned gas temperature this produces results in reduced heat losses and lower cylinder exhaust temperature. In addition, the turbocharger transfers available energy from the cylinder exhaust to the inlet air. The reduced heat loss and lower final exhaust availability level give a substantial performance improvement.[58]

To interpret the second law analysis results, one must remember that the desired output is brake work and increases in this quantity (for a given fuel flow) represent improved performance. All other availability terms represent losses or undesirable transfers from the system; decreasing these terms constitutes an improvement. These undesirable available energy transfer and destruction terms fall into five categories: (1) heat transfer, (2) combustion, (3) fluid flow, (4) exhaust to ambient, (5) mechanical friction. The available energy flows identified as heat transfer represent the summation of all availability transfers that occur due to heat transfers. The most significant of these are the in-cylinder and aftercooler heat rejection. The combustion loss represents the amount of available energy destroyed due to irreversibilities occurring in releasing the chemical potential of the fuel as thermal energy and mixing the combustion products with any excess air. The fluid flow losses include the available energy destroyed within the working fluid in the compressor, aftercooler, intake valve, exhaust valve, exhaust manifold, and turbine due to fluid shear and throttling. The availability destroyed due to fluid shear and mechanical rubbing, exterior to the working fluid, are contained in the mechanical friction category. The effect of variations in engine load and speed on these five categories of losses or transfers will now be described.

Figure 14-27 shows the availability transfers or losses in each of these categories for a turbocharged six-cylinder 10-liter displacement direct-injection diesel engine, expressed as a percentage of the fuel availability, as a function of engine load. The percentage of fuel availability associated with the heat transfers varies

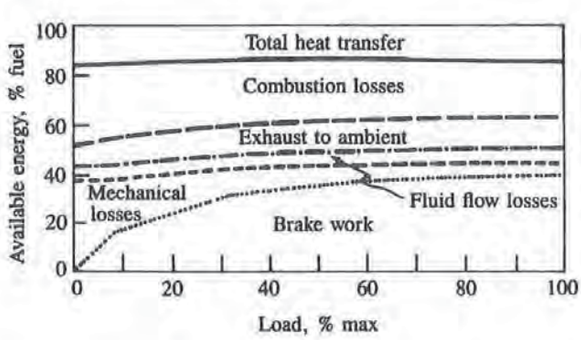


FIGURE 14-27
Distribution of available energy into major categories for the engine of Fig. 14-26 as a function of engine load.[57]

PETITIONER'S EXHIBIT 1002
US PATENT NO. 6,581,565

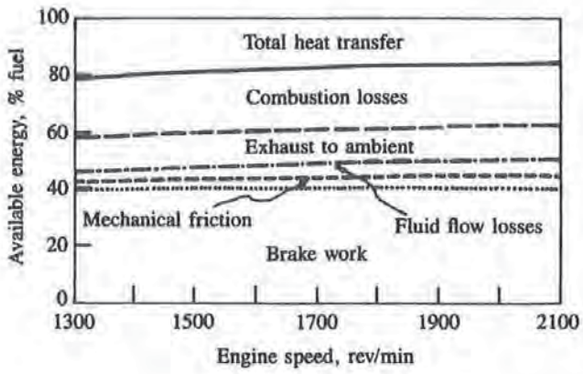


FIGURE 14-28
Distribution of available energy into major categories for the engine of Fig. 14-26 as a function of engine speed.[57]

little over the load range. The combustion loss increases from 21.8 to 32.5 percent as load is decreased due to an increasingly lean operation of the engine. Fluid friction losses, as a percentage, increase slightly as load increases due to larger mass flow rates. Since friction is approximately constant in absolute magnitude, its relative importance increases drastically as the brake output goes to zero. Exhaust flow available energy decreases from 12.2 to 8 percent as load is decreased from 100 to 0 percent.[57]

The effect of varying engine speed (at full load) is shown in Fig. 14-28. The availability associated with heat transfers changes over the speed range shown from 15.6 to 21 percent: more time during each cycle is available for heat transfer at lower speeds. Fluid flow and friction losses decrease with decreasing speed. Other availability losses remain essentially constant as a percentage of the fuel's availability.[57]

14.5 FLUID-MECHANIC-BASED MULTIDIMENSIONAL MODELS

14.5.1 Basic Approach and Governing Equations

The prediction of the details of the flow field within engines, and the heat-transfer and combustion processes that depend on those flow fields, by numerical solution of the governing conservation equations has become a realizable goal. Such methods have been under development for more than a decade, during which time they have steadily improved their ability to analyze the flow field in realistic engine geometries. While the overall dynamic characteristics of intake and exhaust flows can usefully be studied with one-dimensional unsteady fluid dynamic computer calculations (see Sec. 14.3.4), flows within the cylinder and in intake and exhaust ports are usually inherently unsteady and three dimensional. Recent increases in computing power, coupled with encouraging results with two-dimensional calculations, indicate that useful three-dimensional calculations are now feasible. However, they still do not have the capability to predict accurately

PETITIONER'S EXHIBIT 1002
US PATENT NO. 6,581,565

all the features of real engine processes of interest. Gas-flow patterns can be predicted best; predictions of fuel spray behavior are less complete, and combustion calculations present considerable difficulties.

These computational, fluid dynamic, engine process analysis codes solve the partial differential equations for conservation of mass, momentum, energy, and species concentrations. To apply a digital computer to the solution of a continuum problem (such as the flow field inside the cylinder), the continuum must be represented by a finite number of discrete elements. The most common method of discretization is to divide the region of interest into a number of small zones or cells. These cells form a grid or mesh which serves as a framework for constructing finite volume approximations to the governing partial differential equations. The time variable is similarly discretized into a sequence of small time intervals called time steps, and the transient solution is "marched out" in time: the solution at time t_{n+1} is calculated from the known solution at time t_n. Three-dimensional formulations of the finite difference equations are required for most practical engine calculations; two-dimensional (or axisymmetric) formulations can be useful, however, under simpler flow situations, and have been more extensively used to date due to their simpler models and computer codes and requirement for less computer time and storage capacity.

The principal components of these multidimensional engine flow models are the following:[59]

1. The mathematical models or equations used to describe the flow processes. Especially important is the turbulence model, which describes the small-scale features of the flow which are not accessible to direct calculation.
2. The discretization procedures used to transform the differential equations of the mathematical model into algebraic relations between discrete values of velocity, pressure, temperature, etc., located on a computing mesh which (ideally) conforms to the geometry of the combustion chamber with its moving valves and piston.
3. The solution algorithm whose function is to solve the algebraic equations.
4. The computer codes which translate the numerical algorithm into computer language and also provide easy interfaces for the input and output of information.

The basic equations for all existing in-cylinder flow calculation methods are the differential equations expressing the conservation laws of mass, momentum (the Navier-Stokes equations—a set of three), energy, and species concentrations. These equations, in the above order, may be written:

$$\frac{D}{Dt}\begin{pmatrix}1\\ u_i\\ e\\ Y_\alpha\end{pmatrix} = \begin{pmatrix}0\\ 0\\ Q\\ S_\alpha\end{pmatrix} - \frac{\partial}{\partial x_j}\begin{pmatrix}0\\ \tau_{ij}\\ q_j\\ J_{\alpha j}\end{pmatrix} \tag{14.54}$$

PETITIONER'S EXHIBIT 1002
US PATENT NO. 6,581,565

The first term on the right gives the source terms, the second term the diffusive transport. The D/Dt operator provides the convective transport terms and is

$$\frac{Df}{Dt} \equiv \frac{\partial(\rho f)}{\partial t} + \frac{\partial}{\partial x_j}(\rho u_j f) \tag{14.55}$$

Here, ρ is the density, u_i the ith velocity component, e the internal energy per unit mass, and Y_α the concentration of species α per unit mass.

In the IC engine context, the thermal energy source term Q involves a viscous term and source terms arising from chemical reaction of the fuel. Both Q and the species source term, S_α, will depend upon the chemical rate equations, which must be known to close the problem. Note that diffusion of the various species contributes to the diffusive flow of internal energy, q_j, in addition to conductive heat diffusion.

The fact that turbulent flows exhibit important spatial and temporal variations over a range of scales (dictated at the upper end by chamber dimensions and at the lower end by viscous dissipative processes, see Sec. 8.2.1) makes direct numerical solution of these governing equations impractical for flows of engine complexity. Recourse must therefore be made to some form of averaging or filtering which removes the need for direct calculation of the small-scale motions. Two approaches have been developed for dealing with this turbulence modeling problem: full-field modeling (FFM), sometimes called statistical flux modeling; and large-eddy simulation (LES) or subgrid-scale simulation. In FFM, one works with the partial differential equations describing suitably averaged quantities, using the same equations everywhere in the flow. For periodic engine flows, time averaging must be replaced by ensemble or phase averaging (see Sec. 8.2.1). The variables include the velocity field, thermodynamic state variables, and various mean turbulence parameters such as the turbulent kinetic energy, the turbulent stress tensor, etc. In FFM, models are needed for various averages of the turbulence quantities. These models must include the contributions of all scales of turbulent motion.[59, 60]

Large-eddy simulation (LES) is an approach in which one actually calculates the large-scale three-dimensional time-dependent turbulence structure in a single realization of the flow. Thus, only the small-scale turbulence need be modeled. Since the small-scale turbulence structure is more isotropic than the large-scale structure and responds rapidly to changes in the large-scale flow field, modeling of the statistical fluxes associated with the small-scale motions is a simpler task than that faced in FFM where the large-scale turbulence must be included.

An important difference between FFM and LES is their definition of "turbulence." In FFM the turbulence is the deviation of the flow at any instant from the average over many cycles of the flow at the same point in space and oscillation phase [i.e., the fluctuation velocity defined by Eq. (8.16) or (8.18)]. Thus, FFM "turbulence" contains some contribution from cycle-by-cycle flow variations. LES defines turbulence in terms of variations about a local average; hence in LES turbulence is related to events in the current cycle.[60]

PETITIONER'S EXHIBIT 1002
US PATENT NO. 6,581,565

14.5.2 Turbulence Models

In *full-field modeling* (FFM), equations for the averaged variables are formed from Eqs. (14.54). With periodic engine flows, phase or ensemble averaging must be used (see Secs. 8.2.1 and 8.2.2). Since the flow during the engine cycle is compressed and expanded, mass-weighted averaging (called Favre averaging) can be used to make the averaged compressible-flow equations look almost exactly like the averaged equations for incompressible flows. The combined ensemble-Favre averaging approach works as follows.[60]

We denote the phase-averaging process by { }, i.e.:

$$\{\rho(\mathbf{x}, t)\} = \lim_{N\to\infty} \frac{1}{N} \sum_{n=1}^{N} \rho(\mathbf{x}, t + n\tau) \tag{14.56}$$

where τ is the cycle period. We also write $\{\rho\} = \tilde{\rho}$, and decompose ρ into $\rho = \tilde{\rho} + \rho'$. The mass-weighted phase-averaged quantities (indicated by an overbar) are defined by

$$\tilde{\rho}(\mathbf{x}, t)\bar{f}(\mathbf{x}, t) = \lim_{N\to\infty} \sum_{n=1}^{N} \rho(\mathbf{x}, t + n\tau) f(\mathbf{x}, t + n\tau) \tag{14.57}$$

where all flow variables (except density and pressure) have been decomposed as $f = \bar{f} + f'$. Note that $\{\rho'\}$ is zero, $\{\bar{f}\} = \bar{f}$, the mass-weighted phase average of f' is zero, but $\{f'\}$ is not zero. With these definitions:

$$\begin{aligned}
\{\rho f\} &= \tilde{\rho}\bar{f} \\
\{\rho f'\} &= 0 \\
\{\rho f g\} &= \tilde{\rho}(\bar{f}\bar{g} + \overline{f'g'}) \\
\{\rho f g h\} &= \tilde{\rho}(\bar{f}\bar{g}\bar{h} + \bar{f}\overline{g'h'} + \bar{g}\overline{f'h'} + \bar{h}\overline{f'g'} + \overline{f'g'h'})
\end{aligned} \tag{14.58}$$

Phase-averaging Eq. (14.54), one obtains[60]

$$\frac{\bar{D}}{Dt}\begin{pmatrix} 1 \\ \bar{u}_i \\ \bar{e} \\ \bar{Y}_\alpha \end{pmatrix} = \begin{pmatrix} 0 \\ 0 \\ \{Q\} \\ \{S_\alpha\} \end{pmatrix} - \frac{\partial}{\partial x_j}\begin{pmatrix} 0 \\ \{\tau_{ij}\} \\ \{q_j\} \\ \{J_{\alpha j}\} \end{pmatrix} - \frac{\partial}{\partial x_j}\begin{pmatrix} 0 \\ \tilde{\rho}\overline{u_i' u_j'} \\ \tilde{\rho}\overline{e' u_j'} \\ \tilde{\rho}\overline{Y_\alpha' u_j'} \end{pmatrix} \tag{14.59}$$

where

$$\frac{\bar{D}\bar{f}}{Dt} = \frac{\partial}{\partial t}(\tilde{\rho}\bar{f}) + \frac{\partial}{\partial x_j}(\tilde{\rho}\bar{u}_j\bar{f}) \tag{14.60}$$

The terms on the left-hand side in Eq. (14.59) involve only the solution variables $\tilde{\rho}$, $\bar{u}_i$, $\bar{e}$, and $\bar{Y}_\alpha$, and hence require no modeling. However, all of the terms on the right, particularly the last terms that represent turbulent transport, involve turbulence fluctuation quantities and must be modeled in terms of the solution variables. The source terms $\{Q\}$ and $\{S_\alpha\}$ present special difficulties to the engine modeler. Due to the exponential dependence of the heat release Q on tem-

PETITIONER'S EXHIBIT 1002
US PATENT NO. 6,581,565

perature, $\{Q\}$ will be strongly influenced by temperature fluctuations. These issues are discussed more fully in Secs. 14.5.5 and 14.5.6.

The momentum equations contain terms, $-\tilde{\rho}\widetilde{u_i'u_j'}$, which represent turbulent stresses (and are often called the Reynolds stresses). These terms must be modeled with additional equations before the set of equations, (14.59), is "closed" and can be solved. The most widely used *turbulence model* or equation set is the *k-ε model.*[60–63] This assumes a newtonian relationship between the turbulent stresses and mean strain rates, and computes the (fictitious) turbulent viscosity appearing in this relationship from the local turbulent kinetic energy k $(=\overline{u_i u_i}/2)$ and its dissipation rate ε. An equation governing k can be developed by multiplying the u_i equation in Eq. (14.54) by u_i, subtracting from this the equation formed by multiplying the $\bar{u}_i$ equation in Eq. (14.59) by $\bar{u}_i$, and phase-averaging the result. The equation so obtained is

$$\frac{\bar{D}\bar{k}}{Dt} = \tilde{\rho}(P - \varepsilon) - \frac{\partial}{\partial x_j} J_k \tag{14.61a}$$

where P is the rate of turbulence production per unit mass

$$P = -\widetilde{u_i'u_j'}\frac{\partial \bar{u}_i}{\partial x_j} \tag{14.61b}$$

and J_k represents diffusive transport.

In the most commonly used two-equation k-ε model, all the unknown turbulence quantities are modeled in terms of the turbulent velocity scale $k^{1/2}$ and the turbulence length scale $k^{3/2}/\varepsilon$ obtained from the definition of the energy dissipation rate, via

$$\varepsilon \propto \frac{k^{3/2}}{l} \tag{14.62}$$

The rationale is that the rate of energy dissipation is controlled by the rate at which the large eddies feed energy to the smaller dissipative scales which in turn adjust to handle this energy.[60]

A turbulent viscosity μ_T is defined:

$$\mu_T = \frac{C_0 \tilde{\rho} k^2}{\varepsilon} \tag{14.63}$$

where C_0 is a model constant. The turbulent stress terms appearing in Eqs. (14.59) and (14.61) are then modeled in a quasi-newtonian manner:

$$\tilde{\rho}\widetilde{u_i'u_j'} = \tfrac{2}{3}\tilde{\rho}k\delta_{ij} + \tfrac{2}{3}\mu_T \nabla\cdot\tilde{\mathbf{u}}\delta_{ij} - 2\mu_T \bar{S}_{ij} \tag{14.64}$$

where $\bar{S}_{ij}$ is the strain rate of the $\bar{u}_i$ field:

$$\bar{S}_{ij} = \frac{1}{2}\left(\frac{\partial \bar{u}_i}{\partial x_j} + \frac{\partial \bar{u}_j}{\partial x_i}\right) \tag{14.65}$$

PETITIONER'S EXHIBIT 1002
US PATENT NO. 6,581,565

The viscous-stress terms in the momentum equations are evaluated using a newtonian constitutive relation. The turbulent-diffusion terms in the various transport equations are modeled using the turbulent diffusivity. The diffusing flux of a quantity ϕ is given by

$$J_{\phi i} = -\frac{\mu_T}{\sigma_\phi}\frac{\partial \phi}{\partial x_i} \tag{14.66}$$

where σ_ϕ is a turbulent Prandtl number for ϕ.

The model is completed with a transport equation for ε. An exact equation can be developed by suitable manipulation of the Navier-Stokes equations. All ε equation models are of the form[60]

$$\frac{\bar{D}\varepsilon}{Dt} = W - \frac{\partial H_i}{\partial x_i} \tag{14.67}$$

where W is the source term and H_i is the diffusive flux of $\tilde{\rho}\varepsilon$ which is modeled similarly to the other diffusion terms. The appropriate form of W is the subject of much debate. For an incompressible flow, W can be modeled adequately by

$$W = \left(-C_2 + C_1\frac{P}{\varepsilon}\right)\frac{\tilde{\rho}\varepsilon^2}{k} \tag{14.68}$$

C_1 and C_2 are constants: the C_2 term produces the proper behavior of homogeneous isotropic turbulence and the C_1 term modifies this behavior for homogeneous shear. However, for a flow with compression and expansion, an additional term in Eq. (14.68) is needed to account for changes in ε produced by dilation. Several forms for this additional term have been proposed[60, 62] (for example, $C_3\tilde{\rho}\varepsilon\nabla\cdot\tilde{\mathbf{u}}$) and compared.[63] The goal is to construct a W that predicts the appropriate physical behavior under the relevant engine conditions. While different choices for modeling these terms do affect the results (especially the behavior of the turbulence length scale during the cycle[62]), the predictions of mean flow and turbulence intensity do not differ very significantly.[63]

One other FFM that has been applied to engines is the *Reynolds stress model* (RSM) which, in its most general form, comprises seven simultaneous partial differential equations for the six stress components and the dissipation rate ε. This obviously imposes a much greater computing burden compared with the two-equation k-ε model. The limited results available[64] indicate that RSM predictions of the flow field are closer to corresponding measured data than k-ε model predictions.[65]

The large-eddy simulation (LES) approach to turbulence modeling[66] has also been applied to engines. Since here one calculates the large-scale three-dimensional time-dependent flow structure directly, only the turbulence smaller in scale than the grid size need be modeled. Hence these are often referred to as subgrid-scale models. A new dependent variable q, which represents the kinetic energy per unit mass of the turbulent length scales that are too small to resolve in the mesh, is introduced. This variable satisfies a transport equation which con-

PETITIONER'S EXHIBIT 1002
US PATENT NO. 6,581,565

tains terms for production and decay of q and for its convection and diffusion. In the KIVA engine code,[67] this equation has the form:

$$\frac{\partial}{\partial t}(\rho q) + \nabla \cdot (\rho q \mathbf{u}) = -\tfrac{2}{3}\rho q \nabla \cdot \mathbf{u} + \boldsymbol{\sigma} : \nabla \mathbf{u} + \nabla \cdot (\mu \nabla q) - C\rho L^{-1} q^{3/2} + \dot{W}_s \tag{14.69}$$

where $\boldsymbol{\sigma}$ is the turbulent stress tensor, μ the turbulent viscosity, C a constant of order unity, and L a characteristic length on the order of twice the mesh spacing. $\dot{W}_s$ is a source term representing the production of turbulence by the motion of fuel droplets in situations where fuel sprays are important.

The physical meaning of the terms in Eq. (14.69) are as follows. The term $\nabla \cdot (\rho q \mathbf{u})$ is the convection of the turbulence by the resolved (large-scale) velocity field. The term $-\frac{2}{3}\rho q \nabla \cdot \mathbf{u}$ is a compressibility term that is the turbulent analog of $p\,dV$ work. The term $\boldsymbol{\sigma} : \nabla \mathbf{u}$ represents the production of turbulence by shear in the resolved velocity field; $\nabla \cdot (\mu \nabla q)$ is the self-diffusion of the turbulence with diffusivity μ/ρ. The term $-C\rho L^{-1} q^{3/2}$ represents the decay of turbulent energy into thermal energy. This term appears with opposite sign as a source term in the thermal internal energy equation in place of $\boldsymbol{\sigma} : \nabla \mathbf{u}$, which can be thought of as the rate at which kinetic energy of the resolved motions is dissipated by the turbulence. Before it is dissipated, the kinetic energy of the resolved velocity field is first converted into subgrid scale turbulent energy q, which is then converted into heat by the decay term $C\rho L^{-1} q^{3/2}$.[67]

Under most circumstances, the velocity and temperature boundary layers in an engine cylinder will be too thin to be resolved explicitly with a computing mesh that is practical on present-day computers. However, these layers are important because they determine the wall shear and heat flux which are essential boundary conditions for the numerical simulation, and are of practical importance (see Secs. 8.3 and 12.6.5). Special submodels for these boundary layers, referred to as wall functions, are used to connect the wall shear stresses, heat fluxes, wall temperatures, etc., to conditions at the outer edge of the boundary layer. This removes the need to place grid points within the layer. Since the boundary layers are usually turbulent, the logarithmic "turbulent law of the wall" is commonly used. Key assumptions made are: that the finite difference mesh point nearest the wall lies in the law-of-the-wall region and that the law-of-the-wall relation for steady flow past a plane wall is valid under engine cylinder conditions. While these may not be valid assumptions, it is not yet feasible to resolve the flow details within the boundary layer.[68]

14.5.3 Numerical Methodology

The three important numerical features of multidimensional methods are: the computational grid arrangement, which defines the number and positions of the locations at which the flow parameters are to be calculated; the discretization practices used to transform the differential equations of the mathematical model

PETITIONER'S EXHIBIT 1002
US PATENT NO. 6,581,565

into algebraic equations; and the solution algorithms employed to obtain the flow parameters from the discrete equations.[59, 65]

COMPUTING MESH. The requirements of the computing mesh are:

1. It adequately fits the topography of the combustion chamber and/or inlet port, including the moving components.
2. It allows control of local resolution to obtain the maximum accuracy with a given number of grid points.
3. It has the property that each interior grid point is connected to the same number of neighboring points.

The first requirement obviously follows from the need to simulate the effects of changes in engine geometry. The second requirement stems from the fact that computing time increases at least linearly with the number of mesh points. Thus it is desirable that the mesh allow concentration of grid points in regions where steep gradients exist such as jets and boundary layers. The third requirement comes from the need for the mesh to be topologically rectangular in some transformed space so that highly efficient equation solvers for such mesh systems can be utilized.

Early engine models used a grid defined by the coordinate surfaces of a cylindrical-polar frame. Such an approach is adequate provided the combustion chamber walls also coincide with coordinate surfaces. This only occurs for a restricted number of practical chambers (e.g., disc and centered cylindrical bowl-in-piston shapes); even for these, the inlet and exhaust valve circumferences would in general cut across the grid (see Fig. 14-29*a*). While procedures have been devised for modifying the difference equations for such grids to allow for noncoincident boundaries, the preferred approach is to employ some form of flexible "body-fitting" coordinate frame/grid whose surfaces can be shaped to the chamber geometry, as illustrated in Fig. 14-29*b*, which shows a diesel engine combustion chamber fitted by a mesh which is orthogonal-curvilinear in the bowl. This enables the bowl shape to be accurately represented and the boundary layers on its surfaces to be resolved in greater detail. The region between the piston crown and cylinder head surfaces is fitted with a bipolar system which expands and contracts axially to accommodate the piston motion. The orthogonality constraint of this mesh limits its usefulness: the generation of orthogonal meshes for general three-dimensional geometries is cumbersome and the resulting mesh often far from optimal. These problems are largely surmounted by "arbitrary" nonorthogonal lagrangian-eulerian meshes like that used in KIVA,[67] illustrated in Fig. 14-29*c*. This has the additional advantage that the mesh points in the swept volume are not constrained to move axially: their motion can be arbitrarily prescribed.[59]

DISCRETIZATION PRACTICES. These multidimensional engine flow models are time-marching programs that solve finite difference approximations to the gov-

PETITIONER'S EXHIBIT 1002
US PATENT NO. 6,581,565

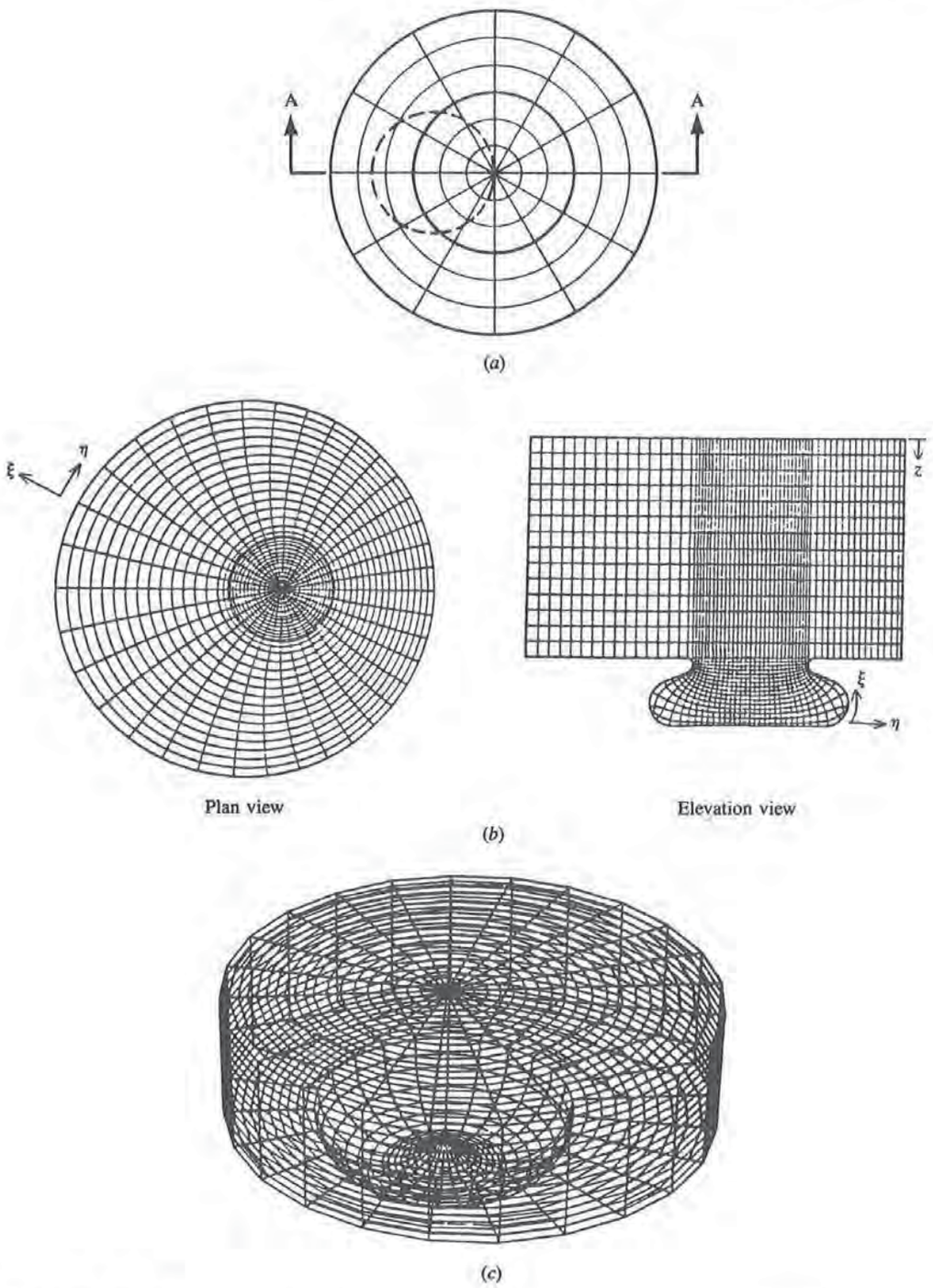


FIGURE 14-29
Different types of computing mesh arrangements for engine combustion chambers. (*a*) Cylindrical polar mesh: dashed line shows valve head circumference.[65] (*b*) Body-fitted orthogonal curvilinear mesh fitted to DI diesel combustion chamber bowl.[69] (*c*) Arbitrary nonorthogonal lagrangian-eulerian (ALE) mesh for offset diesel combustion bowl.[67]

PETITIONER'S EXHIBIT 1002
US PATENT NO. 6,581,565

erning differential equations. The individual cells formed by the mesh or grid serve as the spatial framework for constructing these algebraic finite difference equations. The time variable is similarly discretized into a sequence of small time intervals called time steps: the solution at time t_{n+1} is calculated from the known solution at time t_n. The spatial differencing is made conservative wherever possible. The procedure used is to difference the basic equations in integral form, with the volume of a typical cell used as the control volume and the divergence terms transformed into surface integrals using the divergence theorem.[67]

The discretized equations for any dependent variable ϕ are of the general form:

$$A_p \phi_p^{i+1} = \sum_n A_n \phi_n^{i+1} + S_{\phi,p} V_p + A_p^i \phi_p^i \tag{14.70}$$

where the A's are coefficients expressing the combined influences of convection and diffusion, $S_{\phi,p} V_p$ is the source integral over the cell volume V_p, the subscript p denotes a typical node point in the mesh, the summation $\sum$ is over its (six) nearest neighbors, and the superscripts $i+1$ and i denote "new" and "old" values, at times $t + \delta t$ and t, respectively, where δt is the size of the time step.[69]

Until recently all methods involved similar spatial approximations to calculate convective and diffusive transport, using a blend of first-order upwind differencing for the former and second-order central differencing for the latter. Unfortunately, all discretization practices introduce inaccuracies of some kind, and the standard first-order upwind scheme produces spatial diffusion errors which act in the same way as real diffusion to "smooth" the solutions. The magnitude of the numerical diffusion reduces as the mesh density is increased, but even with as many as 50 mesh points in each coordinate direction, the effect is not eliminated. A recent development has been the introduction of "higher order" spatial approximations which, in the past, had a tendency to produce spurious extrema. This problem has been overcome by the use of "flux blending" techniques. First-order upwind and higher-order approximations are blended in appropriate proportions to eliminate the overshoots of the latter. Even with these schemes, however, true mesh-independent solutions could not be achieved with densities of up to 50 nodes in each coordinate direction; so there is still a need for further improvement.[65]

SOLUTION ALGORITHMS. Numerical calculations of compressible flows are inefficient at low Mach numbers because of the wide disparity between the time scales associated with convection and with the propagation of sound waves. While all methods use first-order temporal discretization and are therefore of comparable accuracy, they differ in whether forward or backward differencing is employed in the transport equations leading to implicit or explicit discrete equations, respectively. In explicit schemes, this inefficiency occurs because the time steps needed to satisfy the sound-speed stability condition are much smaller than those needed to satisfy the convective stability condition alone. In implicit schemes, the inefficiency manifests itself in the additional computational labor

PETITIONER'S EXHIBIT 1002
US PATENT NO. 6,581,565

needed to solve the implicit (simultaneous) system of equations at each time step. This solution is usually performed by iterative techniques.

The computing time requirements of these two approaches scale with the number of equations n and the number of mesh points m, as follows. For explicit methods, computing time scales as nm, but the time step is limited by the stability condition as summarized above. For implicit methods, computing time scales as n^3m and Δt is only limited by accuracy considerations.

One procedure used, a semi-implicit method, is the *acoustic subcycling* method. All terms in the governing equations that are not associated with sound waves are explicitly advanced with a larger time step Δt similar to that used with implicit methods. The terms associated with acoustic waves (the compression terms in the continuity and energy equations and the pressure gradient in the momentum equation) are explicitly advanced using a smaller time step δt that satisfies the sound-speed stability criterion [Eq. (14.23)], and of which the main time step is an integral multiple. While this method works well in many IC engine applications where the Mach number is not unduly low, it is unsuitable for very low Mach number flows since the number of subcycles ($\Delta t/\delta t$) tends to infinity as the Mach number tends to zero. For values of $\Delta t/\delta t$ greater than 50 an implicit scheme becomes more efficient. *Pressure gradient scaling* can be used to extend the method to lower Mach numbers. The Mach number is artificially increased to a larger value (but still small in an absolute sense) by multiplying the pressure gradient in the momentum equation by a time-dependent scaling factor $1/\alpha(t)^2$, where $\alpha(t) > 1$. This reduces the effective sound speed by the factor α. This does not significantly affect the accuracy of the solution because the pressure gradient in low Mach number flows is effectively determined by the flow field and not vice versa. Coupling pressure gradient scaling with acoustic subcycling reduces the number of subcycles by α.[67]

The implicit equations that result from forward differencing consist of simultaneous sets for all variables and thus require more elaborate methods of solution. However, they contain no intrinsic stability constraints. Fully iterative solution algorithms for solution of these equation sets are being replaced with more efficient simultaneous linear equation solvers.[65]

14.5.4 Flow Field Predictions

To illustrate the potential for multidimensional modeling of IC engine flows, examples of the output from such calculations will now be reviewed. A large amount of information on many fluid flow and state variables is generated with each calculation, and the processing, organization, and presentation of this information are tasks of comparable scope to its generation! Flow field results are usually presented in terms of the gas velocity vectors at each grid point of the mesh in appropriately selected planes. Arrows are usually used to indicate the direction and magnitude (by length) of each vector. Examples of such plots—of the flow pattern in the cylinder during the intake process—are shown in Fig. 14-30.[70] The flow field is shown 60° ATC during the intake stroke. A helical intake

PETITIONER'S EXHIBIT 1002
US PATENT NO. 6,581,565

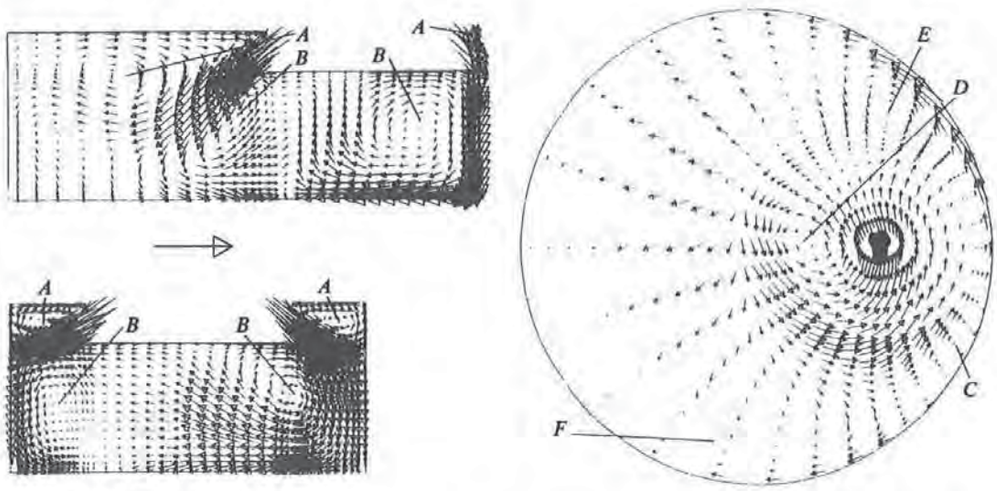


FIGURE 14-30
Computed velocity field within the cylinder at 60° ATC during the intake stroke. Top left: plane through cylinder and inlet valve axes. Bottom left: orthogonal plane through valve axis. Right: circumferential-radial plane halfway between piston and cylinder head. Reference vector arrow corresponds to velocity of 132 m/s. Letters denote centers of toroidal flow structures.[70]

port is used to general swirl, and the flow through the valve curtain area (see Sec. 6.3.2)—the inlet boundary condition for the calculation—was determined by measurement. The calculation used a curvilinear, axially expanding and contracting grid with about 16,000 mesh points of the type shown in Fig. 14-29*b*. It employed a fully iterative solution algorithm with standard upwind differencing and the k-ε turbulence model. Shown in Fig. 14-30 are the plane through the valve and cylinder axis (top left), the perpendicular plane through the valve axis (bottom left), and a circumferential radial plane halfway between the cylinder head and the piston (right).

The major features of the conical jet flow through the inlet valve into the cylinder are apparent (see Sec. 8.1). However, the off-cylinder-axis valve and the swirl generated by the helical port produce substantial additional complexity. The letters on the figures show regions of local recirculation. Regions *A* and *B* correspond to the rotating flow structures observed in simpler geometries (see Fig. 8-3): however, regions *CF* indicate that the swirling motion is far from solid-body rotation.[70]

Figures 14-31 and 14-32 show comparisons of three-dimensional predictions of in-cylinder flow fields with data. The computational and experimental geometries have been matched, as have the inlet flow velocities through the valve open area and engine speed. Figure 14-31 shows predicted and measured mean flow velocities and turbulence intensities within the cylinder, with a conventional inlet port and valve configuration, at 68° ATC during the intake stroke.[71] The experimental values come from LDA measurements (see Sec. 8.2.2). The general features of the mean flow are reproduced by the model with reasonable accuracy, though some details such as the flow along the cylinder toward the head in the

PETITIONER'S EXHIBIT 1002
US PATENT NO. 6,581,565

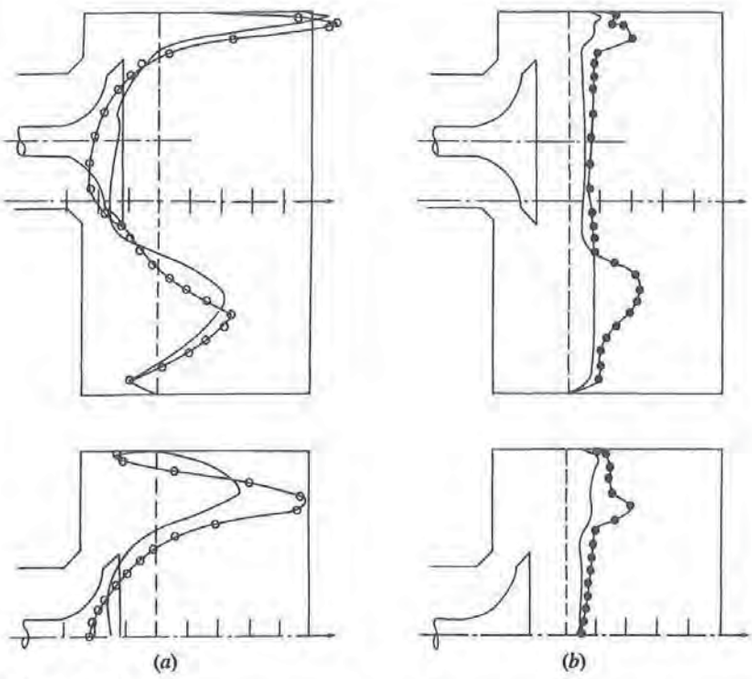


FIGURE 14-31
Comparison of (*a*) measured and predicted axial velocity profiles and (*b*) measured and predicted turbulence intensity profiles at 68° ATC during the intake stroke. Data: line with points. Predictions: line without points. Each interval on the scale on cylinder axes corresponds to 2 times the mean piston speed.[71]

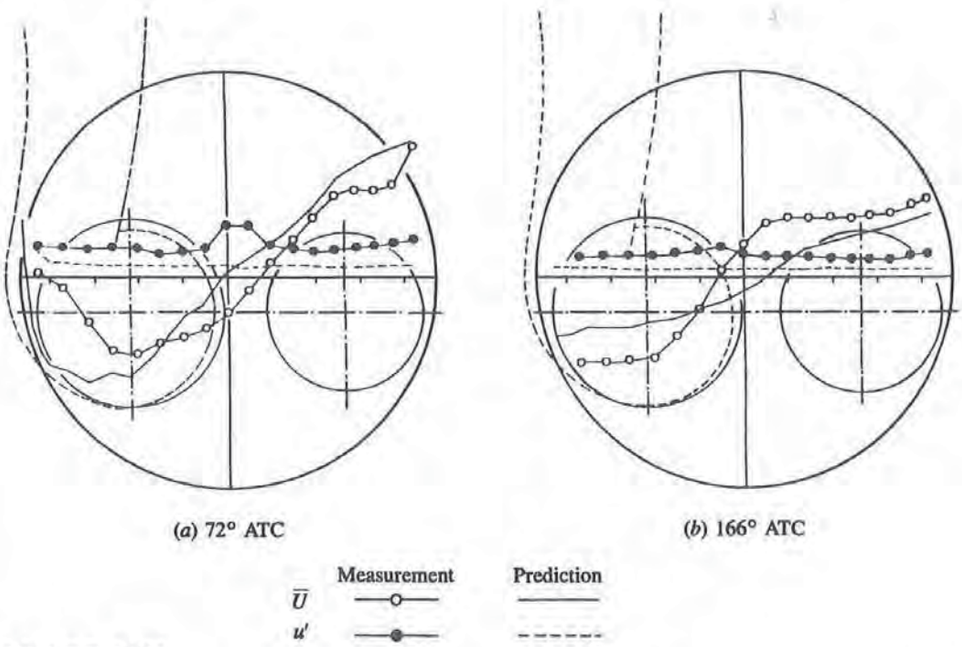


FIGURE 14-32
Comparison between measured and predicted swirl velocities and turbulence intensities at 72 and 166° ATC during the intake stroke. Engine equipped with helical port.[59]

PETITIONER'S EXHIBIT 1002
US PATENT NO. 6,581,565

symmetry plane are not predicted. The approximate magnitude of the turbulence intensity levels are predicted, but the values within the conical intake jet are underestimated. Figure 14-32 shows in-cylinder swirl velocity predictions and measurements in an engine with a disc-shaped chamber and helical intake port, during the intake and compression strokes. Again the major features of the experimental profiles are predicted adequately, though differences in detail are significant.[59]

Comparative multidimensional modeling studies of different turbulence models,[63] differencing schemes,[59, 65] and number of grid points[59] indicate the following. Differences in the form and coefficients of the dilation term in the k-ε turbulence model have only modest effects on flow field predictions. Higher-order turbulence models might provide improved accuracy.[65] Both mesh refinement, more finely spaced grid points, and use of higher-order differencing schemes have been shown to improve significantly the accuracy of the predictions, often of course with substantial increases in computing requirements.[59]

Examples of predictions of other types of engine flow processes are the following. Squish flows into bowl-in-piston combustion chambers have been extensively analyzed. Figure 14-33*a* shows the flow field into and within an off-axis bowl in piston at 20° BTC of the compression stroke. The strong radially inward squish flow at the bowl lip is apparent. However, the bowl-axis offset produces a stronger flow where the squish region is greatest in extent and results in a net flow across the bowl center plane and a complex flow pattern within the bowl. Turbulence intensity results are often displayed on contour plots. Figure 14-33*b* shows the turbulence intensity distribution within the bowl at TC after compression. The correspondence between high-velocity regions generated by the squish flow (Fig. 14-33*a*) and higher turbulence intensities is apparent. A substantial variation in intensity throughout the bowl is predicted. Assimilation of detailed three-dimensional velocity data from individual two-dimensional planar vector maps is cumbersome: computer-generated three-dimensional perspective views of the velocity field are proving valuable.[72]

An alternative method of displaying multidimensional model results, especially from three-dimensional calculations, is through particle traces. Infinitesimal particles are placed at key locations in the flow field at a given crank angle (e.g., at the start of the process of interest) and their trajectories are computed from the velocity field as a function of time through the process. Figure 14-34 shows the traces of four particles, initially located near the center of the entrance to a helical inlet port at 30° ATC, as they traverse the port.[73] The particle traces illustrate the mechanism by which a helical port generates swirl. A second example of particle traces (Fig. 14-35) within the cylinder during the intake stroke indicates the complexity of swirling flows with realistic port and valve geometries.[74] The figure shows the paths traced out by six particles, initially evenly spaced around the valve curtain area at TC at the start of the intake process, during the intake stroke with a tangentially directed inlet port. While all the particles follow a helical path within the cylinder, the steepness of these paths varies substantially depending on the initial location of each particle.

PETITIONER'S EXHIBIT 1002
US PATENT NO. 6,581,565

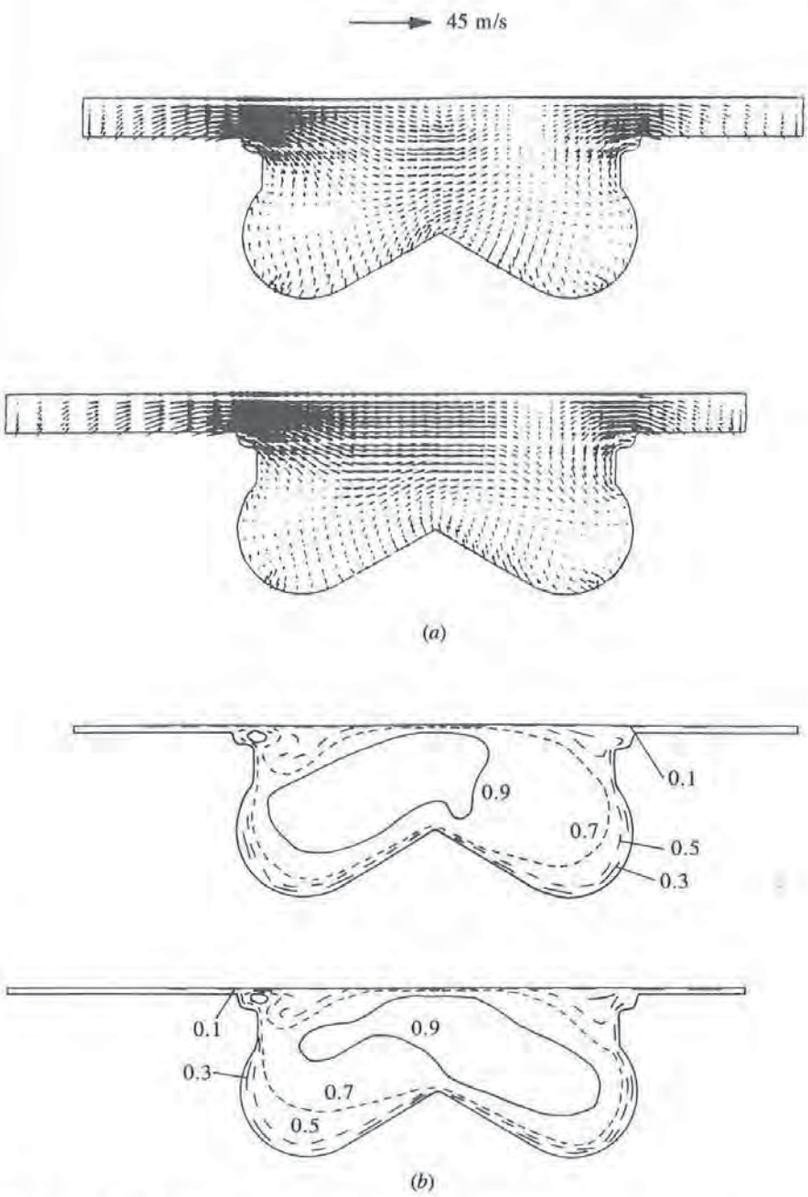


FIGURE 14-33
(*a*) Predicted velocity flow field within the offset bowl of DI diesel chamber in two orthogonal planes through the bowl center, at 20° BTC toward end of compression. Reference vector = 45 m/s. (*b*) Predicted relative turbulence intensity $u'/\bar{S}_p$ within the bowl in the same two planes at TC at the end of compression. Numbered contours show fraction of maximum value.[72]

Multidimensional models also provide local composition information. Studies have been done of two-stroke cycle scavenging flows (e.g., Ref. 75) and of the mixing between fresh mixture and residual gases in four-stroke cycle engines (e.g., Ref. 76). Figure 14-36 shows how the mixing between fresh fuel and air, and

PETITIONER'S EXHIBIT 1002
US PATENT NO. 6,581,565

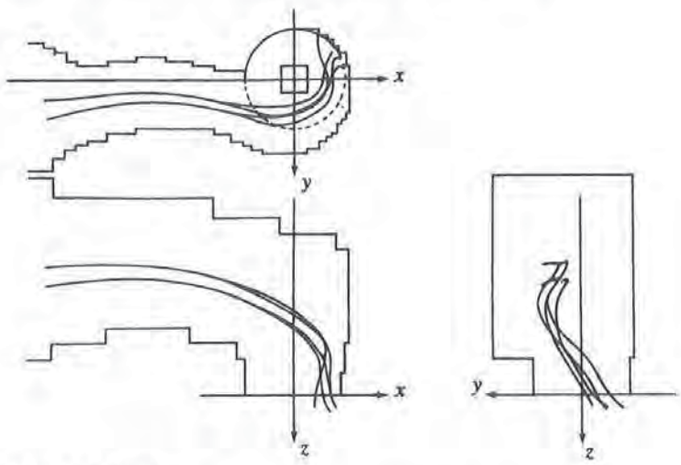


FIGURE 14-34
Computed trajectories of gas particles moving through a helical inlet port during the intake process. Particles initially located near center of port at 30° ATC.[73]

residual gases, proceeds during the intake and compression strokes of a spark-ignition engine four-stroke cycle. Concentrations (defined as fresh mixture mass/total mixture mass) at different locations within the cylinder are plotted against crank angle ($z = 2$ is near the head, $z = 7$ near the piston; $y = 2$ is near the cylinder axis, $y = 7$ near the cylinder liner). A relatively long time is required for the fresh and residual gases to mix and at 30° BTC there is still several percent

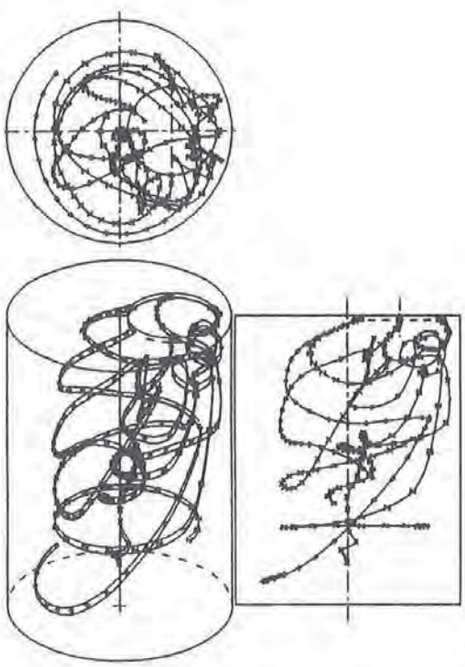


FIGURE 14-35
Computed trajectories traced out during the intake stroke by six gas particles initially evenly spaced around the valve curtain area at TC at the start of the intake process, with a tangentially directed inlet port. Cylinder shown with piston at BC, at the end of the intake stroke.[74]

PETITIONER'S EXHIBIT 1002
US PATENT NO. 6,581,565

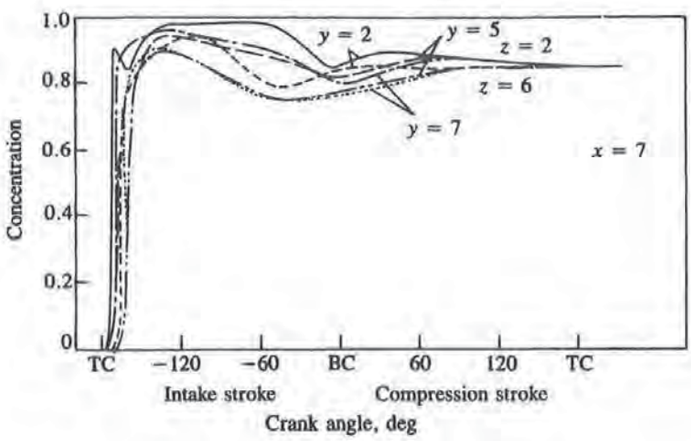


FIGURE 14-36
Computed concentration distribution of fresh fuel-air mixture and residual gas within the cylinder during the intake and compression stroke of a spark-ignition engine. Concentration expressed as fresh mixture mass/total mixture mass. $z = 2$ is near the cylinder head, $z = 7$ near the piston; $y = 2$ near the cylinder axis, $y = 7$ near the cylinder liner; $x = 7$ along the radius passing beneath the inlet valve. 2000 rev/min and wide-open throttle.[76]

nonuniformity. At part load with its higher residual fraction, one would expect these differences to be larger.[76]

14.5.5 Fuel Spray Modeling

The physical behavior of liquid fuel sprays when injected into the engine cylinder, as occurs in compression-ignition (or stratified-charge) engines, has already been described in Sec. 10.5. Here the current status of models for such spray behavior which are used with multidimensional models of gas motion within the cylinder are reviewed. Fuel-injected internal combustion engines present a particularly difficult problem for numerical simulation. The fuel spray produces an inhomogeneous fuel-air mixture: the spray interacts with and strongly affects the flow patterns and temperature distribution within the cylinder. The fuel is injected as liquid, it atomizes into a large number of small droplets with a wide spectrum of sizes, the droplets disperse and vaporize as the spray moves through the surrounding air, droplet coalescence and separation can occur, gaseous mixing of fuel vapor and air then takes place, followed, finally, by combustion. Models which explicitly treat the two-phase structure of this spray describe the spray behavior in terms of differential conservation equations for mass, momentum, and energy.

Two such classes of model exist, usually called the continuum droplet model (CDM) and the discrete droplet model (DDM). Both approaches average over flow processes occurring on a scale comparable to the droplet size, and thus require independent modeling of the interactions occurring at the gas droplet interface: typically this is done with correlations for droplet drag and heat and mass transfer. The CDM attempts to represent the motion of all droplets via an

PETITIONER'S EXHIBIT 1002
US PATENT NO. 6,581,565

eulerian partial differential spray probability equation containing, in its most general case, eight independent variables: time, three spatial coordinates, droplet radius and the three components of the droplet velocity vector. This approach imposes enormous computational requirements. The DDM uses a statistical approach; a representative sample of individual droplets, each droplet being a member of a group of identical non-interacting droplets termed a "parcel," is tracked in a lagrangian fashion from its origin at the injector by solving ordinary differential equations of motion which have time as the independent variable.

This latter type of model is used in engine spray analysis.[77, 78] Droplet parcels are introduced continuously throughout the fuel-injection process, with specified initial conditions of position, size, velocity, number of droplets in the parcel prescribed at the "zone of atomization" according to an assumed or known size distribution, initial spray angle, fuel-injection rate, and fuel temperature at the nozzle exit. The values of these parameters are chosen to represent statistically all such values within the spray. They are then tracked in a lagrangian fashion through the computational mesh used for solving the gas-phase partial differential conservation equations.

The equations describing the behavior of individual droplets are[79]

$$\frac{d}{dt}\,\mathbf{x}_k = \mathbf{u}_k \tag{14.71}$$

$$\frac{d}{dt}\,(m_k\,\mathbf{u}_k) = -\frac{m_k}{\rho_k}\,\nabla p + F_{D,k}(\mathbf{u} - \mathbf{u}_k) \tag{14.72}$$

$$m_k\,\frac{dh_k}{dt} = \dot{q}_k + (h_v - h_k)\,\frac{dm_k}{dt} \tag{14.73}$$

where $\mathbf{x}_k$ is the position vector for droplet k and $\mathbf{u}_k$ its velocity, m_k is the droplet mass and ρ_k the droplet density, $\mathbf{u}$ is the gas velocity, h_k the droplet specific enthalpy, $\dot{q}_k$ the heat-transfer rate from the gas to the droplet, and h_v the specific enthalpy of fuel vapor. $F_{D,k}$ is the droplet drag function:

$$F_{D,k} = \tfrac{1}{2}\pi r_k^2\,\rho C_D\,|\mathbf{u} - \mathbf{u}_k| \tag{14.74}$$

where r_k is the droplet radius, μ and ρ the gas viscosity and density, and C_D is the drag coefficient. $F_{D,k}$ is the sum of the Stokes drag and the form drag, and in the laminar limit where $C_D = 24/\mathrm{Re}$ with $\mathrm{Re} = 2r_k\,\rho\,|\mathbf{u} - \mathbf{u}_k|/\mu$ it goes to $6\pi r_k\,\mu$.

An equation for the evaporation rate completes this set: it is usually assumed that the droplet is in thermal equilibrium at its wet-bulb temperature, T_s. Then a balance between heat transfer to the droplet and the latent heat of vaporization carried away by the fuel vapor exists:

$$(h_v - h_k)\,\frac{dm_k}{dt} = -\dot{q}_k \tag{14.75}$$

While a large portion of the droplet lifetime is spent in this equilibrium, terms

PETITIONER'S EXHIBIT 1002
US PATENT NO. 6,581,565

can be added to Eq. (14.75) so that it describes the heat-up phase where the droplet temperature increases from its initial value to T_s.[79] The heat and mass exchange rates are calculated from experimentally based correlations for droplet Nusselt and Sherwood numbers as functions of Reynolds, Prandtl, and Schmidt numbers.[77, 80]

Account must now be taken of the two-way nature of the coupling between the gas and the liquid. The gas velocity, density, temperature, and fuel vapor concentration required for solving the droplet equations are taken from the values prevailing in the grid cell in which the droplet parcel resides. At the same time, a field of "sources" is assembled for the interphase mass, momentum, and energy transfer, and these are subsequently fed back into the gas-phase solution preserving conservation between phases.[81] The gas-phase mass, momentum, and energy conservation equations require additional terms to account for the displacement effect of the particles, the density change associated with mixing with the fuel vapor, the drag of the droplets, the initial momentum difference and enthalpy difference between evaporated fuel at the drop surface and the surrounding gas, and heat transfer to the droplet.[79]

The above treatment is limited to "thin sprays" where the droplets are sufficiently far apart for interparticle interactions to be unimportant. This assumption is not valid in the immediate vicinity of the injector or in narrow cone sprays. In such "thick sprays" interparticle interactions—collisions which can result in coalescence or in reseparation of droplets—are important.

The most complete models of atomized fuel sprays represent the spray by a Monte Carlo–based discrete-particle technique.[67, 80] The spray is described by a droplet distribution function—a droplet number density in a phase space of droplet position, velocity, radius, and temperature. The development of this distribution function is determined by the so-called spray equation.[80] The distribution function is statistically sampled and the resulting discrete particles are followed as they locally interact and exchange mass, momentum, and energy with the gas, using the above lagrangian droplet equations. Each discrete droplet represents a group or parcel of droplets. Droplet collisions are described by appropriate terms in the spray equation.

Figure 14-37 shows the type of results such spray models can generate. The calculation involves a direct-injection stratified-charge engine with an offset bowl-in-piston combustion chamber and a tilted injector. Injection of a single hollow-cone fuel spray commences at 52° BTC. Figure 14-37*a* and *b* shows the fuel spray at 39° BTC at the end of injection and later, at 28° BTC, just before combustion. Of the 2000 computational particles injected (each representing some number of identical physical droplets), 1218 remain at 39° BTC and 773 at 28° BTC. Evaporation and coalescence have caused these decreases. Figure 14-37*c* shows the gas velocity vectors at the end of injection: the flow field set up by momentum exchange with the injected fuel spray can be seen, and the highest velocities exist in the spray region. Figure 14-37*d* shows the equivalence ratio contours at 28° BTC just prior to ignition. The highly nonhomogeneous fuel vapor distribution within the bowl is evident.[67,82]

PETITIONER'S EXHIBIT 1002
US PATENT NO. 6,581,565

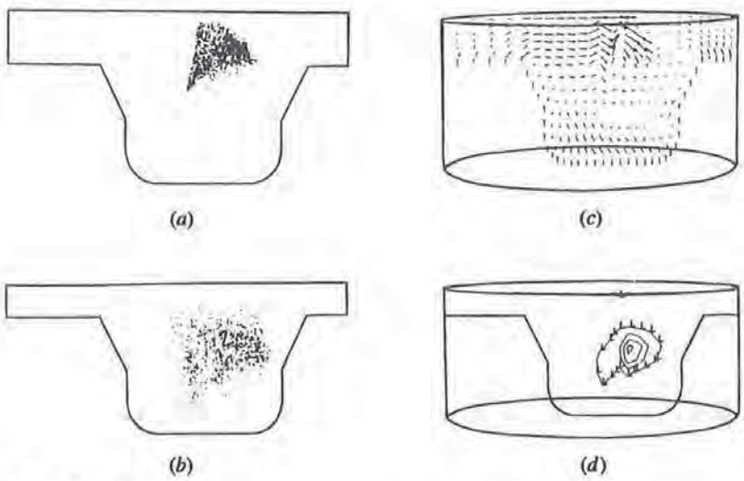


FIGURE 14-37
Predictions of single hollow-cone fuel spray behavior in direct-injection stratified-charge engine. Injection commences at 52° BTC with 2000 computational particles. (*a*) Location of 1218 remaining spray particles at 39° BTC at the end of injection. (*b*) Location of 773 spray particles at 28° BTC, just before combustion. (*c*) Gas velocity vectors at the end of injection at 39° BTC. (*d*) Fuel/air equivalence ratio contours just prior to ignition at 28° BTC. The L contour is $\phi = 0.5$, the contour interval $\Delta\phi$ is 0.5.[82]

14.5.6 Combustion Modeling

In numerical calculations of reacting flows, computer time and storage constraints place severe restrictions on the complexity of the reaction mechanisms that can be incorporated. While it is feasible to include detailed chemical mechanisms for combustion of hydrocarbon-air mixtures in one-dimensional calculations, it becomes increasingly impractical to attempt such complexity in two- and three-dimensional studies. Accordingly, engine calculations have been forced to use greatly simplified reaction schemes. In addition, detailed reaction schemes are only available for the simpler hydrocarbon fuels (e.g., methane, propane, butane): for higher hydrocarbon compounds and practical fuels which are blends of a large number of hydrocarbons, the detailed mechanisms have yet to be defined. Accordingly, multidimensional engine calculations have used highly simplified chemical kinetic schemes, with one or at most a few reactions, to represent the combustion process. While such schemes can be calibrated with experimental data to give acceptable results over a limited range of engine conditions, they lack an adequate fundamental basis.

The most common practice has been to assume the combustion process, fuel + oxidizer → products, is governed by a single rate equation of an Arrhenius form:

$$R_f = A\rho^2 x_f^a x_{ox}^b \exp\left(-\frac{E_A}{\tilde{R}T}\right) \tag{14.76}$$

where R_f is the rate of disappearance of unburned fuel, x_f and x_{ox} are unburned fuel and oxidizer mass fractions, $\tilde{R}$ is the universal gas constant, and a, b, A, and

PETITIONER'S EXHIBIT 1002
US PATENT NO. 6,581,565

E_A are constants (usually a and b are taken to be unity, or to be 0.5). Values for the preexperimental factor A and activation energy E_A are obtained by matching to experimentally determined rates of burning.

While this approach "works" in the sense that, when calibrated, its predictions can show reasonable agreement with data, it has three major problems. The first is the presumption that the complex hydrocarbon fuel oxidation process can be adequately represented by a single (or limited number of) overall reaction(s). The fact that it is usually necessary to adjust the constants in Eq. (14.76) as engine design and operating parameters change is one indication of this problem. Second, Eq. (14.76) uses local *average* values of concentrations and temperatures to calculate the local reaction rate, whereas the *instantaneous* local values will actually determine the reaction rate. These two rates will only be equal if the reaction time scale is much longer than that of the turbulent fluctuations, which is not the case in engine combustion. Third, the implied strong dependence of burning rate on chemical kinetics is at variance with the known experimental evidence on engine combustion (see Secs. 9.3.2 and 10.3). The effects of turbulence on the burning rate, apart from the augmentation of the thermal and mass diffusivities, are not represented by equations of the form of (14.76).[83, 84]

An alternative, equally straightforward, approach assumes that turbulent mixing is the rate-controlling process: the kinetics are sufficiently fast for chemistry modeling to be unimportant. Thus reactions proceed instantly to completion once mixing occurs at a molecular level in the smaller-scale eddies of the turbulent flow; the rate-controlling process is then the communication between and decay of the large-scale eddies. Thus the reaction rate is inversely proportional to the turbulent mixing time τ_T $(= l_I/u')$ which is equated to k/ε. Whether fuel or oxygen concentration is limiting, and the need for sufficient hot products to ensure flame spreading are also incorporated. For extremely lean (or rich) mixtures, the reaction may become kinetically controlled. A choice between Eq. (14.76) and the above mixing-controlled model can be made depending on whether the ratio of a chemical reaction time to the turbulent mixing time is greater or less than unity.[83, 84]

An example of a two-dimensional calculation of flame propagation in a premixed-charge spark-ignition engine illustrates the type of results which have

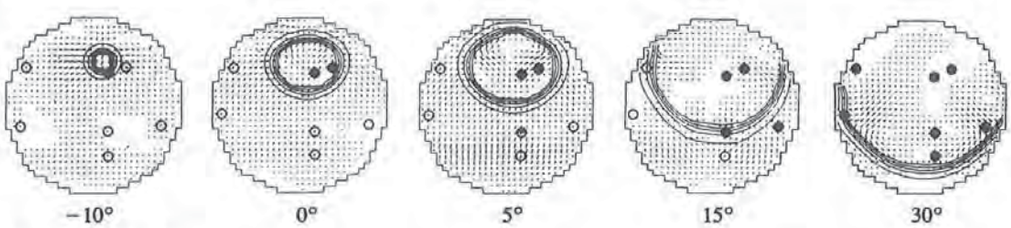


FIGURE 14-38
Isotherms and velocity vectors during the combustion process in premixed spark-ignition engine predicted by two-dimensional computational fluid dynamic code. Points show ionization probe locations in the cylinder head in corresponding experiment: open symbols are before flame arrival; filled symbols are after flame arrival. Crank angle values are relative to TC = 0°.[85]

PETITIONER'S EXHIBIT 1002
US PATENT NO. 6,581,565

been generated to date. Figure 14-38[85] shows computed constant-temperature lines and velocity vectors, looking down on the piston, as the flame develops from the spark. The points show ionization probe locations: open symbols denote prior to and closed symbols after flame arrival. A combustion model of the form of Eq. (14.76) was used and results in a thick "turbulent" flame with an approximately cylindrical front surface. Flame front propagation speeds are adequately predicted; the flame is not modeled in sufficient detail to describe its actual structure (see Sec. 9.3.2). Practical use is now being made of these combustion codes for both spark-ignition engine (e.g., Refs. 83, 86, and 87) and compression-ignition engine studies.[84, 88]

References

1. Streit, E. E., and Borman, G. L.: "Mathematical Simulation of a Large Turbocharged Two-Stroke Diesel Engine," SAE paper 710176, *SAE Trans.*, vol. 80, 1971.
2. Assanis, D. N., and Heywood, J. B.: "Development and Use of Computer Simulation of the Turbocompounded Diesel System for Engine Performance and Component Heat Transfer Studies," SAE paper 860329, 1986.
3. Watson, N., and Janota, M. S.: *Turbocharging the Internal Combustion Engine*, John Wiley, New York, 1982.
4. Janota, M. S., Hallam, A. J., Brock, E. K., and Dexter, S. G.: "The Prediction of Diesel Engine Performance and Combustion Chamber Component Temperatures Using Digital Computers," *Proc. Instn Mech. Engrs*, vol. 182, pt. 3L, pp. 58–70, 1967–1968.
5. Benson, R. S., Garg, R. D., and Woollatt, D.: "A Numerical Solution of Unsteady Flow Problems," *Int. J. Mech. Sci.*, vol. 6, pp. 117–144, 1964.
6. Benson, R. S.: In J. H. Horlock and D. E. Winterbone (eds.), *The Thermodynamics and Gas Dynamics of Internal Combustion Engines*, vol. 1, Clarendon Press, Oxford, 1982.
7. Chapman, M., Novak, J. M., and Stein, R. A.: "Numerical Modeling of Inlet and Exhaust Flows in Multi-Cylinder Internal Combustion Engines," in T. Uzkan (ed.), *Flows in Internal Combustion Engines*, ASME, 1982.
8. Bulaty, T., and Niessner, H.: "Calculation of 1-D Unsteady Flows in Pipe Systems of I.C. Engines," ASME paper ASME-WA7, 1984.
9. Takizawa, M., Uno, T., Oue, T., and Yura, T.: "A Study of Gas Exchange Process Simulation of an Automotive Multi-Cylinder Internal Combustion Engine," SAE paper 820410, *SAE Trans.*, vol. 91, 1982.
10. Baruah, P. C., Benson, R. S., and Balouch, S. K.: "Performance and Emission Predictions of a Multi-Cylinder Spark Ignition Engine with Exhaust Gas Recirculation," SAE paper 780663, 1978.
11. Poulos, S. G., and Heywood, J. B.: "The Effect of Chamber Geometry on Spark-Ignition Engine Combustion," SAE paper 830334, *SAE Trans.*, vol. 92, 1983.
12. Heywood, J. B., Higgins, J. M., Watts, P. A., and Tabaczynski, R. J.: "Development and Use of a Cycle Simulation to Predict SI Engine Efficiency and NO_x Emissions," SAE paper 790291, 1979.
13. Watts, P. A., and Heywood, J. B.: "Simulation Studies of the Effects of Turbocharging and Reduced Heat Transfer on Spark-Ignition Engine Operation, SAE paper 800289, 1980.
14. Lavoie, G. A., and Blumberg, P. N.: "A Fundamental Model for Predicting Fuel Consumption, NO_x and HC Emissions of the Conventional Spark-Ignited Engine," *Combust. Sci. and Technol.*, vol. 21, pp. 225–258, 1980.
15. Novak, J. M., and Blumberg, P. N.: "Parametric Simulation of Significant Design and Operating Alternatives Affecting the Fuel Economy and Emissions of Spark-Ignited Engines," SAE paper 780943, *SAE Trans.*, vol. 87, 1978.
16. Groff, E. G., and Matekunas, F. A.: "The Nature of Turbulent Flame Propagation in a Homogeneous Spark-Ignited Engine," SAE paper 800133, *SAE Trans.*, vol. 89, 1980.

PETITIONER'S EXHIBIT 1002
US PATENT NO. 6,581,565

17. Mattavi, J. N.: "The Attributes of Fast Burning Rates in Engines," SAE paper 800920, *SAE Trans.*, vol. 89, in SP-467, *The Piston Engine—Meeting the Challenge of the 80s*, 1980.
18. Keck, J. C.: "Turbulent Flame Structure and Speed in Spark-Ignition Engines," *Proceedings of Nineteenth Symposium (International) on Combustion*, pp. 1451–1466, The Combustion Institute, 1982.
19. Beretta, G. P., Rashidi, M., and Keck, J. C.: "Turbulent Flame Propagation and Combustion in Spark Ignition Engines," *Combust. Flame*, vol. 52, pp. 217–245, 1983.
20. Keck, J. C., Heywood, J. B., and Noske, G.: "Early Flame Development and Burning Rates in Spark-Ignition Engines," SAE paper 870164, 1987.
21. Tabaczynski, R. J., Ferguson, C. R., and Radhakrishnan, K.: "A Turbulent Entrainment Model for Spark-Ignition Engine Combustion," SAE paper 770647, *SAE Trans.*, vol. 86, 1977.
22. Tabaczynski, R. J., Trinker, F. H., and Shannon, B. A. S.: "Further Refinement and Validation of a Turbulent Flame Propagation Model for Spark-Ignition Engines," *Combust. Flame*, vol. 39, pp. 111–121, 1980.
23. Borgnakke, C.: "Flame Propagation and Heat-Transfer Effects in Spark-Ignition Engines," in J. C. Hilliard and G. S. Springer (eds.), *Fuel Economy in Road Vehicles Powered by Spark Ignition Engines*, chap. 5, pp. 183–224, Plenum Press, 1984.
24. Launder, B. E., and Spalding, D. B.: *Lectures in Mathematical Models of Turbulence*, Academic Press, 1972.
25. Borgnakke, C., Arpaci, V. S., and Tabaczynski, R. J.: "A Model for the Instantaneous Heat Transfer and Turbulence in a Spark Ignition Engine," SAE paper 800287, 1980.
26. Borgnakke, C., Davis, G. C., and Tabaczynski, R. J.: "Predictions of In-Cylinder Swirl Velocity and Turbulence Intensity for an Open Chamber Cup in Piston Engine," SAE paper 810224, *SAE Trans.*, vol. 90, 1981.
27. Davis, G. C., Tabaczynski, R. J., and Belaire, R. C.: "The Effect of Intake Valve Lift on Turbulence Intensity and Burnrate in S.I. Engines," SAE paper 840030, *SAE Trans.*, vol. 93, 1984.
28. Davis, G. C., Mikulec, A., Kent, J. C., and Tabaczynski, R. J.: "Modeling the Effect of Swirl on Turbulence Intensity and Burn Rate in S.I. Engines and Comparison with Experiment," SAE paper 860325, 1986.
29. Stivender, D. L.: "Sonic Throttling Intake Valves Allow Spark-Ignition Engine to Operate with Extremely Lean Mixtures," SAE paper 680399, *SAE Trans.*, vol. 77, 1968.
30. Hires, S. D., Tabaczynski, R. J., and Novak, J. M.: "The Prediction of Ignition Delay and Combustion Intervals for a Homogeneous Charge, Spark Ignition Engine," SAE paper 780232, *SAE Trans.*, vol. 87, 1978.
31. Primus, R. J., and Wong, V. W.: "Performance and Combustion Modeling of Heterogeneous Charge Engines," SAE paper 850343, 1985.
32. Shipinski, J., Uyehara, O. A., and Myers, P. S.: "Experimental Correlation between Rate of Injection and Rate of Heat Release in Diesel Engine," ASME paper 68-DGP-11, 1968.
33. Whitehouse, N. D., and Way, R. J. B.: "Simple Method for the Calculation of Heat Release Rates in Diesel Engines Based on the Fuel Injection Rate," SAE paper 710134, 1971.
34. Woschni, G., and Anisits, F.: "Experimental Investigation and Mathematical Presentation of Rate of Heat Release in Diesel Engines Dependent Upon Engine Operating Conditions," SAE paper 740086, 1974.
35. Watson, N., Pilley, A. D., and Marzouk, M.: "A Combustion Correlation for Diesel Engine Simulation," SAE paper 800029, 1980.
36. Kuo, T., Yu, R. C., and Shahed, S. M.: "A Numerical Study of the Transient Evaporating Spray Mixing Process in the Diesel Environment," SAE paper 831735, *SAE Trans.*, vol. 92, 1983.
37. Chiu, W. S., Shahed, S. M., and Lyn, W. T.: "A Transient Spray Mixing Model for Diesel Combustion," SAE paper 760128, *SAE Trans.*, vol. 85, 1976.
38. Rife, J. M., and Heywood, J. B.: "Photographic and Performance Studies of Diesel Combustion with a Rapid Compression Machine," SAE paper 740948, *SAE Trans.*, vol. 83, 1974.
39. Sinnamon, J. F., Lancaster, D. R., and Steiner, J. C.: "An Experimental and Analytical Study of Engine Fuel Spray Trajectories," SAE paper 800135, *SAE Trans.*, vol. 89, 1980.
40. Kobayashi, H., Yagita, M., Kaminimoto, T., and Matsuoka, S.: "Prediction of Transient Diesel

PETITIONER'S EXHIBIT 1002
US PATENT NO. 6,581,565

Sprays in Swirling Flows Via a Modified 2-D Model," SAE paper 860332, 1986.
41. Ricou, F. P., and Spalding, D. B.: "Measurements of Entrainment by Axisymmetric Turbulent Jets," *J. Fluid Mech.*, vol. 9, pp. 21–32, 1961.
42. Abramovich, G. M.: *The Theory of Turbulent Jets*, MIT Press, Cambridge, Mass., 1963.
43. Shahed, S. M., Flynn, P. F., and Lyn, W. T.: "A Model for the Formation of Emissions in a Direct-Injection Diesel Engine," in J. N. Mattavi and C. A. Amann (eds.), *Combustion Modeling in Reciprocating Engines*, pp. 345–368, Plenum Press, 1980.
44. Hiroyasu, H., Kadota, T., and Arai, M.: "Development and Use of a Spray Combustion Modeling to Predict Diesel Engine Efficiency and Pollutant Emission," paper 214–12, *Bull. JSME*, vol. 26, no. 214, pp. 569–575, 1983.
45. Hiroyasu, H., Kadota, T., and Arai, M.: "Development and Use of a Spray Combustion Modeling to Predict Diesel Engine Efficiency and Pollutant Emissions (Part 2. Computational Procedure and Parametric Study), "paper 214-13, *Bull. JSME*, vol. 26, no. 214, pp. 576–583, 1983.
46. Hiroyasu, H.: "Diesel Engine Combustion and Its Modeling," in *Proceedings of International Symposium on Diagnostics and Modeling of Combustion in Reciprocating Engines*, COMODIA 85, pp. 53–75, Tokyo, September 4–6, 1985.
47. Blumberg, P. N., Lavoie, G. A., and Tabaczynski, R. J.: "Phenomenological Models for Reciprocating Internal Combustion Engines," *Prog. Energy Combust. Sci.*, vol. 5, pp. 123–167, 1979.
48. Hires, S. D., Ekchian, A., Heywood, J. B., Tabaczynski, R. J., and Wall, J. C.: "Performance and NO_x Emissions Modeling of Jet Ignition Prechamber Stratified Charge Engine," SAE paper 760161, *SAE Trans.*, vol. 85, 1976.
49. Hiroyasu, H., Yoshimatsu, A., and Arai, M.: "Mathematical Model for Predicting the Rate of Heat Release and Exhaust Emissions in IDI Diesel Engines," paper C102/82, *Proceedings of Conference on Diesel Engines for Passenger Cars and Light Duty Vehicles*, Institution of Mechanical Engineers, London, 1982.
50. Watson, N., and Kamel, M.: "Thermodynamic Efficiency Evaluation of an Indirect Injection Diesel Engine," SAE paper 790039, *SAE Trans.*, vol. 88, 1979.
51. Mansouri, S. H., Heywood, J. B., and Radhakrishnan, K.: "Divided-Chamber Diesel Engine, Part I: A Cycle-Simulation which Predicts Performance and Emissions," SAE paper 820273, *SAE Trans.*, vol. 91, 1982.
52. Mansouri, S. H., Heywood, J. B., and Ekchian, J. A., "Studies of NO_x and Soot Emissions from an IDI Diesel using an Engine Cycle Simulation," paper C120/82, in *Diesel Engines for Passenger Cars and Light Duty Vehicles*, Institution of Mechanical Engineers Conference Publication 1982-8, pp. 215–227, 1982.
53. Syed, S. A., and Bracco, F. V.: "Further Comparisons of Computed and Measured Divided-Chamber Engine Combustion," SAE paper 790247, 1979.
54. Meintjes, K., and Alkidas, A. C.: "An Experimental and Computational Investigation of the Flow in Diesel Prechambers," SAE paper 820275, *SAE Trans.*, vol. 91, 1982.
55. Watson, N., and Marzouk, M.: "A Non-Linear Digital Simulation of Turbocharged Diesel Engines under Transient Conditions," SAE paper 770123, *SAE Trans.*, vol. 86, 1977.
56. Marzouk, M., and Watson, N.: "Load Acceptance of Turbocharged Diesel Engines," paper C54/78, *Proceedings of Conference on Turbocharging and Turbochargers*, Institution of Mechanical Engineers, London, 1978.
57. Primus, R. J., and Flynn, P. F.: "Diagnosing the Real Performance Impact of Diesel Engine Design Parameter Variation (A Primer in the Use of Second Law Analysis)," in *Proceedings of International Symposium on Diagnostics and Modeling of Combustion in Reciprocating Engines*, COMODIA 85, pp. 529–538, Tokyo, September 4–6, 1985.
58. Primus, R. J., Hoag, K. L., Flynn, P. F., and Brands, M. C.: "An Appraisal of Advanced Engine Concepts Using Second Law Analysis Techniques," SAE paper 841287, *SAE Trans.*, vol. 93, 1984.
59. Gosman, A. D.: "Computer Modeling of Flow and Heat Transfer in Engines, Progress and Prospects," in *Proceedings of International Symposium on Diagnostics and Modeling of Combustion in Reciprocating Engines*, COMODIA 85, pp. 15–26, Tokyo, September 4–6, 1985.
60. Reynolds, W. C.: "Modeling of Fluid Motions in Engines—An Introductory Overview," in J. N.

PETITIONER'S EXHIBIT 1002
US PATENT NO. 6,581,565

Mattavi and C. A. Amann (eds.), *Combustion Modeling in Reciprocating Engines*, pp. 41–68, Plenum Press, 1980.
61. El Tahry, S. H.: "k-ε Equation for Compressible Reciprocating Engine Flows," *J. Energy*, vol. 7, no. 4, pp. 345–353, 1983.
62. Morel, T., and Mansour, N. N.: "Modeling of Turbulence in Internal Combustion Engines," SAE paper 820040, 1982.
63. Ahmadi-Befrui, B., Gosman, A. D., and Watkins, A. P.: "Prediction of In-Cylinder Flow and Turbulence with Three Versions of k-ε Turbulence Model and Comparison with Data," in T. Uzkan (ed.), *Flows in Internal Combustion Engines—II*, FED—vol. 20, p. 27, ASME, New York, 1984.
64. El Tahry, S. H.: "Application of a Reynolds Stress Model to Engine Flow Calculations," in T. Uzkan (ed.), *Flows in Internal Combustion Engines—II*, FED—vol. 20, pp. 39–46, ASME, New York, 1984.
65. Gosman, A. D.: "Multidimensional Modeling of Cold Flows and Turbulence in Reciprocating Engines," SAE paper 850344, 1985.
66. Ferzieger, J. H.: "Large Eddy Simulations of Turbulent Flows," AIAA paper 76-347, 1976.
67. Amsden, A. A., Butler, T. D., O'Rourke, P. J., and Ramshaw, J. D.: "KIVA—A Comprehensive Model for 2-D and 3-D Engine Simulations," SAE paper 850554, 1985.
68. Butler, T. D., Cloutman, L. D., Dukowicz, J. K., and Ramshaw, J. D.: "Multidimensional Numerical Simulation of Reactive Flow in Internal Combustion Engines," in *Prog. Energy Combust. Sci.*, vol. 7, pp. 293–315, 1981.
69. Gosman, A. D., Tsui, Y. Y., and Watkins, A. P.: "Calculation of Three Dimensional Air Motion in Model Engines," SAE paper 840229, *SAE Trans.*, vol. 93, 1984.
70. Brandstatter, W., Johns, R. J. R., and Wigley, G.: "The Effect of Inlet Port Geometry on In-Cylinder Flow Structure," SAE paper 850499, 1985.
71. Gosman, A. D., Tsui, Y. Y., and Watkins, A. P.: "Calculation of Unsteady Three-Dimensional Flow in a Model Motored Reciprocating Engine and Comparison with Experiment," presented at Fifth International Turbulent Shear Flow Meeting, Cornell University, August 1985.
72. Schapertons, H., and Thiele, F.: "Three-Dimensional Computations for Flowfields in DI Piston Bowls," SAE paper 860463, 1986.
73. Isshiki, Y., Shimamoto, Y., and Wakisaka, T.: "Numerical Prediction of Effect of Intake Port Configurations on the Induction Swirl Intensity by Three-Dimensional Gas Flow Analysis," in *Proceedings of International Symposium on Diagnostics and Modeling of Combustion in Reciprocating Engines*, COMODIA 85, pp. 295–304, Tokyo, September 4–6, 1985.
74. Wakisaka, T., Shimamoto, Y., and Isshiki, Y.: "Three-Dimensional Numerical Analysis of In-Cylinder Flows in Reciprocating Engines," SAE paper 860464, 1986.
75. Diwakar, R.: "Multidimensional Modeling of the Gas Exchange Processes in a Uniflow-Scavenged Two-Stroke Diesel Engine," in T. Uzkan, W. G. Tiederman, and J. M. Novak (eds.), *International Symposium on Flows in Internal Combustion Engines—III*, FED—vol. 28, pp. 125–134, ASME, New York, 1985.
76. Yamada, T., Inoue, T., Yoshimatsu, A., Hiramatsu, T., and Konishi, M.: "In-Cylinder Gas Motion of Multivalve Engine—Three Dimensional Numerical Simulation," SAE paper 860465, 1986.
77. Gosman, A. D., and Johns, R. J. R.: "Computer Analysis of Fuel-Air Mixing in Direct-Injection Engines," SAE paper 800091, *SAE Trans.*, vol. 89, 1980.
78. Watkins, A. P., Gosman, A. D., and Tabrizi, B. S.: "Calculation of Three Dimensional Spray Motion in Engines," SAE paper 860468, 1986.
79. Butler, T. D., Cloutman, L. D., Dukowicz, J. K., and Ramshaw, J. D.: "Toward a Comprehensive Model for Combustion in a Direct-Injection Stratified-Charge Engine," in J. N. Mattavi and C. A. Amann (eds.), *Combustion Modelling in Reciprocating Engines*, pp. 231–260, Plenum Press, 1980.
80. Bracco, F. V.: "Modeling of Engine Sprays," SAE paper 850394, 1985.
81. Cartellieri, W., and Johns, R. J. R.: Multidimensional Modeling of Engine Processes: Progress and Prospects," paper presented at the Fifteenth CIMAC-Congress, Paris, June 1, 1983.

PETITIONER'S EXHIBIT 1002
US PATENT NO. 6,581,565

82. Amsden, A. A., Ramshaw, J. D., O'Rourke, P. J., and Dukowicz, J. K.: "KIVA: A Computer Program for Two- and Three-Dimensional Fluid Flows with Chemical Reactions and Fuel Sprays," report LA-10245-MS, Los Alamos National Laboratory, Los Alamos, New Mexico, February 1985.
83. Ahmadi-Befrui, B., Gosman, A. D., Lockwood, F. C., and Watkins, A. P.: "Multidimensional Calculation of Combustion in an Idealized Homogeneous Charge Engine: A Progress Report," SAE paper 810151, *SAE Trans.*, vol. 90, 1981.
84. Gosman, A. D., and Harvey, P. S.: "Computer Analysis of Fuel-Air Mixing and Combustion in an Axisymmetric D.I. Diesel," SAE paper 820036, *SAE Trans.*, vol. 91, 1982.
85. Basso, A., and Rinolfi, R.: "Two-Dimensional Computations of Engine Combustion: Comparisons of Measurements and Predictions," SAE paper 820519, 1982.
86. Basso, A.: "Optimization of Combustion Chamber Design for Spark Ignition Engines," SAE paper 840231, 1984.
87. Schapertons, H., and Lee, W.: "Multidimensional Modeling of Knocking Combustion in SI Engines," SAE paper 850502, 1985.
88. Cheng, W. K., and Theobald, M. A.: "A Numerical Study of Diesel Ignition," paper 87-FE-2, presented at the ASME Energy-Sources Technology Conference, Dallas, February 1987.

PETITIONER'S EXHIBIT 1002
US PATENT NO. 6,581,565

CHAPTER 15

ENGINE OPERATING CHARACTERISTICS

This chapter reviews the operating characteristics of the common types of spark-ignition and compression-ignition engines. The performance, efficiency, and emissions of these engines, and the effect of changes in major design and operating variables, are related to the more fundamental material on engine combustion, thermodynamics, fluid flow, heat transfer, and friction developed in earlier chapters. The intent is to provide data on, and an explanation of, actual engine operating characteristics.

15.1 ENGINE PERFORMANCE PARAMETERS

The practical engine performance parameters of interest are power, torque, and specific fuel consumption. Power and torque depend on an engine's displaced volume. In Chap. 2 a set of normalized or dimensionless performance and emissions parameters were defined to eliminate the effects of engine size. Power, torque, and fuel consumption were expressed in terms of these parameters (Sec. 2.14) and the significance of these parameters over an engine's load and speed range was discussed (Sec. 2.15). Using these normalized parameters, the effect of engine size can be made explicit. The power P can be expressed as:

$$\begin{aligned} P &= \text{mep}\ A_p \bar{S}_p/4 \quad \text{(four-stroke cycle)} \\ P &= \text{mep}\ A_p \bar{S}_p/2 \quad \text{(two-stroke cycle)} \end{aligned} \tag{15.1}$$

PETITIONER'S EXHIBIT 1002
US PATENT NO. 6,581,565

The torque T is given by

$$\begin{aligned} T &= \text{mep } V_d/(4\pi) \qquad \text{(four-stroke cycle)} \\ T &= \text{mep } V_d/(2\pi) \qquad \text{(two-stroke cycle)} \end{aligned} \tag{15.2}$$

Thus for well-designed engines, where the maximum values of mean effective pressure and piston speed are either flow limited (in naturally aspirated engines) or stress limited (in turbocharged engines), power is proportional to piston area and torque to displaced volume. Mean effective pressure can be expressed as

$$\text{mep} = \eta_f \eta_v Q_{\text{HV}} \rho_{a,i} \left(\frac{F}{A}\right) \tag{15.3}$$

for four-stroke cycle engines [Eq. (2.41)], and as

$$\text{mep} = \eta_f \eta_{tr} \Lambda Q_{\text{HV}} \rho_{a,i} \left(\frac{F}{A}\right) \tag{15.4}$$

for two-stroke cycle engines [Eqs. (2.19), (2.38), and (6.25)]. The importance of high fuel conversion efficiency, breathing capacity, and inlet air density is clear. Specific fuel consumption is related to fuel conversion efficiency by Eq. (2.24):

$$\text{sfc} = \frac{1}{\eta_f Q_{\text{HV}}} \tag{15.5}$$

These parameters have both brake and indicated values (see Secs. 2.3, 2.4, and 2.5). The difference between these two quantities is the engine's friction (and pumping) requirements and their ratio is the mechanical efficiency η_m.

The relative importance of these parameters varies over an engine's operating speed and load range. The maximum or normal rated brake power (see Sec. 2.1) and the quantities such as bmep derived from it (see Sec. 2.7) define an engine's full potential. The maximum brake torque (and bmep derived from it), over the full speed range, indicates the ability of the designer to obtain a high air flow through the engine over the full speed range and use that air effectively. Then over the whole operating range, and most especially those parts of that range where the engine will operate for long periods of time, engine fuel consumption and efficiency, and engine emissions are important. Since the operating and emissions characteristics of spark-ignition and compression-ignition engines are substantially different, each engine type is dealt with separately.

15.2 INDICATED AND BRAKE POWER AND MEP

The wide-open-throttle operating characteristics of a production spark-ignition automotive engine are shown in Fig. 15-1. The power shown is the gross power for the basic engine; this includes only the built-in engine accessories.[2] The maximum net power for the fully equipped engine with the complete intake and exhaust system and full cooling system is about 14 percent lower. The indicated

PETITIONER'S EXHIBIT 1002
US PATENT NO. 6,581,565

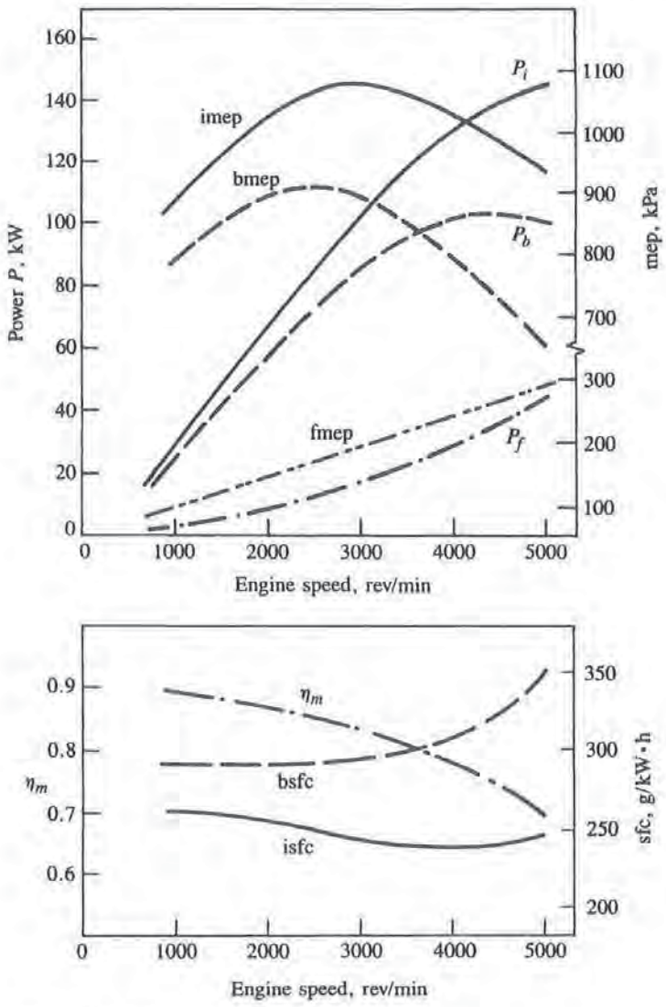


FIGURE 15-1
Gross indicated, brake, and friction power (P_i, P_b, P_f), indicated, brake, and friction mean effective pressure, indicated and brake specific fuel consumption, and mechanical efficiency for 3.8-dm^3 six-cylinder automotive spark-ignition engine at wide-open throttle. Bore = 96.8 mm, stroke = 86 mm, $r_c = 8.6$.[1]

power was obtained by adding the friction power to the brake power; it is the average rate of work transfer from the gases in the engine cylinders to the pistons during the compression and expansion strokes of the engine cycle (see Sec. 2.4). The indicated mean effective pressure shows a maximum in the engine's mid-speed range, just below 3000 rev/min. The shape of the indicated power curve follows from the imep curve. Since the full-load indicated specific fuel consumption (and hence indicated fuel conversion efficiency) varies little over the full speed range, this variation of full-load imep and power with speed is primarily due to the variation in volumetric efficiency, η_v [see Eq. (15.3)]. Since friction mean effective pressure increases almost linearly with increasing speed, friction

PETITIONER'S EXHIBIT 1002
US PATENT NO. 6,581,565

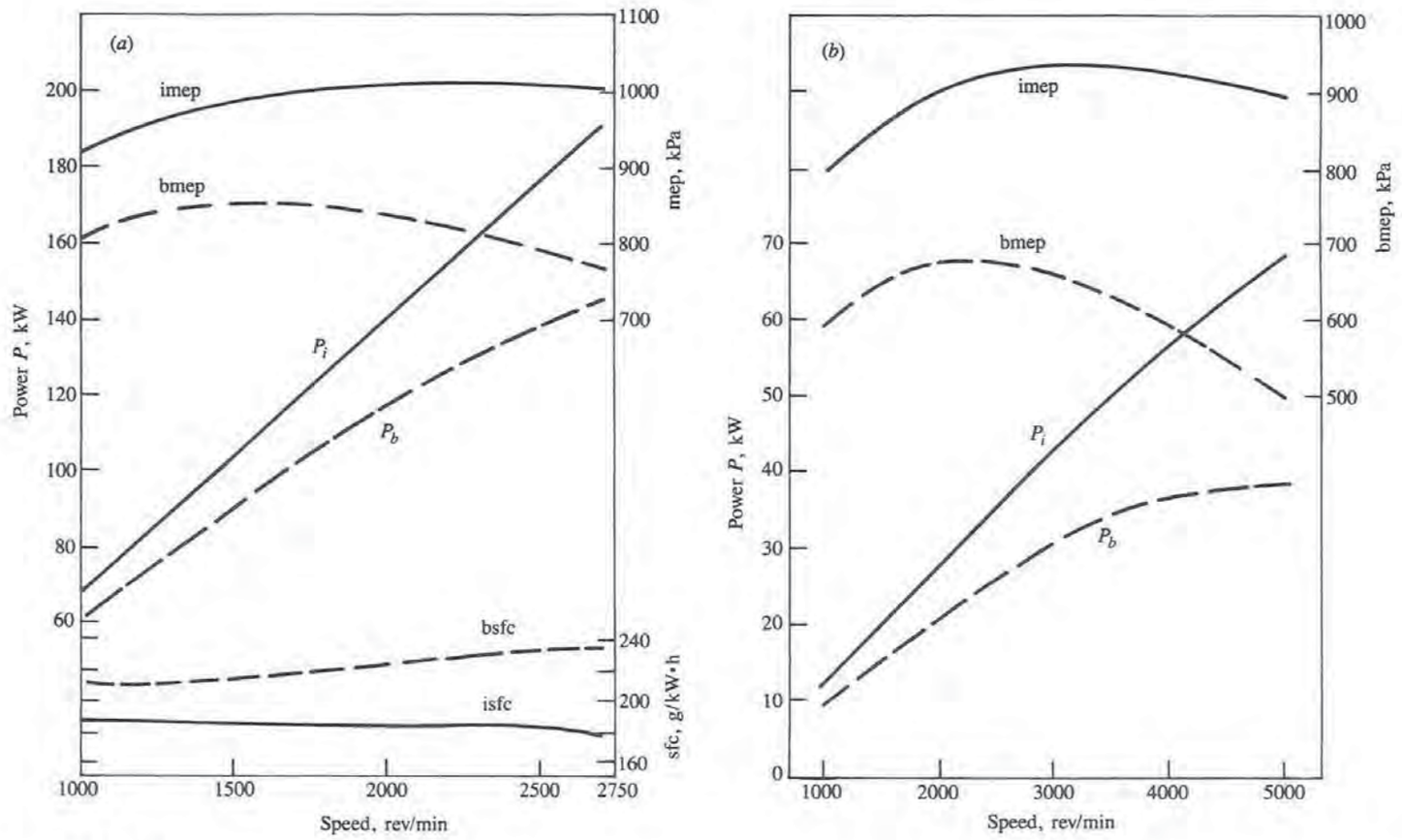


FIGURE 15-2
Gross indicated and brake power (P_i, P_b), mean effective pressure (imep, bmep), and specific fuel consumption (isfc, bsfc) for: (*a*) 8.4-dm^3 six-cylinder naturally aspirated direct-injection diesel engine: bore = 115 mm, stroke = 135 mm, $r_c = 16$;[3] (*b*) 1.8-dm^3 four-cylinder naturally aspirated indirect-injection swirl-chamber diesel engine: bore = 84 mm, stroke = 82 mm, $r_c = 22$.[4]

PETITIONER'S EXHIBIT 1002
US PATENT NO. 6,581,565

power will increase more rapidly. Hence mechanical efficiency decreases with increasing speed from a maximum of about 0.9 at low speed to 0.7 at 5000 rev/min. Thus bmep peaks at a lower speed than imep. The brake power shows a maximum at about 4300 rev/min; increases in speed above this value result in a decrease in P_b. The indicated fuel conversion efficiency increases by about 10 percent from 0.31 to 0.34 over the speed range 1000 to 4000 rev/min. This is primarily due to the decreasing importance of heat transfer per cycle with increasing speed.

At part load at fixed throttle position, these parameters behave similarly; however, at higher speeds torque and mean effective pressure decrease more rapidly with increasing speed than at full load. The throttle chokes the flow at lower and lower speeds as the throttle open area is reduced, increasingly limiting the air flow (see Fig. 7-22). The pumping component of total friction also increases as the engine is throttled, decreasing mechanical efficiency (see Figs. 13-9 and 13-10).

Figure 15-2 shows full-load indicated and brake power and mean effective pressure for naturally aspirated DI and IDI compression-ignition engines. Except at high engine speeds, brake torque and mep vary only modestly with engine speed since the intake system of the diesel can have larger flow areas than the intake of SI engines with their intake-system fuel transport requirements. The part-load torque and bmep characteristics (at fixed amount of fuel injected per cycle) have a similar shape to the full-load characteristics in Fig. 15-2. The decrease in torque and bmep with increasing engine speed is due primarily to the increase in friction mep with speed (see Figs. 13-7, 13-11, and 13-12). Decreasing engine heat transfer per cycle and decreasing air-flow rate, as speed increases, have modest additional impacts.

15.3 OPERATING VARIABLES THAT AFFECT SI ENGINE PERFORMANCE, EFFICIENCY, AND EMISSIONS

The major operating variables that affect spark-ignition engine performance, efficiency, and emissions at any given load and speed are: spark timing, fuel/air or air/fuel ratio relative to the stoichiometric ratio, and fraction of the exhaust gases that are recycled for NO_x emission control. Load is, of course, varied by varying the inlet manifold pressure. The effect of these variables will now be reviewed.

15.3.1 Spark Timing

Figure 9-3 and the accompanying text explain how variations in spark timing relative to top-center affected the pressure development in the SI engine cylinder. If combustion starts too early in the cycle, the work transfer from the piston to the gases in the cylinder at the end of the compression stroke is too large; if combustion starts too late, the peak cylinder pressure is reduced and the expan-

PETITIONER'S EXHIBIT 1002
US PATENT NO. 6,581,565

sion stroke work transfer from the gas to the piston decreases. There exists a particular spark timing which gives maximum engine torque at fixed speed, and mixture composition and flow rate. It is referred to as MBT—maximum brake torque—timing. This timing also gives maximum brake power and minimum brake specific fuel consumption. Figure 15-3*a* shows the effect of spark advance variations on wide-open-throttle brake torque at selected speeds between 1200 and 4200 rev/min for a production eight-cylinder engine. At each speed, as spark is advanced from an initially retarded setting, torque rises to a maximum and then decreases. MBT timing depends on speed; as speed increases the spark must be advanced to maintain optimum timing because the duration of the combustion process in crank angle degrees increases. Optimum spark timing also depends on load. As load and intake manifold pressure are decreased, the spark timing must be further advanced to maintain optimum engine performance.

The maximum in each brake torque curve in Fig. 15-3*a* is quite flat. Thus accurate determination of MBT timing is difficult, but is important because NO and HC emissions vary significantly with spark timing. In practice, to permit a more precise definition of spark timing, the spark is often retarded to give a 1 or 2 percent reduction in torque from the maximum value.

In Fig. 15-3*a* the mixture composition and flow rate were held constant at each engine speed. If the mixture flow rate is adjusted to maintain constant brake

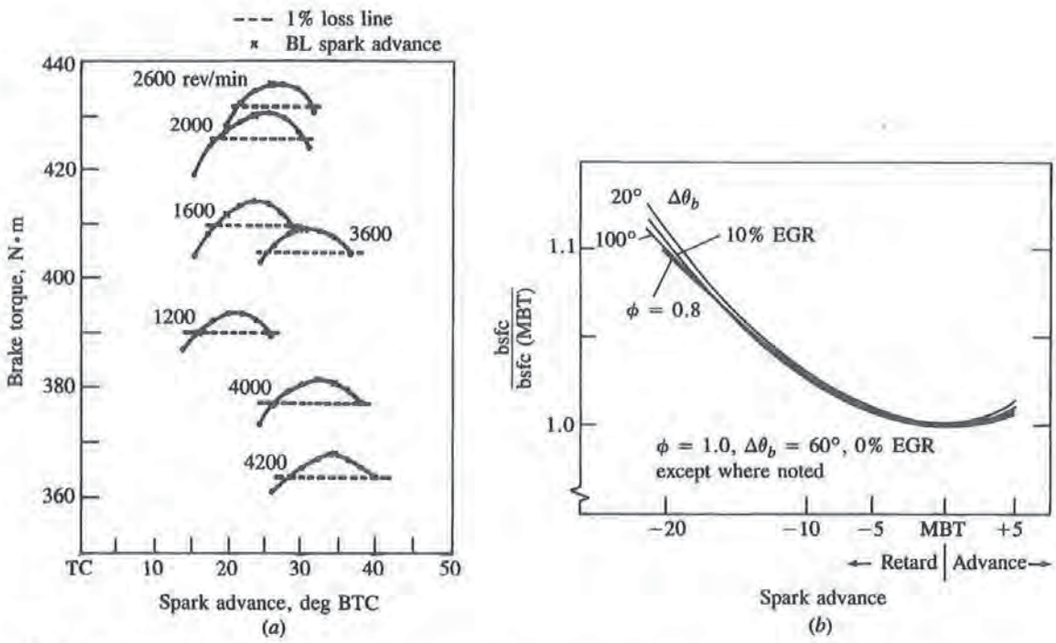


FIGURE 15-3
(*a*) Variation in brake torque with spark advance, eight-cylinder automotive spark-ignition engine at wide-open throttle, at engine speeds from 1200 to 4200 rev/min. 1 percent torque loss from MBT and spark advance for borderline knock are shown.[5] (*b*) Predicted variation in brake specific fuel consumption (normalized by MBT value) with spark retard at several different part-load engine conditions.[6, 7]

PETITIONER'S EXHIBIT 1002
US PATENT NO. 6,581,565

torque, the effect of spark timing variations on fuel consumption at constant engine load can be evaluated. Figure 15-3*b* shows results obtained with a computer simulation of the engine operating cycle.[6, 7] The curves for several different part-load operating conditions and burn durations (from fast to slow) have been normalized and fall essentially on top of each other. Five degrees of retard in spark timing have only a modest effect on fuel consumption; for 10 to 20° retard, the impact is much more significant.

Spark timing affects peak cylinder pressure and therefore peak unburned and burned gas temperatures (see Sec. 9.2.1). Retarding spark timing from the optimum reduces these variables. Retarded timing is sometimes used therefore for NO_x emission control (see Fig. 11-13 and accompanying text) and to avoid knock (see Sec. 9.6.1). The exhaust temperature is also affected by spark timing. Retarding timing from MBT increases exhaust temperature; both engine efficiency and heat loss to the combustion chamber walls (see Fig. 12-27) are decreased. Retarded timing is sometimes used to reduce hydrocarbon emissions by increasing the fraction oxidized during expansion and exhaust due to the higher burned gas temperatures that result (see Sec. 11.4.3). Retarded timing may be used at engine idle to bring the ignition point closer to TC where conditions for avoiding misfire are more favorable.

15.3.2 Mixture Composition

The unburned mixture in the engine cylinder consists of fuel (normally vaporized), air, and burned gases. The burned gas fraction is the residual gas plus any recycled exhaust used for NO control. Mixture composition during combustion is most critical, since this determines the development of the combustion process which governs the engine's operating characteristics. While substantial efforts are made to produce a uniform mixture within the cylinder, some nonuniformities remain (see Sec. 9.4.2). In a given cylinder, cycle-by-cycle variations in average charge composition exist. Also, within each cylinder in a given engine cycle, the fuel, air, EGR, and residual gas are not completely mixed, and composition nonuniformities across the charge may be significant.† These together produce variations in composition at the spark plug location (the critical region since the early stages of flame development influence the rest of the combustion process) which can be of order $\pm$ 10 percent peak-to-peak (see Fig. 9-34). In addition, in multicylinder engines, the average air, fuel, and EGR flow rates to each cylinder are not identical. Typical cylinder-to-cylinder variations have standard deviations of ± 5 percent of the mean for air flow rate and fuel flow rate (giving a

† This aspect of mixture nonuniformity is least well defined. Mixing of the fresh mixture (fuel, air, and EGR) with residual gas is likely to be incomplete (see Fig. 14-36), especially at light load when the residual gas fraction is highest. With intake-port fuel-injection systems, there is evidence of incomplete fuel-air mixing due to the fact that the air flow and fuel flow processes are not in phase.[9] When the engine is cold, fuel distribution within the cylinder is known to be nonuniform.

PETITIONER'S EXHIBIT 1002
US PATENT NO. 6,581,565

± 7 percent variation in the air/fuel ratio) for steady-state engine operation. EGR cylinder-to-cylinder flow rates may have higher variability. Under unsteady engine operating conditions all these variations can be higher.

It is necessary to consider the effect of mixture composition changes on engine operating and emissions characteristics in two regimes: (1) wide-open throttle (WOT) or full load and (2) part throttle or load. At WOT, the engine air flow is the maximum that the engine will induct.† Fuel flow can be varied, but air flow is set by engine design variables and speed. At part throttle, air flow, fuel flow, and EGR flow can be varied. Evaluation of mixture composition changes at part load should be done at fixed (brake) load and speed, i.e., under conditions where the engine provides the desired torque level at the specified speed. To maintain torque (or load or bmep) constant as mixture composition is varied normally requires changes in throttle setting (and if EGR is varied, changes in EGR flow-control valve setting). This distinction between part-load comparisons at specified torque or bmep, rather than at constant throttle settings (which gives essentially constant air flow), is important because the pumping work component of engine friction will vary at constant engine load as mixture composition changes. At constant throttle setting and speed, the pumping work remains essentially unchanged.

AIR/FUEL OR EQUIVALENCE RATIO CHANGES. Mixture composition effects are usually discussed in terms of the air/fuel ratio (or fuel/air ratio) because in engine tests, the air and fuel flow rates to the engine can be measured directly and because the fuel metering system is designed to provide the appropriate fuel flow for the actual air flow at each speed and load. However, the relative proportions of fuel and air can be stated more generally in terms of the fuel/air equivalence ratio ϕ [the actual fuel/air ratio normalized by dividing by the stoichiometric fuel/air ratio, see Eq. (3.8)] or the relative air/fuel ratio λ [see Eq. (3.9)]. The combustion characteristics of fuel-air mixtures and the properties of combustion products, which govern engine performance, efficiency, and emissions, correlate best for a wide range of fuels relative to the stoichiometric mixture proportions. Where appropriate, therefore, the equivalence ratio will be used as the defining parameter. Equation (7.1) converts the air/fuel ratio with gasoline to the equivalence ratio.

The theoretical basis for understanding the effect of changes in the equivalence ratio is the fuel-air cycle results in Figs. 5-9 and 5-10, where the indicated fuel conversion efficiency and mean effective pressure are shown as a function of the fuel/air equivalence ratio, ϕ. The mean effective pressure peaks slightly rich of stoichiometric, between $\phi = 1$ and 1.1. Due to dissociation at the high temperatures following combustion, molecular oxygen is present in the burned gases under stoichiometric conditions, so some additional fuel can be added and par-

† EGR is normally zero at WOT, since maximum torque is usually desired.

PETITIONER'S EXHIBIT 1002
US PATENT NO. 6,581,565

tially burned. This increases the temperature and the number of moles of the burned gases in the cylinder. These effects increase the pressure to give increased power and mep. Fuel conversion efficiency decreases approximately as $1/\phi$, as the mixture is richened above stoichiometric ($\phi > 1$) due to the decreasing combustion efficiency associated with the richening mixture.

For mixtures lean of stoichiometric, the theoretical fuel conversion efficiency increases linearly as ϕ decreases below 1.0. Combustion of mixtures leaner than stoichiometric produces products at lower temperature, and with less dissociation of the triatomic molecules CO_2 and H_2O. Thus the *fraction* of the chemical energy of the fuel which is released as sensible energy near TC is greater; hence a greater *fraction* of the fuel's energy is transferred as work to the piston during expansion, and the fraction of the fuel's available energy rejected to the exhaust system decreases (see Sec. 5.7). There is a discontinuity in the fuel conversion efficiency and imep curves at the stoichiometric point; the burned gas composition is substantially different on the rich and the lean sides of $\phi = 1$.

Figure 15-4 shows gross indicated specific fuel consumption data for a six-cylinder spark-ignition engine at wide-open throttle and 1200 rev/min,[9] and values of gross indicated mean effective pressure and fuel conversion efficiency derived from the isfc data. In these engine tests, the fuel-air mixture was prepared in two different ways: (1) with the normal carburetor and (2) with a heated vaporizing tank to ensure intake-mixture uniformity. Shapes of the practical efficiency curves and the theoretical curves in Fig. 5-9 differ. Cylinder-to-cylinder air/fuel ratio maldistribution prevents the carbureted engine operating leaner than $\phi \approx 0.85$ ($A/F \approx 17$) without misfire under these conditions. While use of a fuel vaporizing and mixing tank essentially removes this maldistribution and extends the lean misfire limit, $\eta_{f,i}$ does not continue to increase as ϕ decreases. The reasons for this are that cycle-to-cycle pressure fluctuations and the total dura-

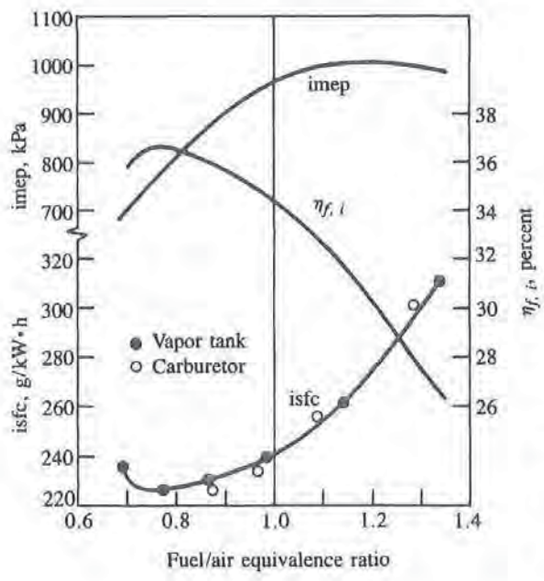
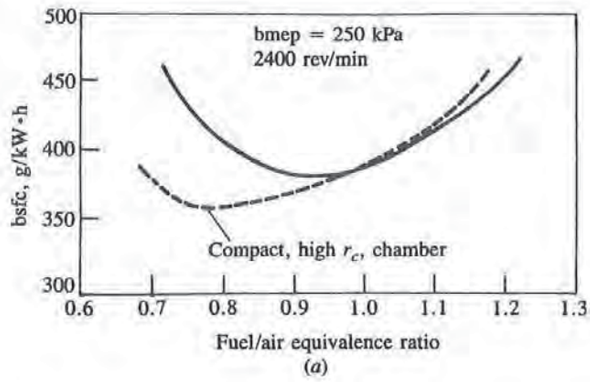
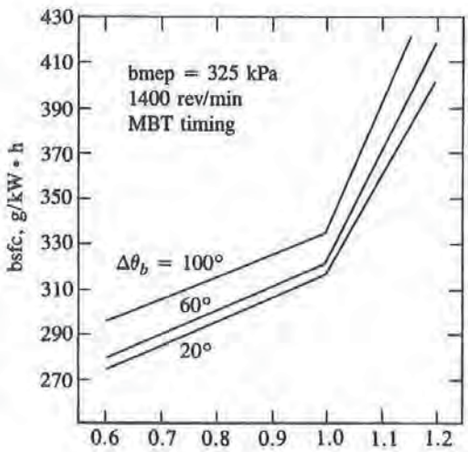


FIGURE 15-4
Effect of the fuel/air equivalence ratio variations on indicated mean effective pressure, specific fuel consumption, and fuel conversion efficiency of six-cylinder spark-ignition engine at wide-open throttle and 1200 rev/min. Data for standard carbureted engine, and engine equipped with vapor tank which extends the lean operating limit, are shown.[9]

PETITIONER'S EXHIBIT 1002
US PATENT NO. 6,581,565



(*a*)



(*b*)

FIGURE 15-5
Effect of combustion chamber design and burn rate on spark-ignition engine brake specific fuel consumption. (*a*) 1.6-dm^3 four-cylinder engine with conventional combustion chamber and 1.5-dm^3 four-cylinder engine with compact fast-burning high-compression-ratio chamber beneath the exhaust valve with $r_c = 13$, both at bmep of 250 kPa and 2400 rev/min.[10] (*b*) Predictions from thermodynamic-based computer simulation of engine cycle for 5.7-dm^3 eight-cylinder engine at bmep of 325 kPa and 1400 rev/min with MBT spark timing.[6]

tion of the burning process increase as the mixture becomes leaner: both these factors degrade engine efficiency. Since the spark advance is set for the average cycle, increasing cycle-to-cycle dispersion produces increasing imep (and hence $\eta_{f,i}$) losses in "nonaverage" cycles due to nonoptimum timing. The lengthening burn duration directly decreases efficiency, even in the absence of cyclic variations.

Engine fuel consumption and efficiency well lean of stoichiometric depend strongly on the engine combustion chamber design. Figure 15-5 shows two sets of engine bsfc data, for a conventional combustion chamber and a compact high-compression-ratio chamber, at constant load and speed (250 kPa bmep and 2400 rev/min) as a function of equivalence ratio. Also shown are bsfc results obtained from a thermodynamic-based computer cycle simulation of the spark-ignition engine operating cycle (at 325 kPa bmep and 1400 rev/min).[6] Though the load and speed are different, the behavior of the data and predictions for rich mixtures, $\phi > 1$, are comparable. On the lean side of stoichiometric, however, fuel consumption depends on the combustion characteristics of the chamber. The faster-burning compact high-compression-ratio chamber shows decreasing bsfc

PETITIONER'S EXHIBIT 1002
US PATENT NO. 6,581,565

until the lengthening burn duration and larger cycle-by-cycle variations cause bsfc to increase. For the slower-burning conventional chamber, this deterioration in combustion starts to occur almost immediately on the lean side of stoichiometric, and fuel consumption worsens for $\phi \leq 0.9$.

Thus the equivalence ratio for optimum fuel consumption at a given load depends on the details of chamber design (including compression ratio) and mixture preparation quality. It also varies for a given chamber over the part-throttle load and speed range. For lighter loads and lower speeds it is closer to stoichiometric since the residual gas fraction is higher and combustion quality is poorer with greater dilution and at lower speeds.

At part load, as the air/fuel ratio is varied at constant brake load, the pumping work varies, and this also contributes to the brake specific fuel consumption and efficiency variation with equivalence ratio. Figure 15-6 shows the gross and net indicated fuel conversion efficiencies and brake efficiency as a function of equivalence ratio at a part-throttle constant load and speed point (325 kPa bmep and 1400 rev/min), calculated using a thermodynamic-based computer simulation of the engine's operating cycle. The difference between the net and gross indicated curves illustrates the magnitude of the effect of the pumping work changes. Part-throttle comparisons of different operating conditions should be done at constant brake load (torque or bmep) and speed: the task the engine is required to perform is then the same. At constant bmep and speed, the mechanical rubbing friction is essentially fixed; thus *net* imep is constant (and *gross* imep will vary if the pumping mep varies).

Note that all the engine data show a smooth transition between the rich and lean characteristics at the stoichiometric point, whereas the calculated sfc and

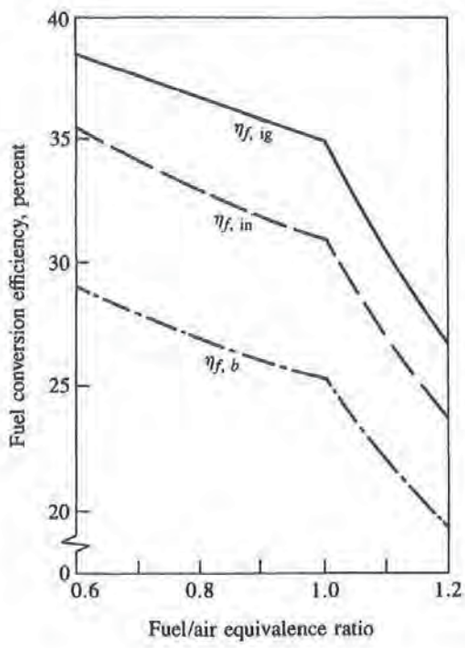


FIGURE 15-6
Gross and net indicated, and brake, fuel conversion efficiencies predicted by thermodynamic-based cycle simulation at constant part-load bmep (325 kPa) and speed (1400 rev/min) for a fixed burn duration (0–100 percent, 60° CA).[6]

PETITIONER'S EXHIBIT 1002
US PATENT NO. 6,581,565

efficiency characteristics show a discontinuity in slope. The difference is due to cylinder-to-cylinder and cycle-by-cycle mixture composition variations[7] and to cycle-by-cycle cylinder pressure variations which exist (though to a lesser extent) even in the absence of these mixture variations. Averaging over these variations smooths out the theoretical discontinuity in slope at $\phi = 1.0$.

The equivalence ratio requirements of a spark-ignition engine over the full load and speed range can now be explained from the point of view of performance and efficiency. However, since emissions depend on ϕ also, emission control requirements may dictate a different engine calibration, as will be discussed later. The mixture requirements in the induction system are usually discussed in relation to *steady* and *transient* engine operation. Steady operation includes operation at a given speed and load over several engine cycles with a warmed-up engine. Transient operation includes engine starting, engine warm-up to steady-state temperatures, and changing rapidly from one engine load and speed to another. The mixture requirements of the engine as defined by the composition of the combustible mixture at the time of ignition, while they vary somewhat with speed and load, are essentially the same for all these operating modes.† However, the methods used to prepare the mixture prior to entry to the cylinder must be modified in the transient modes when liquid fuels are used, to allow for variations in the liquid fuel flow and fuel evaporation rate in the intake manifold as the air flow varies and as the manifold and inlet port pressure and temperature change. The transient fuel metering requirements for adequate mixture preparation are discussed in Chap. 7.

At all load points at a given speed, the ideal equivalence ratio is that which gives minimum brake specific fuel consumption at the required load. However, once wide-open-throttle air flow has been reached, increases in power can only be obtained by increasing the fuel flow rate. The equivalence ratio requirements for optimum-efficiency steady-state engine operation can be summarized on a plot of equivalence ratio versus percent of maximum air flow at any given speed. A typical plot was shown in Fig. 7-1. For part-throttle operation, unless dictated otherwise by emission control requirements, the equivalence ratio is set close to the equivalence ratio for minimum fuel consumption consistent with avoiding partial burning or misfire in one or more cylinders. At very light load the best bsfc mixture is richer to compensate for slower flame speeds at lower mixture density and increased residual fraction. As wide-open throttle is approached, the mixture is richened to obtain maximum power.

The exhaust gas temperature varies with the equivalence ratio. The exhaust gas temperature also varies continuously as the gas leaves the engine cylinder and flows through the exhaust port and the manifold and pipe (see Sec. 6.5), so an appropriate definition of an average exhaust gas temperature should be used

† Except during start-up and cold engine operation, when a substantial part of the fuel within the cylinder can be in the liquid phase.

PETITIONER'S EXHIBIT 1002
US PATENT NO. 6,581,565

in quantifying this variation. However, time-averaged thermocouple measurements from specific locations in the exhaust system can provide useful information on trends. Figure 14-10 shows examples of predictions of the enthalpy-averaged exhaust gas temperature at the exhaust port exit as a function of equivalence ratio compared with time-averaged measurements. The enthalpy-averaged temperature is defined by Eq. (6.19). These are typically 50 to 100 K higher than time-averaged measurements. The exhaust temperature peaks at the stoichiometric point and decreases as the mixture is richened and leaned on either side.

The fuel/air equivalence ratio is an important parameter controlling spark-ignition engine emissions. The critical factors affecting emissions, that are governed by the equivalence ratio, are the oxygen concentration and the temperature of the burned gases. Excess oxygen is available in the burned gases lean of stoichiometric. The maximum burned gas temperatures occur slightly rich of stoichiometric at the start of the expansion stroke, and at the stoichiometric composition at the end of expansion and during the exhaust process. Figure 11-2 illustrates the general trends in emissions with equivalence ratio which have already been discussed.

Figure 15-7 shows the effect of variations in fuel/air equivalence ratio on NO_x and HC emissions and fuel consumption when a special fuel vapor generator was used to produce a uniform fuel-air mixture. As explained in Sec. 11.2.3, the formation rate of NO depends on the gas temperature and oxygen concentration. While maximum burned gas temperatures occur at $\phi \approx 1.1$, at this equiva-

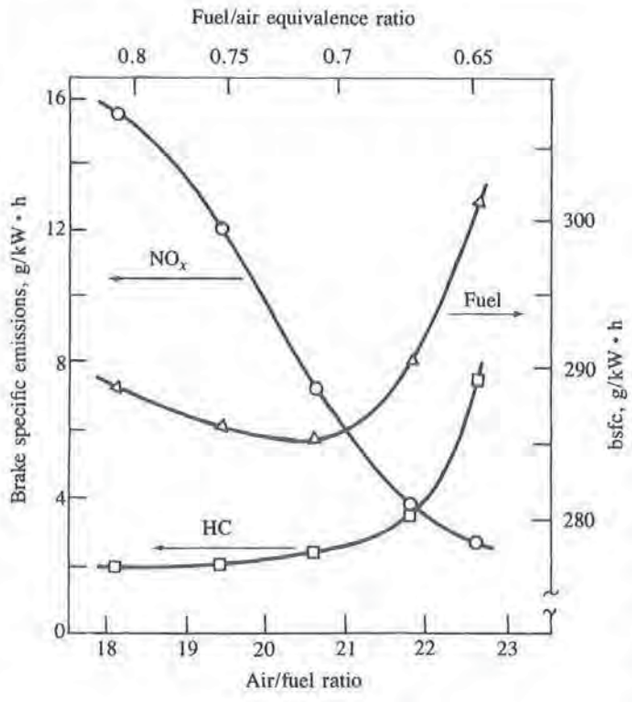


FIGURE 15-7
Variation of brake specific HC and NO_x emissions and fuel consumption with (A/F) and fuel/air equivalence ratio. 5.7-dm^3 eight-cylinder spark-ignition engine at 385 kPa bmep and 1400 rev/min with uniform vaporized fuel-air mixture.[11]

PETITIONER'S EXHIBIT 1002
US PATENT NO. 6,581,565

lence ratio oxygen concentrations are low. As the mixture is leaned out, increasing oxygen concentration initially offsets the falling gas temperatures and NO emissions peak at $\phi \approx 0.9$. Then, decreasing temperatures dominate and NO emissions decrease to low levels.

Figure 15-7 also shows the effect of variations in equivalence ratio for lean mixtures on unburned hydrocarbon emissions. For rich mixtures, Fig. 11-2 shows that emissions are high. This is primarily due to the lack of oxygen for afterburning of any unburned hydrocarbons that escape the primary combustion process, within the cylinder and the exhaust system. HC emissions decrease as the stoichiometric point is approached: increasing oxygen concentration and increasing expansion and exhaust stroke temperatures result in increasing HC burnup. For moderately lean mixtures, HC emission levels vary little with equivalence ratio. Decreasing fuel concentration and increasing oxygen concentration essentially offset the effect of decreasing bulk gas temperatures. As the lean operating limit of the engine is approached, combustion quality deteriorates significantly and HC emissions start to rise again due to the occurrence of occasional partial-burning cycles. For still leaner mixtures, HC emissions rise more rapidly due to the increasing frequency of partial-burning cycles, and even the occurrence of completely misfiring cycles (see Sec. 9.4.3). The equivalence ratio at which partial-burning and misfiring cycles just start to appear depends on details of the engine combustion and fuel preparation systems, as well as the load and speed point.

The effect of equivalence ratio variations on CO emissions has already been explained in Sec. 11.3 (see Fig. 11-20). For rich mixtures, CO levels are high because complete oxidation of the fuel carbon to CO_2 is not possible due to insufficient oxygen. For lean mixtures, CO levels are approximately constant at a low level of about 0.5 percent or less.

Figure 15-7 indicates that if an engine can be designed and operated so that its stable operating limit under the appropriate part-load conditions is sufficiently lean, excellent fuel consumption and substantial control of engine NO, HC, and CO emissions can be achieved. Such an approach requires good control of mixture preparation and a fast-burning combustion chamber design (see Sec. 15.4.1). However, this lean-engine approach is not compatible with the three-way catalyst system (see Sec. 11.6.2) which, with close-to-stoichiometric mixtures, achieves substantial additional reductions in NO, HC, and CO emissions.

EXHAUST GAS RECYCLE. Exhaust gas recycle (EGR) is the principal technique used for control of SI engine NO_x emissions (see Sec. 11.2.3). A fraction of the exhaust gases are recycled through a control valve from the exhaust to the engine intake system. The recycled exhaust gas is usually mixed with the fresh fuel-air mixture just below the throttle valve. EGR acts, at part load, as an additional diluent in the unburned gas mixture, thereby reducing the peak burned gas temperatures and NO formation rates. Note that it is the total burned gas fraction in the unburned mixture in the cylinder that acts as a diluent. These burned gases are comprised of both residual gas from the previous cycle and exhaust gas

PETITIONER'S EXHIBIT 1002
US PATENT NO. 6,581,565

recycled to the intake. As described in Sec. 6.4, the residual gas fraction is influenced by load and valve timing (especially the extent of valve overlap) and, to a lesser degree, by the air/fuel ratio and compression ratio. The total burned gas mass fraction is given by Eq. (4.3). Since the burned gases dilute the unburned mixture, the absolute temperature reached after combustion varies inversely with the burned gas mass fraction. Hence increasing the burned gas fraction reduces the rate of formation of NO emissions.

Figure 11-10 shows the effect on NO emissions of increasing the burned gas fraction by recycling exhaust gases to the intake system. Substantial reductions in NO concentrations are achieved with 10 to 25 percent EGR. However, EGR also reduces the combustion rate which makes stable combustion more difficult to achieve (see Sec. 9.4.3 and Fig. 9-36). The amount of EGR a particular combustion chamber design will tolerate depends on its combustion characteristics, the speed and load, and the equivalence ratio. EGR percentages in the 15 to 30 range are about the maximum amount of EGR a spark-ignition engine will tolerate under normal part-throttle conditions. Faster-burning engines will tolerate more EGR than slower-burning engines. Because of the decrease in burn rate and increase in cycle-by-cycle combustion variations, hydrocarbon emissions increase with increasing EGR, as shown in Fig. 11-29. At first the increase in HC is modest and is due primarily to decreased HC burnup due to lower expansion and exhaust stroke temperatures. The HC increase becomes more rapid as slow combustion, partial burning, and even misfire, in turn, occur with increasing frequency. EGR has no significant effect on engine CO emissions.

The effect of exhaust gas recycle on engine performance and efficiency, for mixtures with $\phi \leq 1.0$, is similar to the addition of excess air. Both EGR and excess air dilute the unburned mixture. In practice since EGR is only used at part-throttle conditions, $\phi \leq 1.0$ is the region of interest. Because three-way catalysts are now used where NO_x emission constraints are severe, greatest attention has focused on dilution with EGR at $\phi \approx 1.0$. Figure 15-8 shows the effect of increasing EGR on bsfc and enthalpy-mean exhaust temperature [defined by Eq. (6.19)] at constant bmep, predicted using a thermodynamic-based computer simulation of the engine's operating cycle. Predictions made for different burn durations are shown, at MBT timing for a stoichiometric mixture. At constant burn duration, bsfc and exhaust temperature decrease with increasing EGR. Only for very long combustion processes is the burn rate especially significant. This improvement in fuel consumption with increasing EGR is due to three factors: (1) reduced pumping work as EGR is increased at constant brake load (fuel and air flows remain almost constant; hence intake pressure increases); (2) reduced heat loss to the walls because the burned gas temperature is decreased significantly; and (3) a reduction in the degree of dissociation in the high-temperature burned gases which allows more of the fuel's chemical energy to be converted to sensible energy near TC. The first two of these are comparable in magnitude and each is about twice as important as the third.[12]

Figure 15-9 shows experimental bsfc versus EGR data for two combustion chambers: a combustion chamber with a moderate burning rate and a faster-

PETITIONER'S EXHIBIT 1002
US PATENT NO. 6,581,565

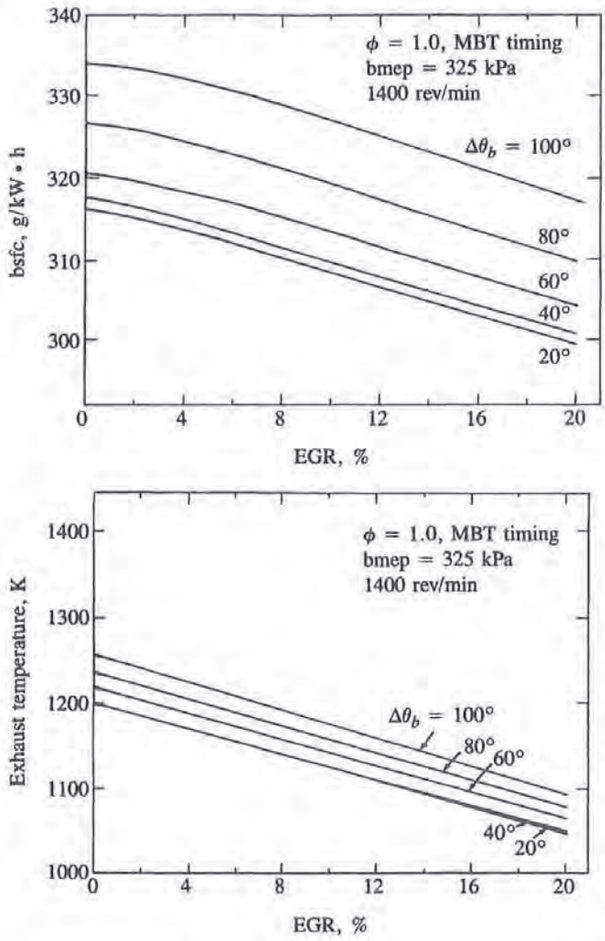


FIGURE 15-8
Effect of recycled exhaust on brake specific fuel consumption and exhaust temperature at constant bmep and speed, stoichiometric mixture, and various burn durations (0–100 percent). Predictions from thermodynamic-based cycle simulation.[6]

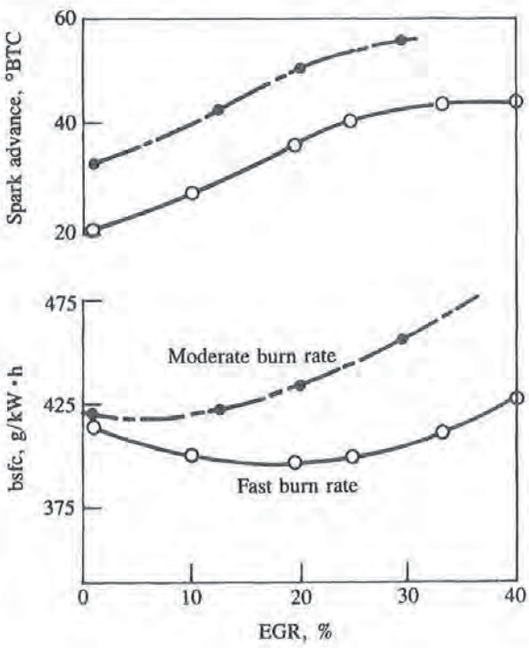


FIGURE 15-9
Brake specific fuel consumption and MBT spark advance as a function of percent recycled exhaust, for four-cylinder spark-ignition engine with a moderate burn rate combustion chamber and a fast burn rate combustion chamber. 1400 rev/min, 324 kPa bmep, equivalence ratio 1.0.[12]

PETITIONER'S EXHIBIT 1002
US PATENT NO. 6,581,565

burning chamber with open geometry and with induction-generated swirl. Though addition of EGR lengthens both the flame development and propagation processes (as indicated by the increasing MBT spark advance requirement with increasing EGR), the faster-burning chamber follows the anticipated pattern of significant bsfc reductions until, at about 20 percent EGR, the combustion quality deteriorates. For the slower-burning combustion chamber, the tolerance to dilution with EGR is much less.

15.3.3 Load and Speed

One common way to present the operating characteristics of an internal combustion engine over its full load and speed range is to plot brake specific fuel consumption contours on a graph of brake mean effective pressure versus engine speed. Operation of the engine coupled to a dynamometer on a test stand, over its load and speed range, generates the torque and fuel flow-rate data from which such a *performance map* is derived. Equation (2.20) relates bmep to torque, and bsfc values are obtained from Eq. (2.22) at each operating point. Figure 15-10 shows an example of such a performance map for a four-cylinder spark-ignition engine. The upper envelope of the map is the wide-open-throttle performance curve. Points below this curve define the part-load operating characteristics. While details differ from one engine to another, the overall shapes of these maps for spark-ignition engines are remarkably similar. When mean piston speed $\bar{S}_p$ is used instead of crankshaft speed for the abscissa, the quantitative similarity of such maps over a wide range of engine sizes is more apparent.

Maximum bmep occurs in the mid-speed range; the minimum bsfc island is located at a slightly lower speed and at part load. These map characteristics can be understood in terms of variations in volumetric efficiency η_v, gross indicated fuel conversion efficiency $\eta_{f,ig}$ and mechanical efficiency η_m as A/F, EGR (if used), and the importance of heat losses and friction change, via Eqs. (15.3) and (15.5).

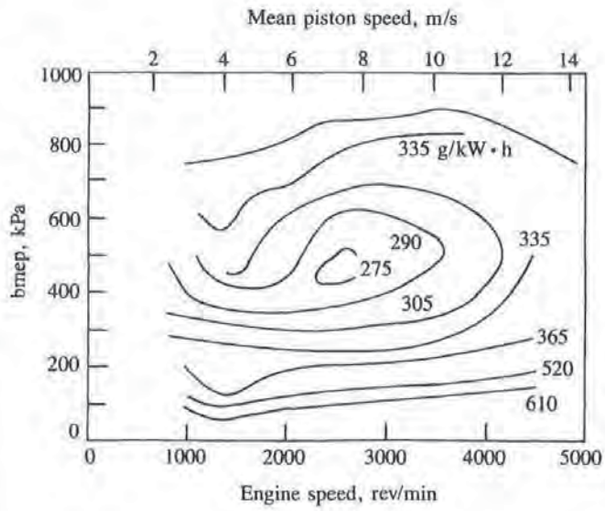


FIGURE 15-10
Performance map for 2-dm³ four-cylinder fast-burn spark-ignition engine showing contours of constant bsfc in grams per kilowatt-hour.[13]

PETITIONER'S EXHIBIT 1002
US PATENT NO. 6,581,565

The maximum bmep curve reflects the variation with speed of η_v, the decrease of η_m as $\bar{S}_p$ increases, and the increase of $\eta_{f,ig}$ as $\bar{S}_p$ increases due to decreasing importance of heat transfer per cycle. The bsfc contours have the following explanation. Starting at the minimum bsfc point, increasing speed at constant load increases bsfc due primarily to the increasing friction mep at higher speeds (which decreases η_m). While $\eta_{f,ig}$ increases as speed increases, friction increases dominate. Decreasing speed at constant load increases bsfc due primarily to the increasing importance of heat transfer per cycle (which decreases $\eta_{f,ig}$). Friction decreases, increasing η_m, but this is secondary. Any mixture enrichment required to maintain a sufficiently repeatable combustion process at low engine speeds (see Fig. 7-1) contributes too. Increasing load at constant speed from the minimum bsfc point increases bsfc due to the mixture enrichment required to increase torque as the engine becomes increasingly air-flow limited. Decreasing load at constant speed increases bsfc due to the increased magnitude of friction (due to increased pumping work), the increased relative importance of friction, and increasing importance of heat transfer (which decreases $\eta_{f,ig}$).

The effects of speed and load variations on NO and HC emissions are shown in Fig. 15-11.[14] NO concentrations increase moderately with increasing speed at constant load. At lower loads, the proportional increase in NO is greater

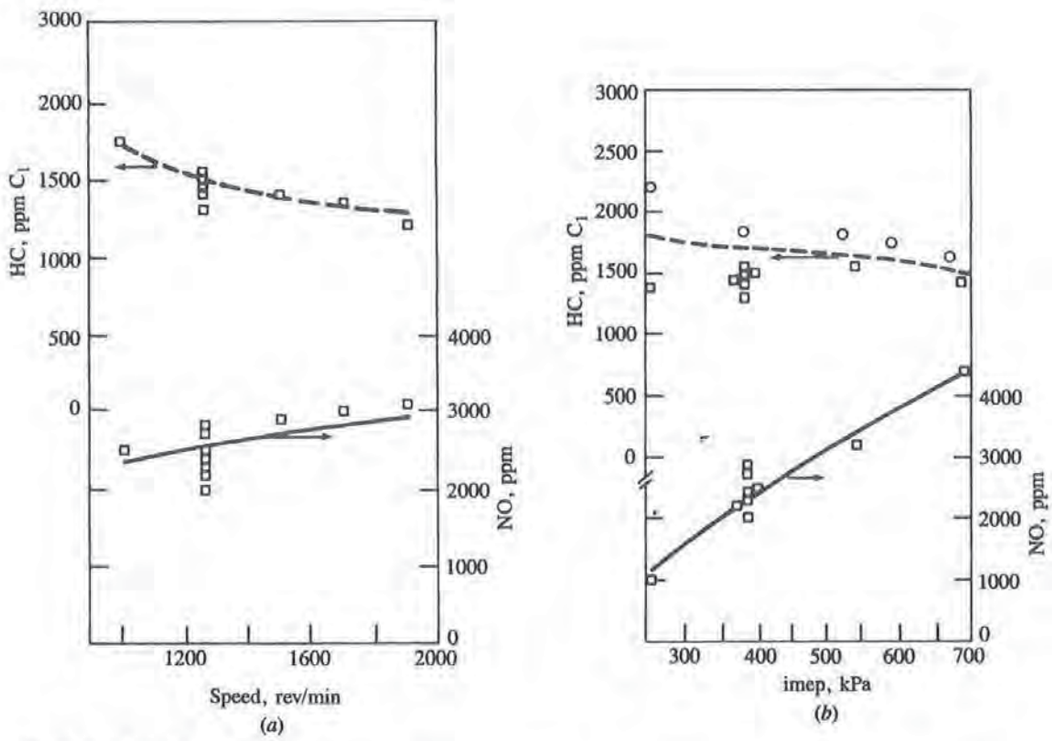


FIGURE 15-11
Variation in spark-ignition engine HC and NO_x emissions with (*a*) engine speed at 379 kPa imep and (*b*) load (or imep) at 1250 rev/min. Equivalence ratio = 0.9, MBT spark timing, $r_c = 7$.[14]

PETITIONER'S EXHIBIT 1002
US PATENT NO. 6,581,565

than at higher loads.[6] The residual gas fraction decreases as speed increases, this effect being greater at lower inlet manifold pressures (lighter loads) (see Fig. 6-19). Also, the relative importance of heat transfer per cycle is less as speed increases (see Fig. 12-25), which would also be expected to increase NO concentration. With increasing load (at constant speed), NO concentrations also increase. Again, as inlet manifold pressure and load increase, the residual gas fraction decreases (Fig. 6-19); also, the relative importance of heat transfer per cycle decreases with increasing load (Fig. 12-25).

The hydrocarbon concentration trends with speed and load changes are the opposite of the NO concentration trends. As indicated in Table 11.7, speed and load are likely to affect several of the HC formation mechanisms, the in-cylinder mixing of unburned hydrocarbons which escape combustion with the bulk gases, and the fraction of the in-cylinder HC which escape into the exhaust. However, not enough is yet known about the details of these processes to make these dependencies explicit. If oxygen is available, oxidation of unburned hydrocarbons both within the cylinder and in the exhaust system will be significantly enhanced by increases in speed since the expansion stroke and exhaust process gas temperatures increase substantially, due to the reduced significance of heat transfer per cycle with increasing speed. This more than offsets the reduced residence time in the cylinder and in the exhaust. Measurements of the percent HC reacted in the exhaust port as a function of engine speed show the same proportional reduction in the exhaust emissions data in Fig. 15-11.[15] The rationale for the variation with load is less clear. As load increases at constant speed, expansion and exhaust stroke temperatures increase, and the in-cylinder oxidation rate, if oxygen is available, will increase. However, as the exhaust gas flow rate increases, the residence time in critical sections of the exhaust system decreases and a reduction in exhaust port HC oxidation occurs.[16] The net trend is for HC concentration to decrease modestly as load is increased.

15.3.4 Compression Ratio

The ideal cycle analysis of Chap. 5 showed that indicated fuel conversion efficiency increased continuously with compression ratio according to Eq. (5.31). With $\gamma = 1.3$, this relation also matches closely the fuel-air cycle predictions with $\phi \approx 1.0$. However, in an actual engine other processes which influence engine performance and efficiency vary with changes in compression ratio: namely, combustion rate and stability, heat transfer, and friction. Over the load and speed range, the relative impact that these processes have on power and efficiency varies also. Hence, the applicability of Eq. (5.31) is open to question. Also, while the geometric compression ratio (ratio of maximum to minimum cylinder volume) is well defined, the actual compression and expansion processes in engines depend on valve timing details and the importance of flow through the valves while they are opening or closing (which depends on engine speed). Of course, our ability to increase the compression ratio is limited by the octane quality of available fuels and knock (see Sec. 9.6.1).

PETITIONER'S EXHIBIT 1002
US PATENT NO. 6,581,565

Only a few studies have examined the effect of compression ratio on spark-ignition engine performance and efficiency over a wide range of compression ratios. Figure 15-12 shows results obtained at wide-open throttle at 2000 rev/min with a series of eight-cylinder 5.3-dm^3 displacement engines, from the most extensive of these studies.[17] Gross-indicated and brake fuel conversion efficiencies and mean effective pressures are shown. Indicated mep was obtained by adding motoring friction mep to brake mep. The mep data were obtained with (A/F) and spark timing adjusted to give maximum torque; for the efficiency data, (A/F) and spark timing were adjusted to give maximum efficiency. The mechanical efficiency remained essentially constant at 0.89 over the full compression ratio range. The volumetric efficiency was also constant at 0.825. Both $\eta_{f,ig}$ and mep show a maximum at a compression ratio of about 17; for higher compression ratios efficiency and mep decrease slightly. This trend was explained as being due to increasing surface/volume ratio and slower combustion, and is also due to the increasing importance of crevice volumes: at the higher compression ratios studied the combustion chamber height became very small.

To assess more broadly the effect of compression ratio variations on fuel conversion efficiency, several data sets have been normalized and compared in Fig. 15-13 which shows the ratio of fuel conversion efficiency at the given compression ratio divided by the efficiency at $r_c = 8$, for wide-open-throttle engine operation. The agreement for $r_c \leq 14$ is good. Over the compression ratio range that is accessible to SI engines with available fuels ($r_c \leq 12$), fuel conversion efficiency increases by about 3 percent per unit of compression ratio increase. Note, of course, that engine power increases by about the same amount.

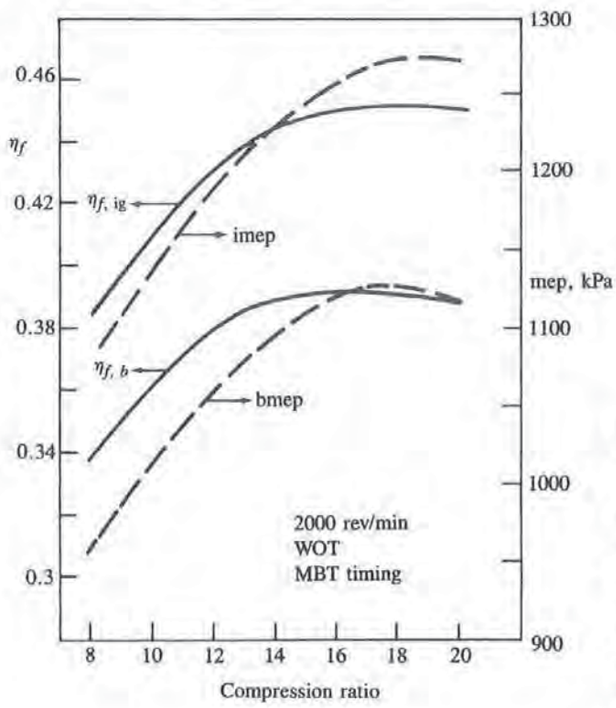


FIGURE 15-12
Effect of compression ratio on indicated mean effective pressure and fuel conversion efficiency. 5.3-dm^3 eight-cylinder spark-ignition engine at 2000 rev/min and wide-open throttle. Equivalence ratio and spark timing adjusted for maximum torque for mep data; adjusted for minimum fuel consumption for efficiency data.[17]

PETITIONER'S EXHIBIT 1002
US PATENT NO. 6,581,565

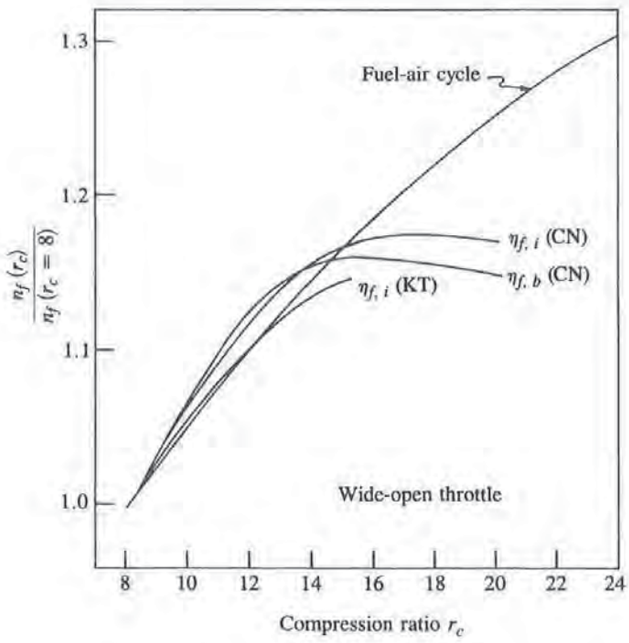


FIGURE 15-13
Relative fuel conversion efficiency improvement with increasing compression ratio, spark-ignition engines at wide-open throttle: CN,[17] KT.[18]

A similar comparison of the effect of compression ratio increases on efficiency at part load is shown in Fig. 15-14.[19] The figure shows brake fuel conversion efficiency data from engines of different cylinder volume. Both the compression ratio for maximum efficiency and the maximum efficiency depend on cylinder size. The wide-open-throttle and road-load data (top two curves[17]) confirm that the increase in efficiency with an increase in the compression ratio at part load apparently depends on the details of engine operation to a significant degree also. For the important compression ratio range of 9 to 11, the relative

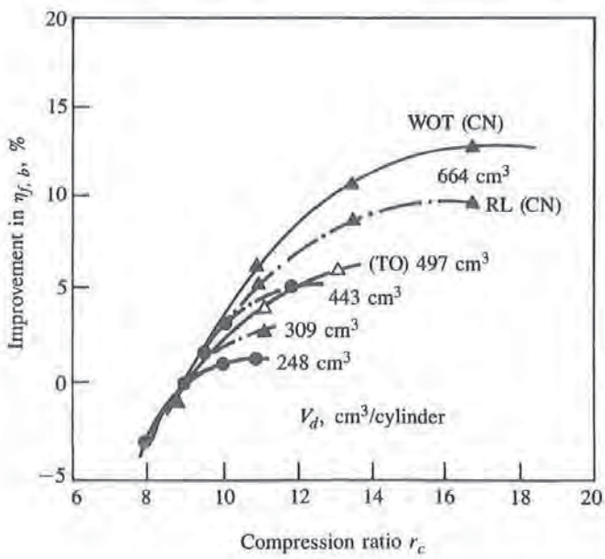


FIGURE 15-14
Relative brake fuel conversion efficiency improvement with increasing compression ratio of spark-ignition engines of different displaced volume per cylinder at part throttle (except top curve at WOT).[19] RL road load. CN,[17] TO.[10]

PETITIONER'S EXHIBIT 1002
US PATENT NO. 6,581,565

efficiency improvement is between 1 and 3 percent per unit of compression ratio increase, depending on cylinder size and operating conditions.

The exhaust temperature decreases as compression ratio and efficiency increase until the compression ratio corresponding to maximum efficiency is reached. It has also been shown that heat losses to the combustion chamber walls, as a fraction of the fuel's chemical energy, also decrease as the compression ratio and efficiency both increase.[17]

The effect of compression ratio changes on NO emissions is small. Some studies show a modest increase in specific NO emissions as the compression ratio increases at constant load and speed; other studies show a slight decrease. Increasing the compression ratio increases exhaust hydrocarbon emissions. Several trends could contribute: increased importance of crevice volumes at high r_c; lower gas temperatures during the latter part of the expansion stroke, thus producing less HC oxidation in the cylinder; decreasing residual gas fraction, thus increasing the fraction of in-cylinder HC exhausted; lower exhaust temperatures, hence less oxidation in the exhaust system.

15.4 SI ENGINE COMBUSTION CHAMBER DESIGN

15.4.1 Design Objectives and Options

There has always been extensive debate over the optimum SI engine combustion chamber design. There are a large number of options for cylinder head and piston crown shape, spark plug location, size and number of valves, and intake port design.[20] Debate revolves around issues such as chamber compactness, surface/volume ratio, flame travel length, and use of swirl and squish types of mixture motion. Figure 15-15 shows examples of several common types of combustion chamber shapes. Over the past few years a consensus has developed which favors faster-burning combustion-chamber designs. A chamber design where the fuel burning process takes place faster, i.e., occupies a shorter crank angle interval at a given engine speed, produces a more robust and repeatable combustion pattern that provides emission control and efficiency gains simultaneously. A faster-burning chamber with its shorter burn time permits operation with substantially higher amounts of EGR, or with very lean mixtures, within the normal constraints of engine smoothness and response. Thus greater emissions control within the engine can be achieved, and at part load at this higher level of dilution a faster-burning chamber shows an improvement in fuel consumption due to the reduced pumping work, reduced heat transfer (due to lower burned gas temperatures), and reduced amount of dissociation in the burned gases.[22]

The major combustion chamber design objectives which relate to engine performance and emissions are: (1) a fast combustion process, with low cycle-by-cycle variability, over the full engine operating range; (2) a high volumetric efficiency at wide-open throttle; (3) minimum heat loss to the combustion chamber walls; (4) a low fuel octane requirement.

PETITIONER'S EXHIBIT 1002
US PATENT NO. 6,581,565

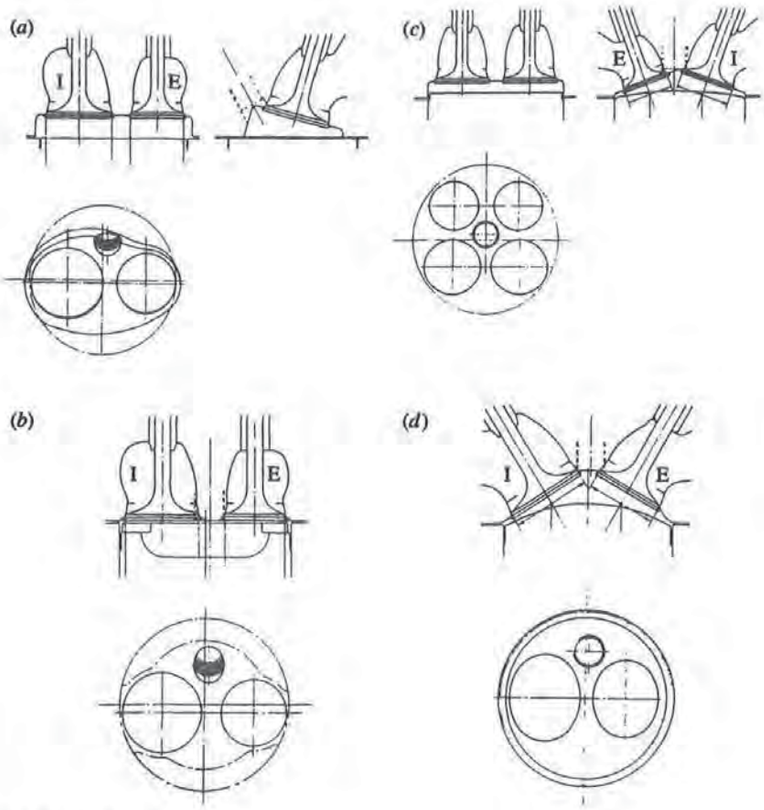


FIGURE 15-15
Examples of common spark-ignition engine combustion chamber shapes: (*a*) bathtub and wedge: (*b*) bowl-in-piston; (*c*) four-valve pent roof; (*d*) hemispherical.[21]

Many methods for producing a "fast burn" have been proposed. These include ways of making the combustion chamber shape more compact, moving the spark plug to a more central location within the chamber, using two plugs, and increasing in-cylinder gas motion by creating swirl during the induction process or during the latter stages of compression.

A faster combustion process relative to more moderate burn rate engines does result in a direct engine efficiency gain, other factors being equal. The magnitude of this direct gain is relatively modest. Experimental studies of the effect of an increase in burn rate from moderate to fast at constant engine load, speed, and mixture composition show that this effect is a few percent at most.[23] Computer simulations of the engine operating cycle confirm these experimental observations: while a decrease in total burn duration from 100 to 60° (slow to moderate burn) does result in a 4 percent decrease in bsfc, a decrease in burn duration from 60 to 20° gives only a further 1.5 percent bsfc decrease.[6]

Of greater importance is the fact that the faster burn process is more robust and results in the engine being able to operate satisfactorily with much more EGR, or much leaner, without a large deterioration in combustion quality. Faster

PETITIONER'S EXHIBIT 1002
US PATENT NO. 6,581,565

burning chamber designs exhibit much less cycle-by-cycle variability. This ability to operate with greater dilution at part load while maintaining a short burn duration and low cycle-by-cycle variability, permits much greater control of NO_x within the engine with 20 or more percent EGR without any substantial increase in HC emissions (see Fig. 11-29), or permits very lean operation. In both cases the efficiency gain relative to moderate burn rate engines, *which must operate with less dilution*, is sizeable.[24]

High volumetric efficiency is required to obtain the highest possible power density. The shape of the cylinder head affects the size of valves that can be incorporated into the design. Effective valve open area, which depends on valve diameter and lift, directly affects volumetric efficiency. Swirl is used in many modern chamber designs to speed up the burning process and achieve greater combustion stability. Induction-generated swirl appears to be a particularly stable in-cylinder flow. Swirl results in higher turbulence inside the chamber during combustion, thus increasing the rate of flame development and propagation. Generating swirl during the intake process decreases volumetric efficiency.

Heat transfer to the combustion chamber walls has a significant impact on engine efficiency. It is affected by cylinder head and piston crown surface area, by the magnitude of in-cylinder gas velocities during combustion and expansion, by the gas temperatures and the wall temperatures. The heat-transfer implications of a combustion chamber should be included in the design process.

Knock effectively limits the maximum compression ratio that can be used in any combustion chamber; it therefore has a direct impact on efficiency. Knock is affected by all the factors discussed above. It is the hardest of all the constraints to incorporate into the design process because of its obvious complexity.

Knowledge of the fundamentals of spark-ignition engine combustion, in-cylinder gas motion, and heat transfer has developed to the point where a rational procedure for evaluating these factors for optimum combustion chamber development and design can be defined. The next two sections develop such a procedure.

15.4.2 Factors That Control Combustion

Our understanding of the structure of the spark-ignition engine flame as it develops and propagates across the combustion chamber (see Secs. 9.3 and 9.4) allows us to relate the physical and chemical factors that control this process to the relevant engine design and operating parameters. The following factors affect the flame development and propagation processes:

1. *Geometry.* Combustion chamber shape and spark plug location.
2. *Flow field characteristics.* Mean velocity, turbulence intensity, and characteristic turbulence length scale in the unburned mixture during combustion.
3. *Unburned mixture composition and state.* Fuel, equivalence ratio, burned gas fraction, mixture pressure and temperature.

PETITIONER'S EXHIBIT 1002
US PATENT NO. 6,581,565

Geometry primarily affects combustion through the flame front surface area. It has a lesser effect on combustion development through its influence on in-cylinder motion. Geometric calculations (see Sec. 14.4.2), based solely on the assumption that the front surface of the flame can be modeled as a portion of a sphere centered at the spark plug, provide data on flame front area and the volume behind the flame front surface (the enflamed volume), contained within the combustion chamber at the appropriate flame radii and piston positions.

Flame area varies significantly from one chamber shape to another for a given enflamed volume. In the example shown in Fig. 14-7, the bowl-in-piston chamber gives flame surface areas 30 to 45 percent larger than those for the disc chamber under equivalent conditions around top-center. Hemispherical and open or clamshell chambers showed gains of about 30 percent relative to the equivalent disc configuration. For a given chamber shape, flame area depends even more significantly on plug location. Figure 14-7 shows that shifting the plug from a side to a center location for the bowl-in-piston chamber increased the peak flame area by 150 percent. For hemispherical and open chambers, the increases for a similar shift in plug location were 75 and 90 percent, respectively.[25]

Maps of flame area as a function of radius at different crank angle locations indicate the following pattern. For chamber geometries with side ignition, as flame radius increases, the flame area first rises slowly, then remains approximately constant, and then decreases slowly to zero. In contrast, chambers with central ignition show, as flame radius increases, a rise in flame area to a peak during the major part of the flame travel followed by a rapid decrease as the flame encounters the chamber walls. Moving the plug location toward the center of the chamber produces a larger increase in flame front area than does making the chamber shape more compact (though this has a positive impact too).

The effect of chamber geometry on burn rate has been examined using thermodynamic-based engine cycle simulations with various types of combustion model (e.g., the type developed by Keck and coworkers, see Sec. 14.4.2). Figure 15-16 shows results from one such study.[25] The combustion characteristics of ten different chamber geometries were compared at fixed part-load engine operating conditions. The flame development and propagation phases were separated into 0 to 10 and 10 to 90 percent mass fraction burned times. These were then normalized by the equivalent burn times of the slowest burning chamber—the disc with side ignition. Chamber geometry has the greatest impact on the 10 to 90 percent burn time; its effect on 0 to 10 percent time is significant but substantially smaller. Total burn times can be reduced by between 20 to 30 percent by optimizing spark plug location—comparing worst to best location for each chamber shape. Comparing worst and best chamber shapes, total burn time with fixed plug location can be reduced by about 10 percent.

Increased turbulence in the unburned mixture at the time of combustion increases the burning rate. Turbulence is usually increased by generating swirl during the induction process (see Sec. 8.3.2 and below). Cycle simulation studies[25] indicate that both the duration of the early stage of the burning process and of the main stage decrease when the turbulent velocity at the start of com-

PETITIONER'S EXHIBIT 1002
US PATENT NO. 6,581,565

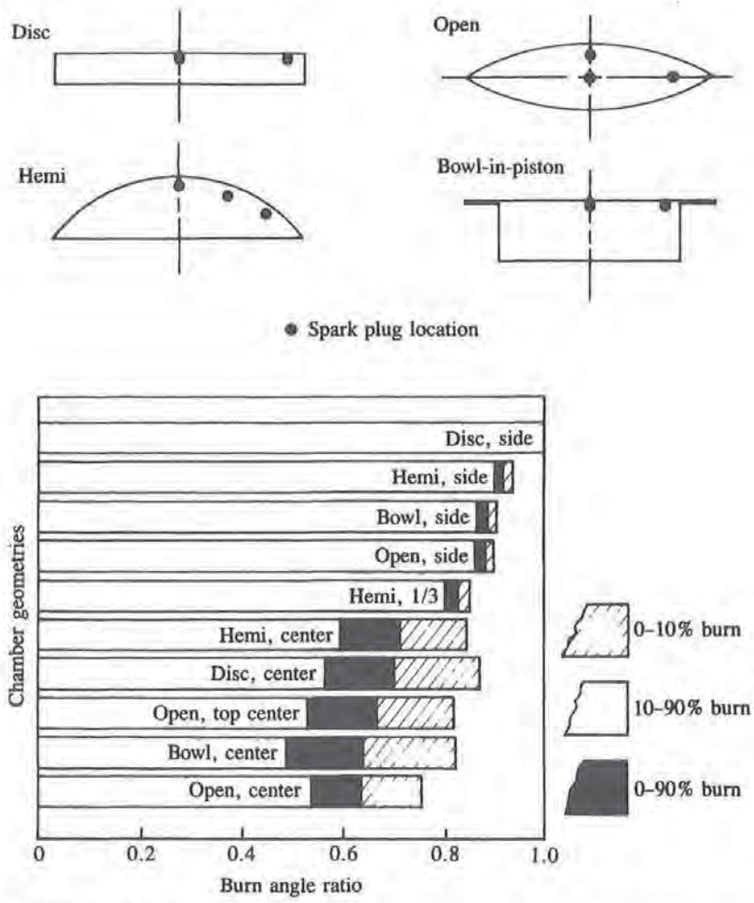


FIGURE 15-16
Comparison of burn angles (0–10 percent burned, 10–90 percent burned, 0–90 percent burned; see Fig. 9-13) for ten different spark-ignition engine combustion chamber geometries and spark plug locations. Burn angles are normalized by angles for slowest burning chamber: disc with side plug.[26]

bustion is increased. The faster combustion process comes primarily from the higher turbulence intensity; however, the decreased characteristic turbulence scale that accompanies the increased turbulence is also significant since it results in a shorter characteristic burning time [see Eq. (14.39) and the accompanying text]. It is important to note that the fuel conversion efficiency of higher-turbulence chambers at the same operating conditions can be lower than for normal chambers, despite the faster burn rates, due to the higher heat transfer that accompanies the higher in-cylinder velocities. For example, predictions based on the combustion model defined by Eqs. (14.33) to (14.35), where the characteristic mixture speed u_T was increased by a factor of two, showed that the 0 to 10 percent and 10 to 90 percent burn durations decreased by about one-third. However, the indicated fuel conversion efficiency decreased by about 6 percent due to the predicted 15 percent increase in heat transfer.[25]

Mixture composition and state affect the burn rate through the dependence

PETITIONER'S EXHIBIT 1002
US PATENT NO. 6,581,565

of laminar flame speed on temperature, pressure, fuel/air equivalence ratio, and burned gas fraction (residual gas and EGR): see Sec. 9.3.3 and Eqs. (14.33) to (14.35). Table 15.1 compares the burn durations for a stoichiometric mixture, a lean mixture with $\phi = 0.8$, and a stoichiometric mixture with 20 percent EGR. The values of the laminar flame speed at the time of spark are also given (conditions at spark as well as composition are different in each case). The longer burn durations of the more dilute mixtures are clear. Note that EGR as a diluent has a much more deleterious effect on combustion than does air at these approximately equal levels of dilution.

All the above-described factors—flame geometry, fluid motion, and mixture composition—can vary cycle-by-cycle, and therefore contribute to combustion variability (see Sec. 9.4). Cyclic differences in gas motion in the vicinity of the spark plug result in differences in motion of the flame kernel during its early stages of development. Differences in turbulence result in differences in the rates at which the initially smooth surface of the flame kernel becomes wrinkled and convoluted by the flow. Different initial flame center motions change the geometrical interaction of the flame front with the combustion chamber walls later in the flame propagation process. Differences in the amount of fuel, air, and EGR which enter each cylinder cycle-by-cycle, the nonuniformity in composition of the entering charge, and any incomplete mixing of that entering charge with the residual gases in the cylinder also contribute to combustion variability. These composition nonuniformities lead to differences in the early stages of flame development. The variations in the amounts of fuel, air, and EGR that enter each cylinder cycle-by-cycle and in the uniformity of that mixture are factors within the direct control of the engine designer.

A fast combustion process reduces cyclic combustion variability for the following reasons. With a faster burn, optimum spark timing is closer to top-center: mixture temperature and pressure at the time of spark are higher, so the laminar flame speed at the start of combustion is greater. This, combined with the higher turbulence of most fast-burn concepts, results in faster flame kernel development.

TABLE 15.1
Effect of excess air and recycled exhaust on burn duration

ϕ	EGR, %	θ_s, degree	Burn durations, degree		S_L at θ_s, cm/s
			0–10%	10–90%	
1.0	0	340	22	17	75
0.8	0	336	26	21	52
1.0	20	324	31	28	23

400 cm^3 per cylinder displaced volume, 80 mm bore, 8.5 compression ratio, disc chamber, center plug location. 1500 rev/min, stoichiometric operation, θ_s = spark timing (MBT), inlet pressure 0.5 atm, inlet temperature 350 K, S_L = laminar flame speed.[26]

PETITIONER'S EXHIBIT 1002
US PATENT NO. 6,581,565

More rapid initial flame growth results in less variation in flame center motion during the critical flame-development phase. The resulting geometric variations in the flame front/chamber wall interaction are therefore reduced; this decreases the variations in burn rate that result from these geometric variations. Also, the faster burning process ends earlier in the expansion stroke. Thus the problem of occasional slow burning cycles, partial burning cycles, and eventually misfire, which occurs with dilute mixtures under normal burning conditions due to quenching of the combustion process as gas temperatures fall during expansion, is largely avoided (see Sec. 9.4.3).

15.4.3 Factors That Control Performance

VOLUMETRIC EFFICIENCY. Combustion chamber shape affects volumetric efficiency through its constraints on maximum valve size and through the degree of swirl (if any) that the chamber and port designs produce to achieve the desired combustion characteristics. To obtain maximum performance and to reduce pumping losses, the size of the valve heads should be as large as practical; the valve sizes that can be accommodated depend on cylinder head layout. Table 6.1 lists the typical maximum valve sizes that can be accommodated into several common chamber shapes (see Fig. 15-15). The approximate mean piston speed at maximum power is a measure of the maximum air flow that each engine design can pump. Note that of the two-valve configurations, the designs with inclined valve stems permit substantially greater maximum air flow. The four-valve pent-roof design, which also has inclined valve stems, is the best of those listed since it accommodates the largest valve and port areas (there are other four-valve head designs which are comparable).

Swirl can be generated during the intake process through suitable port, valve, and head design. It requires either that the flow through the intake valve be directed tangentially into the cylinder so that gas flows through one side of the valve opening preferentially (e.g., through the use of masks to restrict flow at the mask location or through the use of a tangentially directed port or a flow deflector in the port just upstream of the valve), or requires the use of a helical intake port that imparts an angular velocity to the flow before it enters the cylinder. In either case the inlet flow enters the cylinder with higher velocity than it would have in the absence of swirl; hence the pressure drop across the valve is increased, and maximum air flow through the cylinder is reduced. Well-designed helical swirl-generating ports (see Sec. 8.3.2) appear to be the best way to create swirl. However, geometric and production constraints often prevent the incorporation of such ports into the cylinder head design, and other swirl-generating methods must be used. The engine maximum-power penalty associated with generating significant swirl is of order 5 to 10 per cent.

Since swirl is only required at part-throttle operation when enhancement of the burn rate is most critical and is not usually required at full throttle when the flow restriction penalty is most significant, induction systems with a separate passage for the part-throttle air flow, where only this separate passage generates

PETITIONER'S EXHIBIT 1002
US PATENT NO. 6,581,565

swirl, are an attractive option. However, the gains in volumetric efficiency are offset by a higher cost due to the additional complexity in port and manifold of the double passage and the individual throttle valves required in each port for flow control.

Swirl can be *intensified* during compression with bowl-in-piston combustion chambers by decreasing the moment of inertia of the in-cylinder charge as the piston moves toward top-center, and thereby increasing its angular velocity (see Sec. 8.3.3). An advantage here is that the swirl level generated during induction is less than would be required without the compression-produced radially inward motion of the charge. This approach can be used with combustion chamber designs that are axisymmetric and compact. Swirl can also be *generated* by squish motion toward the end of compression with a suitable design of chamber. The advantage of this approach is that there is no induction-stroke swirl-generating volumetric efficiency penalty. However, the cylinder head geometries proposed to date for either intensifying or generating swirl have vertical valve stems, and hence have smaller valve sizes which in themselves restrict air flow. Also, the cylinder head geometry required to generate swirl during compression has a larger surface area than more open chamber designs and, therefore, has significantly higher heat losses.

The impact of conventional radially inward squish motion (see Sec. 8.4) on in-cylinder turbulence, and hence combustion, is unclear. Chambers with significant squish are also more compact; for this reason alone they would be faster burning.

HEAT TRANSFER. The convective engine heat transfer to the combustion chamber walls is described by equations of the form of (12.2): e.g., Eq. (12.21). The heat-transfer coefficient is usually correlated by expressions of the form of Eq. (12.3), which relate the Nusselt, Reynolds, and Prandtl numbers (see Sec. 12.4). Thus combustion chamber surface area, and especially the surface area in contact with the burned gases, is important. Gas velocity is also important; it influences the heat-transfer rate through the Reynolds number. Various characteristic velocities have been used in the Reynolds number to scale heat transfer: mean piston speed, mean in-cylinder gas velocity, turbulence intensity, either individually or in combination. Both of these variables, area and velocity, are affected by combustion chamber design.

Studies of engine performance using thermodynamic-based simulations of the engine's operating cycle (see Sec. 14.4) provide data that indicate the importance of changes in heat transfer. At part-throttle operating conditions, such simulation calculations show that a 10 percent change in combustion chamber heat losses results in a change of between 2 and 5 percent in brake specific fuel consumption; an average fuel consumption change of about one-third the magnitude of the heat-transfer change (and of opposite sign) is an appropriate rule of thumb.[25, 27] At wide-open throttle, the effect on mean effective pressure is comparable: a 10 percent change in heat transfer results in about a 3 percent change in bmep.

PETITIONER'S EXHIBIT 1002
US PATENT NO. 6,581,565

This impact of heat transfer on engine efficiency and performance underlines the importance of combustion chamber details that affect heat transfer. For the chamber shapes shown in Fig. 15-16, the total heat losses as a fraction of the fuel's energy, at fixed engine speed and intake conditions, were also calculated. Both chamber shape and spark plug details affect heat losses since together these govern the surface area of the hot burned gases in contact with the walls. The open and hemispherical chambers had least heat transfer. Geometries such as the bowl-in-piston, which obviously have a higher surface area, had about 10 percent higher heat transfer. The effect of shifting the plug from a side to center location depended on chamber shape. Open and bowl-in-piston chambers showed little change; the hemispherical chamber showed a 4 percent reduction. Given a general chamber shape choice, the details of the actual design are important also; it is easy to add substantial surface area with piston cutouts, plug bosses, and cylinder head masking or squish regions which will deteriorate chamber performance to a measurable degree.

Higher in-cylinder velocities affect heat-transfer rates through the Reynolds number term in the heat-transfer coefficient correlation. Swirl- and squish-generated flows increase in-cylinder gas velocities and will, therefore, increase heat-transfer rates.

15.4.4 Chamber Octane Requirement

Knock limits an engine's compression ratio, and hence its performance and efficiency. The more fundamental aspects of knock were reviewed in Sec. 9.6. Knock occurs when the end-gas autoignites prior to its being burned up by the normal flame-propagation process. The tendency to knock depends on engine design and operating variables which influence end-gas temperature, pressure, and time spent at high values of these two properties before flame arrival.

The presence or absence of knock in an engine depends primarily on the antiknock quality of the fuel, which is defined by the fuel's *octane number* (see Sec. 9.6.3). It determines whether or not a fuel will knock in a given engine under given operating conditions: the higher the octane number, the higher the resistance to knock. The *octane number requirement* of an engine is defined as the minimum fuel octane number that will resist knock throughout its speed and load range. The following factors affect an engine's octane requirement: (1) composition of the fuel; (2) chamber geometry and size; (3) charge motion; (4) spark-advance curve; (5) inlet air, intake manifold, and water jacket temperatures; (6) carburetor or fuel-injector air-fuel ratio calibration; (7) the ambient conditions—pressure, temperature, and relative humidity—during the requirement determination.

The following illustrates the interaction between fuel factors and engine operating variables. Figure 15-17 shows the relation between spark advance, torque, and speed in an engine operating at wide-open throttle. The dashed lines, determined with a fuel of sufficiently high octane rating to avoid knock, show MBT timing as a function of speed, along with the spark-advance limits for con-

PETITIONER'S EXHIBIT 1002
US PATENT NO. 6,581,565

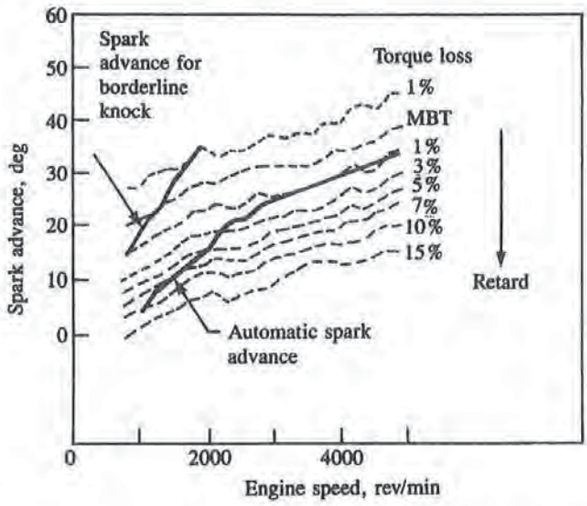


FIGURE 15-17
Relation between spark advance, speed, and torque loss, for spark-ignition engine at wide-open throttle, showing knock limit for specific gasoline and typical spark-advance schedule that avoids knock problems.[28]

stant specified percentage torque reductions. The upper solid line traces the spark advance for borderline knock with a particular commercial gasoline. To avoid knock with this fuel, the spark advance must be set to lose one percent of engine torque at 800 rev/min, with the torque loss diminishing to zero at 1200 rev/min. Above that speed this particular fuel allows operation at MBT timing without knocking. The lower solid curve represents a typical spark-advance schedule at WOT. It lies below the borderline knock advance (and results in a significant torque loss) for the following reasons. One is that different commercial gasolines with the same research octane number can respond differently to variations in engine operating conditions. Calibrating the engine (i.e., specifying the schedules for spark advance, A/F, and EGR) must be done with sufficient margin of conservatism to avoid objectionable knock with the normal range of commercial gasolines over the full operating conditions of the engine. A second reason is engine-to-engine production variability despite the close dimensional tolerances of modern production engineering. For example, the effective compression pressure in each cylinder of a multicylinder engine is not identical, due to geometric and ring-pack behavior differences. The cylinder with the highest compression pressure is most knock-prone. Allowing for corresponding effects of cylinder-to-cylinder variations in A/F, EGR rates, and spark timing, it is obvious that for a given operating condition in a multicylinder engine, one cylinder is more likely to knock than the others. It is that cylinder which limits the spark advance.† A third reason for the discrepancy between actual spark-advance calibration and the knock limit for a given engine and fuel is the octane requirement increase associated with the buildup of deposits on the combustion chamber walls over extended mileage (see Sec. 9.6.3).

† There is no assurance that the same cylinder will be the principal offender in all engines of the same model, nor in a given engine at all operating conditions.

PETITIONER'S EXHIBIT 1002
US PATENT NO. 6,581,565

In the example shown above, it was the problem of knock at low engine speed which required the spark advance calibration to be retarded. Whether low-, medium-, or high-speed knock is the limiting factor in a particular engine depends on the sensitivity of the fuel, on engine design features, and especially upon the engine's spark-advance requirements for MBT. The knock-limited spark advance determined from road octane rating tests will vary with engine speed and fuel sensitivity, as shown in Fig. 15-18. Low sensitivity fuels will tolerate more severe engine operating conditions and vice versa. Figure 15-18*b*, *c*, and *d* shows a typical engine spark-advance characteristic superposed on the knock-limited spark-advance plot. Depending on the fuel sensitivity and shape of the spark-advance curve, the knock region may occur at low, medium, or high speed (or not at all).

It will be apparent from the above discussion that defining the effect of combustion chamber geometry on knock can only be done in an approximate fashion. The importance of fuel composition details, differences in engine design, the variability between engines of the same type, and the effect of deposits all make the quantification of trends as chamber design is varied extremely difficult. One of the most important chamber variables is the compression ratio. Figure 15-19 shows the relationship between the octane requirement and compression ratio for a number of combustion chambers. The octane requirement was defined as the research octane number of the fuel required to operate the engine at WOT with the weakest mixture for maximum power with borderline

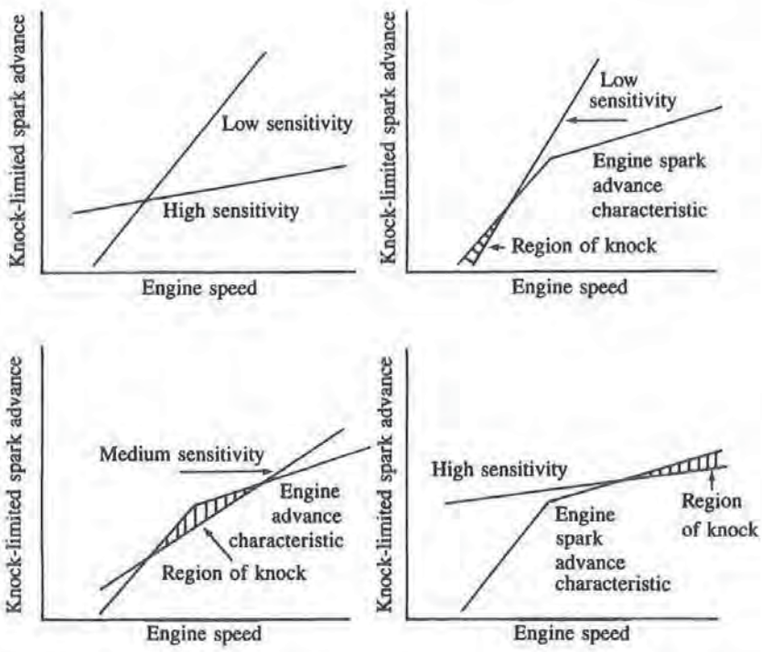


FIGURE 15-18
Diagrams showing knock-limited spark-advance curves for fuels of different sensitivity and how these can give low-, medium-, and high-speed knock in the same engine.[29]

PETITIONER'S EXHIBIT 1002
US PATENT NO. 6,581,565

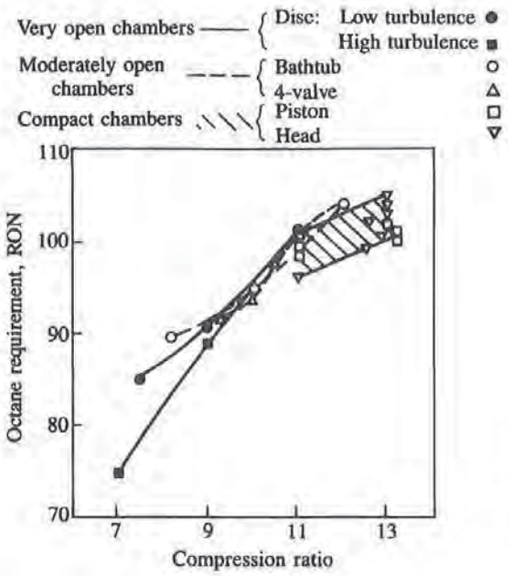


FIGURE 15-19
Octane requirement (gasoline research octane number), at wide-open throttle and MBT timing, to avoid knock as a function of compression ratio for various combustion chamber designs.[10]

(or light) knock coinciding with MBT timing at the given speed. As is well known, the octane requirement increases with increasing compression ratio; there are, however, differences in the octane requirement between different types of chamber at the same compression ratio. The chambers studied were disc-shaped chambers, bathtub and four-valve (open chambers with squish) and compact high compression ratio chambers (bowl or cup-type chambers in the piston crown or in the cylinder head around one of the valves). In the 9 to 11 compression ratio range there are only modest differences between the chambers studied. At higher compression ratios, 11 to 13, the compact chambers show a lower octane requirement which gives them a 1 to 2 compression ratio advantage over the more open chambers. This advantage for the compact (and high-turbulence) chambers comes largely from the increased heat-transfer rates in these chambers. Whether the higher turbulence is generated during intake or at the end of the compression stroke, it increases the heat transfer from the end-gas, reducing its temperature and therefore its propensity to knock. However, this higher heat transfer also reduces engine power and efficiency, so the benefits of the compression ratio advantage are reduced. There is some increase in the knock-limited compression ratio with a given fuel as burn time is decreased by using one, two, three, and then four spark plugs simultaneously, with a given chamber geometry, but the effect is much smaller than the differences suggested by Fig. 15-19.[23]

Spark plug location within the chamber is an important factor affecting octane requirement. More centrally located plug positions shorten the flame travel path to the cylinder walls and decrease the time between spark discharge and flame arrival at the end-gas location. This decreases the octane requirement. The position of the spark plug in relation to the exhaust valve is also important: it is advantageous to burn the unburned mixture which has been heated by contact with the hot exhaust valve early in the combustion process.

PETITIONER'S EXHIBIT 1002
US PATENT NO. 6,581,565

TABLE 15.2
Engine conditions affecting octane number requirement

Octane number requirement tends to go *up* when:	Octane number requirement tends to go *down* when:
1. Ignition timing is advanced.	1. Ignition timing is retarded.
2. Air density rises due to supercharging or a larger throttle opening or higher barometric pressure.	2. Engine is operated at higher altitudes or smaller throttle opening or lower barometric pressure.
3. Humidity or moisture content of the air decreases.	3. Humidity of the air increases.
4. Inlet air temperature is increased.	4. Inlet air temperature is decreased.
5. Coolant temperature is raised.	5. Fuel/air ratio is richer or leaner than that producing maximum knock.
6. Antifreeze (glycol) engine coolant is used.	6. Exhaust gas recycle system operates at part throttle.
7. Engine load is increased.	7. Engine load is reduced.

Operating variables that affect the temperature or pressure time histories of the end-gas during combustion or the basic autoignition characteristics of the unburned fuel, air, residual mixture will also affect the engine's octane requirement. The most important additional variables which increase or decrease octane requirement in a consistent manner are listed in Table 15.2. Relative spark

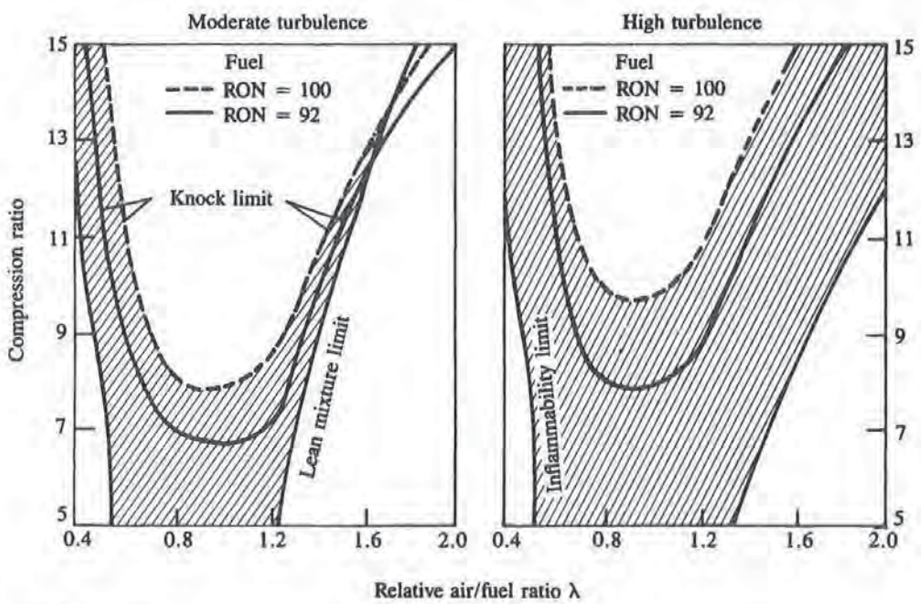


FIGURE 15-20
Knock limits and lean engine operating limits as function of compression ratio and relative air/fuel ratio λ ($\lambda = 1/\phi$) for moderate and high-turbulence engine combustion chambers.[32]

PETITIONER'S EXHIBIT 1002
US PATENT NO. 6,581,565

advance has a major impact on knock; since it is also easy to adjust, it is the engine variable most commonly used to control knock. Studies show that typically 0.5 to 1.0 RON reduction is achieved per degree of retard.[30] Atmospheric conditions—pressure, temperature, and humidity—all affect the octane number requirement.[31]

The fuel/air equivalence ratio affects the octane requirement of an engine. The highest requirement is for slightly rich mixtures; increasing richness and leanness about this point decrease the octane requirement substantially. Figure 15-20 shows the knock-limited compression ratio as a function of the relative air/fuel ratio ($\lambda = 1/\phi$; $\lambda > 1$ for lean mixtures) for conventional and high-turbulence chambers, for two fuels with different octane ratings. Substantially higher compression ratios can be used with lean mixtures, especially with the high-turbulence chamber which extends the lean limit. The coolant temperature affects the octane requirement. Higher coolant temperature increases the inlet mixture temperature, and reduces heat losses from the end-gas to a modest degree.

15.4.5 Chamber Optimization Strategy

The discussion in the previous sections suggests that the following sequence of steps in a combustion chamber development process is most logical. First should come the selection of the best chamber geometry. Geometric optimization can result in substantial benefits and carries no significant penalties. Chamber geometry involves cylinder head and piston crown shape, and plug location. Open chambers such as the hemispherical or pent-roof cylinder head, and clam-shell, with near central plug location, give close to the maximum flame front surface area (and hence a faster burn), have the lowest chamber surface area in contact with the burned gases (and therefore the lowest heat transfer), and have inclined valves which give high volumetric efficiency. Spark plug location close to the center of the chamber is especially important in obtaining a fast burn rate. More compact chamber shapes than the open chambers listed above, such as the bowl-in-piston or chamber-in-head designs, do produce a somewhat faster burn, but with lower volumetric efficiency and higher heat losses.

Following this first step, two problem areas may remain: the chamber may have a higher octane requirement than is desired and the burn rate may not be fast enough to absorb the high dilution required at part load to meet the emissions and fuel consumption goals.

Positioning the spark plug as close to the center as possible will have reduced the octane requirement for that particular chamber shape. Depending on chamber design details, some squish area could be introduced. However, the perceived octane advantage of chamber designs which contain substantial squish is offset, at least in part, by their higher heat losses. A unit compression ratio increase results in a 3 percent or less increase in efficiency at part load. However, if the measures required to increase the compression ratio from, say, 9 to 10 resulted in a 10 percent increase in heat transfer, engine efficiency would not improve.

PETITIONER'S EXHIBIT 1002
US PATENT NO. 6,581,565

The next step should be to reduce the cyclic variability in the combustion process to the maximum extent feasible, by improving the uniformity of the intake fuel, air, and EGR mixture. Delivery of equal amounts of each of these constituents to each cylinder, provision for good mixing between constituents in the intake manifold and port, and accurate control of mixture composition during engine transients are all especially important. Also important is achieving closely similar flow patterns within each engine cylinder during intake so as to obtain equal burn rates in all cylinders. Attention to these intake process and mixture preparation details will always improve engine operation and carries no performance penalties.

However, the burn rate may still not be fast enough, especially during the critical early stages of flame development, and cyclic variability may still be too high to meet the engine's performance goals. Then higher turbulence levels during combustion must be achieved. This is usually best done by creating swirl during the induction process. The appropriate method for introducing swirl will depend on any geometric manufacturing constraints and cost issues. With no geometric constraints, use of helical swirl-generating ports or a divided intake-port system with valves to control the flow at light load are likely to have the lowest power penalties. It is especially important that only the minimum additional turbulence required to achieve the performance objectives be added at this stage. Higher than necessary gas velocities within the cylinder result in excessive heat losses and low volumetric efficiency.

In summary, to meet the objectives of a fast, repeatable, and robust combustion process with high volumetric efficiency, low heat transfer, and acceptable octane requirement, combustion chamber development should proceed through the following steps.

1. Optimize the chamber geometry within the design constraints for the maximum flame front area, minimum burned gas/chamber wall contact area, and largest valve size.
2. Obtain additional reductions in the cyclic combustion variability by improving mixture distribution and uniformity and by creating flow patterns into each cylinder that are essentially identical.
3. Achieve any additional improvement in burn rate and cyclic variability required to meet objectives by increasing turbulence to the minimum extent. This is usually best done by creating swirl during the induction process.

15.5 VARIABLES THAT AFFECT CI ENGINE PERFORMANCE, EFFICIENCY, AND EMISSIONS

15.5.1 Load and Speed

The performance of a naturally aspirated DI heavy-duty truck diesel engine and a small IDI engine at full load over the engine speed range have already been

PETITIONER'S EXHIBIT 1002
US PATENT NO. 6,581,565

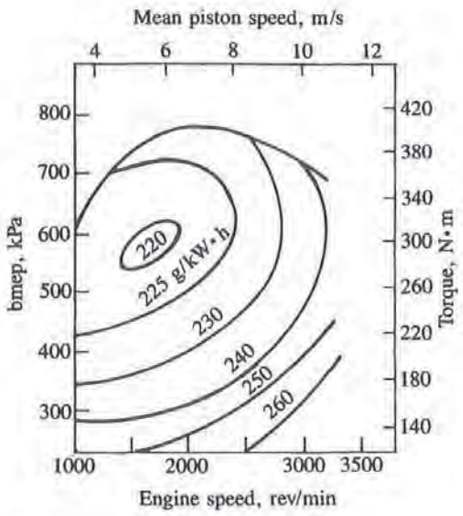


FIGURE 15-21
Performance map for 6.54-dm^3 eight-cylinder air-cooled naturally aspirated medium-swirl DI diesel engine. Contours of constant bsfc in grams per kilowatt-hour shown. Bore = 102 mm, stroke = 100 mm, $r_c = 18$. Multihole fuel nozzle.[33]

discussed in Sec. 15.2. Here we examine the part-load behavior of various types of naturally aspirated diesel engines.

As with SI engines (see Sec. 15.3.3), performance maps where bsfc contours are plotted on a graph of bmep versus engine speed are commonly used to describe the effects of load and speed variations. Figure 15-21 shows the performance map for an air-cooled four-stroke cycle medium-swirl naturally aspirated DI diesel (similar to the engine in Fig. 1-23). Maximum rated power for this 6.54-dm^3 displacement engine at 3200 rev/min is 119 kW, maximum bmep at 2000 rev/min is 784 kPa, and minimum bsfc (at 1600 rev/min and 580 kPa bmep) is 220 g/kW · h, which corresponds to a brake fuel conversion efficiency of 38.5 percent. The gross indicated fuel conversion efficiency would be about 48 percent.

Figure 15-22 shows the performance map for a small high-swirl DI diesel which uses the M.A.N. combustion system with a single fuel jet sprayed tangentially into the swirling air flow. Due to the higher speed and higher swirl than the

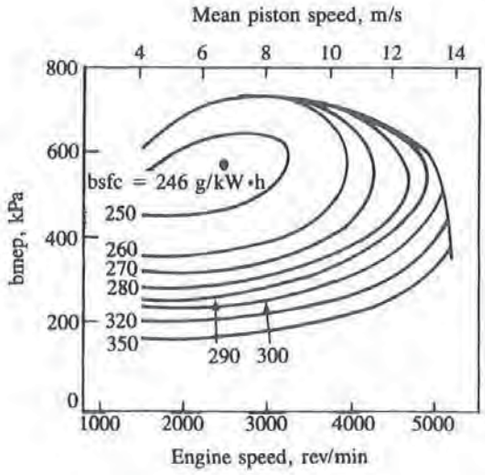


FIGURE 15-22
Performance map for 1.47-dm^3 four-cylinder naturally aspirated DI diesel engine with high-swirl single-hole-nozzle M.A.N. combustion system. Contours of constant bsfc in grams per kilowatt-hour shown. Bore = 76.5 mm, stroke = 80 mm, $r_c = 18.5$.[34]

PETITIONER'S EXHIBIT 1002
US PATENT NO. 6,581,565

larger DI engine in Fig. 15-21, the maximum bmep is slightly lower. The best bsfc is about 10 percent higher largely due to higher friction mep, but in part due to higher heat losses resulting from the less favorable surface/volume ratio of the smaller bore engine and higher swirl, and lower heat-release rate of the M.A.N. system. Note that the maximum mean piston speed for this engine, 13.3 m/s at 5000 rev/min, is comparable to that of the larger medium-swirl engine in Fig. 15-21 (10.7 m/s).

Figure 15-23 gives the performance characteristics of an automotive naturally aspirated swirl-chamber IDI diesel engine. Maximum bmep values are usually higher than those of equivalent size DI engines because without the need to generate swirl during the intake process, the intake port and valve are less restrictive and volumetric efficiency is higher, and because the IDI engine can be run at lower A/F without smoking. The best bsfc values are usually some 15 percent higher than values typical of equivalent DI engines. The best brake fuel conversion efficiency of the engine of Fig. 15-23 is 32.5 percent.

Comparisons between naturally aspirated DI and IDI diesel engines of closely comparable design and size indicate that the DI engine is always more efficient, though the benefit varies with load. At full load, differences of up to 20 percent in bsfc have been noted, especially in engines with larger displacement per cylinder. At part load, the gain is less—of order 10 percent. Comparisons should be made at equal emission levels, a task that is difficult to accomplish in practice. Emission control with the DI engine is more difficult, so this constraint reduces the benefit somewhat. Figure 15-24 shows a breakdown of the indicated efficiency differences between the two systems. At full load ($A/F = 18$ to 20) the IDI suffers a penalty of about 15 to 17 percent due in large part to the retarded timing of the IDI combustion process and its long, late-burning, heat-release profile. At light load, about 300 kPa bmep ($A/F = 50$), these combustion effects are small and the indicated efficiency penalty of the IDI (around 5 to 7 percent) is due to the higher heat losses associated with the larger surface area and high-velocity flow through the connecting nozzle of the divided-chamber geometry and due to the pumping pressure loss between the main and auxiliary chambers.[36]

Note that all these diesel engine performance maps are similar in general

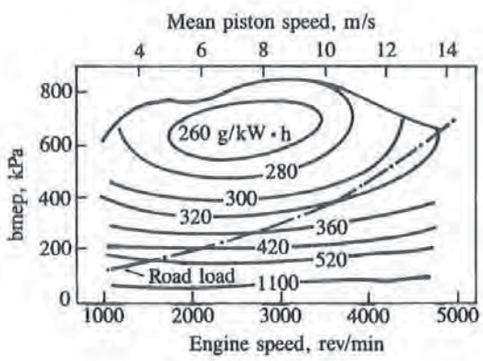


FIGURE 15-23
Performance map for 1.987-dm^3 five-cylinder naturally aspirated IDI swirl-chamber diesel engine. Contours of constant bsfc in grams per kilowatt-hour shown. Bore = 76.5 mm, stroke = 86.4 mm, $r_c = 23$.[35]

PETITIONER'S EXHIBIT 1002
US PATENT NO. 6,581,565

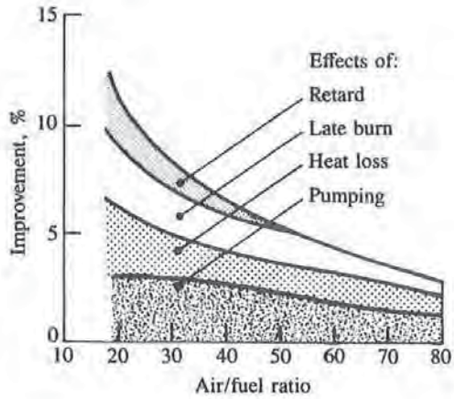


FIGURE 15-24
Factors which improve the indicated efficiency of naturally aspirated small DI diesel combustion systems relative to IDI swirl-chamber combustion system, as a function of A/F or load.[36]

shape and when plotted against $\bar{S}_p$ are quantitatively comparable. The increase in bsfc from the minimum value with increasing speed at constant load is due to the increase in friction mep, partly offset by the effect of decreasing importance of heat losses per cycle on efficiency. The increase in bsfc with decreasing load at constant speed is dominated by the decreasing mechanical efficiency as bmep is reduced. The indicated fuel conversion efficiency increase as the fuel/air equivalence ratio is decreased partly offsets this. The trends in bsfc when increasing load at constant speed and increasing speed at constant load from the minimum are more modest. They are the net results of (1) the increase in mechanical efficiency and decrease in indicated fuel conversion efficiency as the load increases and (2) decreasing indicated efficiency due to increasing importance of heat losses and increasing mechanical efficiency as the speed decreases. The enrichment of the mixture at high load and low speed of spark-ignition engines is, of course, absent.

Figure 15-25 shows the effect of load on NO_x and HC emissions for naturally aspirated DI and IDI diesel engines. For the DI engine NO_x concentrations rise steadily as the fuel/air ratio increases with increasing bmep at constant injection timing. The increasing quantity of fuel injected per cycle results in an increasing amount of close-to-stoichiometric combustion products near the peak pressure and temperature (see Sec. 11.2.4). The IDI engine shows a similiar trend except that, at high load, NO_x concentrations level off. These characteristics do not change substantially with engine speed. The IDI engine shows significantly lower HC emissions than the DI engine. The high HC at idle and light load are thought to result from fuel mixing to too lean an equivalence ratio. If diesel engines are overfueled at high load, HC emissions then rise rapidly. These HC mechanisms are described in Sec. 11.4.4. Injection timing affects NO_x and HC emissions significantly, as discussed in Sec. 15.5.2 below.

Figure 15-26 shows smoke and particulate mass emissions from a naturally aspirated IDI engine. Rapidly increasing black smoke at very high load limits the maximum bmep that a diesel engine can produce. On a specific emission basis [Eq. (2.36)], the particulates typically show a U-shaped behavior due to the predominance of hydrocarbons in their composition at light load and of carbon at high load.[38]

PETITIONER'S EXHIBIT 1002
US PATENT NO. 6,581,565

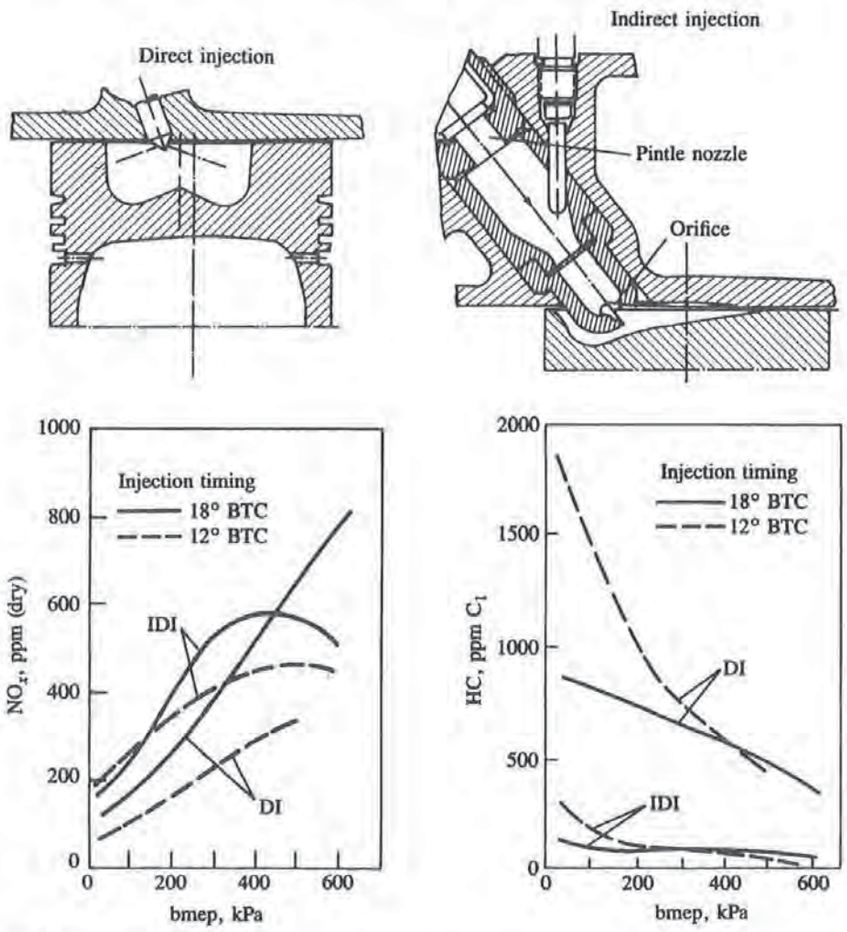


FIGURE 15-25
Effect of load on naturally aspirated diesel engine NO_x and HC emissions at rated speed, with two injection timings. Direct-injection and indirect-injection (prechamber) combustion systems. Six-cylinder, 5.9-dm^3 displaced volume, engine. DI: $r_c = 17$, rated speed = 2800 rev/min; IDI: $r_c = 16.7$, rated speed = 3000 rev/min.[37]

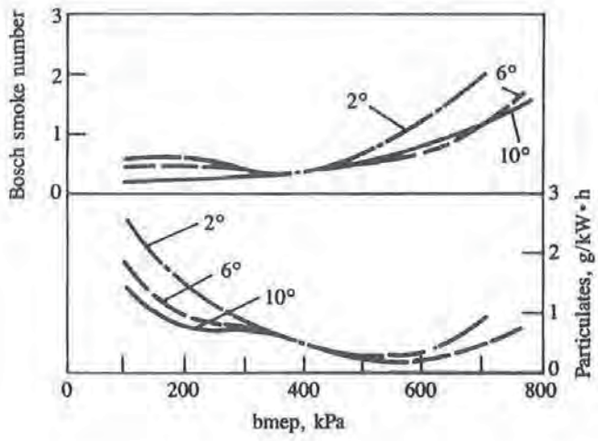


FIGURE 15-26
Smoke (Bosch smoke number) and particulate mass emissions (in grams per kilowatt-hour) as a function of load and injection timing for six-cylinder 3.7-dm^3 IDI swirl-chamber diesel engine at 1600 rev/min (no EGR).[38]

PETITIONER'S EXHIBIT 1002
US PATENT NO. 6,581,565

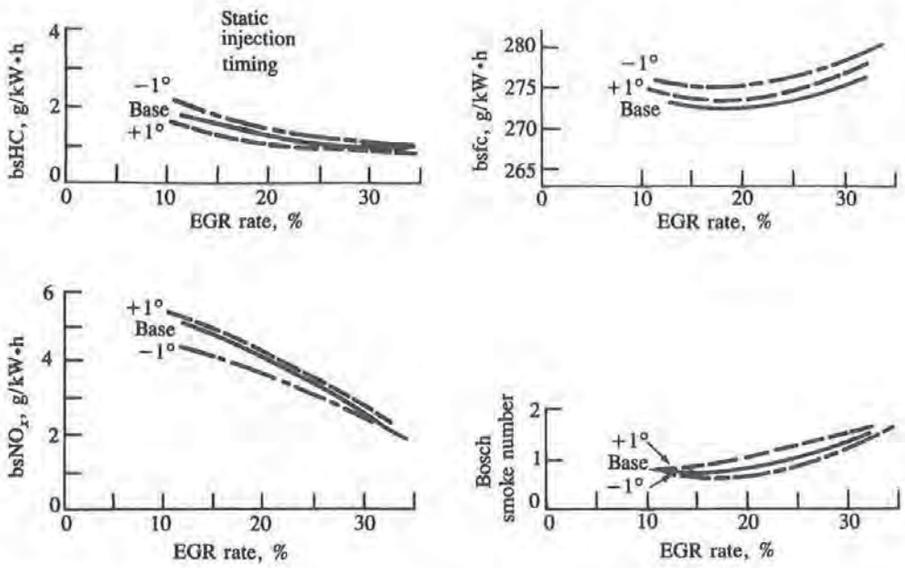


FIGURE 15-27
Brake specific HC, NO_x and fuel consumption, and smoke emissions, as a function of percent recycled exhaust for 2.4-dm^3 four-cylinder high-swirl DI diesel engine at 1250 rev/min and 255 kPa bmep.[39]

Recycled exhaust gas, at part load, can be used to reduce diesel engine NO_x emissions. Note that since diesel engines operate with the air flow unthrottled, at part load the CO_2 and H_2O concentrations in exhaust gas are low; they are essentially proportional to the fuel/air ratio. Because of this, high EGR levels are required for significant reductions in NO_x emissions. Figure 11-18 shows how NO_x concentrations decrease as a DI diesel engine inlet air flow is diluted at a constant fueling rate. The dilution is expressed in terms of oxygen concentration in the mixture after dilution. Figure 15-27 shows how the EGR affects specific NO_x and HC, fuel consumption, and smoke for a small high-swirl DI diesel engine at typical automobile engine part-load conditions. Effective reduction of bsNO_x is achieved and modest reductions in bsHC, with only a slight increase in bsfc. However, smoke increased as the EGR rate increased.[39]

15.5.2 Fuel-Injection Parameters

Fuel-injection timing essentially controls the crank angle at which combustion starts. While the state of the air into which the fuel is injected changes as injection timing is varied, and thus ignition delay will vary, these effects are predictable (see Sec. 10.6.4). The fuel-injection rate, fuel nozzle design (including number of holes), and fuel-injection pressure all affect the characteristics of the diesel fuel spray and its mixing with air in the combustion chamber.

Figure 15-28 shows the effect on performance and emissions of varying injection timing, in (*a*) a medium-swirl DI diesel engine and (*b*) an IDI engine. At fixed speed and constant fuel delivery per cycle, the DI engine shows an optimum

PETITIONER'S EXHIBIT 1002
US PATENT NO. 6,581,565

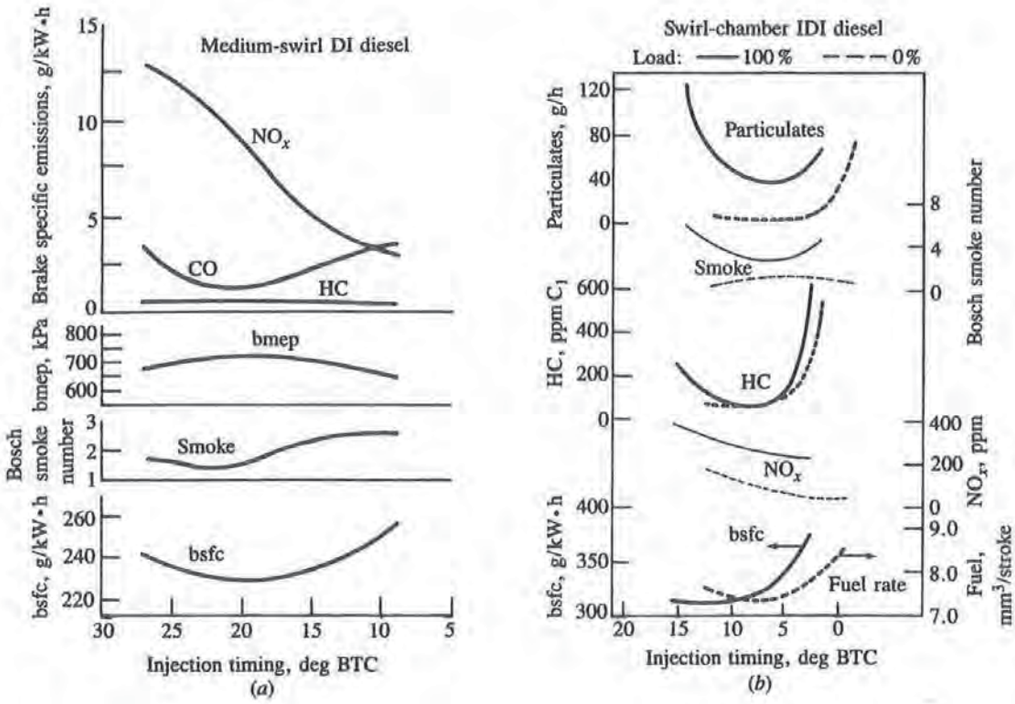


FIGURE 15-28
Effect of start-of-injection timing on diesel engine performance and emissions. (*a*) Medium-swirl DI diesel engine with deep combustion bowl and four-hole injection nozzle, 2600 rev/min, fuel delivery 75 mm^3/cycle, fuel/air equivalence ratio 0.69.[37] (*b*) Swirl-chamber IDI engine, 2500 rev/min, 0 and 100 percent load.[40]

bsfc and bmep at a specific start of injection for a given injection duration.† The IDI engine experiments are at fixed bmep; here, bsfc at full load and fueling rate at idle show a minimum at specific injection timings. Injection timing which is more advanced than this optimum results in combustion starting too early before TC; injection retarded from this optimum results in combustion starting too late.

Injection timing variations have a strong effect on NO_x emissions for DI engines: the effect is significant but less for IDI engines. Retarded injection is commonly used to help control NO_x emissions. It gives substantial reductions, initially with only modest bsfc penalty. For the DI engine, at high load, specific HC emissions are low and vary only modestly with injection timing. At lighter loads, HC emissions are higher and increase as injection becomes significantly retarded from optimum. This trend is especially pronounced at idle. For IDI diesel engines HC emissions show the same trends but are much lower in magnitude than DI engine HC emissions.[41] Figure 15-25 supports this discussion.[37]

† This optimum injection timing gives maximum brake torque, though the designation MBT timing is less commonly used with diesels than with SI engines.

PETITIONER'S EXHIBIT 1002
US PATENT NO. 6,581,565

Retarding timing generally increases smoke, though trends vary significantly between different types and designs of diesel engine. Mass particulate emissions increase as injection is retarded.

The injection rate depends on the fuel-injector nozzle area and injection pressure. Higher injection rates result in higher fuel-air mixing rates, and hence higher heat-release rates (see Sec. 10.7.3). For a given amount of fuel injected per cylinder per cycle, as the injection rate is increased the optimum injection timing moves closer to TC. The effects of injection rate and timing on bsfc in a naturally aspirated DI diesel engine are shown in Fig. 15-29. The higher heat-release rates and shorter overall combustion process that result from the increased injection rate decrease the minimum bsfc at optimum injection timing: however, a limit to these benefits is eventually reached.

Increasing the injection rate increases NO_x emissions and decreases smoke or particulate emissions. The controlling physical process is the rate of fuel-air mixing in the combustion chamber so, at constant fuel injected per cylinder per cycle, both increased injection pressure at fixed nozzle orifice area (which reduces injection duration) and reduced nozzle area at fixed injection duration produce these trends.[42]

The engine designer's goal is obviously to achieve the best bsfc possible

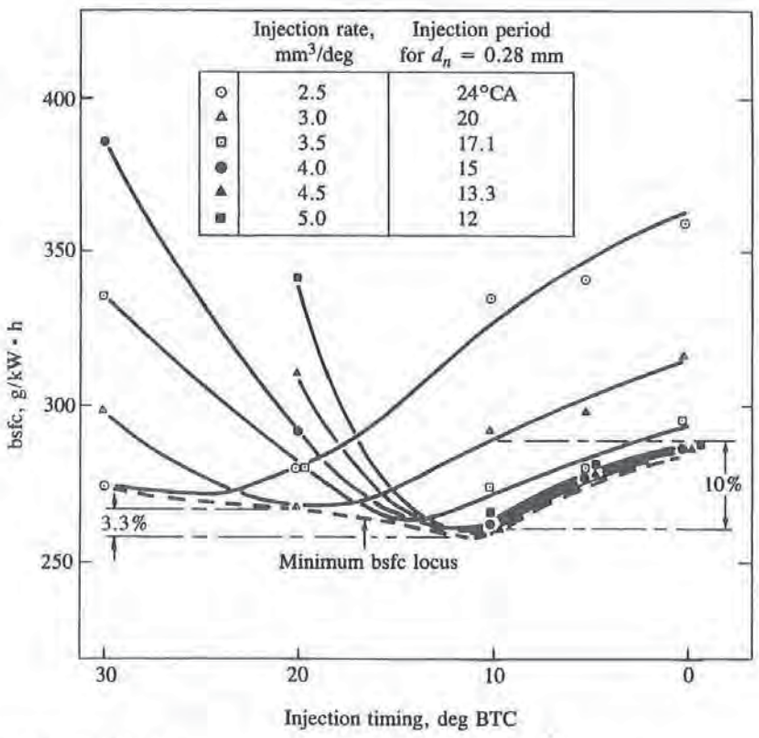


FIGURE 15-29
Effect of injection timing and injection rate on bsfc for 0.97-dm³ single-cylinder naturally aspirated DI diesel engine with swirl. 2000 rev/min, 60 mm³ per stroke fueling rate.[42]

PETITIONER'S EXHIBIT 1002
US PATENT NO. 6,581,565

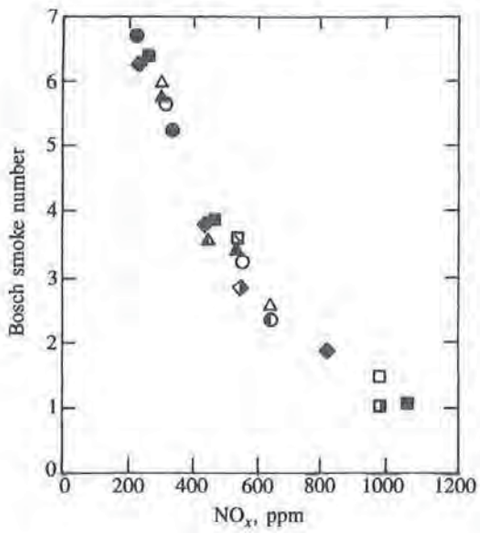


FIGURE 15-30
Tradeoff between NO_x and smoke emissions for quiescent single-cylinder DI diesel engine with bore = 140 mm, stroke = 152 mm, $r_c = 14.3$, eight-hole injector nozzle. Various speeds, fueling rates, injection timings, injection pressures, % EGR; constant $A/F = 25$.[43]

with emission levels low enough to satisfy the constraints imposed by emission standards. The variations of bsfc, NO_x, and particulate emissions described above involve tradeoffs that make achieving this goal especially difficult. One well-established tradeoff is between bsfc and $bsNO_x$. Injection retard from optimum injection timing decreases $bsNO_x$ at the expense of an increase in bsfc. A second important tradeoff is that between NO_x and particulate emissions, illustrated for a DI diesel engine in Fig. 15-30. Smoke is plotted versus NO_x for a range of speeds, loads (fuel per cycle), injection timings, injection pressures, and EGR rates. The air/fuel ratio was maintained constant at 25 ($\phi = 0.58$). The figure indicates that for a well-optimized DI diesel engine, the smoke nitric oxide tradeoff is relatively independent of engine speed, injection rate, injection timing, and amount of EGR. A given reduction in one of these pollutants through changing any one of these variables results in a given increase in the other pollutant. This tradeoff exists for essentially all types of diesel engine, though the magnitude depends on engine details.

15.5.3 Air Swirl and Bowl-in-Piston Design

Increasing amounts of air swirl within the cylinder (see Sec. 8.3) are used in direct-injection diesel engines, as engine size decreases and maximum engine speed increases, to achieve adequately fast fuel-air mixing rates (see Sec. 10.2.1). In these medium-to-small size engines, use of a bowl-in-piston combustion chamber (Fig. 10-1*b* and *c*) results in substantial swirl amplification at the end of the compression process (Sec. 8.3.3). Here, the impacts of varying air swirl on the performance and emissions characteristics of this type of DI engine are reviewed.

Since air swirl is used to increase the fuel-air mixing rate, one would expect the overall duration of the combustion process to shorten as swirl increases and emissions that depend on the local fuel/air equivalence ratio to be dependent on

PETITIONER'S EXHIBIT 1002
US PATENT NO. 6,581,565

swirl level. Figure 15-31 shows the effects of swirl and injection-timing variations on bsfc and emissions of a DI engine of 1.36 dm^3 per cylinder displacement with a toroidal bowl-in-piston chamber (see Fig. 10-3*b*). The swirl ratio [Eq. (8.28)] was varied using shrouded inlet valves with shrouds of different subtended angle (60 to 120°). The injection timing which gives minimum bsfc shifts toward TC as the swirl ratio increases due to the decreasing total combustion duration. The minimum bsfc was achieved with a swirl ratio of 6 to 7: while higher swirl levels continue to increase fuel-air mixing rates, heat transfer increases also and eventually offsets the mixing rate gain. Particulate and CO emissions decrease as swirl increases due to more rapid fuel-air mixing. NO_x emissions increase with increasing swirl. At constant injection timing, however, about half the increase is due to the effect of injection advance relative to the optimum timing and half to the shorter combustion process.[44] Similar trends have been observed as swirl is varied with the M.A.N. single-hole-nozzle diesel combustion system of Fig. 10-1*c*.

In production engines, the various types of port design shown in Fig. 8-13 can be used to generate swirl during the induction process. Of these, the helical ports are most effective at producing relatively uniform high swirl with the minimum loss in volumetric efficiency.

The geometry of the bowl-in-piston combustion chamber governs the extent to which induction-generated swirl is amplified during compression. The flow field in the bowl during fuel injection is also dependent on the interaction between this swirling flow and the squish motion which occurs as the top of the piston crown approaches the cylinder head (see Sec. 8.4). Various types of bowl-in-piston design for multihole fuel nozzle DI engines are shown in Fig. 15-32 (for the M.A.N. single-hole-nozzle system a spherical bowl is used; see Fig. 10-1*c*). More conventional designs (e.g., Fig. 15-32*a*) have the bowl sides essentially parallel to the cylinder liner. Note that it is often necessary to offset the bowl axis from the cylinder axis and the injector nozzle hole locations from the bowl axis,

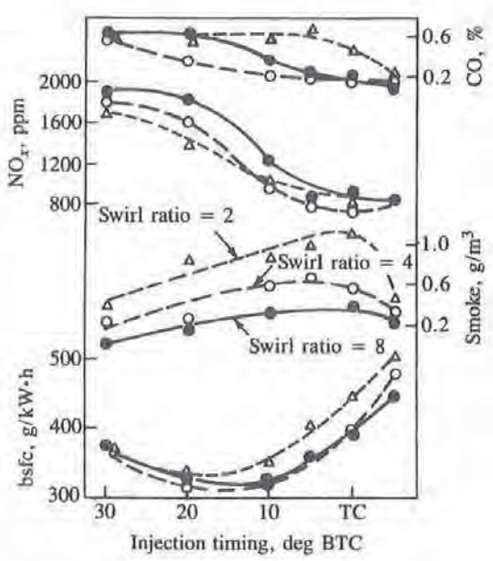


FIGURE 15-31
Effect of air swirl on bsfc and emissions of single-cylinder DI diesel engine with toroidal bowl-in-piston chamber. 1.36-dm^3 displacement, $r_c = 16$, bowl diameter/bore = 0.5, 2000 rev/min, full load. Swirl ratio measured in bowl-in-piston at injection.[44]

PETITIONER'S EXHIBIT 1002
US PATENT NO. 6,581,565

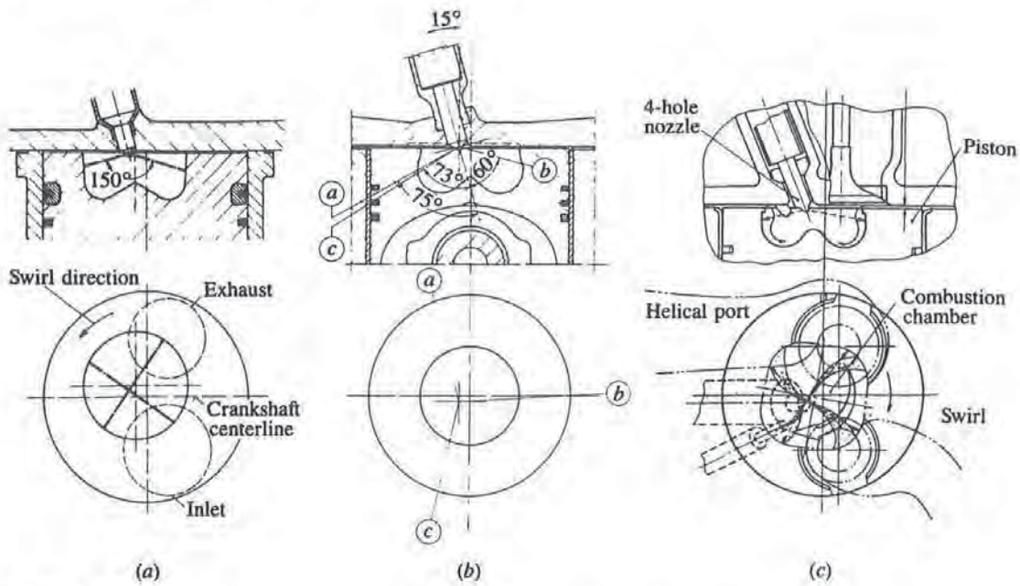


FIGURE 15-32
Various bowl-in-piston chamber designs for DI diesel engines with swirl: (*a*) conventional straight-sided bowl,[37] (*b*) reentrant bowl,[45] (*c*) square reentrant bowl.[46]

due to the geometric constraints imposed by the valves. An alternative design with a reentrant bowl (Fig. 15-32*b*) is sometimes used to promote more rapid fuel-air mixing within the bowl. The squish-swirl interaction with highly reentrant bowl designs differs markedly from the interaction in nonreentrant bowls. Figure 15-33 shows the two different flow patterns set up in a diametral plane. With a conventional bowl, the swirling air entering the bowl flows down to the base of the bowl, then inward and upward in a toroidal motion. In reentrant bowls the swirling air entering the bowl spreads downward and outward into the undercut region, and then divides into a stream rising up the bowl sides and a stream flowing along the bowl base. Reentrant chambers generally produce higher swirl at the end of compression, and maintain a high swirl level further

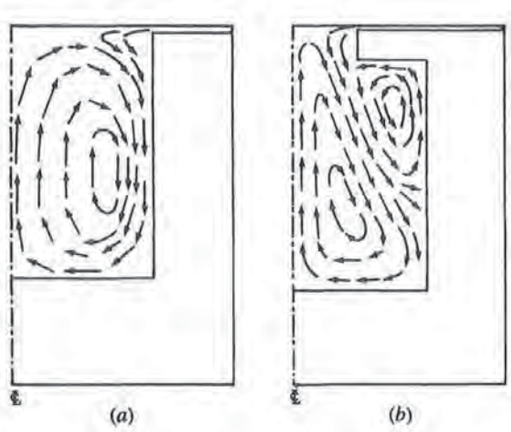


FIGURE 15-33
Flow pattern set up in diametral plane by squish-swirl interaction in (*a*) conventional and (*b*) reentrant bowl-in-piston combustion chambers. ℄ cylinder axis.[47]

PETITIONER'S EXHIBIT 1002
US PATENT NO. 6,581,565

into the expansion stroke.[47] Reentrant chambers usually achieve lower HC and smoke emissions and slightly lower bsfc, especially at retarded injection timings.

Square cavity chambers (see Fig. 15-32*c*) are also used with swirl to achieve low emissions in smaller-size DI diesel engines. The interaction between the swirl and the chamber corners produces additional turbulence which, with fuel injected into the corners as shown, achieves a more uniform mixture within the bowl.

The air flow field within bowl-in-piston combustion chambers when fuel injection occurs is highly complex. Certain generalizations hold: e.g., reducing the bowl diameter at a constant compression ratio increases the swirl levels in the bowl at TC [see Eq. (8.35) and the accompanying text] which decreases smoke and increases NO_x and HC emissions.[37] However, the squish-swirl interaction is difficult to unravel, especially with the off-center bowls often required due to the constraints on injector location caused by the valves. Figure 14-33 gives an example of such a flow. It shows velocity vectors and turbulence intensities in two orthogonal bowl-diametral planes within an off-center reentrant bowl as TC is approached in a small high-swirl DI engine. The off-center bowl location coupled with the swirl-squish interaction cause substantial asymmetry in the flow within the bowl.

15.6 SUPERCHARGED AND TURBOCHARGED ENGINE PERFORMANCE

The equations for power, torque, and mep in Sec. 2.14 show that these engine performance parameters are proportional to the mass of air inducted per cycle. This depends primarily on inlet air density. Thus the performance of an engine of given displacement can be increased by compressing the inlet air prior to entry to the cylinder. Methods for achieving higher inlet air density in the gas exchange processes—mechanical supercharging, turbocharging, and pressure-wave supercharging—are discussed in Sec. 6.8. The arrangements of the various practical supercharging and turbocharging configurations are shown in Fig. 6-37. Figures 1-11, 6-40, 6-43, 6-49, 6-53, and 6-58 show examples of the different devices used to achieve higher inlet air densities. In this section the effects of boosting air density on engine performance are examined. Spark-ignition and compression-ignition engines are dealt with separately. Power boosting via supercharging and/or turbocharging is common in diesel engines: few spark-ignition engines are turbocharged. Knock prevents the full potential of boosting from being realized in the latter type of engine. A more extensive discussion of turbocharged engine operation is provided by Watson and Janota.[48]

15.6.1 Four-Stroke Cycle SI Engines

The bmep of most production spark-ignition engines at wide-open throttle is knock-limited over part of the engine speed range (see Sec. 15.4.4). The compression ratio is usually set at a sufficiently high value so that some spark retard from

PETITIONER'S EXHIBIT 1002
US PATENT NO. 6,581,565

MBT timing is needed to avoid knock for the expected range of available fuel octane rating and sensitivity (see Fig. 15-17). The propensity of the end-gas to knock is increased by increases in end-gas temperature and pressure (see Sec. 9.6.2). Hence attempts to boost the output of a given size spark-ignition engine by an inlet air compression device that increases air pressure and temperature will aggravate the knock problem, since end-gas pressure and temperature will increase. However, the potential advantages of power boosting are significant. The higher output for a given displaced volume will decrease engine specific weight and volume (Sec. 2.11). Also, if the power requirements in a specific application (such as an automobile) can be met with either a naturally aspirated SI engine of a certain size or with a *smaller* size engine which is turbocharged to the same maximum power, the smaller turbocharged engine should offer better fuel economy at part load. At a given part-load torque requirement, the mechanical efficiency of the smaller turbocharged engine is higher, and if the gross indicated efficiencies of the engines are the same, the smaller engine will show a brake efficiency benefit. In practice, it proves difficult to realize much of this potential efficiency gain for the reasons described below.

While a naturally aspirated spark-ignition engine may have sufficient margin of safety relative to knock to allow modest inlet-air boost, any substantial air compression prior to cylinder entry will require changes in engine design and/or operating variables to offset the negative impact on knock. The variables which are adjusted to control knock in turbocharged SI engines are: compression ratio, spark retard from optimum, charge air temperature, and fuel/air equivalence ratio.† Figure 15-34 shows how the knock limits depend on charge pressure, temperature, fuel/air equivalence ratio and compression ratio for given octane rating fuels. The difference in boost achievable with the premium and the regular quality gasoline is significant, as expected (Sec. 9.6.3). Charge-air temperature has a strong influence on allowable boost levels: lowering the compressed air temperature prior to entry to the cylinder with a charge-air cooler allows a substantially higher compression ratio to be used at a given boost level, with a corresponding impact on engine efficiency.‡ The boost pressure benefits of the richer mixtures in Fig. 15-34*a* ($\phi = 1.1$ compared with 0.9) are largely due to the cooling effect of the additional fuel on the air charge. For example, Fig. 15-34*b* shows that, with a rich mixture and charge cooling to 60°C, a charge pressure of 1.5 atm can be utilized at optimum spark timing with a compression ratio of 8. Without charge cooling, the same charge pressure can only be used with a compression ratio of 6.[49]

In turbocharged SI engines, the knock limit is usually reached at spark timings retarded from the MBT optimum. Figure 15-35 shows the brake mean

† Valve timing changes are often made too. These are done primarily to improve low-speed torque where turbocharging has a limited impact.

‡ The turbocharged engine in Fig. 1-10 has an intercooler to reduce the inlet charge temperature.

PETITIONER'S EXHIBIT 1002
US PATENT NO. 6,581,565

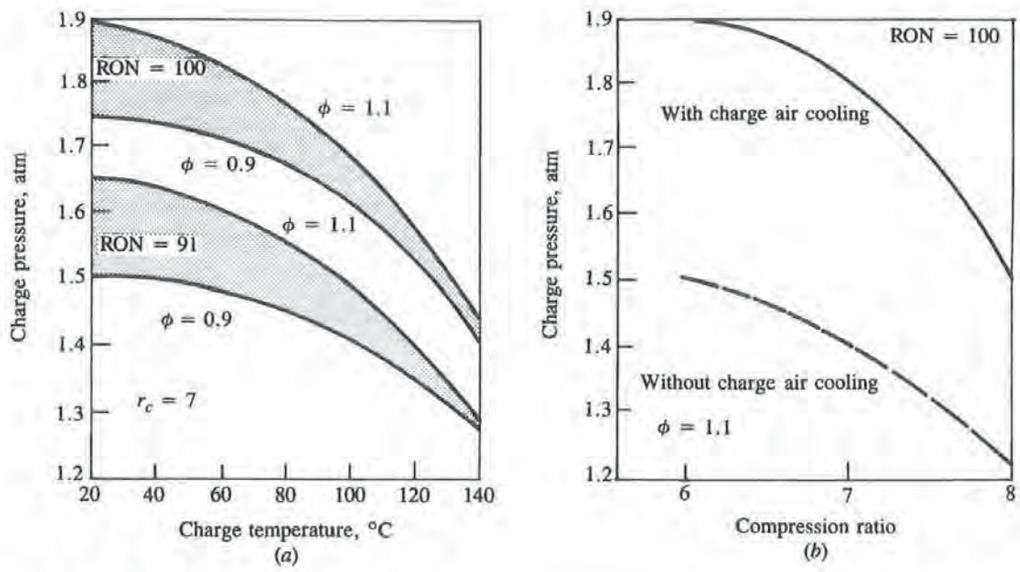


FIGURE 15-34
Dependence of SI engine knock limits on: (*a*) charge pressure, temperature, and equivalence ratio ϕ, with $r_c = 7$, 2500 rev/min, MBT timing, 91 and 100 research octane number fuel; (*b*) charge pressure and compression ratio, without and with (to 60°C) charge air cooling, 2500 rev/min, MBT timing, $\phi = 1.1$, 100 RON fuel.[49]

effective pressure achievable at a fixed compression ratio as a function of charge pressure and ignition timing with and without charge-air cooling. Additional retard allows higher boost pressures to be utilized; however, at a constant safety margin from the knock limit, the resulting gains in bmep decrease as retard is increased. To avoid an unnecessary fuel consumption penalty, retarded timing should only be used when the turbocharger does develop a high boost pressure.

The above discussion illustrates why turbocharged spark-ignition engines normally have lower compression ratios than naturally aspirated engines, use substantial mixture enrichment (up to $\phi \approx 1.3$) at high boost to cool the charge, often use an intercooler to reduce the charge-air temperature, and operate with

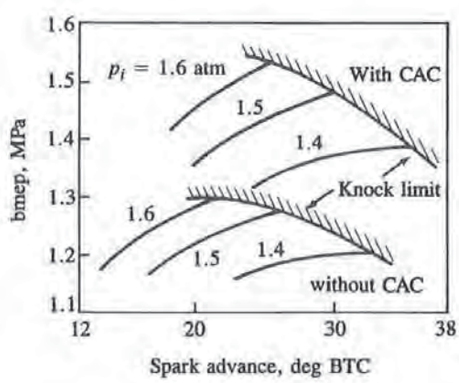


FIGURE 15-35
Brake mean effective pressure and knock limits for turbocharged SI engines as a function of spark advance and inlet pressure p_i (in atmospheres). 2500 rev/min, $r_c = 7$, $\phi = 1.1$, 99 RON fuel, without and with ($\Delta T = 45$°C) charge-air cooling.[49]

PETITIONER'S EXHIBIT 1002
US PATENT NO. 6,581,565

retarded timing at high boost pressures. Since compression ratio reductions and retarded ignition timings result in losses in efficiency, and unintended knock with high boost pressures would be especially damaging, precise control of ignition timing is critical. Most turbocharged SI engines now use a knock sensor and ignition-timing control system so that timing can be adjusted continuously to avoid knock without unnecessary retard. The sensor is usually an accelerometer which senses above-normal vibration levels on the cylinder head at the characteristic knock frequency. With a knock sensor, ignition timing can be automatically adjusted in response to changes in fuel octane rating and sensitivity, and ambient conditions.

Turbocharged SI engines where fuel is mixed with the air upstream or downstream of the compressor, using carburetors or fuel-injection systems, have been developed and used. Most modern turbocharged engines use port fuel injection. This provides easier electronic control of fuel flow, avoids filling most of the pressurized manifold volume with fuel-air mixture, and improves the dynamic response of the system by reducing fuel transport delays.

We now consider the performance of actual turbocharged spark-ignition engines. Examples of compressor outlet or boost pressure schedules as a function of speed at wide-open throttle for three turbocharged engines are shown in Fig. 15-36. The essential features of the curves are the same. Below about 1000 engine rev/min the turbocharger achieves negligible boost. Boost pressure then rises with increasing speed to 1.4 to 1.8 atm (absolute pressure) at about 2000 rev/min. Boost pressure then remains essentially constant with increasing engine speed. The rising portion of the curve is largely governed by the relative size of the turbine selected for a given engine. This is usually expressed in terms of the A/R ratio of the turbine—the ratio of the turbine's inlet casing or volute area A to the radius of the centroid of that area. Lower A/R values (smaller-capacity turbines) give a more rapid boost pressure rise with increasing speed; however, they give higher boost pressures at high engine speed, which is undesirable.[48, 50]

Avoidance of knock is the reason why boost must be limited at medium to

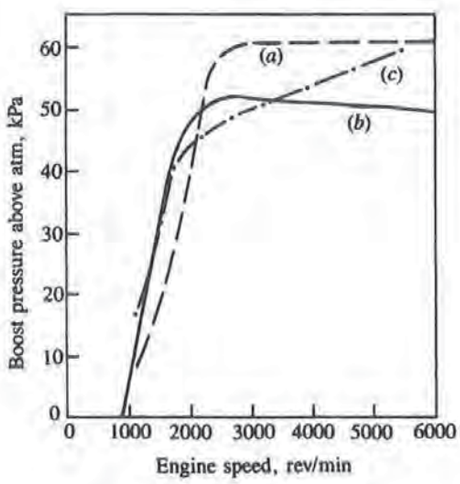


FIGURE 15-36
Boost pressure schedules for three turbocharged spark-ignition engines: (*a*) 3.8-dm^3 V-6 engine, 86.4 mm stroke, $r_c = 8$;[50] (*b*) 2.2-dm^3 four-cylinder engine, 92 mm stroke, $r_c = 8.1$;[51] (*c*) 2.32-dm^3 four-cylinder engine, 80 mm stroke, $r_c = 8.7$.[52] All schedules are wastegate controlled.

PETITIONER'S EXHIBIT 1002
US PATENT NO. 6,581,565

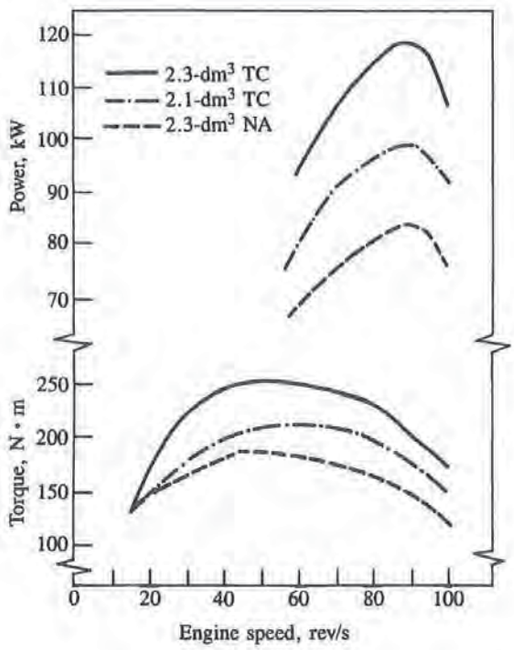


FIGURE 15-37
Power and torque as a function of engine speed for two turbocharged and one naturally aspirated four-cylinder spark-ignition engine. See Table 15.3.[52]

high engine speed; the details of this problem have already been discussed above. Even with the use of very rich mixtures and spark retard at WOT, lower compression ratios for turbocharged engines, and intercooling, knock avoidance requires that boost pressures (which would continue to rise with increasing engine speed in the absence of any control) be maintained approximately constant. This is normally achieved by reducing the exhaust flow through the turbine as speed increases by bypassing a substantial fraction of the exhaust around the turbine through the *wastegate* or flow control valve (see Sec. 6.8.4). A wastegate is a spring-loaded valve acting in response to the inlet manifold pressure on a controlling diaphragm. Although other methods of controlling boost can be used,[48] the wastegate is the most common. About 30 to 40 percent of the exhaust bypasses the turbine at maximum engine speed and load.

Figure 15-37 compares the performance of two turbocharged spark-ignition engines (four-cylinder, 2.1- and 2.3-dm³ displacement) with that of the base 2.3-dm³ engine in its naturally aspirated form. Table 15.3 gives details of these

TABLE 15.3
Turbocharged spark-ignition engine performance[52]

Type	2.1-dm³ TC	2.3-dm³ NA	2.3-dm³ TC/AC
Displacement, dm³	2.127	2.316	2.316
Bore × stroke, mm	92 × 80	96 × 80	96 × 80
Compression ratio	7.5	9.5	8.7
Maximum power, kW at rev/min	98 at 5400	83 at 5400	117 at 5300
Maximum torque, N · m at rev/min	210 at 3800	184 at 2800	250 at 2900
Maximum bmep, kPa	1241	998	1356

PETITIONER'S EXHIBIT 1002
US PATENT NO. 6,581,565

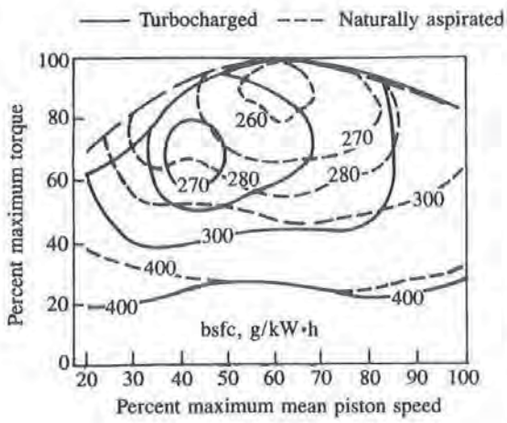


FIGURE 15-38
Comparison of bsfc contours (in grams per kilowatt-hour) on performance maps of turbocharged and naturally aspirated versions of the same spark-ignition engine, scaled to the same maximum torque and mean piston speed.[53]

three engines. The 2.1-dm^3 turbocharged but *not* intercooled engine (which also does not have a knock sensor to control spark advance) requires a lower compression ratio and achieves less of a bmep gain than the 2.3-dm^3 turbocharged intercooled engine with its knock-sensor spark-advance control, which together permit use of a higher compression ratio. Turbocharging the naturally aspirated 2.3-dm^3 engine, with the modifications indicated, results in a 36 percent increase in maximum engine torque and a flatter torque-versus-speed profile.

The brake specific fuel consumption contours of an engine produced in both naturally aspirated and turbocharged versions are shown in Fig. 15-38. The data have been scaled to represent engines of different displaced volume but the same maximum engine torque. The smaller-displacement low-compression-ratio turbocharged engine ($r_c = 6.9$) shows a reduction in bsfc at low speed and part load due to improved mechanical efficiency. At high speed and load the larger-displacement naturally aspirated engine has an advantage in bsfc due to its higher compression ratio (8.2), less enrichment, and more optimum timing.[53] In a vehicle context, the low-speed part-load advantage of the smaller size but equal power turbocharged engine should result in an average fuel economy benefit relative to the larger naturally aspirated engine. This benefit has been estimated as a function of load. At full load the average efficiencies should be comparable; at half load, the turbocharged engine should show a benefit of about 10 percent, the benefit increasing as load is decreased.[49]

15.6.2 Four-Stroke Cycle CI Engines

The factors that limit turbocharged diesel engine performance are completely different to those that limit turbocharged spark-ignition engines. The output of naturally aspirated diesel engines is limited by the maximum tolerable smoke emission levels, which occur at overall equivalence ratio values of about 0.7 to 0.8. Turbocharged diesel engine output is usually constrained by stress levels in critical mechanical components. These maximum stress levels limit the maximum cylinder pressure which can be tolerated under continuous operation, though the

PETITIONER'S EXHIBIT 1002
US PATENT NO. 6,581,565

thermal loading of critical components can become limiting too. As boost pressure is raised, unless engine design and operating conditions are changed, maximum pressures and thermal loadings will increase almost in proportion. In practice, the compression ratio is often reduced and the maximum fuel/air equivalence ratio must be reduced in turbocharged engines (relative to naturally aspirated engines) to maintain peak pressures and thermal loadings at acceptable levels. The fuel flow rate increases at a much lower rate than the air flow rate as boost pressure is increased. Limitations on turbocharged engine performance are discussed more fully by Watson and Janota.[48]

Small automotive indirect-injection (IDI) turbocharged engines are limited by structural and thermal considerations to about 130 atm maximum swirl- or pre-chamber pressure, 14 m/s maximum mean piston speed, and 860°C maximum exhaust temperature.[54] Smoke and NO_x emission standards are additional constraints. Figure 15-39 shows the full-load engine and turbocharger performance characteristics of a six-cylinder 2.38-dm^3 displacement Comet V swirl-chamber automobile diesel engine. The maximum boost pressure is controlled by a poppet-valve-type wastegate to 0.75 bar above atmospheric. The fuel consumption map for this engine is shown in Fig. 15-40. Superimposed on the turbocharged engine map is the map for the base naturally aspirated swirl-chamber IDI engine of the same geometry and compression ratio ($r_c = 23$). The turbocharged engine has a maximum torque 46 percent higher and a maximum power 33 percent higher than the naturally aspirated engine. The best bsfc values are closely comparable.

The different methods of supercharging internal combustion engines were reviewed in Sec. 6.8. Turbocharging, mechanical supercharging with a Roots blower, and pressure wave supercharging with the Comprex are alternative methods of boosting the performance of a small automotive swirl-chamber IDI

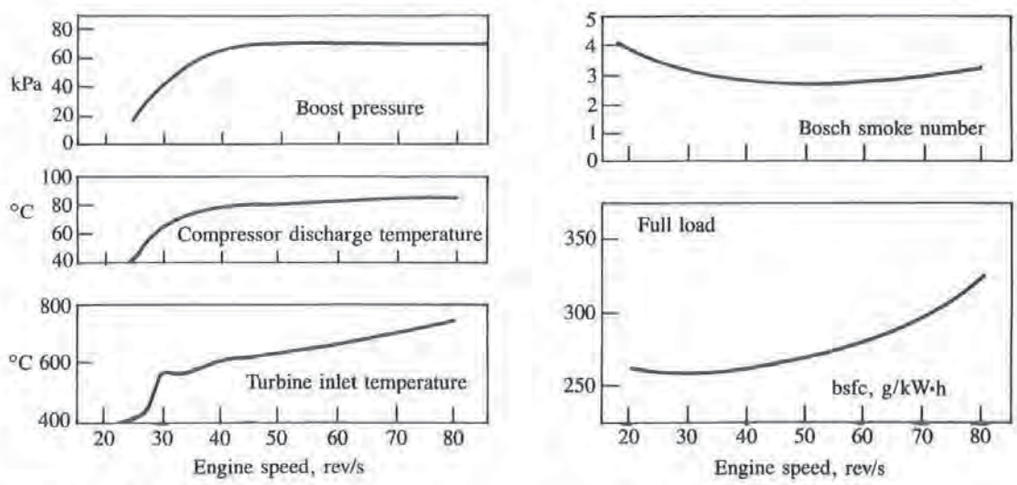


FIGURE 15-39
Engine and turbocharger characteristics of six-cylinder 2.38-dm^3 swirl-chamber IDI automotive diesel engine at full load.[54]

PETITIONER'S EXHIBIT 1002
US PATENT NO. 6,581,565

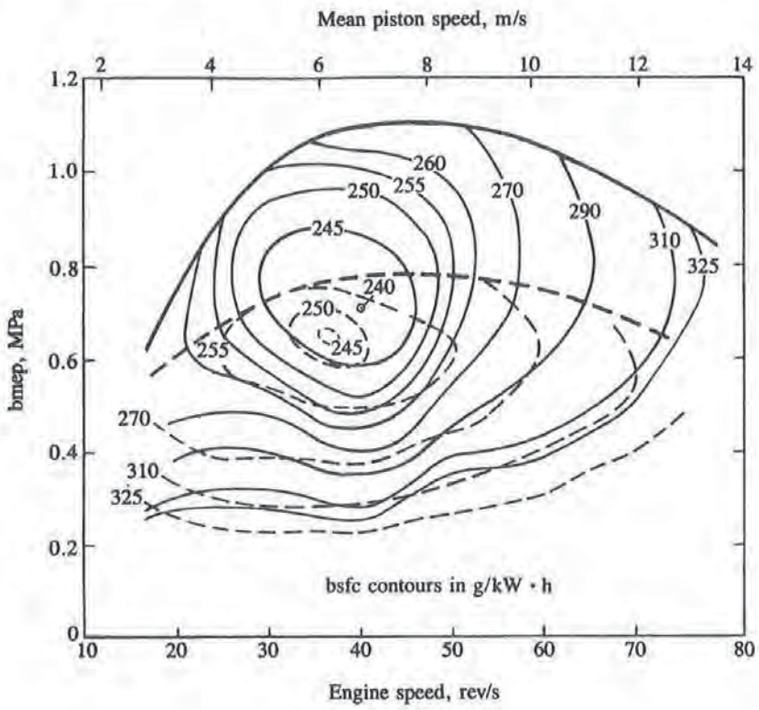


FIGURE 15-40
Fuel consumption map (bsfc in grams per kilowatt-hour) for turbocharged (——) and naturally aspirated (- - -) versions of 2.38-dm^3 six-cylinder swirl-chamber IDI diesel engine.[54]

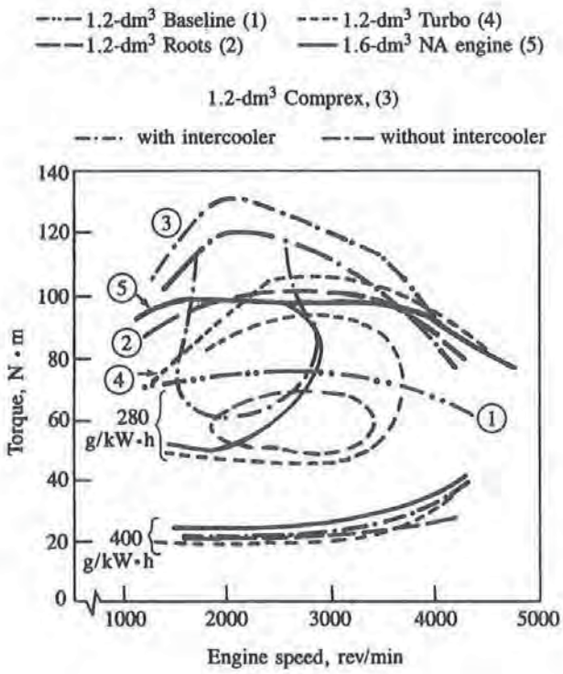


FIGURE 15-41
Torque and brake specific fuel consumption of naturally aspirated and supercharged 1.2-dm^3 swirl-chamber IDI diesel engine. Baseline (1): naturally aspirated. Supercharged with (2) Roots blower; (3) Comprex (with and without intercooler); (4) turbocharger. Larger displacement 1.6-dm^3 naturally aspirated engine (5).[55]

PETITIONER'S EXHIBIT 1002
US PATENT NO. 6,581,565

diesel engine. Figure 15-41 compares the torque and bsfc values obtained with each of these supercharging methods on a performance map for a 1.2-dm^3 engine. Values for a 1.6-dm^3 naturally aspirated IDI diesel engine are also shown. All three approaches achieve close to the desired maximum power of the 1.6-dm^3 NA engine (40 kW at 4800 rev/min): e.g., 1.2-dm^3 turbo, 41.2 kW at 4500 rev/min; 1.2-dm^3 Comprex with intercooler, 42.3 kW at 3500 rev/min; 1.2-dm^3 Roots, 37.6 kW at 4000 rev/min. The Comprex system produces the highest torque at low engine speeds, even under unsteady engine operating conditions. The density of the charge air determines the amount of charge, and hence the torque. Charge-air pressure and temperature for the three supercharging systems are shown in Fig. 15-42. The Comprex (here without an intercooler) must have the highest charge pressure because it has the highest charge temperature. Intercooling would be particularly effective in this case.[55]

Small high-speed high-swirl turbocharged direct-injection diesel engines (e.g., suitable for automobile or light-truck applications) have similar performance maps to those of equivalent IDI engines (Figs. 15-39 and 15-40). Maximum bmep values are closely comparable: usually slightly higher boost is required to offset the lower volumetric efficiency of the high-swirl-generating port and valve of the DI engine. Best bsfc values for the DI engine are usually about 15 percent lower than of comparable IDI engines (see Ref. 56).

The operating characteristics of larger medium-swirl turbocharged DI diesel engines are illustrated by the data shown in Fig. 15-43. The engine is a 12-dm^3 displacement six-cylinder heavy-duty truck engine. The combustion chamber is similar to that shown in Fig. 15-32*c*, with a square combustion cavity and relatively low levels of swirl. The swirl is generated by a helical port in one of the two intake ports and a tangential port in the other in the four-valve cylinder head. Both the engine's operating map and the turbocharger compressor map with the boost pressure curve superposed are shown for two different compressor impellors. The adoption of the backward-vaned rake-type impellor compared to a more conventional design significantly increases low- and medium-speed per-

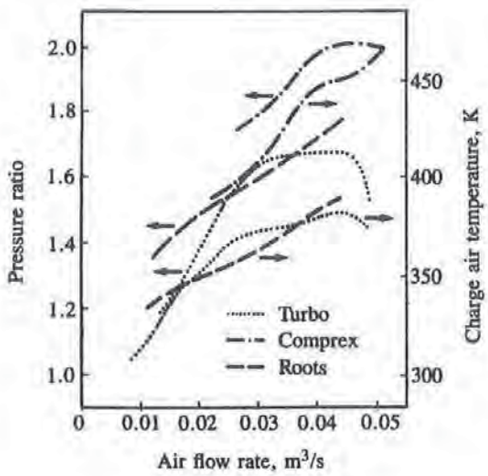


FIGURE 15-42
Charge pressure and temperature with the IDI diesel engine and different supercharging methods of Fig. 15-41.[55]

PETITIONER'S EXHIBIT 1002
US PATENT NO. 6,581,565

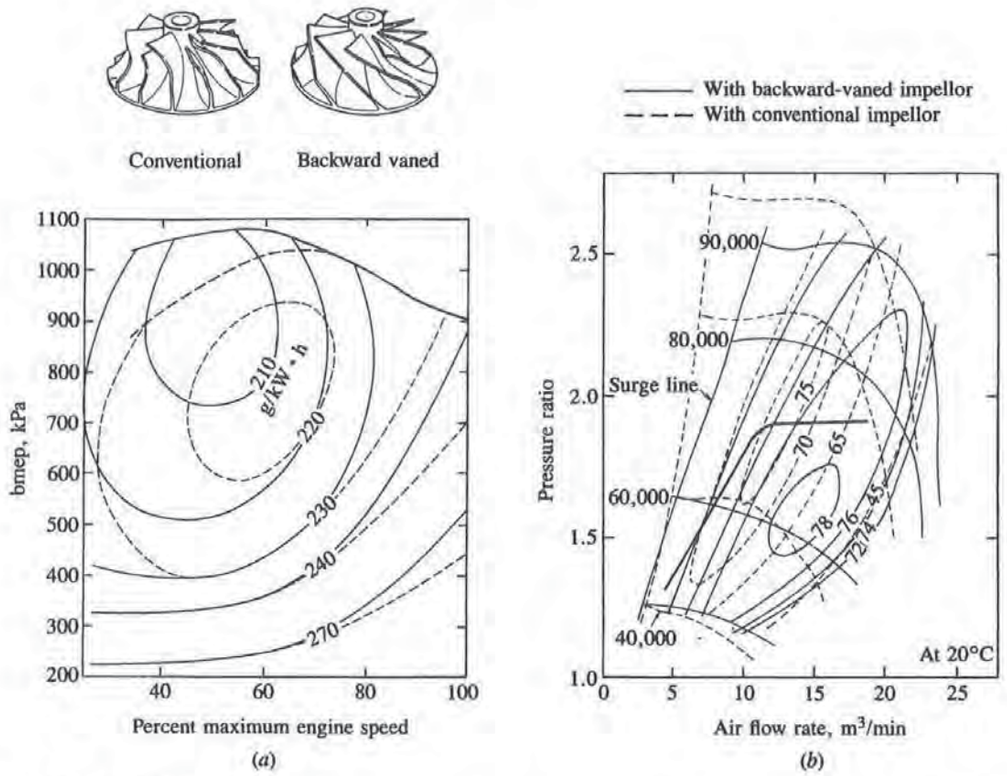


FIGURE 15-43
Performance characteristics of turbocharged 12-dm^3 six-cylinder medium-swirl heavy-duty truck DI diesel engine, with two different compressor impellors: (*a*) fuel consumption maps; (*b*) compressor maps with full-load boost operating line for engine with backward-vaned impellor superposed. Bore = 135 mm, stroke = 140 mm, $r_c = 16$.[57]

formance by improving the compressor efficiency over the engine's boost pressure curve (Fig. 15-43*b*). A wastegate is then used to control the boost level at high engine speeds. The improvement in low-speed engine torque is apparent in Fig. 15-43*a*. The dependence of the maximum torque curve on both engine and turbocharger design details is clear. With boost pressure ratios limited to below 2, in the absence of air-charge cooling, maximum bmep values of 1.1 MPa are typical of this size and type of diesel engine.

With structurally more rugged component designs, aftercooled turbocharged medium-speed diesel engines with swirl in this cylinder size range can utilize higher boost and generate much higher bmep. Wastegate control of boost is no longer required. Figure 15-44 shows the performance characteristics of a V-8 cylinder engine with its compressor map and full-load boost characteristic. This turbocharged intercooled engine achieves a maximum bmep of about 1.5 MPa and bsfc below 200 g/kW · h between the maximum torque speed and rated power. Boost pressure at full load increases continuously over the engine speed range.[58]

PETITIONER'S EXHIBIT 1002
US PATENT NO. 6,581,565

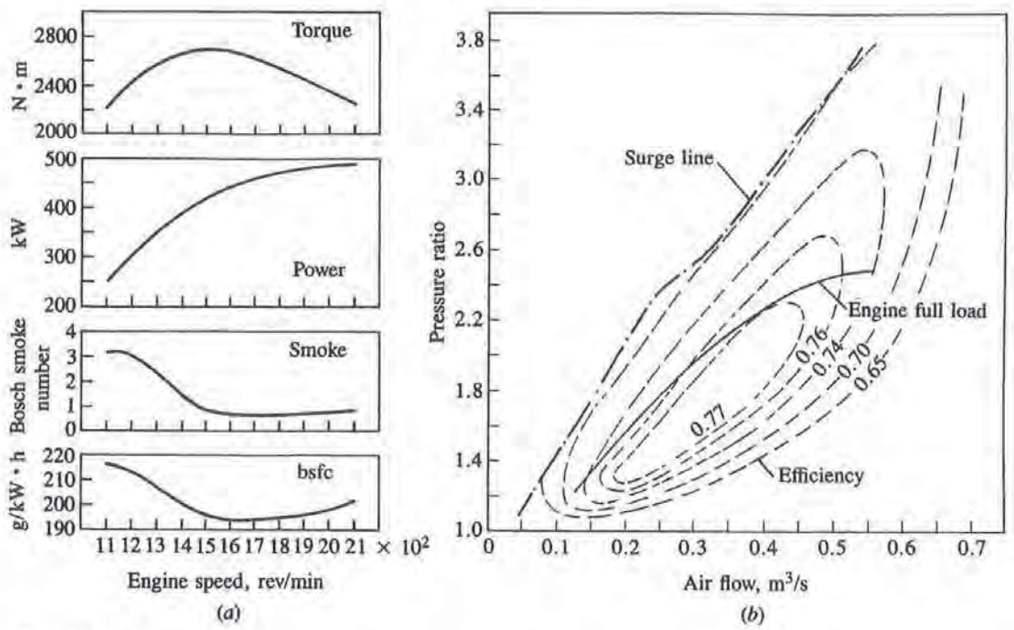


FIGURE 15-44
Performance characteristics of medium-speed turbocharged aftercooled DI diesel engine. (*a*) Torque, power, smoke number, and bsfc for V twelve-cylinder version. (*b*) Compressor characteristics and engine full-load line for V-8 cylinder version. Bore = 128 mm, stroke = 140 mm, $r_c = 15$.[58]

Examples of values of combustion-related parameters for this type of engine over the load range at its maximum rated speed are shown in Fig. 15-45 for a 14.6-dm^3 six-cylinder turbocharged aftercooled DI diesel engine with a boost pressure ratio of 2 at rated power. The ignition delay decreases to about 10° (0.9 ms at 1800 rev/min) as load is increased. The bmep at 100 percent rated load at this speed is 1.2 MPa. Exhaust temperature increases substantially with increasing load: maximum cylinder pressure increases to about 10 MPa at the rated load. In this particular study it was found that these operating parameters were relatively insensitive to fuel variations. The cross-hatched bands show data for an additional nine fuels of varying sulfur content, aromatic content, 10 and 90 percent distillation temperatures.[59]

Higher outputs can be obtained with two-stage turbocharged aftercooled diesel engines, the arrangement shown in Fig. 6-37*d*. The performance characteristics of such a high bmep (1.74 MPa) six-cylinder engine of 14-dm^3 displacement are shown in Fig. 15-46. The high air flow requires an overall pressure ratio of 3 at sea level ambient conditions (rising to 4 at 3658 m altitude). This was obtained at lower cost with two turbochargers in series than with a multistage single turbocharger. At rated conditions, the maximum cylinder pressure is 12.7 MPa and the maximum mean piston speed is 10.6 m/s.

Additional gains in efficiency with these heavy-duty automotive diesel engines can be achieved with turbocompounding: some of the available energy in the exhaust gases is captured in a turbine which is geared directly to the engine

PETITIONER'S EXHIBIT 1002
US PATENT NO. 6,581,565

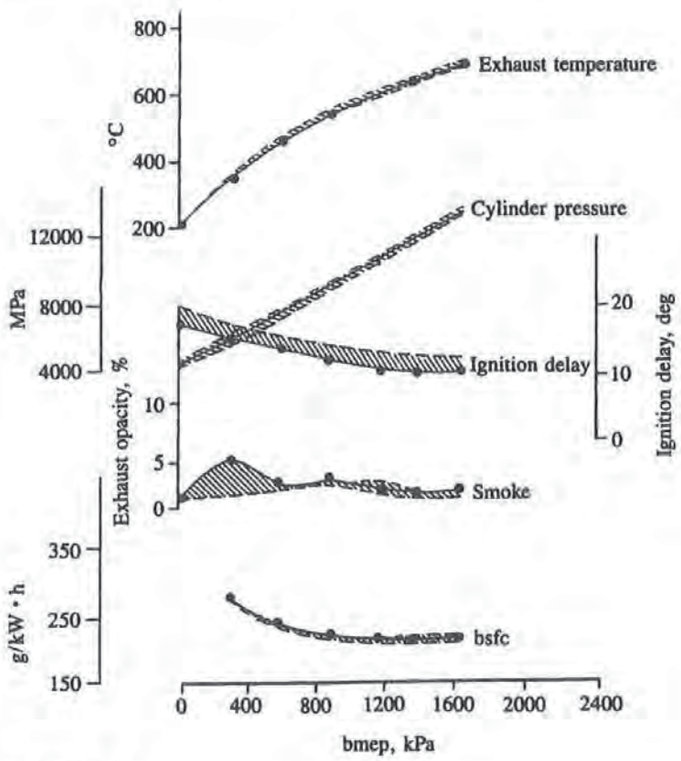


FIGURE 15-45
Operating parameters of 14.6-dm³ six-cylinder turbocharged aftercooled DI diesel engine as a function of load at maximum rated speed of 1800 rev/min. Maximum rated power = 261 kW at bmep = 1192 kPa. Points: standard diesel fuel. Shaded band: nine fuels of varying sulfur content, aromatic content, 10 and 90 per cent distillation temperatures.[59]

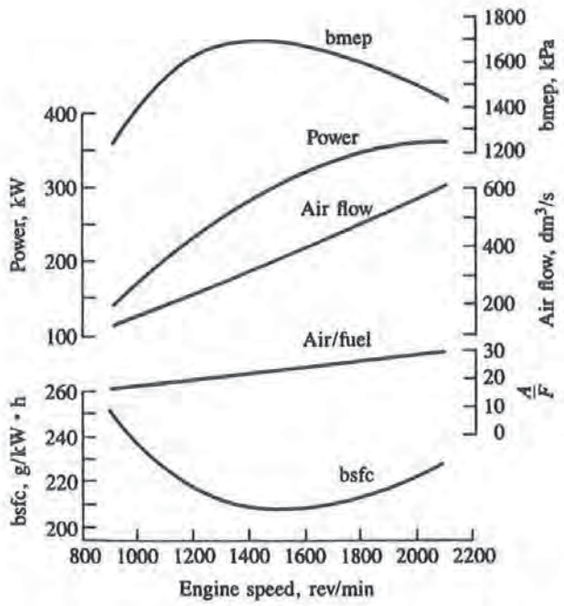


FIGURE 15-46
Operating characteristics of 14-dm³ six-cylinder two-stage turbocharged aftercooled quiescent-chamber DI diesel engine. Maximum bmep = 1.74 MPa. Boost pressure ratio at rated power = 3. Bore = 140 mm, stroke = 152 mm.[60]

PETITIONER'S EXHIBIT 1002
US PATENT NO. 6,581,565

drive shaft. The above discussion indicates that typical turbocharged DI diesel engines achieve bsfc levels of 210 to 220 g/kW · h (brake fuel conversion efficiencies of 0.4 to 0.38). With the increased cylinder pressure capability, higher fuel-injection pressures, and lower-temperature aftercooling of the above higher bmep engines, bsfc values of 200 g/kW · h (0.42 brake efficiency) or lower can be achieved. With turbocompounding, bsfc values can be reduced another 5 to 6 percent to about 180 g/kW · h, or a brake efficiency of 0.47, at rated power.[61]

The largest four-stroke cycle DI diesel engines are used for marine propulsion. An example is the Sulzer 400 mm bore 480 mm stroke engine which produces 640 kW per cylinder at 580 rev/min ($\bar{S}_p = 9.3$ m/s). Very high bmep levels (2.19 MPa) are achieved at maximum continuous rated power through progress in turbocharger design and engine improvements which allow higher maximum cylinder pressures. These, combined with optimization of gas exchange and combustion processes, achieve bsfc values of 185 to 190 g/kW · h (45 to 46 percent brake efficiency).[62]

Many diesel system concepts are being examined which promise even higher output and/or efficiency. Variable-geometry turbocharger-turbine nozzles improve utilization of exhaust gas available energy at low engine speeds. The hyperbar turbocharging system—essentially a combination of a diesel engine with a free-running gas turbine (a combustion chamber is placed between the engine and the turbocharger turbine)—has the potential of much higher bmep. Diesel systems with thermally insulated combustion chambers which reduce heat losses and increase the available exhaust energy have the potential for improving efficiency and for increasing power through additional exhaust energy recovery in devices such as compounded turbines and exhaust-heated Rankine cycle systems.[48]

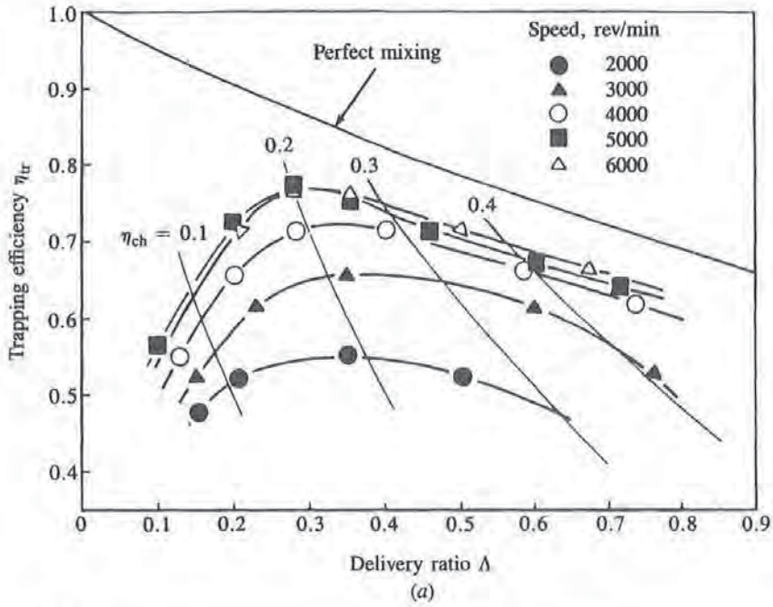
15.6.3 Two-Stroke Cycle SI Engines

The two-stroke cycle spark-ignition engine in its standard form employs sealed crankcase induction and compression of the fresh charge prior to charge transfer, with compression and spark ignition in the engine cylinder after charge transfer. The fresh mixture must be compressed to above exhaust system pressures, prior to entry to the cylinder, to achieve effective scavenging of the burned gases. Two-stroke cycle scavenging processes were discussed in Sec. 6.6. The two-stroke spark-ignition engine is an especially simple and light engine concept and finds its greatest use as a portable power source or on motorcycles where these advantages are important. Its inherent weakness is that the fresh fuel-air mixture which short-circuits the cylinder directly to the exhaust system during the scavenging process constitutes a significant fuel consumption penalty, and results in excessive unburned hydrocarbon emissions.

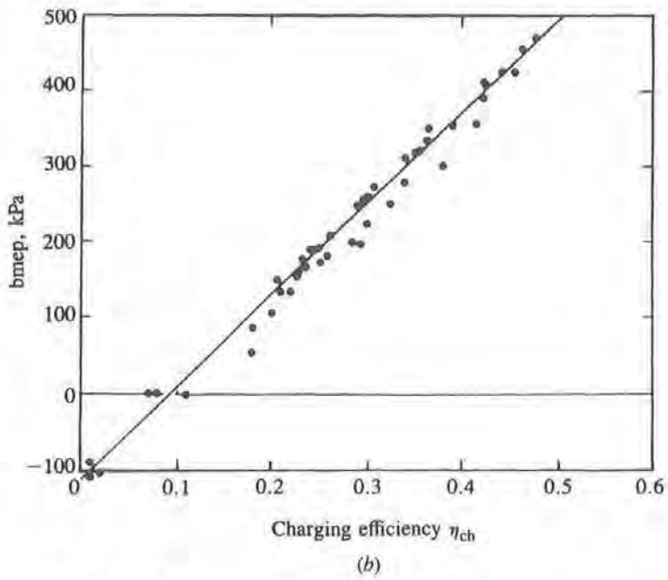
This section briefly discusses the performance characteristics of small crankcase compression two-stroke cycle SI engines. The performance characteristics (power and torque) of these engines depend on the extent to which the displaced volume is filled with fresh mixture, i.e., the charging efficiency [Eq. (6.24)]. The

PETITIONER'S EXHIBIT 1002
US PATENT NO. 6,581,565

fuel consumption will depend on both the trapping efficiency [Eq. (6.21)] and the charging efficiency. Figure 15-47*a* shows how the trapping efficiency η_{tr} varies with increasing delivery ratio Λ at several engine speeds for a two-cylinder 347-cm^3 displacement motorcycle crankcase compression engine. The delivery ratio increases from about 0.1 at idle conditions to 0.7 to 0.8 at wide-open throt-



(*a*)



(*b*)

FIGURE 15-47
(*a*) Trapping and charging efficiencies as a function of the delivery ratio. (*b*) Dependence of brake mean effective pressure on fresh-charge mass defined by charging efficiency. Two-cylinder 347-cm^3 displacement two-stroke cycle spark-ignition engine.[63]

PETITIONER'S EXHIBIT 1002
US PATENT NO. 6,581,565

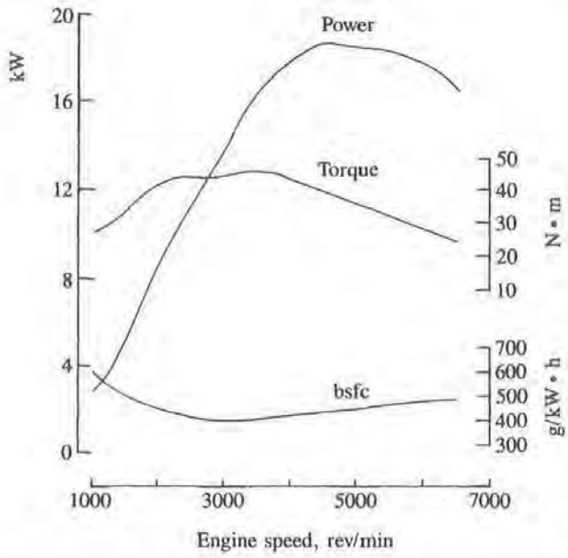


FIGURE 15-48
Performance characteristics of a three-cylinder 450-cm^3 two-stroke cycle spark-ignition engine. Maximum bmep = 640 kPa. Bore = 58 mm, stroke = 56 mm.[64]

tle. Lines of constant charging efficiency η_{ch} [which equals $\Lambda\eta_{tr}$; see Eq. (6.25)] are shown. Figure 15-47*b* shows bmep plotted against these charging efficiency values and the linear dependence on fresh charge mass retained is clear.

Performance curves for a three-cylinder 450-cm^3 two-stroke cycle minicar engine are shown in Fig. 15-48. Maximum bmep is 640 kPa at about 4000 rev/min. Smaller motorcycle engines can achieve slightly higher maximum bmep at higher speeds (7000 rev/min). Fuel consumption at the maximum bmep point is about 400 g/kW · h. Average fuel consumption is usually one-and-a-half to two times that of an equivalent four-stroke cycle engine.

CO emissions from two-stroke cycle engines vary primarily with the fuel/air equivalence ratio in a manner similar to that of four-stroke cycle engines (see Fig. 11-20). NO_x emissions are significantly lower than from four-stroke engines due to the high residual gas fraction resulting from the low charging efficiency. Unburned hydrocarbon emissions from carbureted two-stroke engines are about five times as high as those of equivalent four-stroke engines due to fresh mixture short-circuiting the cylinder during scavenging. Exhaust mass hydrocarbon emissions vary approximately as $\Lambda(1 - \eta_{tr})\phi$, where ϕ is the fuel/air equivalence ratio.[63]

15.6.4 Two-Stroke Cycle CI Engines

Large marine diesel engines (0.4 to 1 m bore) utilize the two-stroke cycle. These low-speed engines with relatively few cylinders are well suited to marine propulsion since they are able to match the power/speed requirements of ships with simple direct-drive arrangements. These engines are turbocharged to achieve high brake mean effective pressures and specific output. The largest of these engines can achieve brake fuel conversion efficiencies of up to 54 percent. An example of a large marine two-stroke engine is shown in Fig. 1-24. Over the past 25 years

PETITIONER'S EXHIBIT 1002
US PATENT NO. 6,581,565

the output per cylinder of such engines has increased by a factor of more than two, and fuel consumption has decreased by 25 percent. These changes have been achieved by increasing the maximum firing pressure to 13 MPa, and by refining critical engine processes such as fuel injection, combustion, supercharging, and scavenging. The uniflow-scavenging process is now preferred to loop scavenging since it achieves higher scavenging efficiency at high stroke/bore ratios and allows increases in the expansion stroke.[62]

The performance characteristics of a 580 mm bore Sulzer two-stroke marine diesel engine with a stroke/bore ratio of 2.9 are shown in Fig. 15-49. The solid lines show the standard turbocharged engine characteristics. The rated speed for the engine is 125 rev/min, corresponding to a maximum mean piston speed of 7.2 m/s. The rated bmep is 1.66 MPa. The minimum bsfc is 175 g/kW · h which equals a brake fuel conversion efficiency of 48 percent. For larger lower-speed engines, the efficiency is higher. The dashed lines show how the performance of this engine can be improved by turbocompounding. A proportion of the engine's exhaust flow, at loads higher than 50 percent, is diverted from the turbocharger inlet to a separate turbine coupled to the engine power takeoff gear via an epicyclic speed-reduction gear and hydraulic coupling. The additional power recovered in this manner from the engine exhaust flow improves bsfc by 5 g/kW · h. At part load, when the full exhaust flow passes through the turbocharger, an efficiency gain is also obtained, due to the higher scavenging pressure (and therefore increased cylinder pressure) obtained with the full exhaust flow.

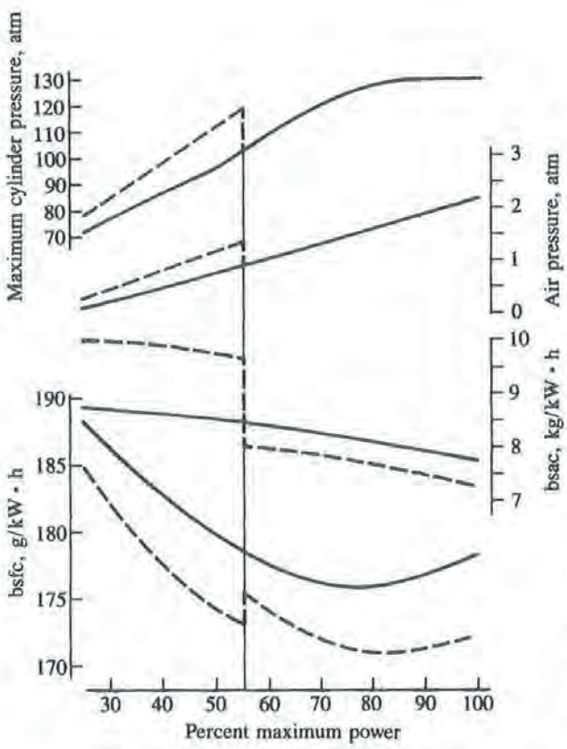


FIGURE 15-49
Performance characteristics of large marine two-stroke cycle uniflow-scavenged DI diesel engine. Bore = 580 mm, stroke/bore = 2.9, maximum rated speed = 125 rev/min (mean piston speed = 7.2 m/s), bmep (at rated power) = 1.66 MPa. Solid line: standard turbocharged configuration. Dashed lines: parallel turbocompounded configuration at greater than 50 percent load. bsac: brake specific air consumption.[62]

PETITIONER'S EXHIBIT 1002
US PATENT NO. 6,581,565

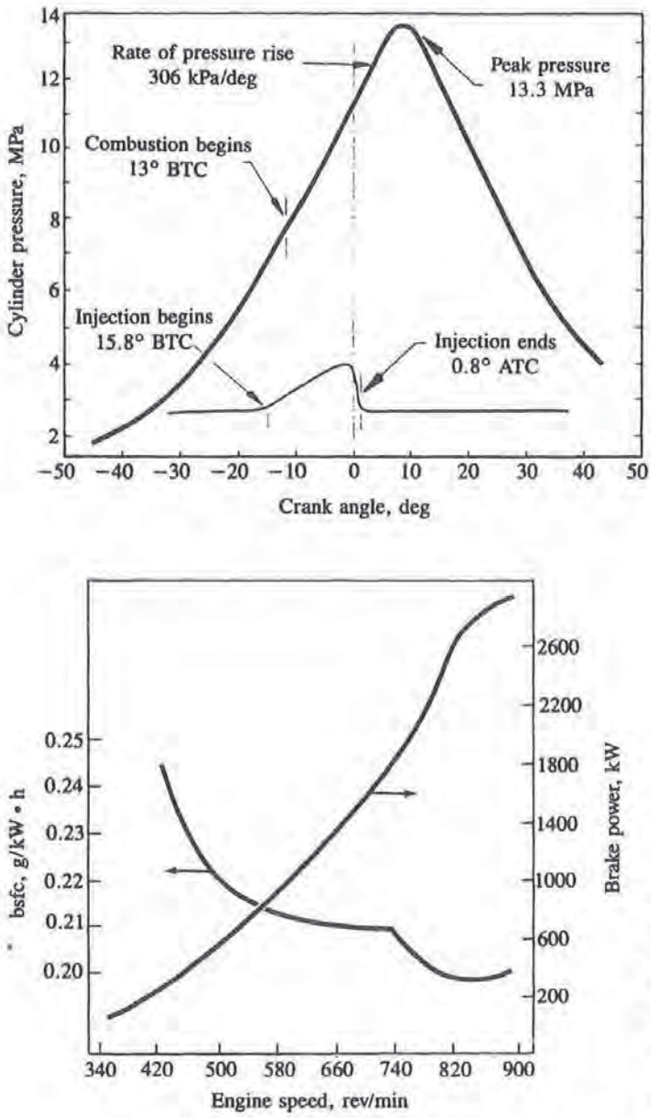


FIGURE 15-50
Injection, combustion, and performance characteristics of intermediate-size turbocharged two-stroke cycle uniflow-scavenged DI diesel engine. Bore = 230.2 mm, stroke = 279.4 mm and $r_c = 16$. Shallow dish-in-piston combustion chamber with swirl. At maximum rated power at 900 rev/min, bmep = 0.92–1.12 MPa depending on application.[65]

Both two-stroke and four-stroke cycle diesel engines of intermediate size (200 to 400 mm bore) are used in rail, industrial, marine, and oil drilling applications. The performance characteristics of a turbocharged two-stroke cycle uniflow-scavenged DI diesel engine (similar to the engine in Fig. 1-5), with 230.2 mm bore, 279.4 mm stroke, and a compression ratio of 16, are shown in Fig. 15-50. Combustion in the shallow dish-in-piston chamber with swirl occurs smoothly yielding a relatively low rate of pressure rise. The pressure curve shown with peak pressure of 13.3 MPa is for full-load operation. The bmep at rated power at 900 rev/min is 0.92 to 1.12 MPa depending on application. The maximum mean piston speed is 8.4 m/s. The bsfc of 200 g/kW · h corresponds to $\eta_{f,b} = 0.42$.

PETITIONER'S EXHIBIT 1002
US PATENT NO. 6,581,565

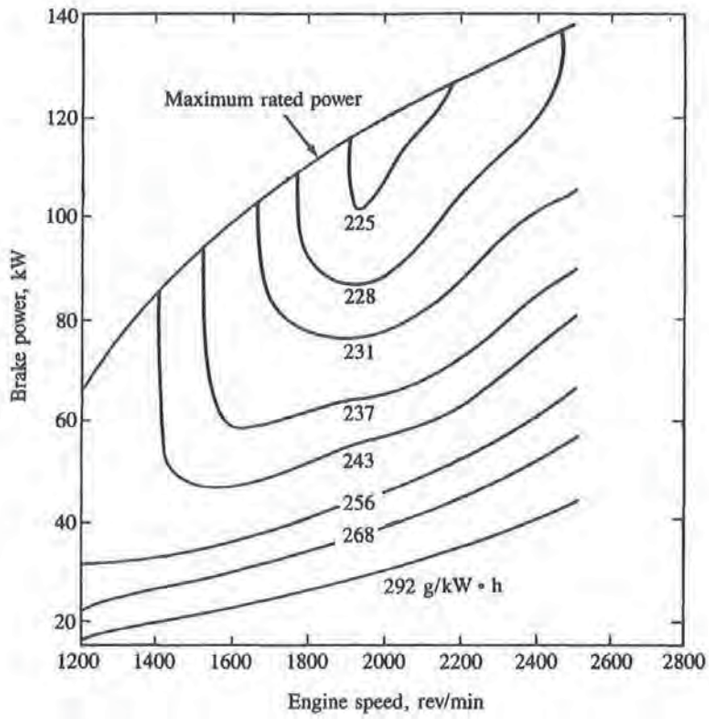


FIGURE 15-51
Brake power and specific fuel consumption (grams per kilowatt-hour) map of four-cylinder 3.48-dm^3 uniflow-scavenged two-stroke cycle DI diesel engine. Engine turbocharged at mid and high loads; Roots blown at low loads. Maximum boost pressure ratio = 2.6. Bore = 98.4 mm, stroke = 114.3 mm, $r_c = 18$.[66]

Smaller turbocharged two-stroke cycle DI diesel engines also compete with four-stroke cycle engines in the marine, industrial, and construction markets. The fuel consumption map of such a four-cylinder 3.48-dm^3 displacement uniflow-scavenged two-stroke cycle diesel engine is shown in Fig. 15-51. The engine uses a Roots blower to provide the required scavenging air pressure for starting and light-load operation. At moderate and high loads the turbocharger supplies sufficient boost and the blower is not needed; the blower is unloaded (air flow is bypassed around the blower) under these conditions. The engine generates 138 kW at its rated speed of 2500 rev/min (mean piston speed of 9.5 m/s) and a maximum bmep of 951 kPa at 1500 rev/min. The best bsfc is 225 g/kW · h and the maximum boost pressure ratio is 2.6.

15.7 ENGINE PERFORMANCE SUMMARY

The major performance characteristics of the spark-ignition and compression-ignition engines described in previous sections of this chapter are summarized here to highlight the overall trends. Table 15.4 lists the major design features of these engines, the bmep at maximum engine torque, bmep and the value of the mean piston speed $\bar{S}_p$ at maximum rated power, and the minimum value of bsfc

PETITIONER'S EXHIBIT 1002
US PATENT NO. 6,581,565

TABLE 15.4
Performance of representative engines in different categories

Engine type†	Bore, mm	Stroke, mm	Stroke/bore	r_c	Volume per cylinder, dm^3	Number of cylinders	Maximum torque		Rated maximum power				Maximum efficiency		Reference
							bmep, kPa	Speed, rev/min	bmep, kPa	Speed, rev/min	Boost pressure ratio	$\bar{S}_p$, m/s	bsfc g/kW·h	$\eta_{f,b}$	
SI/4S/NA	96.8	86	0.88	8.6	0.632	6	910	2500	750	4300	—	12.3			1
SI/4S/NA	84.5	88	1.04	8.5	0.494	4	966	2800	767	5200	—	15.3			67
SI/4S/NA	86*	86*	1*	8.5*	0.5	4	910	3500	758	5000	—	14.3	274	0.30	13
SI/4S/NA	96	80	0.83	9.5	0.579	4	998	2800	796	5400	—	14.4			52
SI/4S/TC	92	80	0.87	7.5	0.532	4	1241	3800	1024	5400	1.6*	14.4			52
SI/4S/TCAC	96	80	0.83	8.7	0.579	4	1356	2900	1144	5300	1.6	14.1			52
SI/2S/C	58	56	0.97		0.144	3	654	3500	575	4500		8.4	~400*	~0.2	64
SI/2S/C	64	54	0.84		0.174	2	686	7000	590	8200		14.8	~340*	~0.24	63
IDI/4S/NA	76.5	86.4	1.13	23	0.397	5	850	3100	670	4800	—	13.8	280	0.30	35
IDI/4S/NA	84	82	0.98	22	0.454	4	675	2000	502	5000	—	13.7			4
IDI/4S/NA	102	100	0.98	19	0.817	4	848	2200	743	3500	—	11.7	251	0.34	46
IDI/4S/TC	76.5	86.4	1.13	23	0.397	6	1080	2400	840	4800	1.7	13.8	240	0.35	54
DI/4S/NA	76.5	80	1.05	18.5	0.368	4	735	2800	600	5000	—	13.3	246	0.34	34
DI/4S/NAA	102	100	0.98	18	0.817	8	784	2000	682	3200	—	10.7	220	0.39	33
DI/4S/NA	102	100	0.98	17	0.817	4	886	2200	782	3500	—	11.7	221	0.38	46
DI/4S/NA	115	135	1.17	16	1.40	6	851	1400	777	2700	—	12.2	204	0.42	3
DI/4S/NA	135	140	1.04		2.00	6	862	1400	763	2500	—	11.7			57
DI/4S/TC	115	135	1.17		1.40	6	1098	1500	941	2500		11.2	203	0.42	3
DI/4S/TCAC	115	135	1.17		1.40	6	1344	1600	1240	2300		10.4			3
DI/4S/TCAC	128	140	1.09	15	1.8	6–16	1560	1500	1280	2100	2.5	9.8	195	0.43	58
DI/4S/TC	135	140	1.04	16	2.00	6	1087	1300	911	2300	1.9	10.7	210	0.40	57
DI/4S/2TCAC	140	152	1.09		2.33	6	1740	1400	1445	2100	3	10.6	207	0.41	60
DI/4S/TCAC	400	480	1.20		60.3	6–18			2190	580		9.3	185	0.46	62
DI/2S/TC	98.4	114.3	1.16	18	0.870	3, 4, 6	1065	1500	952	2500	2.6	9.5	226	0.37	66
DI/2S/TC	230	279.4	1.21	16	11.6	8–20			920–1122	900	2.8	8.4	200	0.42	65
DI/2S/TCAC	380–840	1100–2900	2.9–3.4		125–1607	4–12			1660	196–90	3.5	7.2	180–160	0.47–0.53	62

† Engine type: SI = spark-ignition; IDI = indirect-injection compression-ignition; DI = direct-injection compression-ignition; 4S = four-stroke; 2S = two-stroke; NA = naturally aspirated; NAA = NA and air-cooled; C = crankcase compression of scavenging mixture; TC = turbocharged; TCAC = turbocharged and aftercooled; 2TC = two-stage turbocharged.
* Denotes estimated value.

PETITIONER'S EXHIBIT 1002
US PATENT NO. 6,581,565

and the corresponding brake fuel conversion efficiency. It should be stressed that there are many different engine configurations and uses, and that for each of these there are variations in design and operating characteristics. However, these representative values of performance parameters illustrate the following trends:

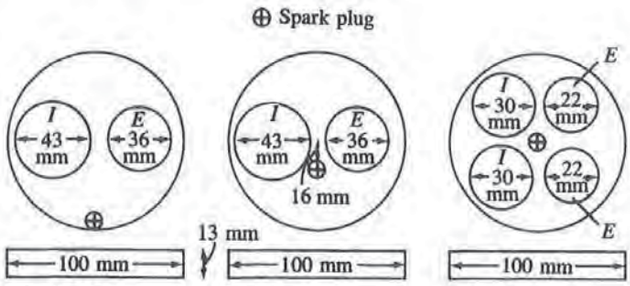
1. Within a given category of engines (e.g., naturally aspirated four-stroke SI engines) the values of maximum bmep, and bmep and $\bar{S}_p$ at maximum rated power, are closely comparable. Within an engine category where the range in size is substantial, there is an increase in maximum bmep and a decrease in minimum bsfc as size increases due to the decreasing relative importance of friction and heat loss per cycle. There is also a decrease in $\bar{S}_p$ at maximum power as engine size increases. Note the higher bmep of naturally aspirated SI engines compared to equivalent NA diesels due to the fuel-rich operation of the former at wide-open throttle.
2. Two-stroke cycle spark-ignition engines have significantly lower bmep and higher bsfc than four-stroke cycle SI engines.
3. The effect of increasing inlet air density by increasing inlet air pressure increases maximum bmep values substantially. Turbocharging with aftercooling gives increased bmep gains relative to turbocharging without aftercooling at the same pressure level. The maximum bmep of turbocharged SI engines is knock-limited. The maximum bmep of turbocharged compression-ignition engines is stress-limited. The larger CI engines are designed to accept higher maximum cylinder pressures, and hence higher boost.
4. The best efficiency values of modern automobile SI engines and IDI diesel engines are comparable. However, the diesel has a significant advantage at lower loads due to its low pumping work and leaner air/fuel ratio. Small DI diesels have comparable (or slightly lower) maximum bmep to equivalent IDI diesels. The best bsfc values for DI diesels are 10 to 15 percent better, however.
5. In the DI diesel category (which is used over the largest size range—less than 100 mm bore to almost 1 m), maximum bmep and best brake fuel conversion efficiency steadily improve with increasing engine size due to reduced impact of friction and heat loss per cycle, higher allowable maximum cylinder pressure so higher boost can be used, and (additionally in the larger engines) through turbocompounding.

PROBLEMS

15.1. The schematics show three different four-stroke cycle spark-ignition engine combustion chambers. A and B are two-valve engines, C is a four-valve engine (two inlet valves which open simultaneously, two exhaust valves). Dimensions in millimeters are indicated. A and C have normal inlet ports and do not generate any swirl, B has a helical inlet port and generates substantial swirl. Spark plug locations are indicated. All three engines operate at the same speed (3000 rev/min), with the same inlet mixture composition, temperature, and pressure, and have the same displaced volume.

PETITIONER'S EXHIBIT 1002
US PATENT NO. 6,581,565

(*a*) Rank the chambers 1, 2, 3 in the order of their volumetric efficiency (1 = highest η_v).
(*b*) Rank the chambers in order (1, 2, 3) of their flame frontal area (1 = highest) when the mass fraction burned is about 0.2 and the piston is at TC.
(*c*) Given this relative flame front area ranking, discuss whether the ranking by mass burning rate dm_b/dt will be different from the flame area ranking.
(*d*) Briefly discuss the knock implications of these three chamber designs. Which is likely to have the worst knock problem?



A. 2-valve, Side plug, Normal port
B. 2-valve, Plug 16 mm from axis, Helical port
C. 4-valve, Center plug, Normal ports

FIGURE P15-1

15.2. Figures 15-23 and 15-10 show the variation in brake specific fuel consumption (bsfc) for a swirl-chamber IDI automobile diesel (D) and a conventional automobile spark-ignition (SI) engine as a function of load and speed, respectively. From these graphs determine, and then plot, brake fuel conversion efficiency: (1) as a function of speed at *full load* and (2) as a function of load at a mid-speed of 2500 rev/min. Both engines are naturally aspirated. Assume the engine details are:

	Compression ratio	Equivalence ratio range	Displacement, dm^3
Diesel	22	0.3–0.8	2.3
SI engine	9	1.0–1.2	1.6

(*a*) List the major engine design and operating variables that determine brake fuel conversion efficiency.
(*b*) Explain briefly the reasons for the shapes of the curves you have plotted and the relative relationship of the D and SI curves.
(*c*) At 2500 rev/min, estimate which engine will give the higher maximum brake power.

15.3. The diesel system shown in the figure consists of a multicylinder reciprocating diesel engine, a turbocharger (with a compressor C and turbine T_T mechanically connected to each other), an intercooler (I), and a power turbine (T_P) which is geared to the engine drive shaft. The gas and fuel flow paths and the gas states at the numbered points are shown. You can assume that the specific heat at constant pressure c_p of the gas throughout the entire system is 1.2 kJ/kg · K and $\gamma = c_p/c_v = 1.333$. The engine operates at 1900 rev/min. The fuel has a lower heating value of 42 MJ/kg of fuel.

PETITIONER'S EXHIBIT 1002
US PATENT NO. 6,581,565

(*a*) What is the power (in kilowatts) which the turbocharger turbine (T_T) must produce? What is the gas temperature at exit to the turbocharger turbine?
(*b*) What is the power turbine power output?
(*c*) The heat losses in the engine are 15 percent of the fuel's chemical energy ($\dot{m}_f Q_{LHV}$). Find the engine power output, the total system power output, and the total system brake fuel conversion efficiency (friction effects in the engine and power turbine are internal to these devices and do not need to be explicitly evaluated).

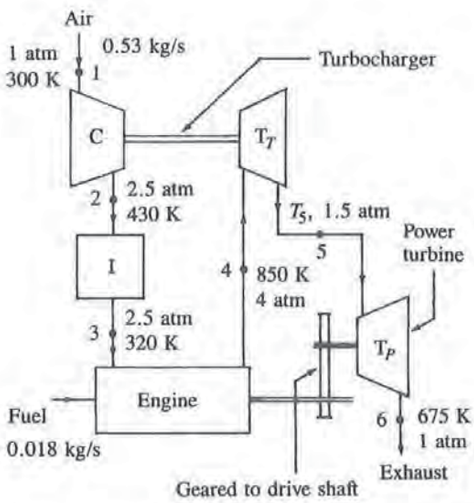


FIGURE P15-3

15.4. The attached graph shows how the brake power and specific fuel consumption of a four-stroke cycle single-cylinder spark-ignition engine vary with the fuel/air equivalence ratio at wide-open throttle. It also shows how the following efficiencies vary with equivalence ratio:

The volumetric efficiency: η_v
The mechanical efficiency: η_m [Eq. (2.17)]

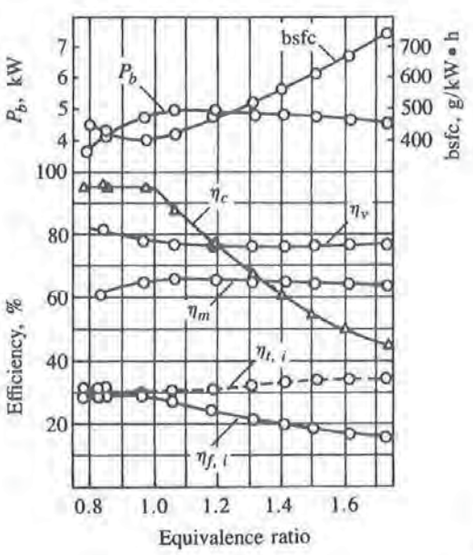


FIGURE P15-4

PETITIONER'S EXHIBIT 1002
US PATENT NO. 6,581,565

The combustion efficiency: η_c [Eq. (3.27)]
The indicated fuel conversion efficiency: $\eta_{f,i}$ [Eq. (2.23)]
The indicated thermal conversion efficiency: $\eta_{t,i}$ [Eq. (3.31)]

(*a*) Derive a relation between the variables $\eta_{f,i}$, η_c, and $\eta_{t,i}$.
(*b*) Derive an equation which relates the brake power P_b to η_v, η_m, η_c, $\eta_{t,i}$, and any other engine and fuel parameters required.
(*c*) Explain briefly why the variations of η_v, η_m, η_c, $\eta_{f,i}$, $\eta_{t,i}$ with equivalence ratio in the figure have the form shown (e.g., why the parameter is approximately constant, or has a maximum/minimum, or decreases/increases with increasing richness or leanness, etc.).

15.5. The diagram shows the layout of a low heat loss turbocharged turbocompounded diesel engine. The engine and exhaust system is insulated with ceramics to reduce heat losses to a minimum. Air flows steadily at 0.4 kg/s and atmospheric conditions into the compressor C, and exits at 445 K and 3 atm. The air is cooled to 350 K in the intercooler I. The specific heat of air, c_p, is 1 kJ/kg·K. In the reciprocating diesel engine, the fuel flow rate is 0.016 kg/s, the fuel heating value is 42.5 MJ/kg, and the heat lost through the ceramic walls is 60 kW.

The exhaust gases leave the reciprocating engine at 1000 K and 3 atm, and enter the first turbine T_A, which is mechanically linked to the compressor. The pressure between the two turbines is 1.5 atm. The second turbine T_B is mechanically coupled to the engine drive shaft and exhausts to the atmosphere at 800 K. The specific heat of exhaust gases, c_p, is 1.1 kJ/kg·K.

(*a*) Analyze the reciprocating diesel engine E and determine the indicated power obtained from this component of the total system. If the engine mechanical efficiency is 0.9 what is the brake power obtained from component E?
(*b*) Determine the power obtained from the power turbine T_B.
(*c*) Determine the total brake power obtained from the complete engine system and the fuel conversion efficiency of the system. You can neglect mechanical losses in the coupling between the power turbine and the engine drive shaft.

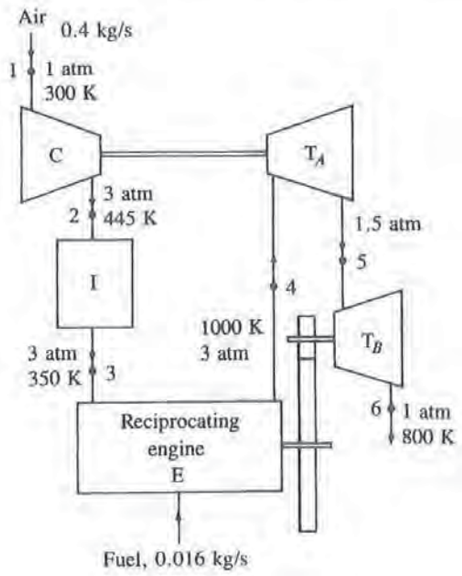


FIGURE P15-5

PETITIONER'S EXHIBIT 1002
US PATENT NO. 6,581,565

15.6. New automobile spark-ignition engines employ "fast-burn technology" to achieve an improvement in fuel consumption and reductions in hydrocarbon (HC) and oxides of nitrogen (NO_x) emissions. This question asks you to explain the experimental data which shows that faster-burning combustion chambers do provide these benefits relative to more moderate burn-rate chambers.

(*a*) Figure 9-36*b* shows the effect of increasing the percent of the exhaust gas recycled to the intake (for NO_x control) in a moderate burn-rate engine at constant speed and load, stoichiometric air/fuel ratio, with timing adjusted for maximum brake torque at each condition. COV_{imep} is the standard deviation in imep divided by the average imep, in percent. The different types of combustion are: *misfire*, *partial burn*, *slow burn*, *normal burn*, defined in Sec. 9.4.3. Frequency is percent of cycles in each of these categories. Use your knowledge of the spark-ignition engine flame-propagation process and HC emission mechanism to explain these trends in COV_{imep}, HC, and frequency as EGR is increased.

(*b*) The fast-burn combustion chamber uses two spark plugs and generates swirl inside the chamber by placing a vane in the inlet port to direct the air to enter the chamber tangentially. The swirl angular velocity in the cylinder at the end of intake is six times the crankshaft angular velocity. There is no swirl in the moderate burn-rate chamber which has a single spark plug and a relatively quiescent in-cylinder flow. The table shows spark timing, average time of peak pressure, average flame-development angle (0 to 10 percent mass burned) and rapid burning period (10 to 90 percent mass burned) for these two engines. Figures 11-29 and 15-9 show how the operating and emission characteristics of the fast burn and moderate burn-rate engines change as percent EGR is increased. Explain the reasons for the differences in these trends in COV_{imep}, bsfc (brake specific fuel consumption), and HC, and similarity in NO_x. The operating conditions are held constant at the same values as before.

	Fast burn	**Moderate burn**	
Spark timing	18°	40°	BTC
Crank angle for average p_{max}	15°	16°	ATC
0–10% burned	24°	35°	
10–90% burned	20°	50°	

15.7. Two alternative fuels, methanol and hydrogen, are being studied as potential future spark-ignition engine fuels which might replace gasoline (modeled by isooctane C_8H_{18}). The table gives some of the relevant properties of these fuels.

(*a*) For each fuel calculate the energy content per unit volume (in joules per cubic meter) of a stoichiometric mixture of fuel vapor and air at 1 atm and 350 K. The universal gas constant is 8314 J/kmol · K. What implications can you draw from these numbers regarding the maximum power output of an engine of fixed geometry operating with these fuels with stoichiometric mixtures?

(*b*) The octane rating of each fuel, and hence the knock-limited compression ratio of an engine optimized for each fuel, is different. Estimate the ratio of the maximum indicated mean effective pressure for methanol- and hydrogen-fueled

PETITIONER'S EXHIBIT 1002
US PATENT NO. 6,581,565

engines to that of the gasoline-fueled engine, allowing for energy density effects at intake (at 1 atm and 350 K), at the knock-limited compression ratio for each fuel, for stoichiometric mixtures. You can assume that the fuel-air cycle results for isooctane apply also for methanol and hydrogen cycles to a good approximation, when the energy density is the same.

(*c*) The lean operating limit for the three fuels is different as indicated. Estimate the ratio of indicated fuel conversion efficiency for methanol and hydrogen at their lean limit and knock-limited compression ratio, relative to gasoline at its lean limit and knock-limited compression ratio, at the same inlet pressure (0.5 atm). Under these conditions, rank the fuel-engine combinations in order of decreasing power output.

	Gasoline (isooctane) C_8H_{18}	Methanol CH_3OH	Hydrogen H_2
Stoichiometric F/A	0.066	0.155	0.0292
Lower heating value, MJ/kg	44.4	20.0	120.1
Molecular weight of fuel	114	32	2
Molecular weight of stoichiometric mixture	30.3	29.4	21
Research octane number	95	106	~90
Knock-limited compression ratio	9	12	8
Equivalence ratio at lean misfire limit	0.9	0.8	0.6

15.8. Small-size direct-injection (DI) diesel engines are being developed as potential replacements for indirect-injection (IDI) or prechamber engines in automobile applications. Figures 10-1*b* and 10-2 show the essential features of these two types of diesel. The DI engine employs high air swirl, which is set up with a helical swirl-generating inlet port (Fig. 8-13). The injector is centrally located over the bowl-in-piston combustion chamber and the injector nozzle has four holes, one in each quadrant. The IDI engine (a Ricardo Comet swirl chamber), in contrast, has no swirl in the main chamber, but generates high velocities and a rotating flow in the prechamber during compression.

Figures 15-21 and 15-23 show performance maps for typical versions of these two types of engines. Bmep, brake mean effective pressure, is plotted against engine speed. Brake specific fuel consumption contours are shown with the numbers in grams per kilowatt-hour.

The heat-release-rate profiles for these two types of engine at a typical mid-load mid-speed point are shown versus crank angle in the sketch. $\dot{Q}$ has units of joules per second.

(*a*) Explain the reasons for the differences in shape and relative timing in the cycle of the heat-release-rate profiles.

(*b*) Suggest reasons for the differences (magnitude and shape) in the maximum bmep versus mean-piston-speed line for the DI and IDI engines.

PETITIONER'S EXHIBIT 1002
US PATENT NO. 6,581,565

(*c*) Evaluate the brake fuel conversion efficiency of each engine at its maximum efficiency point, and at 2000 rev/min and road load (road load is the power requirement to maintain a vehicle at constant speed; it is 2 bar bmep at 2000 rev/min). Explain the origin of the observed differences in efficiency at these two operating conditions.

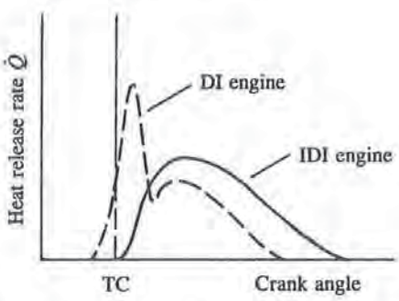


FIGURE P15-8

15.9. A four-stroke cycle naturally aspirated direct-injection diesel is being developed to provide 200 kW of power at the engine's maximum rated speed. Using information available in Chaps. 2, 5, and 15, on typical values of critical engine operating parameters at maximum power and speed for good engine designs, estimate the following:

(*a*) The compression ratio, the number of cylinders, the cylinder bore and stroke, and the maximum rated speed of an appropriate engine design that would provide this maximum power.

(*b*) The brake specific fuel consumption of this engine design at the maximum power operating point.

(*c*) The approximate increase in brake power that would result if the engine was turbocharged.

15.10. Natural gas (which is close to 100 percent methane, CH_4) is being considered as a spark-ignition engine fuel. The properties of methane and gasoline (assume the same properties as isooctane) and the engine details for each fuel are summarized below (ϕ is the fuel/air equivalence ratio).

	Natural gas	**Gasoline**
Composition	CH_4	C_8H_{18}
Heating value, MJ/kg	50.0	44.3
Research octane number	120	94
Compression ratio	14	8
Displaced volume, dm^3	2	2
Lean misfire limit	$\phi = 0.5$	$\phi = 0.8$
Part-load equivalence ratio	$\phi = 0.6$	$\phi = 0.9$
Full-load equivalence ratio	$\phi = 1.1$	$\phi = 1.2$

As indicated in the table, the displaced volume of the engine is unchanged when the conversion for natural gas is made; however, the clearance height is reduced to increase the compression ratio.

(*a*) Estimate the ratio of the volumetric efficiency of the engine operating on natural gas to the volumetric efficiency with gasoline, at wide-open throttle and 2000 rev/min. Both fuels are in the gaseous state in the intake manifold.

PETITIONER'S EXHIBIT 1002
US PATENT NO. 6,581,565

(*b*) Estimate the ratio of the maximum indicated power of the engine operating with natural gas to the maximum power of the gasoline engine.

(*c*) Estimate the ratio of the gross indicated fuel conversion efficiency of the natural gas engine to that of the gasoline engine, at the part-load conditions given.

(*d*) Explain whether the NO, CO, and hydrocarbon specific emissions (grams of pollutant per hour, per unit indicated power) at part-load conditions of the natural gas engine will be higher, about the same, or lower than the NO, CO, and HC emissions from the gasoline engine. Explain briefly why.

You can assume that the fuel-air cycle results derived for isooctane-air mixtures are also appropriate for methane-air mixtures.

15.11. Spark-ignition and prechamber diesel engines are both used as engines for passenger cars. They must meet the same exhaust emission requirements. Of great importance are their emission characteristics when optimized for maximum power at wide-open throttle (WOT) and when optimized at cruise conditions for maximum efficiency.

(*a*) Give typical values for the equivalence ratio for a passenger car spark-ignition engine and a prechamber diesel optimized for maximum power at WOT and 2000 rev/min, and optimized for maximum efficiency at part load (bmep = 300 kPa) and 1500 rev/min. Briefly explain the values you have chosen.

(*b*) Construct a table indicating whether at these two operating conditions the specific emissions of CO, HC, NO_x, and particulates are low (L), medium (M), or high (H) relative to the other load point and to the other engine. Explain your reasoning for each table entry.

15.12. For a naturally aspirated four-stroke cycle diesel engine:

(*a*) Show from the definition of mean effective pressure that

$$\text{bmep} \propto \eta_m \eta_{f,i} \eta_v (F/A)$$

where bmep = brake mean effective pressure
η_m = mechanical efficiency
$\eta_{f,i}$ = indicated fuel conversion efficiency
η_v = volumetric efficiency
F/A = fuel/air ratio

(*b*) Sketch carefully proportioned qualitative graphs of η_m, $\eta_{f,i}$, η_v, and $(F/A)/(F/A)_{\text{stoich}}$ versus speed N at full load, and explain the reasons for the shapes of the curves. Then explain why the maximum bmep versus speed curve has the shape shown in Fig. P15-12.

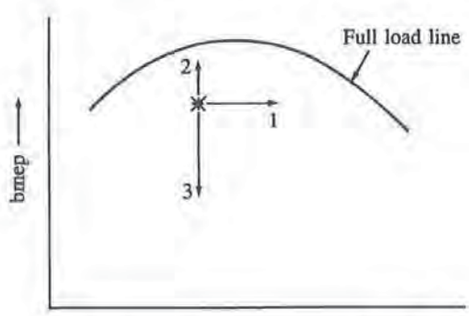


FIGURE P15-12

PETITIONER'S EXHIBIT 1002
US PATENT NO. 6,581,565

(*c*) The minimum brake specific fuel consumption point is indicated by the asterisk (*) in Fig. P15-12 (see Figs. 15-21 and 15-22). Explain why brake specific fuel consumption *increases* with (1) increasing speed, (2) increasing bmep, (3) decreasing bmep.

REFERENCES

1. Armstrong, D. L., and Stirrat, G. F.: "Ford's 1982 3.8L V6 Engine," SAE paper 820112, 1982.
2. "Engine Rating Code—Spark-Ignition," SAE Standard J245, in *SAE Handbook*.
3. Okino, M., Okada, K., and Abe, M.: "Isuzu New 8.4L Diesel Engine," SAE paper 850258, 1985.
4. Higashisono, M., Takeuchi, K., and Hara, H.: "The New Isuzu 1.8 Liter 4-Cylinder Diesel Engine for the United States Market," SAE paper 820116, *SAE Trans.*, vol. 91, 1982.
5. *General Motors Automotive Engine Test Code For Four Cycle Spark Ignition Engines*, 6th ed., 1975.
6. Heywood, J. B., Higgins, J. M., Watts, P. A., and Tabaczynski, R. J.: "Development and Use of a Cycle Simulation to Predict SI Engine Efficiency and NO_x Emissions," SAE paper 790291, 1979.
7. Heywood, J. B., and Watts, P. A.: "Parametric Studies of Fuel Consumption and NO Emissions of Dilute Spark-Ignition Engine Operation Using a Cycle Simulation," paper C98/79, in *Proceedings of Conference on Fuel Economy and Emissions of Lean Burn Engines*, Institution of Mechanical Engineers, London, 1979.
8. Quader, A. A.: "The Axially-Stratified-Charge Engine," SAE paper 820131, *SAE Trans.*, vol. 91, 1982.
9. Robison, J. A., and Brehob, W. M.: "The Influence of Improved Mixture Quality on Engine Exhaust Emissions and Performance," *J. Air Pollution Control Ass.*, vol. 17, no. 7, pp. 446–453, July 1967.
10. Thring, R. H., and Overington, M. T.: "Gasoline Engine Combustion—The High Ratio Compact Chamber," SAE paper 820166, *SAE Trans.*, vol. 91, 1982.
11. Hamburg, D. R., and Hyland, J. E.: "A Vaporized Gasoline Metering System for Internal Combustion Engines," SAE paper 760288, 1976.
12. Nakajima, Y., Sugihara, K., and Takagi, Y.: "Lean Mixture or EGR—Which is Better for Fuel Economy and NO_x Reduction?," paper C94/79, in *Proceedings of Conference on Fuel Economy and Emissions of Lean Burn Engines*, Institution of Mechanical Engineers, London, 1979.
13. Wade, W., and Jones, C.: "Current and Future Light Duty Diesel Engines and Their Fuels," SAE paper 840105, *SAE Trans.*, vol. 93, 1984.
14. Lavoie, G. A., and Blumberg, P. N.: "A Fundamental Model for Predicting Fuel Consumption, NO_x and HC Emissions of a Conventional Spark-Ignited Engine," *Combust. Sci. Technol.*, vol. 21, pp. 225–258, 1980.
15. Caton, J. A., Heywood, J. B., and Mendillo, J. V.: "Hydrocarbon Oxidation in a Spark-Ignition Engine Exhaust Port," *Combust. Sci. Technol.*, vol. 37, nos. 3 and 4, pp. 153–169, 1984.
16. Caton, J. A., and Heywood, J. B.: "Models for Heat Transfer, Mixing and Hydrocarbon Oxidation in an Exhaust Port of a Spark-Ignited Engine," SAE paper 800290, 1980.
17. Caris, D. F., and Nelson, E. E., "A New Look at High Compression Engines," *SAE Trans.*, vol. 67, pp. 112–124, 1959.
18. Kerley, R. V., and Thurston, K. W.: "The Indicated Performance of Otto-Cycle Engines," *SAE Trans.*, vol. 70, pp. 5–30, 1962.
19. Muranaka, S., Takagi, Y., and Ishida, T.: "Factors Limiting the Improvement in Thermal Efficiency of S.I. Engine at Higher Compression Ratio," SAE paper 870548, 1987.
20. Gruden, D. O.: "Combustion Chamber Layout for Modern Otto Engines," SAE paper 811231, 1981.
21. Barnes-Moss, H. W.: "A Designers Viewpoint," paper C343/73, in *Proceedings of Conference on Passenger Car Engines*, pp. 133–147, Institution of Mechanical Engineers, Conference publication 19, London, 1973.

PETITIONER'S EXHIBIT 1002
US PATENT NO. 6,581,565

22. Kuroda, H., Nakajima, Y., Sugihara, K., Takagi, Y., and Maranaka, S.: "Fast Burn with Heavy EGR Improves Fuel Economy and Reduces NO_x Emission," *JSAE Rev.*, no. 5, pp. 63–69, 1980.
23. Thring, R. H.: "The Effects of Varying Combustion Rate in Spark Ignited Engines," SAE paper 790387, 1979.
24. Harada, M., Kadota, T., and Sugiyama, Y.: "Nissan NAPS-Z Engine Realizes Better Fuel Economy and Low NO_x Emission," SAE paper 810010, 1981.
25. Poulos, S. G., and Heywood, J. B.: "The Effect of Chamber Geometry on Spark-Ignition Engine Combustion," SAE paper 830334, *SAE Trans.*, vol. 92, 1983.
26. Heywood, J. B.: "Combustion Chamber Design for Optimum Spark-Ignition Engine Performance," *Int. J. Vehicle Des.*, vol. 5, no. 3, pp. 336–357, 1984.
27. Novak, J. M., and Blumberg, P. N.: "Parametric Simulation of Significant Design and Operating Alternatives Affecting the Fuel Economy and Emissions of Spark-Ignited Engines," SAE paper 780943, *SAE Trans.*, vol. 87, 1978.
28. Amann, C. A.: "Control of the Homogeneous-Charge Passenger-Car Engine: Defining the Problem," SAE paper 801440, 1980.
29. Bell, A. G.: "The Relationship between Octane Quality and Octane Requirement," SAE paper 750935, 1975.
30. Leppard, W. R.: "Individual-Cylinder Knock Occurrence and Intensity in Multicylinder Engines," SAE paper 820074, 1982.
31. Ingamells, J. C., Stone, R. K., Gerber, N. H., and Unzelman, G. H.: "Effects of Atmospheric Variables on Passenger Car Octane Number Requirements," SAE paper 660544, *SAE Trans.*, vol. 75, 1966.
32. Gruden, D.: "Performance, Exhaust Emissions and Fuel Consumption of an IC Engine Operating with Lean Mixtures," paper C111/79, in *Proceedings of Conference on Fuel Economy and Emissions of Lean Burn Engines*, Institution of Mechanical Engineers, London, 1979.
33. Slezak, P. J., and Vossmeyer, W.: "New Deutz High Performance Diesel Engine," SAE paper 810905, 1981.
34. Neitz, A., and D'Alfonso, N.: "The M.A.N. Combustion System with Controlled Direct Injection for Passenger Car Diesel Engines," SAE paper 810479, 1981.
35. Sator, K., Buttgereit, W., and Sturzebecher, U.: "New 5- and 6-Cylinder VW Diesel Engines for Passenger Cars and Light Duty Trucks," SAE paper 790206, 1979.
36. Monaghan, M. L.: "The High Speed Direct Injection Diesel for Passenger Cars," SAE paper 810477, 1981.
37. Pischinger, R., and Cartellieri, W.: "Combustion System Parameters and Their Effect upon Diesel Engine Exhaust Emissions," SAE paper 720756, *SAE Trans.*, vol. 81, 1972.
38. Ball, W. F., and Hil, R. W.: "Control of a Light Duty Indirect Injection Diesel Engine for Best Trade-Off between Economy and Emissions," paper C122/82, in *Proceedings of Conference on Diesel Engines for Passenger Cars and Light Duty Vehicles*, Publication 1982-8, Institution of Mechanical Engineers, London, 1982.
39. Wade, W. R., Idzikowski, T., Kukkonen, C. A., and Reams, L. A.: "Direct Injection Diesel Capabilities for Passenger Cars," SAE paper 850552, 1985.
40. Greeves, G., and Wang, C. H. T.: "Origins of Diesel Particulate Mass Emission," SAE paper 810260, *SAE Trans.*, vol. 90, 1981.
41. Greeves, G., Khan, I. M., and Wang, C. H. T.: "Origins of Hydrocarbon Emissions from Diesel Engines," SAE paper 770259, *SAE Trans.*, vol. 86, 1977.
42. Greeves, G.: "Response of Diesel Combustion Systems to Increase of Fuel Injection Rate," SAE paper 790037, *SAE Trans.*, vol. 88, 1979.
43. Yu, R. C., and Shahed, S. M.: "Effects of Injection Timing and Exhaust Gas Recirculation on Emissions from a D.I. Diesel Engine," SAE paper 811234, *SAE Trans.*, vol. 90, 1981.
44. Khan, I. M., Greeves, G., and Wang, C. H. T.: "Factors Affecting Smoke and Gaseous Emissions from Direct Injection Engines and a Method of Calculation," SAE paper 730169, 1973.
45. Bassoli, C., Cornetti, G. M., and Cuniberti, F.: "IVECO Diesel Engine Family for Medium Duty Vehicles," SAE paper 820031, 1982.

PETITIONER'S EXHIBIT 1002
US PATENT NO. 6,581,565

46. Kawamura, H., Kihara, R., and Kinbara, M.: "Isuzu's New 3.27L Small Direct Injection Diesel," SAE paper 820032, 1982.
47. Arcoumanis, C., Bicen, A. F., and Whitelaw, J. H.: "Squish and Swirl-Squish Interaction in Motored Model Engines," *ASME Trans., J. Fluids Engng*, vol. 105, pp. 105–112, 1983.
48. Watson, N., and Janota, M. S.: *Turbocharging the Internal Combustion Engine*, Wiley-Interscience Publications, John Wiley, New York, 1982.
49. Hiereth, H., and Withalm, G.: "Some Special Features of the Turbocharged Gasoline Engine," SAE paper 790207, 1979.
50. Wallace, T. F.: "Buick's Turbocharged V-6 Powertrain for 1978," SAE paper 780413, *SAE Trans.*, vol. 87, 1978.
51. Allen, F. E., and Rinschler, G. L.: "Turbocharging the Chrysler 2.2 Liter Engine," SAE paper 840252, *SAE Trans.*, vol. 93, 1984.
52. Andersson, J., and Bengtsson, A.: "The Turbocharged and Intercooled 2.3 Liter Engine for the Volvo 760," SAE paper 840253, *SAE Trans.*, vol. 93, 1984.
53. Watson, N.: "Turbochargers for the 1980s—Current Trends and Future Prospects," SAE paper 790063, *SAE Trans*, vol. 88, 1979.
54. Grandinson, A., and Hedin, I.: "A Turbocharged Engine for a Growing Market," paper C119/82, in *Diesel Engines for Passenger Cars and Light Duty Vehicles*, Institution of Mechanical Engineers, Conference publication 1982–8, London, 1982.
55. Walzer, P., and Rottenkolber, P.: "Supercharging of Passenger Car Diesels," paper C117/82, in *Diesel Engines for Passenger Cars and Light Duty Vehicles*, Institution of Mechanical Engineers, Conference publication 1982–8, London, 1982.
56. Carstens, U. G., Isik, T., Biaggini, G., and Cornetti, G.: "Sofim Small High-Speed Diesel Engines—D.I. Versus I.D.I.," SAE paper 810481, 1981.
57. Okada, K., and Takatsuki, T.: "Isuzu's New 12.0L Turbocharged Diesel with Wastegate Boost Control for Fuel Economy," SAE paper 820029, 1982.
58. Schittler, M.: "MWM TBD 234 Compact High-Output Engines for Installation in Heavy Equipment and Military Vehicles," SAE paper 850257, 1985.
59. Barry, E. G., McCabe, L. J., Gerke, D. H., and Perez, J. M.: "Heavy-Duty Diesel Engine/Fuels Combustion Performance and Emissions—A Cooperative Research Program," SAE paper 852078, 1985.
60. Robinson, R. H., and Schnapp, J. P.: "Cummins NTC-475 Series Turbocharged Engine," SAE paper 820982, 1982.
61. Wilson, D. E.: "The Design of a Low Specific Fuel Consumption Turbocompound Engine," SAE paper 860072, 1986.
62. Lustgarten, G. A.: "The Latest Sulzer Marine Diesel Engine Technology," SAE paper 851219, 1985.
63. Tsuchiya, K., and Hirano, S.: "Characteristics of 2-Stroke Motorcycle Exhaust HC Emission and Effects of Air-Fuel Ratio and Ignition Timing," SAE paper 750908, 1975.
64. Uchiyama, H., Chiku, T., and Sayo, S.: "Emission Control of Two-Stroke Automobile Engine," SAE paper 770766, *SAE Trans.*, vol. 86, 1977.
65. Kotlin, J. J., Dunteman, N. R., Chen, J., and Heilenbach, J. W.: "The GM/EMD Model 710 G Series Turbocharged Two-Stroke Cycle Engine," ASME paper 85-DGP-24, 1985.
66. Fellberg, M., Huber, J. W., and Duerr, J. W.: "The Development of Detroit Diesel Allison's New Generation Series 53 Engines," SAE paper 850259, 1985.
67. Hisatomi, T., and Iida, H.: "Nissan Motor Company's New 2.0 Liter Four-Cylinder Gasoline Engine," SAE paper 820113, *SAE Trans.*, vol. 91, 1982.

PETITIONER'S EXHIBIT 1002
US PATENT NO. 6,581,565

APPENDIX A

UNIT CONVERSION FACTORS

This table provides conversion factors for common units of measure for physical quantities to the International System (SI) units. The conversion factors are presented in two ways: columns 2 and 3 give the conversion to the base or derived SI unit with the conversion factor as a number between one and ten with six or fewer decimal places, followed by the power of ten that the number must be multiplied by to obtain the correct value; columns 4 and 5 provide conversion to a recommended multiple or submultiple of the SI unit with the conversion factor given as a four-digit number between 0.1 and 1000.

1 To convert from	2 To	3 Multiply by	4 To	5 Multiply by
Area				
foot^2	m^2	$9.290\,304 \times 10^{-2}$	cm^2	929.0
inch^2	m^2	$6.451\,600 \times 10^{-4}$	cm^2	6.452
Energy, heat, and work				
Btu (International Table)	J	$1.055\,056 \times 10^{3}$	kJ	1.055
calorie (thermochemical)	J	$4.184\,000 \times 10^{0}$	J	4.184
erg	J	$1.000\,000 \times 10^{-7}$	μJ	0.1000
foot pound-force (ft · lbf)	J	$1.355\,818 \times 10^{0}$	J	1.356
horsepower-hour (hp · h)	J	$2.684\,520 \times 10^{6}$	MJ	2.685
kilowatt-hour (kW · h)	J	$3.600\,000 \times 10^{6}$	MJ	3.600
metre kilogram-force (m · kgf)	J	$9.806\,650 \times 10^{0}$	J	9.807

PETITIONER'S EXHIBIT 1002
US PATENT NO. 6,581,565

1 To convert from	2 To	3 Multiply by	4 To	5 Multiply by
Energy (specific, specific heat)				
Btu (IT)/lb	J/kg	$2.326\,000 \times 10^{3}$	kJ/kg	2.326
Btu (IT)/lb · °F	J/kg · K	$4.186\,800 \times 10^{3}$	kJ/kg · K	4.187
calorie (thermo.)/g	J/kg	$4.184\,000 \times 10^{3}$	kJ/kg	4.184
calorie (thermo.)/g · °C	J/kg · K	$4.184\,000 \times 10^{3}$	kJ/kg · K	4.184
Force				
dyne	N	$1.000\,000 \times 10^{-5}$	μN	10.00
kilogram-force	N	$9.806\,650 \times 10^{0}$	N	9.807
pound-force	N	$4.448\,222 \times 10^{0}$	N	4.448
Force per unit length (includes surface tension)				
dyne/centimeter	N/m	$1.000\,000 \times 10^{-3}$	mN/m	1.000
pound-force/inch	N/m	$1.751\,268 \times 10^{2}$	N/m	175.1
pound-force/foot	N/m	$1.459\,390 \times 10^{1}$	N/m	14.59
Fuel consumption (economy)				
pound/horsepower-hour	kg/J	$1.689\,660 \times 10^{-7}$	g/kW · h	608.3
gram/kilowatt-hour	kg/J	$2.777\,778 \times 10^{-10}$	μg/J	0.2778
mile/gallon (U.S.)	m/m^3	$4.251\,437 \times 10^{5}$	km/dm^3	0.4251
mile/gallon (Imp.)	m/m^3	$3.540\,060 \times 10^{5}$	km/dm^3	0.3540
Heat flux (includes thermal conductivity)				
Btu (IT) · in/h · ft^2 · °F	W/m · K	$1.442\,279 \times 10^{-1}$	W/m · K	0.1442
Btu (IT)/ft^2	J/m^2	$1.135\,653 \times 10^{4}$	kJ/m^2	11.36
Btu (IT)/h · ft^2 · °F	$W/m^2 \cdot K$	$5.678\,263 \times 10^{0}$	$W/m^2 \cdot K$	5.678
calorie (thermo.)/cm^2	J/m^2	$4.184\,000 \times 10^{4}$	kJ/m^2	41.84
Length				
foot	m	$3.048\,000 \times 10^{-1}$	m	0.3048
inch	m	$2.540\,000 \times 10^{-2}$	mm	25.40
micron	m	$1.000\,000 \times 10^{-6}$	μm	1.000
mile	m	$1.609\,344 \times 10^{3}$	km	1.609
Mass				
ounce	kg	$2.834\,952 \times 10^{-2}$	g	28.35
pound	kg	$4.535\,924 \times 10^{-1}$	kg	0.4536
ton (long or Imp., 2240 lb)	kg	$1.016\,047 \times 10^{3}$	Mg	1.016
ton (short, 2000 lb)	kg	$9.071\,847 \times 10^{2}$	Mg	0.9072
tonne (metric)	kg	$1.000\,000 \times 10^{3}$	Mg	1.000
Mass per unit time (flow)				
pound/second	kg/s	$4.535\,924 \times 10^{-1}$	kg/s	0.4536
pound/minute	kg/s	$7.559\,873 \times 10^{-3}$	g/s	7.560
pound/hour	kg/s	$1.259\,979 \times 10^{-4}$	g/s	0.1260
Mass per unit volume				
gram/gallon (U.S.)	kg/m^3	$2.641\,724 \times 10^{-1}$	g/dm^3	0.2642
pound/$foot^3$	kg/m^3	$1.601\,846 \times 10^{1}$	kg/m^3	16.02
pound/$inch^3$	kg/m^3	$2.767\,990 \times 10^{4}$	kg/dm^3	27.68
pound/gallon (Imp.)	kg/m^3	$9.977\,644 \times 10^{1}$	kg/dm^3	0.0998
pound/gallon (U.S.)	kg/m^3	$1.198\,264 \times 10^{2}$	kg/dm^3	0.1198
Power, heat flow				
Btu (IT)/hour	W	$2.930\,711 \times 10^{-1}$	W	0.2931
horsepower (550 ft · lbf/s)	W	$7.456\,999 \times 10^{2}$	kW	0.7457
horsepower (metric, CV, PS)	W	$7.354\,99 \times 10^{2}$	kW	0.7355

PETITIONER'S EXHIBIT 1002
US PATENT NO. 6,581,565

1 To convert from	2 To	3 Multiply by	4 To	5 Multiply by
Pressure, stress (force per unit area)				
atmosphere (normal, 760 torr)	Pa	$1.013\,250 \times 10^{5}$	kPa	101.3
inch of mercury (60°F)	Pa	$3.376\,85 \times 10^{3}$	kPa	3.377
kilogram-force/centimeter^2	Pa	$9.806\,650 \times 10^{4}$	kPa	98.07
mm of mercury, 0°C (torr)	Pa	$1.333\,224 \times 10^{2}$	Pa	133.3
pound-force/foot^2	Pa	$4.788\,026 \times 10^{1}$	Pa	47.88
pound-force/inch^2 (psi)	Pa	$6.894\,757 \times 10^{3}$	kPa	6.895
Temperature interval				
degree Celsius	K	$1.000\,000 \times 10^{0}$		
degree Fahrenheit	K	$5.555\,556 \times 10^{-1}$	K	0.5556
Temperature				
temperature (°C)	K	°C + 273.15		
temperature (°F)	K	(°F + 459.67)/1.80	°C	(°F − 32)/1.80
Torque				
kilogram-force meter	N·m	$9.806\,650 \times 10^{0}$	N·m	9.807
pound-force foot	N·m	$1.355\,818 \times 10^{0}$	N·m	1.356
Velocity				
foot/second	m/s	$3.048\,000 \times 10^{-1}$	m/s	0.3048
kilometer/hour	m/s	$2.777\,778 \times 10^{-1}$	m/s	0.2778
mile/hour	m/s	$4.470\,400 \times 10^{-1}$	km/h	1.609
Viscosity				
centipoise	Pa·s	$1.000\,000 \times 10^{-3}$	mPa·s	1.000
centistoke	m^2/s	$1.000\,000 \times 10^{-6}$	mm^2/s	1.000
poise	Pa·s	$1.000\,000 \times 10^{-1}$	Pa·s	0.1000
stoke	m^2/s	$1.000\,000 \times 10^{-4}$	mm^2/s	100.0
Volume				
barrel (42 U.S. gallon)	m^3	$1.589\,873 \times 10^{-1}$	m^3	0.1590
foot^3	m^3	$2.831\,685 \times 10^{-2}$	dm^3	28.32
gallon (Imp.)	m^3	$4.546\,092 \times 10^{-3}$	dm^3	4.546
gallon (U.S.)	m^3	$3.785\,412 \times 10^{-3}$	dm^3	3.785
inch^3	m^3	$1.638\,706 \times 10^{-5}$	cm^3	16.39
liter	m^3	$1.000\,000 \times 10^{-3}$	dm^3	1.000
Volume per unit time				
foot^3/minute (cfm)	m^3/s	$4.719\,474 \times 10^{-4}$	dm^3/s	0.4719
foot^3/second	m^3/s	$2.831\,685 \times 10^{-2}$	dm^3/s	28.32
gallon (U.S.)/minute (gpm)	m^3/s	$6.309\,020 \times 10^{-5}$	cm^3/s	63.09

Notes:

1. Derived units such as that for torque (newton-metre, N·m) are written with a period between each component unit for clarity. In practice, the period is often omitted.
2. Derived from Mobil Technical Bulletin *SI Units, The Modern Metric System.* Copyright Mobil Oil Corporation, 1974. Sections reproduced courtesy Mobil Oil Corporation.

PETITIONER'S EXHIBIT 1002
US PATENT NO. 6,581,565

APPENDIX B

IDEAL GAS RELATIONSHIPS

B.1 IDEAL GAS LAW

The gas species which make up the working fluids in internal combustion engines (e.g., oxygen, nitrogen, carbon dioxide, etc.) can usually be treated as ideal gases. This Appendix reviews the relationships between the thermodynamic properties of ideal gases.

The pressure p, specific volume v, and absolute temperature T of an ideal gas are related by the ideal gas law

$$pv = RT \tag{B.1}$$

For each gas species, R is a constant (the gas constant). It is different for each gas and is given by

$$R = \frac{\tilde{R}}{M} \tag{B.2}$$

where $\tilde{R}$ is the universal gas constant (for all ideal gases) and M is the molecular weight of the gas. Since v is given by V/m, where V is the volume of a mass of gas m, Eq. (B.1) can be rewritten as

$$pV = mRT = \frac{m\tilde{R}T}{M} \tag{B.3}$$

PETITIONER'S EXHIBIT 1002
US PATENT NO. 6,581,565

B.2 THE MOLE

It is convenient to introduce a mass unit based on the molecular structure of matter, the mole:

> The mole is the amount of substance which contains as many molecules as there are carbon atoms in 12 grams of carbon-12.†

Thus, the number of moles n of gas is given by

$$n = \frac{m}{M} \tag{B.4}$$

and Eq. (B.3) becomes

$$pV = n\tilde{R}T \tag{B.5}$$

Values for the universal gas constant in different units are given in Table B.1. In the SI system, the value is 8314.3 J/kmol · K.

TABLE B.1
Values of universal gas constant $\tilde{R}$

8314.3 J/kmol · K
8.3143 J/mol · K
1.9859 Btu/lb-mole · °R
1543.3 ft · lbf/lb-mole · °R

B.3 THERMODYNAMIC PROPERTIES

It follows from Eq. (B.1) that the internal energy u‡ of an ideal gas is a function of temperature only:

$$u = u(T) \tag{B.6}$$

Since the enthalpy h is given by $u + pv$, it follows also that

$$h = h(T) \tag{B.7}$$

† This is the SI system definition of the mole; it was formerly called the gram-mole. The kilogram-mole (kmol) is also used; it is 1000 times as large as the mole.

‡ The symbol u will be used for internal energy per unit mass, $\tilde{u}$ for internal energy per mole, and U for internal energy of a previously defined system of mass m. Similar notation will be used for enthalpy, entropy, and specific heats, per unit mass and per mole.

PETITIONER'S EXHIBIT 1002
US PATENT NO. 6,581,565

The specific heats at constant volume and constant pressure of an ideal gas, c_v and c_p, respectively, are defined by

$$c_v = \left(\frac{\partial u}{\partial T}\right)_v = \frac{du}{dT} \tag{B.8}$$

$$c_p = \left(\frac{\partial h}{\partial T}\right)_p = \frac{dh}{dT} \tag{B.9}$$

From Eq. (B.1) it follows that

$$c_p - c_v = R \tag{B.10}$$

The ratio of specific heats, γ, is a useful quantity:

$$\gamma = \frac{c_p}{c_v} \tag{B.11}$$

An *additional* restrictive assumption is often made that the specific heats are constants. This is not a necessary part of the ideal gas relationships.

In general, the internal energy and enthalpy of an ideal gas at a temperature T relative to its internal energy and enthalpy at some reference temperature T_0 are given by

$$u = u_0 + \int_{T_0}^{T} c_v(T)\, dT \tag{B.12}$$

and

$$h = h_0 + \int_{T_0}^{T} c_p(T)\, dT \tag{B.13}$$

The entropy at T, v, and p, relative to the entropy at some reference state T_0, v_0, p_0, can be obtained from the relationships

$$ds = \frac{c_v}{T}\, dT + R\frac{dv}{v} = \frac{c_p}{T}\, dT - R\frac{dp}{p} \tag{B.14}$$

which integrate to give

$$s = s_0 + \int_{T_0}^{T} \frac{c_v}{T}\, dT + R \ln \frac{v}{v_0} \tag{B.15a}$$

and

$$s = s_0 + \int_{T_0}^{T} \frac{c_p}{T}\, dT - R \ln \frac{p}{p_0} \tag{B.15b}$$

The properties u, h, and s can be evaluated on a per unit mass or per mole basis. On a mass basis, c_v, c_p, and R would have the units J/kg · K (Btu/lbm · °R); on a mole basis u, h, and s are replaced by $\tilde{u}$, $\tilde{h}$, and $\tilde{s}$. R is then the universal gas constant $\tilde{R}$, c_v and c_p are replaced by $\tilde{c}_v$ and $\tilde{c}_p$, and $\tilde{c}_v$, $\tilde{c}_p$, and $\tilde{R}$ would have the units J/kmol · K (Btu/lb-mol · °R).

PETITIONER'S EXHIBIT 1002
US PATENT NO. 6,581,565

B.4 MIXTURES OF IDEAL GASES

The working fluids in engines are mixtures of gases. The composition of a mixture of ideal gases can be expressed in terms of the following properties of each component:

Partial pressure p_i. The pressure each component would exert if it alone occupied the volume of the mixture at the temperature of the mixture.

Parts by volume V_i/V. The fraction of the total mixture volume each component would occupy if separated from the mixture, at the mixture temperature and pressure.

Mass fraction x_i. The mass of each component m_i, divided by the total mass of mixture m.

Mole fraction $\tilde{x}_i$. The number of moles of each component n_i, divided by the total number of moles of mixture n.

From Eq. (B.5) it follows that

$$\frac{p_i}{p} = \frac{V_i}{V} = x_i \frac{M}{M_i} = \tilde{x}_i \tag{B.16}$$

The thermodynamic properties of mixtures of ideal gases can be computed from the following relationships:

Molecular weight

$$M = \frac{1}{n} \sum_i n_i M_i = \sum_i \tilde{x}_i M_i \tag{B.17}$$

Internal energy, enthalpy, and entropy
On a mass basis:

$$u = \sum_i x_i u_i \qquad h = \sum_i x_i h_i \qquad s = \sum_i x_i s_i \tag{B.18a, b, c}$$

On a mole basis:

$$\tilde{u} = \sum_i \tilde{x}_i \tilde{u}_i \qquad \tilde{h} = \sum_i \tilde{x}_i \tilde{h}_i \qquad \tilde{s} = \sum_i \tilde{x}_i \tilde{s}_i \tag{B.19a, b, c}$$

PETITIONER'S EXHIBIT 1002
US PATENT NO. 6,581,565

APPENDIX C

EQUATIONS FOR FLUID FLOW THROUGH A RESTRICTION

In many parts of the engine cycle, fluid flows through a restriction or reduction in flow area. Real flows of this nature are usually related to an equivalent ideal flow. The equivalent ideal flow is the steady adiabatic reversible (frictionless) flow of an ideal fluid through a duct of identical geometry and dimensions. For a real fluid flow, the departures from the ideal assumptions listed above are taken into account by introducing a flow coefficient or discharge coefficient C_D, where

$$C_D = \frac{\text{actual mass flow}}{\text{ideal mass flow}}$$

Alternatively, the flow or discharge coefficient can be defined in terms of an effective cross-sectional area of the duct and a reference area. The reference area A_R is usually taken as the minimum cross-sectional area. The effective area of the flow restriction A_E is then the cross-sectional area of the throat of a frictionless nozzle which would pass the measured mass flow between a large upstream reservoir at the upstream stagnation pressure and a large downstream reservoir at the downstream measured static pressure. Thus

$$C_D = \frac{A_E}{A_R}$$

PETITIONER'S EXHIBIT 1002
US PATENT NO. 6,581,565

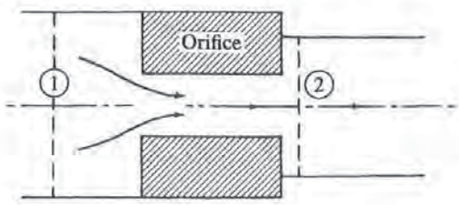


FIGURE C-1
Schematic of liquid flow through orifice.

C.1 LIQUID FLOW

Consider the flow of a liquid through an orifice as shown in Fig. C-1. For the ideal flow, Bernoulli's equation can be written

$$p_1 + \rho \frac{V_1^2}{2} = p_2 + \rho \frac{V_2^2}{2}$$

For an incompressible flow, continuity gives $V_1 A_1 = V_2 A_2$ and the ideal mass flow rate through an orifice is given by

$$\dot{m}_{\text{ideal}} = A_2 \left[\frac{2\rho(p_1 - p_2)}{1 - (A_2/A_1)^2} \right]^{1/2} \tag{C.1}$$

The real mass flow rate is obtained by introducing the discharge coefficient:

$$\dot{m}_{\text{real}} = C_D A_2 \left[\frac{2\rho(p_1 - p_2)}{1 - (A_2/A_1)^2} \right]^{1/2} \tag{C.2}$$

The discharge coefficient is a function of orifice dimensions, shape and surface roughness, mass flow rate, and fluid properties (density, surface tension, and viscosity). The use of the orifice Reynolds number

$$\text{Re}_o = \frac{\rho V_2 D_2}{\mu} = \frac{V_2 D_2}{\nu}$$

as a correlating parameter for the discharge coefficient accounts for the effects of $\dot{m}$, ρ, ν, and D_2 to a good approximation.[1]

C.2 GAS FLOW

Consider the flow of an ideal gas with constant specific heats through the duct shown in Fig. C-2. For the *ideal flow*, the stagnation temperature and pressure, T_0 and p_0, are related to the conditions at other locations in the duct by the steady flow energy equation

$$T_0 = T + \frac{V^2}{2c_p}$$

and the isentropic relation

$$\left(\frac{T}{T_0}\right) = \left(\frac{p}{p_0}\right)^{(\gamma-1)/\gamma}$$

PETITIONER'S EXHIBIT 1002
US PATENT NO. 6,581,565

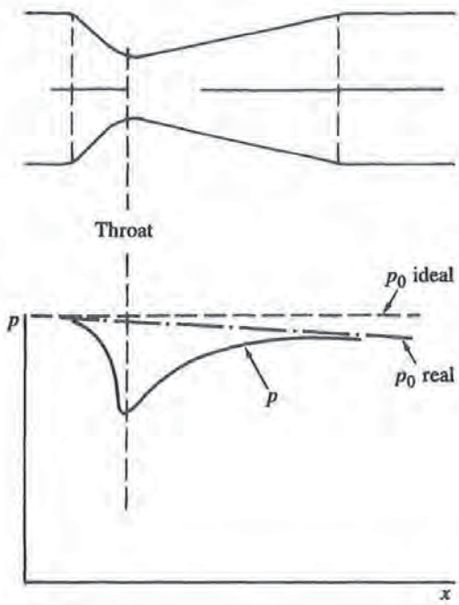


FIGURE C-2
Pressure distribution for gas flow through a nozzle.

By introducing the Mach number $M = V/a$, where a is the sound speed $(= \sqrt{\gamma RT})$, the following equations are obtained:

$$\frac{T_0}{T} = 1 + \frac{\gamma - 1}{2} M^2 \tag{C.3}$$

$$\frac{p_0}{p} = \left(1 + \frac{\gamma - 1}{2} M^2\right)^{\gamma/(\gamma-1)} \tag{C.4}$$

The mass flow rate $\dot{m}$ is

$$\dot{m} = \rho A V$$

With the ideal gas law and the above relations for p and T, this can be rearranged as

$$\frac{\dot{m}_{\text{ideal}}\sqrt{\gamma RT_0}}{Ap_0} = \gamma M\left(1 + \frac{\gamma - 1}{2} M^2\right)^{-(\gamma+1)/2(\gamma-1)} \tag{C.5}$$

or

$$\frac{\dot{m}_{\text{ideal}}\sqrt{\gamma RT_0}}{Ap_0} = \gamma\left(\frac{p}{p_0}\right)^{1/\gamma}\left\{\frac{2}{\gamma - 1}\left[1 - \left(\frac{p}{p_0}\right)^{(\gamma-1)/\gamma}\right]\right\}^{1/2} \tag{C.6}$$

For given values of p_0 and T_0, the maximum mass flow occurs when the velocity at the minimum area or throat equals the velocity of sound. This condition is called choked or critical flow. When the flow is choked the pressure at the throat, p_T, is related to the stagnation pressure p_0 as follows:

$$\frac{p_T}{p_0} = \left(\frac{2}{\gamma + 1}\right)^{\gamma/(\gamma-1)}$$

PETITIONER'S EXHIBIT 1002
US PATENT NO. 6,581,565

This ratio is called the critical pressure ratio. For (p_T/p_0) less than or equal to the critical pressure ratio,

$$\frac{\dot{m}_{\text{ideal}}\sqrt{\gamma RT_0}}{A_T p_0} = \gamma\left(\frac{2}{\gamma+1}\right)^{(\gamma+1)/2(\gamma-1)} \tag{C.7}$$

The critical pressure ratio is 0.528 for $\gamma = 1.4$ and 0.546 for $\gamma = 1.3$.

For a real gas flow, the discharge coefficient is introduced. Then, for subcritical flow, the real mass flow rate is given in terms of conditions at the minimum area or throat by

$$\dot{m}_{\text{real}} = \frac{C_D A_T p_0}{\sqrt{RT_0}}\left(\frac{p_T}{p_0}\right)^{1/\gamma}\left\{\frac{2\gamma}{\gamma-1}\left[1-\left(\frac{p_T}{p_0}\right)^{(\gamma-1)/\gamma}\right]\right\}^{1/2} \tag{C.8}$$

For a choked flow,

$$\dot{m}_{\text{real}} = \frac{C_D A_T p_0}{\sqrt{RT_0}}\,\gamma^{1/2}\left(\frac{2}{\gamma+1}\right)^{(\gamma+1)/2(\gamma-1)} \tag{C.9}$$

Equation (C.8) can be rearranged in the form of Eq. (C.2) (with $A_2 \ll A_1$) as

$$\dot{m}_{\text{real}} = C_D A_R[2\rho_0(p_0 - p_T)]^{1/2}\Phi \tag{C.10}$$

where Φ is given by

$$\Phi = \left\{\frac{[\gamma/(\gamma-1)][(p_T/p_0)^{2/\gamma} - (p_T/p_0)^{(\gamma+1)/\gamma}]}{1 - p_T/p_0}\right\}^{1/2} \tag{C.11}$$

Figure C-3 shows the variation of Φ and $(\dot{m}/\dot{m}^*)_{\text{ideal}}$ with $(p_0 - p_T)/p_0$. $\dot{m}^*$ is the mass flow rate through the restriction under choked flow conditions (when the Mach number at the throat is unity). For flow rates less than about 60 percent of the choked flow, the effects of compressibility on the mass flow rate are less than 5 percent.

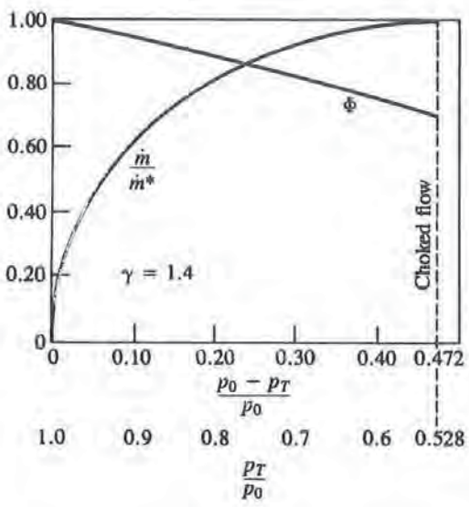


FIGURE C-3
Relative mass flow rate $\dot{m}/\dot{m}^*$ and compressible flow function Φ [Eq. (C.11)] as function of nozzle or restriction pressure ratio for ideal gas with $\gamma = 1.4$. (*From Taylor.*[2])

PETITIONER'S EXHIBIT 1002
US PATENT NO. 6,581,565

Flow coefficients are determined experimentally and are a function of the shape of the passage, the Reynolds number and Mach number of the flow, and the gas properties. For a Mach number at the throat less than about 0.7 and for passages of similar shape, the flow coefficient is essentially a function of Reynolds number only.

Orifice plates are frequently used to measure gas flow rates. Standard methods for determining flows through orifice plates can be found in Ref. 3.

REFERENCES

1. Lichtarowicz, A., Duggins, R. K., and Markland, E.: "Discharge Coefficients for Incompressible Non-Cavitating Flow through Long Orifices," *J. Mech. Eng. Sci.*, vol. 7, no. 2, pp. 210–219, 1965.
2. Taylor, C. F.: *The Internal Combustion Engine in Theory and Practice*, vol. I, p. 506, MIT Press, 1966.
3. *Marks' Standard Handbook for Mechanical Engineers*, 8th ed., McGraw-Hill, 1978.

PETITIONER'S EXHIBIT 1002
US PATENT NO. 6,581,565

APPENDIX D

DATA ON WORKING FLUIDS

PETITIONER'S EXHIBIT 1002
US PATENT NO. 6,581,565

TABLE D.1
Thermodynamic properties of air at low density†

T, K	h, kJ/kg	u, kJ/kg	Ψ kJ/(kg·K)	Φ kJ/(kg·K)	p_r	v_r	c_p kJ/(kg·K)	c_v kJ/(kg·K)	γ
250	409.9	338.1	4.4505	7.6603	38.81	1849.0	1.003	0.715	1.401
275	435.0	356.0	4.5187	7.7559	54·14	1458.0	1.003	0.716	1.401
300	460.1	374.0	4.5811	7.8432	73.39	1173.0	1.004	0.717	1.400
325	485.2	391.9	4.6385	7.9236	97.13	960.6	1.006	0.718	1.400
350	510.4	409.9	4.6919	7.9982	125.9	797.8	1.007	0.720	1.399
375	535.6	427.9	4.7416	8.0678	160.5	670.8	1.010	0.723	1.397
400	560.8	446.0	4.7884	8.1330	201.4	570.0	1.013	0.725	1.396
425	586.2	464.2	4.8324	8.1945	249.6	488.9	1.016	0.729	1.394
450	611.6	482.5	4.8742	8.2527	305.6	422.7	1.020	0.733	1.392
475	637.2	500.8	4.9139	8.3079	370.4	368.1	1.024	0.737	1.390
500	662.8	519.3	4.9518	8.3606	445.0	322.6	1.028	0.741	1.387
525	688.6	537.9	4.9881	8.4109	530.2	284.3	1.033	0.746	1.385
550	714.5	556.6	5.0229	8.4590	627.1	251.8	1.039	0.752	1.382
575	740.5	575.5	5.0565	8.5053	736.8	224.0	1.044	0.757	1.379
600	766.7	594.5	5.0888	8.5499	860.6	200.1	1.050	0.763	1.376
625	793.0	613.6	5.1201	8.5929	999.5	179.5	1.056	0.768	1.374
650	819.5	632.9	5.1503	8.6344	1155.0	161.5	1.061	0.774	1.371
675	846.1	652.3	5.1796	8.6745	1329.0	145.9	1.067	0.780	1.368
700	872.9	671.9	5.2081	8.7135	1521.0	132.1	1.073	0.786	1.365
725	899.8	691.7	5.2358	8.7512	1735.0	119.9	1.079	0.792	1.362
750	926.8	711.5	5.2628	8.7879	1972.0	109.2	1.085	0.798	1.360
775	954.0	731.6	5.2891	8.8236	2233.0	99.63	1.091	0.804	1.357
800	981.4	751.7	5.3147	8.8584	2520.0	91.12	1.097	0.810	1.354
825	1008.9	772.1	5.3397	8.8922	2836.0	83.52	1.103	0.816	1.352
850	1036.5	792.5	5.3641	8.9252	3181.0	76.71	1.108	0.821	1.350
875	1064.3	813.1	5.3880	8.9574	3559.0	70.58	1.114	0.827	1.347
900	1092.2	833.8	5.4114	8.9889	3971.0	65.07	1.119	0.832	1.345
925	1120.2	854.7	5.4342	9.0196	4419.0	60.08	1.124	0.837	1.343
950	1148.4	875.7	5.4566	9.0496	4907.0	55.58	1.129	0.842	1.341
975	1176.7	896.8	5.4786	9.0790	5436.0	51.49	1.134	0.847	1.339
1000	1205.1	918.1	5.5001	9.1078	6009.0	47.77	1.139	0.852	1.337
1025	1233.7	939.4	5.5212	9.1360	6629.0	44.39	1.144	0.856	1.335
1050	1262.3	960.9	5.5419	9.1636	7299.0	41.30	1.148	0.861	1.333
1075	1291.1	982.5	5.5622	9.1907	8020.0	38.48	1.152	0.865	1.332
1100	1319.9	1004.1	5.5821	9.2172	8797.0	35.90	1.157	0.870	1.330
1125	1348.9	1025.9	5.6017	9.2432	9632.0	33.53	1.161	0.874	1.329
1150	1378.0	1047.8	5.6209	9.2688	10529.0	31.35	1.165	0.878	1.327
1175	1407.1	1069.8	5.6399	9.2939	11490.0	29.36	1.168	0.881	1.326
1200	1436.4	1091.9	5.6585	9.3185	12520.0	27.51	1.172	0.885	1.324

† Abstracted with permission from *Thermodynamic Properties in SI* (Graphs, Tables, and Computational Equations for Forty Substances), by W. C. Reynolds, Published by the Department of Mechanical Engineering, Stanford University, Stanford, CA 94305, 1979.

PETITIONER'S EXHIBIT 1002
US PATENT NO. 6,581,565

TABLE D.2
Standard enthalpy of formation and molecular weight of species

Species	Formula	Molecular weight g/mole	State†	$\Delta\bar{h}_f^\circ$ MJ/kmol	$\Delta\bar{h}_f^\circ$ kcal/mol
Oxygen	O_2	32.00	gas	0	0
Nitrogen	N_2	28.01	gas	0	0
Carbon	C	12.011	solid	0	0
Carbon monoxide	CO	28.01	gas	−110.5	−26.42
Carbon dioxide	CO_2	44.01	gas	−393.5	−94.05
Hydrogen	H_2	2.016	gas	0	0
Water	H_2O	18.02	gas	−241.8	−57.80
Water	H_2O	18.02	liquid	−285.8	−68.32
Methane	CH_4	16.04	gas	−74.9	−17.89
Propane	C_3H_8	44.10	gas	−103.8	−24.82
Isooctane	C_8H_{18}	114.23	gas	−224.1	−53.57
Isooctane	C_8H_{18}	114.23	liquid	−259.28	−61.97
Cetane	$C_{16}H_{34}$	226.44	liquid	−454.5	−108.6
Methyl alcohol	CH_3OH	32.04	gas	−201.2	−48.08
Methyl alcohol	CH_3OH	32.04	liquid	−238.6	−57.02
Ethyl alcohol	C_2H_5OH	46.07	gas	−234.6	−56.08
Ethyl alcohol	C_2H_5OH	46.07	liquid	−277.0	−66.20

† At 298.15 K (25°C) and 1 atm.

PETITIONER'S EXHIBIT 1002
US PATENT NO. 6,581,565

TABLE D.3
Enthalpy of C, CO, CO_2, H_2, H_2O, N_2, O_2

	$\tilde{h}°(T) - \tilde{h}°(298.15)$, kcal/mol						
T(K)	C	CO	CO_2	H_2	H_2O	N_2	O_2
298	0.000	0.000	0.000	0.000	0.000	0.000	0.000
300	0.004	0.013	0.016	0.013	0.015	0.013	0.013
400	0.250	0.711	0.958	0.707	0.825	0.710	0.724
500	0.569	1.417	1.987	1.406	1.654	1.413	1.455
600	0.947	2.137	3.087	2.106	2.509	2.125	2.210
700	1.372	2.873	4.245	2.808	3.390	2.853	2.988
800	1.831	3.627	5.453	3.514	4.300	3.596	3.786
900	2.318	4.397	6.702	4.226	5.240	4.355	4.600
1000	2.824	5.183	7.984	4.944	6.209	5.129	5.427
1100	3.347	5.983	9.296	5.670	7.210	5.917	6.266
1200	3.883	6.794	10.632	6.404	8.240	6.718	7.114
1300	4.432	7.616	11.988	7.148	9.298	7.529	7.971
1400	4.988	8.446	13.362	7.902	10.384	8.350	8.835
1500	5.552	9.285	14.750	8.668	11.495	9.179	9.706
1600	6.122	10.130	16.152	9.446	12.630	10.015	10.583
1700	6.696	10.980	17.565	10.233	13.787	10.858	11.465
1800	7.275	11.836	18.987	11.030	14.964	11.707	12.354
1900	7.857	12.697	20.418	11.836	16.160	12.560	13.249
2000	8.442	13.561	21.857	12.651	17.373	13.418	14.149
2100	9.029	14.430	23.303	13.475	18.602	14.280	15.054
2200	9.620	15.301	24.755	14.307	19.846	15.146	15.966
2300	10.212	16.175	26.212	15.146	21.103	16.015	16.882
2400	10.807	17.052	27.674	15.993	22.372	16.886	17.804
2500	11.403	17.931	29.141	16.848	23.653	17.761	18.732
2600	12.002	18.813	30.613	17.708	24.945	18.638	19.664
2700	12.602	19.696	32.088	18.575	26.246	19.517	20.602
2800	13.203	20.582	33.567	19.448	27.556	20.398	21.545
2900	13.807	21.469	35.049	20.326	28.875	21.280	22.493
3000	14.412	22.357	36.535	21.210	30.201	22.165	23.446

Source: *JANAF Thermochemical Tables*, National Bureau of Standards Publication NSRDS-NBS37, 1971.

PETITIONER'S EXHIBIT 1002
US PATENT NO. 6,581,565

TABLE D.4
Data on fuel properties

Fuel	Formula (phase)	Molecular weight	Specific gravity: (density,† kg/dm³)	Heat of vaporization, kJ/kg‡	Specific heat		Higher heating value, MJ/kg	Lower heating value, MJ/kg	LHV of stoich. mixture, MJ/kg	$(A/F)_s$	$(F/A)_s$	Fuel octane rating	
					Liquid, kJ/kg · K	Vapor c_p, kJ/kg · K						RON	MON
Practical fuels§													
Gasoline	$C_nH_{1.87n}$(l)	~110	0.72–0.78	350	2.4	~1.7	47.3	44.0	2.83	14.6	0.0685	91–99	82–89
Light diesel	$C_nH_{1.8n}$(l)	~170	0.78–0.84	270	2.2	~1.7	46.1	43.2	2.79	14.5	0.0690	—	—
Heavy diesel	$C_nH_{1.7n}$(1)	~200	0.82–0.88	230	1.9	~1.7	45.5	42.8	2.85	14.4	0.0697	—	—
Natural gas	$C_nH_{3.8n}N_{0.1n}$(g)	~18	(~0.79†)	—	—	~2	50	45	2.9	14.5	0.069	—	—
Pure hydrocarbons													
Methane	CH_4(g)	16.04	(0.72†)	509	0.63	2.2	55.5	50.0	2.72	17.23	0.0580	120	120
Propane	C_3H_8(g)	44.10	0.51 (2.0†)	426	2.5	1.6	50.4	46.4	2.75	15.67	0.0638	112	97
Isooctane	C_8H_{18}(l)	114.23	0.692	308	2.1	1.63	47.8	44.3	2.75	15.13	0.0661	100	100
Cetane	$C_{16}H_{34}$(l)	226.44	0.773	358		1.6	47.3	44.0	2.78	14.82	0.0675	—	—
Benzene	C_6H_6(l)	78.11	0.879	433	1.72	1.1	41.9	40.2	2.82	13.27	0.0753		115
Toluene	C_7H_8(l)	92.14	0.867	412	1.68	1.1	42.5	40.6	2.79	13.50	0.0741	120	109
Alcohols													
Methanol	CH_4O(l)	32.04	0.792	1103	2.6	1.72	22.7	20.0	2.68	6.47	0.155	106	92
Ethanol	C_2H_6O(l)	46.07	0.785	840	2.5	1.93	29.7	26.9	2.69	9.00	0.111	107	89
Other fuels													
Carbon	C(s)	12.01	~2§	—	—	—	33.8	33.8	2.70	11.51	0.0869		
Carbon monoxide	CO(g)	28.01	(1.25†)	—	—	1.05	10.1	10.1	2.91	2.467	0.405		
Hydrogen	H_2(g)	2.015	(0.090†)	—	—	1.44	142.0	120.0	3.40	34.3	0.0292		

(l) liquid phase; (g) gaseous phase; (s) solid phase.
† Density in kg/m³ at 0°C and 1 atm.
‡ At 1 atm and 25°C for liquid fuels: at 1 atm and boiling temperature for gaseous fuels.
§ Typical values.
RON, research octane number; MON, motor octane number.

Sources:
E. M. Goodger, *Hydrocarbon Fuels; Production, Properties and Performance of Liquids and Gases*, Macmillan, London, 1975.
E. F. Obert, *Internal Combustion Engines and Air Pollution*, Intext Educational Publishers, 1973 edition.
C. F. Taylor, *The Internal Combustion Engine in Theory and Practice*, vol. I, MIT Press, 1966.
J. W. Rose and J. R. Cooper (eds.), *Technical Data on Fuel*, 7th ed., British National Committee, World Energy Conference, London, 1977.

PETITIONER'S EXHIBIT 1002
US PATENT NO. 6,581,565

PETITIONER'S EXHIBIT 1002
US PATENT NO. 6,581,565

INDEX

Adiabatic flame temperature, 81, 94
Air:
  constituents of, 65
  table of thermodynamic properties, 912
  viscosity, 143
Air/fuel ratio:
  definition, 53
  feedback control, 301–304
  lambda sensor, 301–303
  relative, 71
  stoichiometric, 69–70, 915
    of gasoline, 280
Air pollution, automotive:
  emissions mechanisms, summary, 568–572
  nature of problem, 5–6
  sources of emissions, 567–568
  (see also Carbon monoxide; NO_x; Particulates; Unburned HC emissions)
Alcohols:
  antiknock rating, 476–477
  composition, 68
  methanol combustion, 382
  oxygenates:
    emissions of, 598
    as extenders, 476–477
  stoichiometric equation, 72
Aldehyde emissions, 568, 598
Alkyl compounds (acetylenes, napthenes, olefins, paraffins), 67–68
Aromatics, 68
Atkinson:
  cycle, 184–186
  James, 3
Atomization of sprays:
  regimes of, 525–529, 532
  secondary, 532–533
Autoignition, 462–470, 542–545
  chemistry of, 463–467
  cool flames, 465
  of hydrogen, 463–464
  induction-time correlations, 468, 543–545
  Shell model, 469–470
  single-, two-stage, 465–466
Availability:
  analysis, 186–193, 792–797
  balances, 191–192, 196, 793, 795
  combustion loss, 192–193, 196, 795
  conversion efficiency, 84–85
  definitions, 84, 186–188, 792–793
  distribution, by category, 796–797
  losses, actual cycle, 196, 794–797
  steady-flow function, 187, 793

Balance, 20
Bearings:
  journal, 716
    eccentricity, 735
    friction, 717, 736–737
    load diagram, 734–735
    schematic, 735
  slider, 716
Beau de Rochas, Alphonse, 2–3

PETITIONER'S EXHIBIT 1002
US PATENT NO. 6,581,565

Blowby, 361–365
  unburned HC emissions, 6n, 567, 606–607
Brake parameters, definition, 46, 48–49
Burn angles (SI engines):
  flame development, 389–390, 421–423, 777
  overall, 389–390
  rapid-burning, 389–390, 422–423, 777–778
  variations in, 415, 422–423
Burn rate (SI engines):
  and combustion chamber geometry, 847–848
  effect on cycle-by-cycle variations, 415–417, 845–846, 849–850
  effect on performance, 195
  EGR, effect of, 837–839
  turbulence effects, 846–848
  (see also Burn angles; Heat-release rate)
Burned gas:
  composition:
    equilibrium, 93
    low temperature, 104
    fraction, 102–103
Burning rate analysis, Krieger and Borman, 511–514
  (see also Heat-release analysis)

Carbon monoxide:
  background, 6, 567–571
  diesels, 592
  oxidation kinetics, 593–596
  SI engines, 592–596, 836
  (see also Catalytic converters)
Carburetors, 16–17, 282–294
  accelerator pump, 286, 291
  air-bleed compensation, 287–290
  altitude compensation, 286, 292–293
  boost venturis, 16, 286–287
  choke, 286, 291–292
  elementary, 282–285
  idle system, 286, 290–291
  main metering system, 286–290
  modern design, 16–17, 285–294
  multiple-barrel, 287
  power enrichment, 286, 291
  transient effects, 293–294
Catalytic converters:
  catalyst conversion efficiency, 651–652, 656
  catalytic materials, 649, 651–652, 654, 655–657
  degradation, poisoning, 651–653
  design of, 649–650
  light-off temperature, 651, 653
  NO reduction, 654–655
  oxidation, 649–654
  three-way, 655–657

Cetane:
  index, 542
  n-hexadecane, 541, 915
  number, 541, 550–552
    fuel structure dependence, 550–551
Charts (see Thermodynamic charts)
Chemical equilibrium:
  computer codes, 90–92
  constants, 87–90
  general principles, 86–94
Chemical reaction:
  rate constants, 96
  rates, 92–96
  steady state assumption, 96
Combustion:
  constant pressure, 74–75, 126, 172
  constant volume, 73–74, 125, 169
  efficiency, 81–83, 509, 601
  inefficiency, 154, 195, 509
  products composition:
    equilibrium, 93
    low temperature, 104
  stoichiometry, 68–72
  (see also Flame development; Flame propagation; Flame structure; Flames)
Combustion chambers:
  bowl-in-piston, 342, 353–357, 811, 866–869
  design of, SI engines:
    air breathing, 220–222, 846, 850–851
    burn rate, 844–846
    common types, 845
    knock, 854–857
    objectives, 844–846
    optimization strategy, 857–858
    swirl, 846, 850–852
  surface area, 44
Combustion (CI engines):
  consequences, of 492–493
  fuel-air mixing and burning rates, 558–562
  models for, 504–508, 779–780, 782–784, 786–788, 816–818
  phases of, 505–506
    mixing-controlled phase, 506, 558–562
    premixed, rapid burning phase, 505, 558–560
    (see also Ignition delay)
  photographs of, color plate (between 498 and 499), 497–502
  role of, 493, 555–558
  summary of, 491–493
  (see also Diesel combustion systems; Ignition delay; Fuel sprays)
Combustion modeling, 766–778, 779–780, 782–784, 786–788, 816–818

PETITIONER'S EXHIBIT 1002
US PATENT NO. 6,581,565

Combustion (SI engines):
abnormal phenomena, 451
burned gas:
mixed model, 378–381
temperatures, 379–380, 383
unmixed model, 378–381
composition effects, 395
cycle-by-cycle variations, 413–424
burn rate effects, 415–417, 845–846, 849–850
causes of, 282, 419–422
description of, 372–373, 413–415, 829, 832, 849–850
measures of, 415–418
cylinder-to-cylinder variations, 282, 413, 420, 829–830, 831
description of, 371–373, 376
factors that control, 846–850
lean/dilute operating limits, 424–426
misfire, 414–415, 424–427, 611
motion produced by, 380, 411
partial burning, 414–415, 424–427, 611
speed, effects on, 394, 400–402, 411–412
stages of, 372, 389–390, 397–402, 412
thermodynamics of, 376–383
turbulent flame regimes, 396–397
(see also Flame propagation relations; Flame structure; Flames; Heat release; Knock; Spark ignition)
Compression, crankcase, 11, 238, 244
Compression-ignition engines:
operating cycle, 25–31
(see also Diesel engines)
Compression ratio:
definition, 43
effect on efficiency, 170, 172, 175, 182, 197, 841–844
effect on mep, 176, 183, 842
knock limited (critical), 470–472, 854–857
typical values, 43, 58, 492, 887
Compressors:
centrifugal, 238, 258–262, 877–878
corrected mass flow, 255, 262
corrected speed, 255, 262
isentropic efficiency, 251
performance maps, 255, 257–258, 261–262, 270, 273, 878–879
roots blower, 15, 256–258, 886
screw, 256–258
sliding vane, 255–257
velocity diagrams, 260
Comprex (see Supercharging)
Conservation equations, open system:
energy, 751–753
mass, 750–751
Coolant heat flow, 673–675
Courant number, 760
Crank angle, definition, 44
Crevices:
effect on performance, 195, 387–388
flows in/out, 360–365
geometry, 361–362
model for, 387–388
piston/ring assembly, 361–363
unburned HC emissions, 604–608
Critical pressure ratio, 909
Cycles:
Alkinson, 184–186
constant-pressure, 163–164, 178
constant-volume, 163–164, 169–172, 178
availability analysis, 189–195
fuel conversion efficiency, 170, 197
four-stroke, 10–11
fuel-air, 162, 177–183
assumptions, 177
CI engine, 181
results, 181–183, 197
SI engine, 178–180
ideal gas standard, 162, 169–177
availability analysis, 189–192
comparison, 173–177
entropy changes, 188–189, 192
limited-pressure, 163–164, 178
Otto, 11
overexpanded, 183–186
two-stroke, 11–12
Cylinder pressure:
analysis of:
CI engines, 508–517
Rassweiler and Withrow method, 385–386
SI engines, 384–389
(see also Heat release)
cycle sample size, 418
data (CI engines), 504, 513, 885
data (SI engines), 162, 372–374, 384, 414
with knock, 453–454, 459–462
measurement of, 384
p_{max}, $\theta_{p_{max}}$, 415–418, 829
Cylinder volume:
equation for, 43–44

Damkohler number, 396, 399
Delivery ratio, 237–240, 244, 882–883
Diesel combustion systems:
direct-injection, 32–37, 493–494, 496
bowl-in-piston, swirl, multihole nozzle, 493–494, 496–501
M.A.N. "M", 494, 496–501
quiescent, 493–494, 496–500

PETITIONER'S EXHIBIT 1002
US PATENT NO. 6,581,565

Diesel combustion systems (*continued*):
indirect-injection, 33–34, 494–496
swirl prechamber, 494–502
turbulent prechamber, 494–497
(see also Combustion (CI engines); Fuel sprays)
Diesel emissions:
NO_x/particulates trade off, 865–866
(see also Carbon monoxide; NO_x; Particulates; Unburned HC emissions)
Diesel engines:
four-stroke cycle
air-cooled, 35–36, 859
examples (DI), 32–36, 877–881
examples (IDI), 33–34, 875–877
large (marine), 36–37, 883–886
two-stroke cycle, 14, 37, 883–886
Diesel, Rudolf, 4
Droplets:
equations for individual, 814–815
Sauter mean diameter, 434–436
size distribution, 352–354
vaporization, 536–539, 814–815
Dynamometer, 45–46

Efficiency, definitions of:
availability conversion, 84
catalyst conversion, 651–652, 656
charging, 239, 244
combustion, 81–83
compressor isentropic, 251
fuel conversion, 52, 85, 164, 169
mechanical, 49, 723
scavenging, 238, 244
thermal conversion, 85
trapping, 238, 244
turbine isentropic, 253
volumetric, 53–54
Emissions (see Carbon monoxide; NO_x; Particulates; Unburned HC emissions)
Emissions index, 56
Energy, available (see Availability)
Energy balance, engine, 673–676
Engine processes:
availability analysis of, 186–193
thermodynamic relations for, 164–169
Engines:
classification, 7–9
components, 12–15
compression-ignition (diesel), 25–37
energy balance, 673–676
historical, 1–7
maximum work, 83–85
multifuel, 39
prechamber (see Prechamber engines)
spark-ignition, 15–25
stratified-charge (see Stratified-charge engines)
Wankel (see Wankel engines)
Enthalpy, 108–111, 116, 123–127, 903–905
sensible, 113–114, 122
tables of, 914
stagnation, 251
Enthalpy of formation:
datum reference state, 77
definition, 76
standard values, individual species, 77, 124, 913
of unburned mixture, 123–125
Equilibrium (see Chemical equilibrium)
Equivalence ratio (see Fuel/air equivalence ratio)
Evaporative HC emissions, 6n, 567
Exhaust:
blowdown process, 166, 206, 231–233, 613
displacement process, 167, 206, 231–233
(see also Intake and exhaust flow models)
Exhaust gas:
composition
data, diesels, 148–149
data, SI engines, 146–148
equivalence ratio determination, 148–152
F/A nonuniformities, 152–154
measurement, 145–146
mass flow rate, 231–232
recycle, recirculation (EGR), 103
temperatures, 232–234, 648
enthalpy-averaged, 234
equivalence ratio effects, 834–835
EGR, effects of, 837–838
thermodynamic state, 167
EGR tolerance, SI engines, 837–839
Exhaust gas treatment, 648–660
(see also Catalytic converters; Particulate traps; Thermal reactors)
Exhaust manifold pressures, 214

Flame development process:
effects of combustion chamber geometry, 846–847
effects of mixture composition and state, 846, 848–849
effects of turbulence, 846–849
factors that control, 846–850
Flame ionization detector, 145–146, 597n, 620
Flame photographs:
CI engines, color plate (between 498 and 499)
SI engine, 390–394, 397–399, 401, 458–460, color plate (between 498 and 499)
Flame propagation data, 409, 412, 773–774

PETITIONER'S EXHIBIT 1002
US PATENT NO. 6,581,565

Flame propagation relations, 406–412
  characteristic length, 410, 412
  "entrainment" burning laws, 771–778
  flame areas, 406–409, 766–767
  turbulent burning speed, 408–409, 411–412
  velocity parameters, 408–412
Flame quenching, 599–601
Flame structure (CI engines):
  ignition, location of, 502, 556–557
  species concentration data, 557–559
  spray/flame photos, color plate (between 498 and 499), 502, 523, 525, 527, 537
  (see also Combustion (CI engines); Diesel combustion systems)
Flame structure (SI engines), 390–402
  flame area, 394, 406–410, 846–847
  flame thickness, 398–402, 410
  swirl, effect of, 393
Flame volume (SI engines):
  data, 372–373, 409
  relationships, 406–410
Flames:
  classification, 62–64, 395–397
  diffusion, 63
  laminar, 63
  premixed, 63
  turbulence, effect on, 390–392, 398–402
  turbulent, 63, 395–397
Flow modeling (see Models, fluid-dynamic based)
Flows (in-cylinder):
  exhaust stroke vortex, 365–367
  laser doppler anemometry, 336, 808–809
  piston/cylinder corner, 365–367, 613–614
  through intake valve, 224–225, 227, 229, 326–330
  valve-jet driven, 327–330, 807–809
  velocities at intake valve, 326–327, 808–810
  (see also Blowby; Crevices; Squish; Swirl; Turbulence)
Flows through nozzles, orifices, restrictions, 906–910
Four-stroke cycle:
  definition, 10–11
  exhaust process, 206–208
  inlet process, 206–208
  p-V diagram, 47, 162, 284, 727
Friction:
  accessory requirements (fan, generator, pumps), 739–740
  background, 712–713
  coefficient of, 716
    boundary lubrication, 716–718
    hydrodynamic lubrication, 718
    mixed lubrication, 718
    Stribeck diagram, 716–717
  crankshaft, 734–737
  difference, motoring/firing, 720–721
  losses, categories of, 713
  measurement methods, 719–721
  piston assembly, 730, 732–734
  pumping, 47, 168–169, 713–715, 725, 726–728
    throttling work, 727–728
    valve flow work, 727–728
  turbulent dissipation, 719
  valve train, 737–739
Friction correlations:
  Bishop, 727, 733, 736, 738
  crankshaft, con rods, 736
  piston and rings, 733–734
  total friction mep, 719, 722
  valve train, 738
Friction data:
  diesels, 722, 724, 725
  engine breakdown tests, 722, 725–726
  SI engines, 721, 723
Friction definitions:
  accessory mep, power, work, 714–715
  pumping mep, power, work, 47, 714–715
  rubbing friction mep, power, work, 714–715
  total friction mep, power, work, 714–715
Friction/lubrication regimes:
  boundary, 716–718
  mixed, 716
  hydrodynamic, 716
Fuel-air cycle (see Cycles)
Fuel-air equivalence ratio, 71
  availability analysis, effect on, 192–193
  from exhaust composition, 148–152
  for optimum SI engine efficiency, 831–835
Fuel-air mixing, diesels, 493, 504–508, 555–558
  and burning rates, 558–562
Fuel/air ratio:
  definition, 53
  stoichiometric, 69
Fuel conversion efficiency:
  constant-volume cycle, 170, 182
    compression ratio effects, 170, 175, 182, 197
    equivalence ratio effects, 182, 197
  constant-pressure cycle, 172, 175
  definition, 52, 85
  DI vs IDI diesel, 860–861
  limited-pressure cycle, 170, 175
  overexpanded cycle, 184–185
Fuel conversion efficiency (SI engines):
  effect of:
    burn rate, 832–833
    compression ratio, 841–844

PETITIONER'S EXHIBIT 1002
US PATENT NO. 6,581,565

Fuel conversion efficiency (SI engines) (*continued*):
equivalence ratio, 830–834
Fuel injection (diesels):
distributor pump, 30–32, 518
in-line pump, 28, 30, 518
nozzle flow rate, 521
nozzle geometry, 526–529
nozzles, 29, 31, 519–520
objectives, 518
single-barrel pump, 518–519
systems, 27–31, 517–522
unit injectors, 520–521
Fuel injection (SI engines):
injection timing, 298–299
injector design, 295–296
multipoint port systems, 16–17, 294–299
air-flow meter, 297–299
fuel transport, 320–321
mechanical, 298
speed-density, 294–296, 299
single-point systems, 299–301
Fuel sprays:
adiabatic saturation, 538–539
breakup, 522–523, 530–531, 532
evaporation, 535–539, 814–815
and flame structure, 555–558
ignition sites, 525, 556–557
modeling, 538–539, 780–784, 813–816
equations for droplets, 814–815
1-D turbulent jet, 780–781
multidimensional, 813–816
multipackage, 782–784
multizone, 781–782
penetration, 529–532
photographs of, color plate (between 498 and 499), 523, 525, 527, 537
spray angle, 526–528
structure, 522–527, 529, 535–537, 555–558
swirl, effect of, 524–525, 531–532, 558
temperature distribution, 538–539
wall interaction, 523–524
(see also Atomization; Droplets)
Fuels:
additives:
antiknock, 473, 475–476
ignition-accelerating, 551–552
octane improvers, 476–477
API gravity, 542
distillate:
cetane rating, 541–542
diesel index, 542
nitrogen content, 577
sulfur content, 568
enthalpy of formation, 913
gasoline:
composition, 280, 915
equilibrium vaporization, 314–315
heating values, 78–90, 915
hydrocarbons:
classes of, 66–68
knocking tendency, 470–472
hydrogen, 915
autoignition of, 463–464
combustion, 398, 773–774
stoichiometric equation, 72
ignition quality of, 492, 541–542, 550–552
isooctane, 67, 915
octane rating, 471
stoichiometry, 69–71
laminar flame speeds, 395, 402–406
primary reference, 475
properties:
table of, 915
thermodynamic, 77, 130–133
stoichiometric A/F, 70, 915
(see also Alcohols; Cetane; Octane)

Gas constant, 903
Gas properties:
computer routines for, 130–140
isentropic compression functions, 113–115
molar and mass basis, 107, 904–905
molecular weight, 106, 136, 905, 913
polynomial functions
fuels, 130–133
gas species, 130–131
ratio specific heats, 134, 137, 139, 904
specific heats, 132, 134, 136, 138, 904
stagnation values, 251, 907
tables, 127–129, 912, 914
unburned mixture, 130–135
(see also Ideal gas; Thermodynamic charts; Transport properties)
Gasoline (see Fuels, gasoline)

Heat-release analysis:
gross, net, 387–388, 510–511
IDI diesel engines, 514–517
one zone, 386–388, 508–511
problems with (diesels), 508–509
two zone (SI engines), 376–382
Heat-release rate:
diesels:
apparent, 509
data, 504, 511, 516–517, 560–561
definition of, 497
mixing-controlled, 560–562
variables, effects of, 560–562

PETITIONER'S EXHIBIT 1002
US PATENT NO. 6,581,565

Heat-release rate (*continued*):
SI engines:
cycle-by-cycle variations, 414–415
results, 390, 413–414
Heat transfer:
characteristics of, in engines, 668–670, 672–673
coefficient, 671
conduction, 670
convective, 670–671
dimensional analysis, 676–677
cycle-simulation predictions, 702–704, 707, 769–771
effect of engine variables, 701–707
compression ratio, 703–704
coolant temperature, 704–705
equivalence ratio, 703
load, 702, 796–797
spark timing, 704
speed, 673, 675, 679, 702–703, 797
squish, swirl, 704
wall material, 705–707
effect on performance, efficiency, 194–195, 770–771, 851–852
exhaust system, 682–683
intake system, 682
(see also Intake manifold)
prechamber diesels, 787
radiation:
apparent emissivity, 684–688
apparent flame temperature, 685–686
from gases, 683–684
monochromatic absorption coefficient, 687–688
prediction formula, 688–689
relative importance, 693–694
from soot, 683, 684–689
Heat transfer correlations:
evaluation of, 694–696
exhaust port, 682–683
instantaneous local, 681–682, 695–696
instantaneous, spatial average, 678–680, 694–695
Annand, 678–679, 695
Woschni, 679–680, 694–695
time-average, 677–679
zonal models, 682, 696, 768–769
Heat transfer measurements:
methods, 689–690
results, diesels, 692–694
results, SI engines, 690–692
Heating values, 78–90, 915
higher heating value, 78
lower heating value, 78
Humidity:
effect on air properties, 67
psychrometric chart, 66
relative, 65
Hydrocarbon emissions (see Unburned HC emissions)
Hydrocarbons:
burnup, 600, 614–618
classes of, 66–68
knocking tendency, 470–474
oxidation mechanism, 467
Hydrogen:
autoignition of, 463–464
combustion, 773–774
stoichiometric equation, 72

Ideal gas:
analytic model for, 109–112
law, 64, 902
mixtures, 905
relationships, 107–109, 902–905
thermodynamic properties, 903–905
(see also Burned gas; Gas properties; Unburned mixture; Working fluids)
Ignition delay:
correlations for, 543–545
in engines, 553–554
definition, 505, 539–540
factors affecting:
air temperature, pressure, 547–548
chamber wall, 548–549
injection timing, 546
load, 546–548
oxygen concentration, 549–550
speed, 548
spray parameters, 546–547
swirl, 549
fuel property effects, 550–553
processes occurring, 540–541
(see also Autoignition; Cetane)
Indicated parameters, definition:
gross, 47–49, 714–715
net, 47–49, 714–715
Intake and exhaust flow models:
boundary conditions, 761
example results, 311–312, 761–762
finite-difference methods, 759–762
gas dynamic models, 313, 756–762
homentropic flow, 758
1-D unsteady flow equations, 756–758
manifold models:
filling and emptying, 311–312, 753–755
Helmholtz resonator, 312–313
method of characteristics, 759
quasi-steady models, 232, 753—754

PETITIONER'S EXHIBIT 1002
US PATENT NO. 6,581,565

Intake manifold:
air flow, 309–313
description of, 309–311
transient behavior, 310–312
(see also Intake and exhaust flow models)
design, 308–309
fuel transport, 314–321
droplet behavior, 316–317
liquid films, 315–316, 318–320
transient behavior, 310–312, 318–321
vaporization, 314–321
pressure variation, 212–214, 216, 310–311
IC engines (see Engines)
Internal energy, 108–111, 116–127, 903–905
sensible, 113–114, 122
Internal energy of formation:
standard values, 124
of unburned mixture, 123–125

Knock:
antiknock additives, 4, 473, 475–476
lead alkyls, 4, 473, 475–476
MMT, 475–476
characterization of, 454–456
combustion photographs, 458–461
damage, 456–457
deposit effects on, 477–478
description of, 375, 450–457
detection, 454
effect on heat transfer, 707
end gas, 457–462, 467–470
temperature, 468–469
impact of, 456–457, 852–854
intensity, 455–456
pressure waves, 461–462
sensors, 872
theories:
autoignition, 457–458, 462
detonation, 457–458
(see also Autoignition; Compression ratio; Fuels; Octane)

Laminar flame:
speed, 395, 402–406
correlations, 403–406
data, 403–405
and SI engine combustion, 771–775, 777–778, 848–849
straining effects, 406
thickness, 395, 402
Langen, Eugen, 2
Lead alkyls, 4, 473, 475–476
Lenoir, J. J. E., 2
Lubricant:
requirements, 741–745
SAE viscosity classification, 744–745
Lubrication:
of bearings, 715–718, 734–737
of piston assembly, 729–734
regimes of, 716–718
system layout, 740–741
(see also Friction; Bearings)

Manifolds:
tuning of, 215, 217–218
(see also Exhaust manifold; Intake manifold)
Mass fraction burned, SI engines:
data, 372–373, 382, 777–778
equations for, 377–378, 381–382, 390
Wiebe function, 390, 768
Maximum work, 83–85
(see also Availability)
Mean effective pressure:
coefficient of variation (COV), 417, 424–425
cycle-by-cycle variations, 417, 425
definitions, 50, 714–715
friction, 714–715, 825–827
fuel-air cycle results, 183
ideal cycles, 171, 173, 176
importance of, 59, 823–824
overexpanded cycle, 185–186
pumping, 169, 714–715
relationships for, 50–51, 57, 823–824
Mean effective pressure (DI diesels):
effect of:
injection parameters, 863–864
load and speed, 858–860, 877–878
full load, 826–827
Mean effective pressure (IDI diesels):
effect of:
injection parameters, 863–864
load and speed, 860, 875–876
full load, 826–827
Mean effective pressure (SI engines):
effect of:
compression ratio, 842
equivalence ratio, 830–832
heat transfer, 851
wide open throttle, 824–827, 839–840
Mechanical efficiency:
definition, 49
values, SI engine, 722–723
Methanol combustion (SI engine), 382
Mixture nonuniformity, quality, 152–154, 282, 314, 829–832
Mixture requirements (SI engines), 279–282, 833–834
steady, transient, 834
typical schedules, 281–282

PETITIONER'S EXHIBIT 1002
US PATENT NO. 6,581,565

Models of engine processes, rationale, 748–750
Models, fluid-dynamic based (multidimensional):
  for boundary layers, 803
  of combustion, 816–818
  flow field predictions, 360, 807–813
    concentration distributions, 811–813
    particle traces, 810–812
    velocities, 807–811
  governing equations, 798–799
  KIVA code, 803, 804, 815–816
  numerical methodology, 798, 803–807
    computing mesh, 804–805, 810
    discretization practices, 804–806
    solution algorithms, 806–807
  overview, 797–798
  sprays, 813–816
  turbulence models:
    full-field modeling, 799–802
    k-ε models, 775–777, 801–802, 808, 810
    large-eddy simulation, 799
    Reynolds stress, 802
    subgrid scale, 802–803
Models, thermodynamic-based (phenomenological, zero-dimensional):
  complex engine systems, 789–792
    transient behavior, 791–792
    turbocharged/turbocompounded, 789–792
  DI diesels:
    model structure, 784–785
    simulation results, 784–785
    single zone combustion models, 778–780
    spray models, 780–784
    (see also Fuel sprays)
  emissions, 765, 787–788
  IDI diesels, 784–788
    prechamber phenomena, 784–787
    simulation results, 787–788
  open system conservation equations, 763–765
  overall structure, 762–763
  SI engines:
    combustion models, 766–778
    cycle simulation results, 769–771
    "entrainment" burning laws, 771–778
    flame geometry models, 766–768
  stochastic models, 787–788
  turbulence intensity models, 775–777
  (see also Mass fraction burned)
Mole, 903
Molecular weights, values, 913
Moment of inertia of charge, 353

NO concentrations, in-cylinder:
  DI diesel, 587–589
  IDI diesel, 589–590
  SI engines, 579–581
NO formation:
  description of, CI engines, 586–587
  equivalence ratio, effect of, 575–576
  kinetics of, 572–576
    rate constants, 573
    Zeldovich mechanism, 572
  model for, SI engines, 578–581
  rate equation for, 573–574
  temperature, effect of, 574–576
NO from fuel N, 577
Nitrogen, atmospheric, 65
NO_2 formation, 577–578
NO_x, definition of, 567, 572
NO_x emissions (diesels):
  effect of:
    diluents, 590–591, 861–863
    equivalence ratio, 588–589
    EGR, 590–591, 861–863
    injection parameters, 863–867
    load, 861–862
    swirl, 866–867
  flame temperature correlation, 591–592
  (see also NO formation)
NO_x emissions (SI engines):
  effect of:
    compression ratio, 844
    diluents, 582–584
    equivalence ratio, 581–585, 835–836
    EGR, 582–585, 836–838
    load, speed, 840–841
    spark timing, 585–586, 829
  (see also Catalytic converters; NO formation)
Noise, 5, 571–572

Octane:
  antiknock index, 474
  fuel sensitivity, 473–474
    and knock, 854–855
  number, 471–474
    motor method, 471–473
    requirement, 453, 474, 478, 852–857
    research method, 471–473
    road, 474
  oxygenates as extenders, 476–477
  ratings of fuels, 915
Odor, diesel, 568
Oil consumption rate, 610
Organic compounds:
  classes of, 66–68
  (see also Fuels)
Otto:
  cycle, 11

PETITIONER'S EXHIBIT 1002
US PATENT NO. 6,581,565

Otto (*continued*):
Nicolaus, A., 2–3
Oxygen (lambda) sensor, 301–303
Oxygenate emissions, 568, 598

Paraffins:
ignition limits, 465–466
knocking tendency, 470–472
molecular structure, 67
Part-throttle (SI engines):
efficiency, 833–834, 843–844
mixture requirements, 280–282, 834
performance, 833
Particulate emissions (diesels):
effect of:
injection parameters, 864–866
load, 861–862
Particulate traps, 659–660
Particulates, diesels:
Ames test, 631
composition of, 627–630, 647–648
distribution in cylinder, 631–635
HC absorption, condensation, 646–648
measurement techniques, 626–627
dilution ratio effects, 646–647
oil, contribution from, 629–630, 647–648
size, 628–631
soluble fraction, 629, 646–648
soot formation fundamentals, 635–642
soot oxidation, 642–646
specific surface area, 631, 646
spherules, 627–628
structure, 627–631
(see also Particulate emissions; Soot formation; Soot oxidation)
Particulates, SI engines, 626
Peclet number, 599–600
Performance of engines, summary, 58, 866–888
Performance maps:
description of, 839
DI diesels, 858–860, 878–879
IDI diesels, 860, 875–876
SI engines, 839–840, 874
Performance parameters:
importance of, 42–43, 59, 823–824
relationships for, 56–57, 823–824
typical values, 58, 824–827, 887
Piston:
acceleration, 732
heat outflow, 701
temperature distribution, 698–699, 700–701, 705
velocity, 44–45
Piston assembly:
description of, 13–14, 729
forces on, 731–733
friction, 729–734
Piston rings:
functions, 729–730
lubrication, 730–732
oil film thickness, 731–732
Reynolds equation, 731
nomenclature, 729
sealed ring-orifice design 605–606, 610
Piston speed:
instantaneous, 45
mean:
definition, 44
importance of, 59, 839
maximum values of, 45, 887
Pollutant formation mechanisms:
equivalence ratio, effect of, 570–571
summary (CI engine), 571–572
summary (SI engine), 568–571
(see also Carbon monoxide; NO formation; Particulates; Unburned HC emissions)
Polytropic compression relation, 385, 554
Ports (four-stroke cycle):
effect on:
flow discharge coefficient, 229–230
valve flow area, 222–224
geometry of, 220–224
Ports (two-stroke cycle):
discharge coefficients, 247–248
flow through, 246–248
geometry of, 245–248
timing, 237
Power:
brake, definition of, 46
correction factors for, 54
friction, 48, 825–827
full load:
DI diesels, 826–827, 879–890, 885
IDI diesels, 826–827
SI engines, 824–827, 873, 883
rated, definition of, 43
relationships for, 45–46, 49, 823
road-load, 49
specific, definition of, 57
Prandtl number, expressions for, 142, 144
Prechamber engines:
designs, 33–34
flows, 357–360
gas displacement, 359–360
nozzle throat, 358–359
swirl velocities, 360
Pressure:
mean effective (see Mean effective pressure)

PETITIONER'S EXHIBIT 1002
US PATENT NO. 6,581,565

Pressure (*continued*):
stagnation, 251, 907–908
(see also Cylinder pressure)
Pressure-volume diagram:
four-stroke cycle, 47, 162, 384
ideal cycles, 163, 176, 194
log p vs log V, 384–385
polytropic relation, 385, 554
pumping loop, 727
two-stroke cycle, 47
Pumping mean effective pressure, 169
Pumping work:
definition, 47, 714
diesel engines, 492
ideal cycle, 168
SI engines, 827
(see also Friction, pumping)

Rapid compression machines:
results from, 466, 502, 523–524, 556, 560–561
Residual gas flow, 206, 224, 327
Residual gas fraction:
data, 230–231
definition, 102
Residual gas mixing, 420, 811–813
Roots blowers, 15, 256–258, 886

Scavenging, 235–245
charge short-circuiting, 240, 242
crankcase, 11–12, 881
cross-scavenged, 235–236
data, 244–245
flow visualization of, 240–242
loop-scavenging, 235–236, 242–243
models for, 239–240, 811
uniflow, 235–237, 243, 245, 884–886
Second Law analysis (see Availability)
Smoke, effect of:
EGR 863
injection parameters, 864–866, 867
load, 861–862
swirl, 867
(see also Particulate emissions)
Soot formation:
particle formation, 636, 638–639
particle growth, 636, 639–642
polycyclic aromatic HC, 636, 639
pyrolysis, 633, 635, 638
regions of, diesel, 498–502, 536–537
Soot limit on diesel performance, 492
Soot oxidation, 642–646
Soot, radiation from, 684–689
Spark discharge:
chemistry, 431–433
energy, by phase, 429–431
expansion velocities, 430–431
phases (arc, breakdown, glow), 427–429
plasma volumes, 430, 434
temperature distributions, 431–434
Spark ignition:
current and duration effects, 445–446
description of, 17, 397, 427
flow effects, 435–436
fundamentals, 427–437
models of, 433–435
requirements for, 437–438
(see also Spark ignition systems, Spark plugs)
Spark ignition engines:
examples, 13, 21–24
mixture requirements, 279–282, 833–834
operating cycle, 15–19
Spark ignition systems:
available voltage, 439
breakdown, 446
capacitive-discharge, 441
coil, 438–440
flame-jet, 447–450
higher energy, 445–446
magneto, 442
plasma-jet, 446–447
required voltage, 439
transistorized coil, 440–441
Spark kernal, photographs, 397–398, 436
Spark plugs:
design, 442–443
electrode geometry effects, 443–445
fouling, 437
heat rating, 443
Spark timing:
EGR, effect of, 838
and knock, 852–854
maximum brake torque (MBT), 18, 373–375, 827–829
rules for optimum, 375, 828–829
Specific emissions:
definition, 56
importance of, 59
Specific fuel consumption, definition, 51, 59
Specific fuel consumption (diesels):
effect of:
EGR, 863
injection parameters, 863–865, 867
load and speed, 858–860, 875–881
swirl, 866–867
full load, 826–827
Specific fuel consumption (SI engines):
effect of:
A/F, equivalence ratio, 831–835

PETITIONER'S EXHIBIT 1002
US PATENT NO. 6,581,565

Specific fuel consumption (SI) (*continued*):
burn rate, 832–833
EGR, 837–839
heat transfer, 851–852
spark timing, 828
part throttle, 839–840
wide-open throttle, 824–827
Specific power, 57, 59
Specific volume, 54, 59
Specific weight, 54, 59
Speed, rated engine, 43, 493
Squish:
area, 353
impact of, 851–852
motion, 353–354
swirl interaction, 868–869
velocity, 353–357:
bowl-in-piston, 354–357, 810–811, 868
decrements, 355–356
wedge chamber, 354
Stagnation pressure, 251, 907–908
Stratified-charge engines, 37–40
direct-injection, 38–39, 815–816
M.A.N., 38–39
Texaco type, 38, 815–816
prechamber designs, 39–40, 448–450
Sulfate emissions, 568, 626, 653–654
Supercharging:
aftercooling, intercooling, 249–250, 870–871, 873–874, 876–877, 878–881
charge cooling, 22, 249–250
Comprex, 249, 270–273
diesel performance, 875–877
performance map, 273
wave processes in, 271–273
mechanical, 249–250, 875–877
pressure wave, 249, 270–273, 875–877
methods of, 248–250
Roots blower, 256–258, 876–877, 886
(see also Turbocharging)
Surface ignition, 375
different types of, 450–453
preignition damage, 456–457
Swirl, 342–353
amplification, 349–353
and bowl-in-piston chambers, 349–353, 496, 866–869
coefficient, 344–345
definition of, 342
in diesels, 493–497, 866–869
flame structure impact, 393–394
friction effects on, 349–351
measurements, 343–349
ratio, 344–345, 352
squish interaction, 810–811, 868–869
velocity distribution, 351–353, 809, 810–812
Swirl generation:
during compression, 349–353, 496–497
during intake, 345–349, 496–497
with ports (4-stroke):
helical, 346, 348–349, 810–812
tangential, 345–346, 348–349, 812
valve masking, 346–347

Temperature-entropy diagram, 188–189, 793–794
Temperatures:
combustion chamber, 672
components, 698–707
cylinder head, 699, 705
cylinder liner, 699–700, 705
exhaust valve, 700, 705
piston, 698–699, 700–701, 705
Thermal boundary layers, 697–698, 768–769
Thermal insulation of engines, 705–707, 881
Thermal properties:
ceramics, 706
metals, 706
Thermal reactors, 648, 657–659
Thermodynamic charts:
burned mixture, 116–123
datum, 116
low temperature, 122
isentropic compression, 115
mixture composition for, 113
for unburned mixture, 112–115
Thermodynamic relations:
engine processes, 164–169
ideal gas, 107–109, 902–905
Throttle plate:
flow through, 305–308
fuel atomization at, 317
geometry, 304–306
Torque:
brake, data, 828, 859, 873, 876, 883
brake, definition, 46
relationships for, 45–46, 823–824
spark timing, effect of, 828, 853
Transport properties, 141–145
thermal conductivity, 141
viscosity, 141–144
Turbines:
A/R ratio, 872
axial, 263, 266–269
isentropic efficiency, 253
performance maps, 266–269
radial, 263–267, 269
velocity diagrams, 265–268

PETITIONER'S EXHIBIT 1002
US PATENT NO. 6,581,565

Turbocharged diesels:
combustion characteristics, 879–880
DI engine performance, 877–881
different supercharging methods, 249–250, 875–877, 879–881
hyperbar system, 881
IDI engine performance, 875–877
two-stage, 249–250, 879–880
two-stroke, 883–886
turbocompounding, 249–250, 789–791, 879–881, 884
Turbocharged SI engines:
advantages of, 870
boost pressure, 872–873
charge, p, T, 870–871
compared with NA engines, 873–874
compression ratio, 871–872, 874
knock impact, 869–872
power, torque, 873–874
spark advance, 871–872
Turbocharger:
dynamics, 789–792
layout, 20–23, 208, 790
matching, 791
operating characteristics, 269–270, 877–879
thermodynamic relationships, 249–254, 259, 264–265
Turbocharging, 249–250
constant pressure, 263
pulse, 263
two-stage, 249–250, 791, 879–880
wastegate, 270, 873, 875, 878
(see also Supercharging)
Turbocompounding, 249–250, 789–791, 881, 884
Turbulence:
character of, 330–331, 339–340
flames, effect on, 390–392, 410–412, 771–778, 847–850
models, 775–777, 799–803
scales:
data, 342, 401, 410, 412
integral, 333–334
Kolmogorov, 335
microscale, 335
velocities:
autocorrelations, 333–334
data, 338–342, 410–412, 809
definitions, 331–333
ensemble-averaged, 331–333, 336–337, 410–411
individual-cycle mean, 332–333, 337, 410–411
intensity, 331, 336–337, 353, 410–412, 775–777, 809, 811
intensity at TC, 341
laser doppler anemometry, 336, 808
mean, 331–332, 336
with swirl, 342, 353
Two-stroke cycle, 11–12
charge compression, 237–238
diesels:
combustion characteristics, 885
efficiency of, 883–886
performance of, 883–886, 887
scavenging data, 244–245
charge purity, 238, 244–245
p-V diagram, 47
scavenging, 235–245, 881–884
SI engines:
bsfc, 883
charging efficiency, 243–244, 881–883
emissions, 883
examples, 24, 881–883
performance of, 881–883, 887
trapping efficiency, 243–244, 882–883

Unburned HC emissions (diesels):
contribution to particulates, 620
effect of:
EGR, 863
injection parameters, 863–864
load, 861–862
mechanisms, 620–622, 625
nozzle sac volume, 623–624
overleaning, 622–623
quenching and misfire, 625
undermixing, 623–625
Unburned HC emissions (SI engines):
absorption/desorption in oil, 608–610
burn rate effects, 611–612, 845–846
combustion quality effects, 610–612
composition of, 597, 614–615
crevice mechanism, 604–608
deposit mechanism, 612
effect of:
compression ratio, 844
equivalence ratio, 570–571, 835–836
load, speed, 840–841
spark timing, 829
exhaust concentrations, 602–603
flame quenching, 603–604
mechanisms, 568–570, 601–603, 618–619
oxidation, 600, 614–618
oxygenates, 598
reactivity, 597–598
secondary air, 616–617
transport mechanisms, 612–614
(see also Catalytic converters)

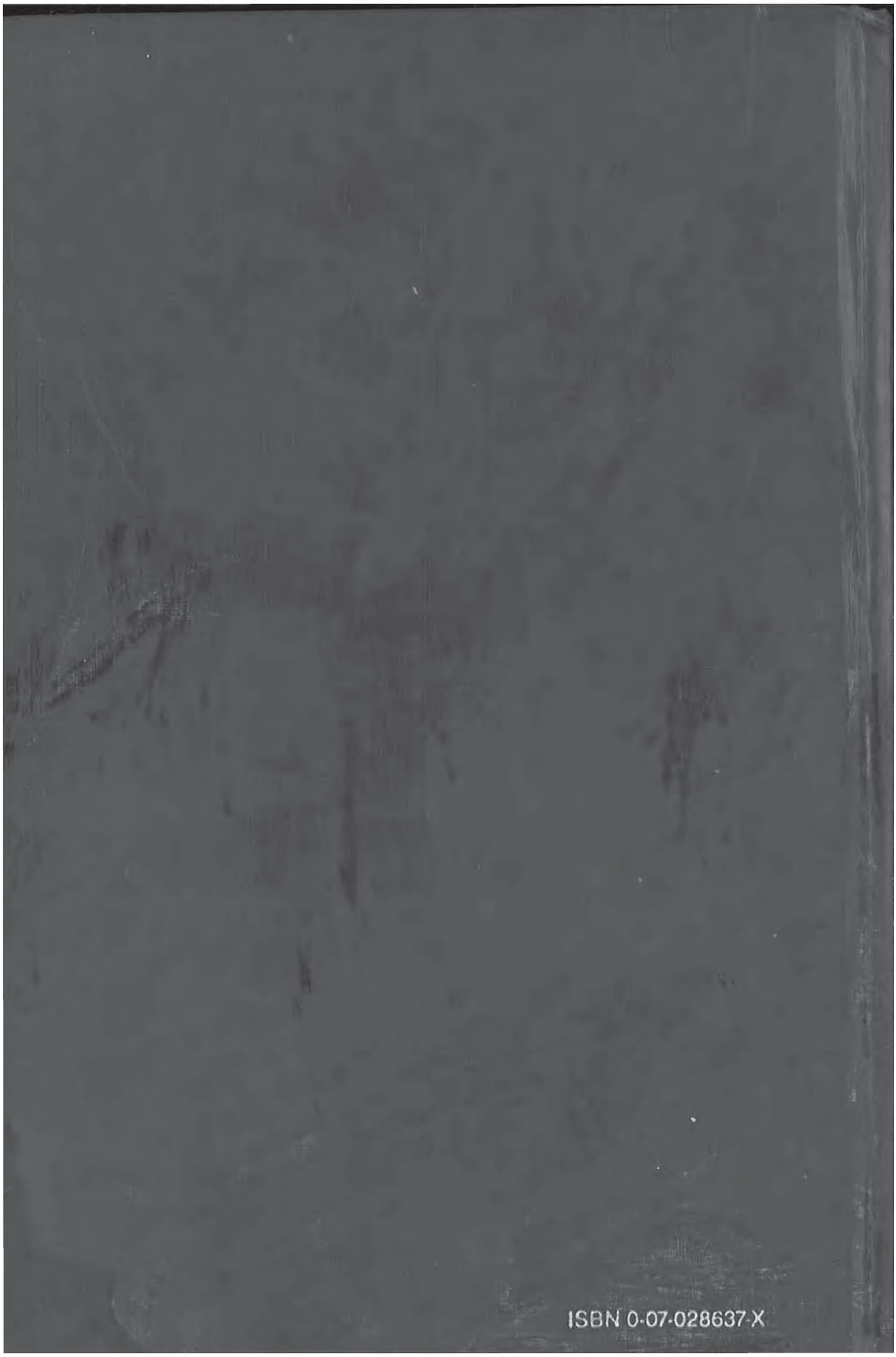
PETITIONER'S EXHIBIT 1002
US PATENT NO. 6,581,565

Unburned mixture:
composition, 102–107
properties, 112–116, 130–135
Unit conversion factors, 899–901

Valve:
choking, 217, 228
curtain area, 226
diameters, 222
discharge coefficient, 226–230
flow area, 222–224
flow pattern, 227, 229, 327–329, 333, 807–808
flow rate, 225–226, 231–232
geometry, 220–224
Mach index, 228
mean inlet Mach no., 228
overlap, 206, 224
pseudo flow velocity, 224–225
timing, 224–225
velocities, through, 327, 348–349, 808–810
Valve train configurations, 737–739
Valve train friction, 737–739
Volumetric efficiency:
correction factors for, 54–55
definition of, 53–54
effects of:
fuel factors, 210–211
heat transfer, 211, 217–218
manifold pressures, 211–216
runner length, 218
speed, 216–220, 761–762
valve timing, 215, 217–220
ideal cycle, 179, 209–212
and performance, 850–851

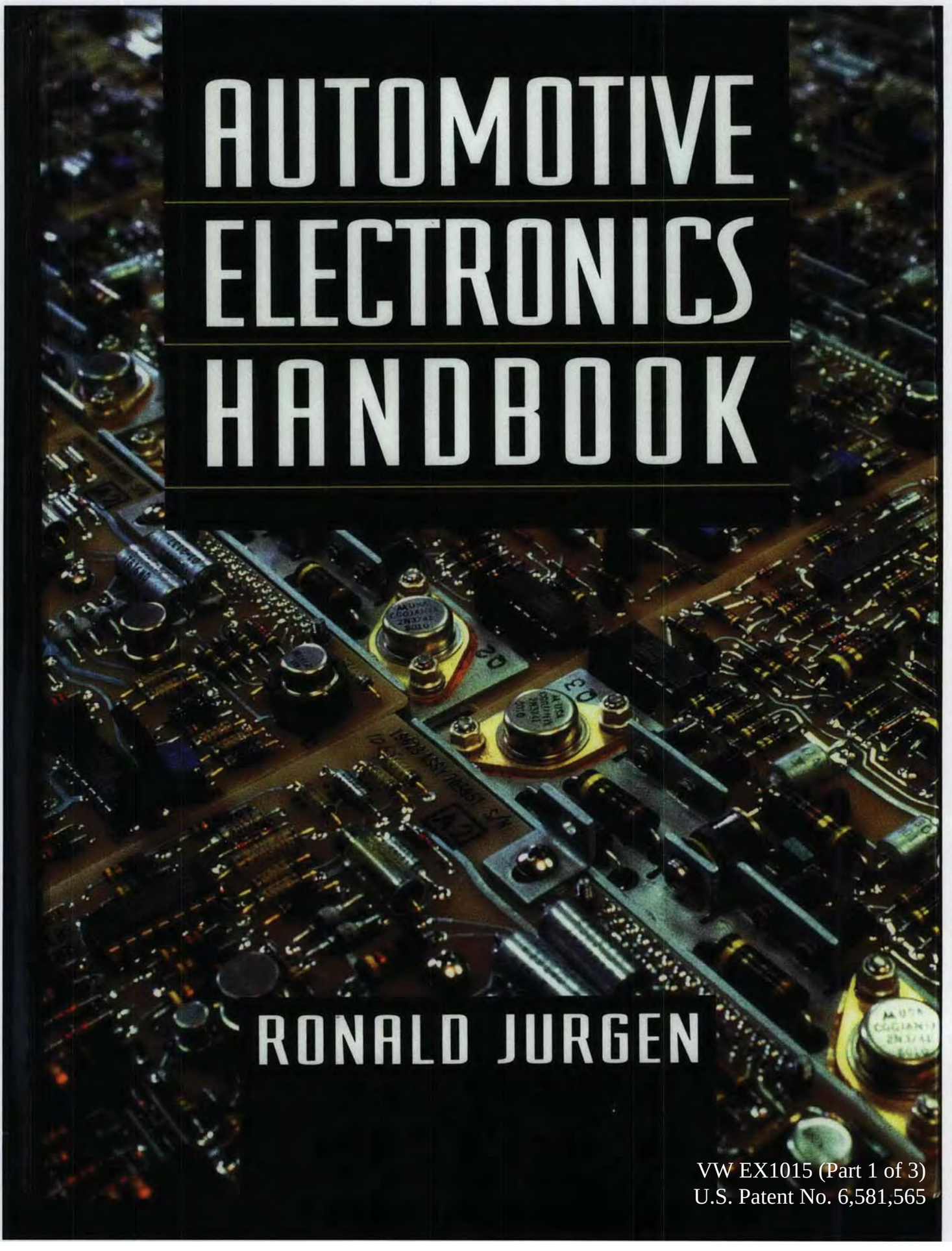
Wankel:
Felix, 4
rotary engine, 4
components, 23–25
example, 26
operation, 24–25
Wastegate, 270, 873, 875, 878
Weber number, 532
Work per cycle, indicated, 46–47, 164
Working fluids:
constituents, 100–102
properties and composition:
computer routines, 130–139
data on, 911–915
thermodynamic models, categories of, 101–102
(see also Air: Burned gas; Exhaust gas; Fuels; Gas properties; Unburned mixture)

PETITIONER'S EXHIBIT 1002
US PATENT NO. 6,581,565



PETITIONER'S EXHIBIT 1002
US PATENT NO. 6,581,565

AUTOMOTIVE ELECTRONICS HANDBOOK



RONALD JURGEN

VW EX1015 (Part 1 of 3)
U.S. Patent No. 6,581,565

PETITIONER'S EXHIBIT 1002
US PATENT NO. 6,581,565

AUTOMOTIVE ELECTRONICS HANDBOOK

JURGEN

EMS Lib

TL
272.5
A982
1995

PETITIONER'S EXHIBIT 1002
US PATENT NO. 6,581,565

AUTOMOTIVE ELECTRONICS HANDBOOK

PETITIONER'S EXHIBIT 1002
US PATENT NO. 6,581,565

Related McGraw-Hill Books of Interest

Handbooks

Avallone and Baumeister • MARK'S STANDARD HANDBOOK FOR MECHANICAL ENGINEERS
Benson • AUDIO ENGINEERING HANDBOOK
Brady • MATERIALS HANDBOOK
Chen • COMPUTER ENGINEERING HANDBOOK
Considine • PROCESS/INDUSTRIAL INSTRUMENTS AND CONTROL HANDBOOK
Coombs • PRINTED CIRCUITS HANDBOOK
Coombs • ELECTRONIC INSTRUMENT HANDBOOK
Di Giacomo • DIGITAL BUS HANDBOOK
Fink and Beaty • STANDARD HANDBOOK FOR ELECTRICAL ENGINEERS
Fink and Christiansen • ELECTRONICS ENGINEERS' HANDBOOK
Ganic • MCGRAW-HILL HANDBOOK OF ESSENTIAL ENGINEERING INFORMATION
Harper • ELECTRONIC PACKAGING AND INTERCONNECTION HANDBOOK
Harper and Sampson • ELECTRONIC MATERIALS AND PROCESSES HANDBOOK
Hicks • STANDARD HANDBOOK OF ENGINEERING CALCULATIONS
Hodson • MAYNARD'S INDUSTRIAL ENGINEERING HANDBOOK
Johnson • ANTENNA ENGINEERING HANDBOOK
Juran and Gryna • JURAN'S QUALITY CONTROL HANDBOOK
Kaufman and Seidman • HANDBOOK OF ELECTRONICS CALCULATIONS
Lenk • MCGRAW-HILL ELECTRONIC TESTING HANDBOOK
Lenk • LENK'S DIGITAL HANDBOOK
Mason • SWITCH ENGINEERING HANDBOOK
Schwartz • COMPOSITE MATERIALS HANDBOOK
Townsend • DUDLEY'S GEAR HANDBOOK
Tuma • ENGINEERING MATHEMATICS HANDBOOK
Waynant • ELECTRO-OPTICS HANDBOOK
Woodson • HUMAN FACTORS DESIGN HANDBOOK

Other

Boswell • SUBCONTRACTING ELECTRONICS
Gieck • ENGINEERING FORMULAS
Ginsberg • PRINTED CIRCUIT BOARD DESIGN
Johnson • ISO 9000
Lenk • MCGRAW-HILL CIRCUIT ENCYCLOPEDIA AND TROUBLESHOOTING GUIDE, VOLS. 1 AND 2
Lubben • JUST-IN-TIME MANUFACTURING
Markus and Sclater • MCGRAW-HILL ELECTRONICS DICTIONARY
Saylor • TQM FIELD MANUAL
Soin • TOTAL QUALITY CONTROL ESSENTIALS
Whitaker • ELECTRONIC DISPLAYS
Young • ROARK'S FORMULAS FOR STRESS AND STRAIN

To order or to receive additional information on these or any other McGraw-Hill titles, please call 1-800-822-8158 in the United States. In other countries, please contact your local McGraw-Hill office. **BC14BCZ**

PETITIONER'S EXHIBIT 1002
US PATENT NO. 6,581,565

AUTOMOTIVE ELECTRONICS HANDBOOK

Ronald K. Jurgen Editor in Chief

McGraw-Hill, Inc.

New York San Francisco Washington, D.C. Auckland Bogotá
Caracas Lisbon London Madrid Mexico City Milan
Montreal New Delhi San Juan Singapore
Sydney Tokyo Toronto

PETITIONER'S EXHIBIT 1002
US PATENT NO. 6,581,565

Library of Congress Cataloging-in-Publication Data

Automotive electronics handbook / Ronald Jurgen, editor in chief.
p. cm.
Includes index.
ISBN 0-07-033189-8
1. Automobiles—Electronic equipment. I. Jurgen, Ronald K.
TL272.5.A982 1994
629.25'49—dc 94-39724
CIP

Copyright © 1995 by McGraw-Hill, Inc. All rights reserved. Printed in the United States of America. Except as permitted under the United States Copyright Act of 1976, no part of this publication may be reproduced or distributed in any form or by any means, or stored in a data base or retrieval system, without the prior written permission of the publisher.

3 4 5 6 7 8 9 0 AGM/AGM 9 0 9 8 7 6 5

ISBN 0-07-033189-8

The sponsoring editor for this book was Stephen S. Chapman, the editing supervisor was Virginia Carroll, and the production supervisor was Suzanne W. B. Rapcavage. It was set in Times Roman by North Market Street Graphics.

Printed and bound by Arcata Graphics/Martinsburg.

McGraw-Hill books are available at special quantity discounts to use as premiums and sales promotions, or for use in corporate training programs. For more information, please write to the Director of Special Sales, McGraw-Hill, Inc., 11 West 19th Street, New York, NY 10011. Or contact your local bookstore.

Information contained in this work has been obtained by McGraw-Hill, Inc. from sources believed to be reliable. However, neither McGraw-Hill nor its authors guarantee the accuracy or completeness of any information published herein, and neither McGraw-Hill nor its authors shall be responsible for any errors, omissions, or damages arising out of use of this information. This work is published with the understanding that McGraw-Hill and its authors are supplying information, but are not attempting to render engineering or other professional services. If such services are required, the assistance of an appropriate professional should be sought.

This book is printed on acid-free paper.

PETITIONER'S EXHIBIT 1002
US PATENT NO. 6,581,565

EMS
LIB
TL
272.5
A982
1995

This book is dedicated to Robert H. Lewis and to the memories of Douglas R. Jurgen and Marion Schappel.

PETITIONER'S EXHIBIT 1002
US PATENT NO. 6,581,565

PETITIONER'S EXHIBIT 1002
US PATENT NO. 6,581,565

CONTENTS

Contributors xv
Preface xvii

Part 1 Introduction

Chapter 1. Introduction *Ronald K. Jurgen* 1.3

1.1 The Dawn of a New Era / *1.3*
1.2 The Microcomputer Takes Center Stage / *1.4*
1.3 Looking to the Future / *1.5*
References / *1.6*

Part 2 Sensors and Actuators

Chapter 2. Pressure Sensors *Randy Frank* 2.3

2.1 Automotive Pressure Measurements / *2.3*
2.2 Automotive Applications for Pressure Sensors / *2.5*
2.3 Technologies for Sensing Pressure / *2.15*
2.4 Future Pressure-Sensing Developments / *2.23*
Glossary / *2.24*
Bibliography / *2.24*

Chapter 3. Linear and Angle Position Sensors *Paul Nickson* 3.1

3.1 Introduction / *3.1*
3.2 Classification of Sensors / *3.1*
3.3 Position Sensor Technologies / *3.2*
3.4 Interfacing Sensors to Control Systems / *3.16*
Glossary / *3.17*
References / *3.17*

Chapter 4. Flow Sensors *Robert E. Bicking* 4.1

4.1 Introduction / *4.1*
4.2 Automotive Applications of Flow Sensors / *4.1*
4.3 Basic Classification of Flow Sensors / *4.3*
4.4 Applicable Flow Measurement Technologies / *4.4*
Glossary / *4.8*
Bibliography / *4.9*

PETITIONER'S EXHIBIT 1002
US PATENT NO. 6,581,565

Chapter 5. Temperature, Heat, and Humidity Sensors *Randy Frank* 5.1

5.1 Temperature, Heat, and Humidity / *5.1*
5.2 Automotive Temperature Measurements / *5.5*
5.3 Humidity Sensing and Vehicle Performance / *5.12*
5.4 Sensors for Temperature / *5.14*
5.5 Humidity Sensors / *5.21*
5.6 Conclusions / *5.22*
Glossary / *5.23*
Bibliography / *5.23*

Chapter 6. Exhaust Gas Sensors *Hans-Martin Wiedenmann, Gerhard Hötzel, Harald Neumann, Johann Riegel, and Helmut Weyl* 6.1

6.1 Basic Concepts / *6.1*
6.2 Principles of Exhaust Gas Sensors for Lambda Control / *6.5*
6.3 Technology of Ceramic Exhaust Gas Sensors / *6.11*
6.4 Factors Affecting the Control Characteristics of Lambda = 1 Sensors / *6.14*
6.5 Applications / *6.18*
6.6 Sensor Principles for Other Exhaust Gas Components / *6.20*
Bibliography / *6.22*

Chapter 7. Speed and Acceleration Sensors *William C. Dunn* 7.1

7.1 Introduction / *7.1*
7.2 Speed-Sensing Devices / *7.2*
7.3 Automotive Applications for Speed Sensing / *7.6*
7.4 Acceleration Sensing Devices / *7.8*
7.5 Automotive Applications for Accelerometers / *7.18*
7.6 New Sensing Devices / *7.22*
7.7 Future Applications / *7.24*
7.8 Summary / *7.26*
Glossary / *7.27*
References / *7.28*

Chapter 8. Engine Knock Sensors *William G. Wolber* 8.1

8.1 Introduction / *8.1*
8.2 The Knock Phenomenon / *8.2*
8.3 Technologies for Sensing Knock / *8.4*
8.4 Summary / *8.9*
Glossary / *8.9*
References / *8.9*

Chapter 9. Engine Torque Sensors *William G. Wolber* 9.1

9.1 Introduction / *9.1*
9.2 Automotive Applications of Torque Measurement / *9.3*
9.3 Direct Torque Sensors / *9.6*
9.4 Inferred Torque Measurement / *9.8*
9.5 Summary / *9.13*
Glossary / *9.13*
References / *9.14*

PETITIONER'S EXHIBIT 1002
US PATENT NO. 6,581,565

Chapter 10. Actuators *Klaus Müller* 10.1

10.1 Preface / *10.1*
10.2 Types of Electromechanical Actuators / *10.2*
10.3 Automotive Actuators / *10.19*
10.4 Technology for Future Application / *10.27*
Acknowledgments / *10.30*
Glossary / *10.30*
Bibliography / *10.31*

Part 3 Control Systems

Chapter 11. Automotive Microcontrollers *David S. Boehmer* 11.3

11.1 Microcontroller Architecture and Performance Characteristics / *11.3*
11.2 Memory / *11.24*
11.3 Low-Speed Input/Output Ports / *11.31*
11.4 High-Speed I/O Ports / *11.36*
11.5 Serial Communications / *11.41*
11.6 Analog-to-Digital Converter / *11.45*
11.7 Failsafe Methodologies / *11.49*
11.8 Future Trends / *11.51*
Glossary / *11.54*
Bibliography / *11.55*

Chapter 12. Engine Control *Gary C. Hirschlieb, Gottfried Schiller, and Shari Stottler* 12.1

12.1 Objectives of Electronic Engine Control Systems / *12.1*
12.2 Spark Ignition Engines / *12.5*
12.3 Compression Ignition Engines / *12.32*

Chapter 13. Transmission Control *Kurt Neuffer, Wolfgang Bullmer, and Werner Brehm* 13.1

13.1 Introduction / *13.1*
13.2 System Components / *13.2*
13.3 System Functions / *13.7*
13.4 Communications with Other Electronic Control Units / *13.17*
13.5 Optimization of the Drivetrain / *13.18*
13.6 Future Developments / *13.19*
Glossary / *13.20*
References / *13.20*

Chapter 14. Cruise Control *Richard Valentine* 14.1

14.1 Cruise Control System / *14.1*
14.2 Microcontroller Requirements for Cruise Control / *14.3*
14.3 Cruise Control Software / *14.4*
14.4 Cruise Control Design / *14.6*
14.5 Future Cruise Concepts / *14.7*
Glossary / *14.8*
Bibliography / *14.8*

PETITIONER'S EXHIBIT 1002
US PATENT NO. 6,581,565

Chapter 15. Braking Control *Jerry L. Cage* 15.1

15.1 Introduction / *15.1*
15.2 Vehicle Braking Fundamentals / *15.1*
15.3 Antilock Systems / *15.8*
15.4 Future Vehicle Braking Systems / *15.14*
Glossary / *15.15*
References / *15.16*

Chapter 16. Traction Control *Armin Czinczel* 16.1

16.1 Introduction / *16.1*
16.2 Forces Affecting Wheel Traction: Fundamental Concepts / *16.3*
16.3 Controlled Variables / *16.5*
16.4 Control Modes / *16.6*
16.5 Traction Control Components / *16.11*
16.6 Applications on Heavy Commercial Vehicles / *16.13*
16.7 Future Trends / *16.14*
Glossary / *16.14*
Bibliography / *16.15*

Chapter 17. Suspension Control *Akatsu Yohsuke* 17.1

17.1 Shock Absorber Control System / *17.1*
17.2 Hydropneumatic Suspension Control System / *17.4*
17.3 Electronic Leveling Control System / *17.5*
17.4 Active Suspension / *17.8*
17.5 Conclusion / *17.17*
Glossary / *17.18*
Nomenclature / *17.18*
Bibliography / *17.18*

Chapter 18. Steering Control *Makoto Sato* 18.1

18.1 Variable-Assist Steering / *18.1*
18.2 Four-Wheel Steering Systems (4WS) / *18.15*
Glossary / *18.33*
References / *18.33*

Chapter 19. Lighting, Wipers, Air Conditioning/Heating
Richard Valentine 19.1

19.1 Lighting Controls / *19.1*
19.2 Windshield Wiper Control / *19.9*
19.3 Air Conditioner/Heater Control / *19.15*
19.4 Miscellaneous Load Control Reference / *19.20*
19.5 Future Load Control Concepts / *19.25*
Glossary / *19.26*
Bibliography / *19.27*

PETITIONER'S EXHIBIT 1002
US PATENT NO. 6,581,565

Part 4 Displays and Information Systems

Chapter 20. Instrument Panel Displays *Ronald K. Jurgen* 20.3

20.1 The Evolution to Electronic Displays / *20.3*
20.2 Vacuum Fluorescent Displays / *20.3*
20.3 Liquid Crystal Displays / *20.4*
20.4 Cathode-Ray Tube Displays / *20.6*
20.5 Head-up Displays / *20.6*
20.6 Electronic Analog Displays / *20.8*
20.7 Reconfigurable Displays / *20.9*
References / *20.9*

Chapter 21. Trip Computers *Ronald K. Jurgen* 21.1

21.1 Trip Computer Basics / *21.1*
21.2 Specific Trip Computer Designs / *21.2*
21.3 Conclusion / *21.4*
References / *21.6*

Chapter 22. On- and Off-Board Diagnostics *Wolfgang Bremer, Frieder Heintz, and Robert Hugel* 22.1

22.1 Why Diagnostics? / *22.1*
22.2 On-Board Diagnostics / *22.6*
22.3 Off-Board Diagnostics / *22.7*
22.4 Legislation and Standardization / *22.8*
22.5 Future Diagnostic Concepts / *22.15*
Glossary / *22.18*
References / *22.19*

Part 5 Safety, Convenience, Entertainment, and Other Systems

Chapter 23. Passenger Safety and Convenience *Bernhard K. Mattes* 23.3

23.1 Passenger Safety Systems / *23.3*
23.2 Passenger Convenience Systems / *23.11*
Glossary / *23.13*
Bibliography / *23.13*

Chapter 24. Antitheft Systems *Shinichi Kato* 24.1

24.1 Vehicle Theft Circumstances / *24.1*
24.2 Overview of Antitheft Regulations / *24.2*
24.3 A Basic Antitheft System / *24.3*

PETITIONER'S EXHIBIT 1002
US PATENT NO. 6,581,565

Chapter 25. Entertainment Products *Tom Chrapkiewicz* 25.1

25.1 Fundamentals of Audio Systems / *25.1*
25.2 A Brief History of Automotive Entertainment / *25.4*
25.3 Contemporary Audio Systems / *25.5*
25.4 Future Trends / *25.12*
Glossary / *25.17*
References / *25.18*

Chapter 26. Multiplex Wiring Systems *Fred Miesterfeld* 26.1

26.1 Vehicle Multiplexing / *26.1*
26.2 Encoding Techniques / *26.9*
26.3 Protocols / *26.23*
26.4 Summary and Conclusions / *26.53*
Glossary / *26.56*
References / *26.64*

Part 6 Electromagnetic Interference and Compatibility

Chapter 27. Electromagnetic Standards and Interference *James P. Muccioli* 27.3

27.1 SAE Automotive EMC Standards / *27.3*
27.2 IEEE Standards Related to EMC / *27.11*
27.3 The Electromagnetic Environment of an Automobile Electronic System / *27.13*
Bibliography / *27.18*

Chapter 28. Electromagnetic Compatibility *James P. Muccioli* 28.1

28.1 Noise Propagation Modes / *28.1*
28.2 Cabling / *28.2*
28.3 Components / *28.4*
28.4 Printed Circuit Board EMC Checklist / *28.9*
28.5 Integrated Circuit Decoupling—A Key Automotive EMI Concern / *28.10*
28.6 IC Process Size Affects EMC / *28.14*
Bibliography / *28.19*

Part 7 Emerging Technologies

Chapter 29. Navigation Aids and Intelligent Vehicle-Highway Systems *Robert L. French* 29.3

29.1 Background / *29.3*
29.2 Automobile Navigation Technologies / *29.4*
29.3 Examples of Navigation Systems / *29.10*
29.4 Other IVHS Systems and Services / *29.15*
References / *29.18*

PETITIONER'S EXHIBIT 1002
US PATENT NO. 6,581,565

Chapter 30. Electric and Hybrid Vehicles *George G. Karady, Tracy Blake, Raymond S. Hobbs, and Donald B. Karner* **30.1**

30.1 Introduction / *30.1*
30.2 System Description / *30.5*
30.3 Charger and Protection System / *30.6*
30.4 Motor Drive System / *30.8*
30.5 Battery / *30.17*
30.6 Vehicle Control and Auxiliary Systems / *30.19*
30.7 Infrastructure / *30.21*
30.8 Hybrid Vehicles / *30.23*
Glossary / *30.24*
References / *30.25*

Chapter 31. Noise Cancellation Systems *Jeffrey N. Denenberg* **31.1**

31.1 Noise Sources / *31.1*
31.2 Applications / *31.5*
Glossary / *31.10*
Bibliography / *31.10*

Chapter 32. Future Vehicle Electronics *Randy Frank and Salim Momin* **32.1**

32.1 Retrospective / *32.1*
32.2 IC Technology / *32.1*
32.3 Other Semiconductor Technologies / *32.5*
32.4 Enabling the Future / *32.11*
32.5 Impact on Future Automotive Electronics / *32.15*
32.6 Conclusions / *32.20*
Glossary / *32.21*
Bibliography / *32.23*

Index / *I.1*

PETITIONER'S EXHIBIT 1002
US PATENT NO. 6,581,565

PETITIONER'S EXHIBIT 1002
US PATENT NO. 6,581,565

CONTRIBUTORS

Robert E. Bicking *Honeywell, Micro Switch Division* (CHAP. 4)
Tracy Blake *Arizona State University* (CHAP. 30)
David S. Boehmer *Intel Corporation* (CHAP. 11)
Werner Brehm *Robert Bosch GmbH* (CHAP. 13)
Wolfgang Bremer *Robert Bosch GmbH* (CHAP. 22)
Wolfgang Bullmer *Robert Bosch GmbH* (CHAP. 13)
Jerry L. Cage *Allied Signal, Inc.* (CHAP. 15)
Tom Chrapkiewicz *Philips Semiconductor* (CHAP. 25)
Armin Czinczel *Robert Bosch GmbH* (CHAP. 16)
Jeffrey N. Denenberg *Noise Cancellation Technologies, Inc.* (CHAP. 31)
William C. Dunn *Motorola Semiconductor Products* (CHAP. 7)
Randy Frank *Motorola Semiconductor Products* (CHAPS. 2, 5, 32)
Robert L. French *R. L. French & Associates* (CHAP. 29)
Frieder Heintz *Robert Bosch GmbH* (CHAP. 22)
Gary C. Hirschlieb *Robert Bosch GmbH* (CHAP. 12)
Raymond S. Hobbs *Arizona Public Service Company* (CHAP. 30)
Gerhard Hötzel *Robert Bosch GmbH* (CHAP. 6)
Robert Hugel *Robert Bosch GmbH* (CHAP. 22)
Ronald K. Jurgen *Editor* (CHAPS. 1, 20, 21)
George G. Karady *Arizona State Univeristy* (CHAP. 30)
Donald B. Karner *Electric Transportation Application* (CHAP. 30)
Shinichi Kato *Nissan Motor Co., Ltd.* (CHAP. 24)
Bernhard K. Mattes *Robert Bosch GmbH* (CHAP. 23)
Fred Miesterfeld *Chrysler Corporation* (CHAP. 26)
Salim Momin *Motorola Semiconductor Products* (CHAP. 32)
James P. Muccioli *JASTECH* (CHAPS. 27, 28)
Klaus Müller *Robert Bosch GmbH* (CHAP. 10)
Kurt Neuffer *Robert Bosch GmbH* (CHAP. 13)
Harald Neumann *Robert Bosch GmbH* (CHAP. 6)
Paul Nickson *Analog Devices, Inc.* (CHAP. 3)
Johann Riegel *Robert Bosch GmbH* (CHAP. 6)

PETITIONER'S EXHIBIT 1002
US PATENT NO. 6,581,565

Makoto Sato *Honda R&D Co., Ltd.* (CHAP. 18)
Gottfried Schiller *Robert Bosch GmbH* (CHAP. 12)
Shari Stottler *Robert Bosch GmbH* (CHAP. 12)
Richard Valentine *Motorola Inc.* (CHAPS. 14, 19)
Helmut Weyl *Robert Bosch GmbH* (CHAP. 6)
Hans-Martin Wiedenmann *Robert Bosch GmbH* (CHAP. 6)
William G. Wolber *Cummins Electronics Co., Inc.* (CHAPS. 8, 9)
Akatsu Yohsuke *Nissan Motor Co., Ltd.* (CHAP. 17)

PETITIONER'S EXHIBIT 1002
US PATENT NO. 6,581,565

PREFACE

Automotive electronics as we know it today encompasses a wide variety of devices and systems. Key to them all, and those yet to come, is the ability to sense and measure accurately automotive parameters. Equally important at the output is the ability to initiate control actions accurately in response to commands. In other words, sensors and actuators are the heart of any automotive electronics application. That is why they have been placed first in this handbook where they are described in technical depth. In other chapters, application-specific discussions of sensors and actuators can be found.

The importance of sensors and actuators cannot be overemphasized. The future growth of automotive electronics is arguably more dependent on sufficiently accurate and low-cost sensors and actuators than on computers, controls, displays, and other technologies. Yet it is those nonsensor, nonactuator technologies that are to many engineers the more "glamorous" and exciting areas of automotive electronics.

In the section on control systems, a key in-depth chapter deals with automotive microcontrollers. Without them, all of the controls described in the chapters that follow in that section—engine, transmission, cruise, braking, traction, suspension, steering, lighting, windshield wipers, air conditioner/heater—would not be possible. Those controls, of course, are key to car operation and they have made cars over the years more drivable, safe, and reliable.

Displays, trip computers, and on- and off-board diagnostics are described in another section, as are systems for passenger safety and convenience, antitheft, entertainment, and multiplex wiring. Displays and trip computers enable the driver to readily obtain valuable information about the car's operation and anticipated trip time. On- and off-board diagnostics have of necessity become highly sophisticated to keep up with highly sophisticated electronic controls. Passenger safety and convenience items and antitheft devices add much to the feeling of security and pleasure in owning an automobile. Entertainment products are what got automotive electronics started and they continue to be in high demand by car buyers. And multiplex wiring, off to a modest start in production cars, holds great promise for the future in reducing the cumbersome wiring harnesses presently used.

The section on electromagnetic interference and compatibility emphasizes that interference from a variety of sources, if not carefully taken into account early on, can raise havoc with what otherwise would be elegant automotive electronic designs. And automotive systems themselves, if not properly designed, can cause interference both inside and outside the automobile.

In the final section on emerging technologies, some key newer areas are presented:

- Navigation aids and intelligent vehicle-highway systems are of high interest worldwide since they hold promise to alleviate many of vehicle-caused problems and frustrations in our society.
- While it may be argued that electric vehicles are not an emerging technology, since they have been around for many years, it certainly is true that they have yet to come into their own in any really meaningful way.
- Electronic noise cancellation is getting increasing attention from automobile designers seeking an edge over their competitors.

PETITIONER'S EXHIBIT 1002
US PATENT NO. 6,581,565

The final chapter on future vehicle electronics is an umbrella discussion that runs the gamut of trends in future automotive electronics hardware and software. It identifies potential technology developments and trends for future systems.

Nearly every chapter contains its own glossary of terms. This approach, rather than one overall unified glossary, has the advantage of allowing terms to be defined in a more application-specific manner—in the context of the subject of each chapter. It should also be noted that there has been no attempt in this handbook to cover, except peripherally, purely mechanical and electrical devices and systems. To do so would have restricted the number of pages available for automotive electronics discussions.

Finally, the editor would like to thank all contributors to the handbook and particularly two individuals: Otto Holzinger of Robert Bosch GmbH in Stuttgart, Germany and Randy Frank of Motorola Semiconductor Products in Phoenix, Arizona. Holzinger organized the many contributions to this handbook from his company. Frank, in addition to contributing two chapters himself and cocontributing a third, organized the other contributions from Motorola. Without their help, this handbook would not have been possible.

Ronald K. Jurgen

PETITIONER'S EXHIBIT 1002
US PATENT NO. 6,581,565

AUTOMOTIVE ELECTRONICS HANDBOOK

PETITIONER'S EXHIBIT 1002
US PATENT NO. 6,581,565

PETITIONER'S EXHIBIT 1002
US PATENT NO. 6,581,565

P · A · R · T · 1

INTRODUCTION

PETITIONER'S EXHIBIT 1002
US PATENT NO. 6,581,565

PETITIONER'S EXHIBIT 1002
US PATENT NO. 6,581,565

CHAPTER 1
INTRODUCTION

Ronald K. Jurgen
Editor

1.1 THE DAWN OF A NEW ERA

In today's world of sophisticated automotive electronics, it is easy to forget how far the technology has come in a relatively short time. In the early 1970s, other than radios and tape players, the only standard electronic components and systems on most automobiles were alternator diodes and voltage regulators.[1] By the fall of 1974, "there were twelve electronic systems available, none of which were across the board standard production items. . . . The twelve electronic systems or subsystems were: alternator diodes, voltage regulators, electronic fuel injection, electronic controlled ignition, intermittent windshield wipers, cruise control, wheel lock control, traction control, headlamp control, climate control, digital clocks, and air bag crash sensors."[1]

1.1.1 Car Makers and the Electronics Industry: Friendly Adversaries

In the early days of automotive electronics, the automotive industry and the electronics industry were often at odds. Carmakers needed inexpensive components and systems that would operate reliably in the extremely harsh automotive environment. The electronics industry, on the other hand, used to producing high-quality but expensive parts and systems for the military, was skeptical about its ability to produce the components the automobile industry wanted at the prices they demanded. But both industries realized that electronics could provide the capability to solve automotive problems that defied conventional mechanical or electromechanical approaches.

Some of the leading electronics engineers who worked in the automotive industry—as well as their counterparts in the electronics industry—realized that this existing friendly adversarial relationship had to be converted to a mutual effort to find cost-effective and reliable solutions to urgent automotive problems.

Thus it was in 1973 that Trevor Jones (then with General Motors), Joseph Ziomek (then with Ford), Ted Schaller (Allen Bradley), Jerry Rivard (then with Bendix), Oliver McCarter (General Motors), and William Saunders (Society of Automotive Engineers), proposed that a new conference be held in 1974.[1] Dubbed Convergence to signify the coming together of the two industries, the first conference was successful and, sponsored alternately by the Society of Automotive Engineers and the Institute of Electrical and Electronics Engineers, it has been held successfully every other year ever since.

PETITIONER'S EXHIBIT 1002
US PATENT NO. 6,581,565

1.1.2 The United States Government Forces the Issue

One of the major problems facing the automotive industry at the time of the first Convergence conference was upcoming stricter government-mandated exhaust emissions controls. When the United States government first mandated emissions standards for all United States cars, car makers met the challenge through the use of catalytic converters for hydrocarbon and carbon monoxide emissions and exhaust gas recirculation techniques for nitrogen oxides emissions. But they knew that in 1981, when the standards would be tightened from the previous limit of 2.0 grams per mile to 1.0 gram per mile, those approaches would no longer in themselves be sufficient. A new approach was necessary and it involved use of a three-way catalyst for all three emissions together with a closed-loop, engine control system.[2]

Tighter emissions control solved one problem but created another—fuel economy. The two seemed to be mutually exclusive. Charles M. Heinen and Eldred W. Beckman, writing in *IEEE Spectrum* in 1977,[3] said, "The simple truth is that there is very direct interaction between emissions and fuel economy. Probably the clearest example of that interaction is the fact that automobiles equipped to meet California's tight emissions control regulations have consistently demonstrated about 10 percent poorer fuel economy than have comparable cars equipped to meet the less stringent Federal U.S. standards." As a result of this interdependence, emissions and fuel economy measures tended to be compromises. Greater fuel economies could be achieved if emissions levels were not a problem.

1.2 THE MICROCOMPUTER TAKES CENTER STAGE

The microcomputer, introduced in 1971, had yet to make major inroads in automobiles. But it became increasingly obvious that it was the key to meeting government exhaust emission and fuel economy demands while also providing car buyers with cars that performed well. Meeting these needs necessitated precise engine control in such areas as the air/fuel ratio and idle speed.

1.2.1 Early Applications of Microcomputers

One of the first microcomputer applications in cars was an advanced ignition system built by Delco-Remy for the 1977 Oldsmobile Toronado. Called the MISAR (microprocessed sensing and automatic regulation) system, it controlled spark timing precisely no matter what load and speed conditions prevailed while meeting emissions control requirements and providing good driveability. Input signals from sensors provided data on crankshaft position, manifold vacuum, coolant temperature, and reference timing.[4] The microprocessor used had a capacity of 10,240 bits.

Early applications such as the MISAR paved the ground for what would later become the prolific use of microcomputers in cars. Once reliable microcomputers met the cost restraints of carmakers, there was no end in sight to microcomputer applications in cars. In the late 1970s, total engine control with microcomputers became widespread and, as time went on, use of microcomputers spread to other controls for transmission, braking, traction, suspension, steering, lighting, air conditioning, and so forth.

1.2.2 The Bells and Whistles Period

There was also a time in the early 1980s when carmakers, heady with success with microcomputers in other areas, went through a period of electronic overkill. Notable in this regard were voice commands and warnings that tended to wear out their welcome quickly with car drivers

PETITIONER'S EXHIBIT 1002
US PATENT NO. 6,581,565

and elaborate and flashy information displays that also turned off many car buyers. It was a period of doing things with microcomputers because they could be done rather than doing them because they were needed.

That overindulgent microcomputer period quickly waned as car buyers made their feelings known. Voice commands were all but totally abandoned and displays were made less garish. There was even a return to analog displays for speedometers, for example, albeit electronically based rather than the old mechanical or electromechanical system. Carmakers returned to using microcomputers in truly functional ways to answer real needs.

1.3 LOOKING TO THE FUTURE

The future for automotive electronics is bright. Electronic solutions have proven to be reliable over time and have enabled carmakers to solve problems otherwise unsolvable. But what does the future hold? Some predictions for the future have been discussed in the following pages by contributors.

1.3.1 Contributors' Predictions

Although there have been many significant automotive electronics advances over the years, the end is certainly not in sight. The final chapter in this handbook describes many upcoming advances in detail. Authors Frank and Momin, for example, state that a likely future scenario "will be a combination of centralization and distributed intelligence where the centralization would be based along the lines of body, chassis and safety, powertrain, and audio/entertainment and communications. Within these centralized systems would be distributed intelligence based on multiplex wiring with smart sensors, switch decoders, and smart actuators all controlled by a central intelligence."

Here are additional selected future developments cited by contributors in other chapters:

- Expansion of the air bag system to include side impact protection (Dunn, Chap. 7)
- Magnetic transistors and diodes that can be directly integrated with signal conditioning circuits (Dunn, Chap. 7)
- Electronic switched stop lamps involving a rate-of-closure detector system to determine if the vehicle's speed is safe for objects ahead of it. If the closure rate is unsafe, the stop lights could be activated to alert trailing drivers to a pending accident (Valentine, Chap. 14)
- The integration of watchdog and failsafe functions onto a microcontroller (Boehmer, Chap. 11)
- Microcontrollers that operate at frequencies of 24 MHz or 32 MHz to allow more code to be executed in the same amount of time (Boehmer, Chap. 11)
- In the mid-90s, cars will have twice the electronic content of today's cars but will be easier to manufacture because there will be half the number of modules due to feature content integration. The data network interconnecting the modules will reduce the size and number of cables and cut the number of circuits by 50 percent (Miesterfeld, Chap. 26)
- A move from switching units to stepped operation actuators and the substitution of continuous for discrete time control (Müller, Chap. 10)
- Electrorheological and magnetorheological fluid actuators (Müller, Chap. 10)
- Micromechanical valves as actuators for converting low control power as in regulating the flow of fluids in hydraulic or pneumatic systems (Müller, Chap. 10)

PETITIONER'S EXHIBIT 1002
US PATENT NO. 6,581,565

REFERENCES

1. Trevor O. Jones, "Convergence—past and future," *Proceedings*, 1992 International Congress on Transportation Electronics (Convergence), P-260, Society of Automotive Engineers, Inc., Warrendale, Pa., Oct. 1992, pp. 1–3.
2. George W. Niepoth, and Stonestreet, Stephen P., "Closed-loop engine control," *IEEE Spectrum*, Nov. 1977, pp. 52–55.
3. Charles M. Heiner, and Beckman, Eldred W., "Balancing clean air against good mileage," *IEEE Spectrum*, Nov. 1977, pp. 46–50.
4. Trevor O. Jones, "Automotive electronics I: smaller and better," *IEEE Spectrum*, Nov. 1977, pp. 34–35.

PETITIONER'S EXHIBIT 1002
US PATENT NO. 6,581,565

P · A · R · T · 2

SENSORS AND ACTUATORS

PETITIONER'S EXHIBIT 1002
US PATENT NO. 6,581,565

PETITIONER'S EXHIBIT 1002
US PATENT NO. 6,581,565

CHAPTER 2
PRESSURE SENSORS

Randy Frank
Technical Marketing Manager
Motorola Semiconductor Products

2.1 AUTOMOTIVE PRESSURE MEASUREMENTS

Various pressure measurements are required in both the development and usage of vehicles to optimize performance, determine safe operation, assure conformance to government regulations, and advise the driver. These sensors monitor vehicle functions, provide information to control systems, and measure parameters for indication to the driver. The sensors can also provide data log information for diagnostic purposes.

Depending on the parameter being measured, different units for indicating pressure will be used. Since pressure is force per unit area, basic units are pounds per square inch (psi) or kilograms per square centimeter. For example, tire pressure is usually indicated in psi. Manifold pressure is typically specified in kiloPascals (kPa). A Pascal, which is the international unit (SI or Systems Internationale) for pressure, is equal to 1 Newton per meter^2 or 1 kg · m^{-1} · s^{-2}. Other common units of pressure measurement include: inches, feet, or centimeters of water; millibars or bars, inches, or millimeters of mercury (Hg), and torr. The conversion constants as defined per international convention are indicated in Table 2.1.

Pressure can be measured by a number of devices that provide a predictable variation when pressure is applied. Sensors used on vehicles range from mechanical devices—with position movement when pressure is applied—to a rubber or elastomer diaphragm, to semiconductor-based silicon pressure sensors. Various pressure-sensing techniques are explained in Sec. 2.3.

The type of pressure measurement that is made can be divided into five basic areas which are independent of the technology used for the measurement: gage, absolute, differential, liquid level, and pressure switch.

2.1.1 Gage Pressure Measurements

The silicon pressure sensor technology explained in Sec. 2.3.5 is used to visualize the difference between gage, absolute, and differential pressure (refer to Fig. 2.1). For gage pressure measurements, the pressure is applied to the top of a (silicon) diaphragm (Fig. 2.1), creating a positive output. The opposite (back) side of the diaphragm is exposed to atmospheric pressure. Gage vacuum is a special case of gage pressure. For gage vacuum measurements, vacuum is applied to the back side of the diaphragm resulting in a positive output signal. Gage and gage vacuum are single-sided pressure measurements. Gage pressure is frequently indicated by psig.

PETITIONER'S EXHIBIT 1002
US PATENT NO. 6,581,565

TABLE 2.1 Pressure Unit Conversion Constants

(Most commonly used per international conventions)

	psi*	In $H_2O^{\dagger}$	In $Hg^{\ddagger}$	K Pascal	Millibar	cm $H_2O^{\S}$	mm $Hg^{\P}$
psi*	1.000	27.680	2.036	6.8947	68.947	70.308	51.715
In $H_2O^{\dagger}$	3.6127×10^{-2}	1.000	7.3554×10^{-2}	0.2491	2.491	2.5400	1.8683
In $Hg^{\ddagger}$	0.4912	13.596	1.000	3.3864	33.864	34.532	25.400
K Pascal	0.14504	4.0147	0.2953	1.000	10.000	10.1973	7.5006
Millibar	0/01450	0.40147	0.02953	0.100	1.000	1.01973	0.75006
cm $H_2O^{\S}$	1.4223×10^{-2}	0.3937	2.8958×10^{-2}	0.09806	0.9806	1.000	0.7355
mm $Hg^{\P}$	1.9337×10^{-2}	0.53525	3.9370×10^{-2}	0.13332	1.3332	1.3595	1.000

* PSI = pounds per square inch
† At 39 °F
‡ At 32 °F
§ At 4 °C
¶ At 0 °C

2.1.2 Absolute Pressure Measurements

An absolute pressure measurement is made with respect to a fixed (usually a vacuum) reference sealed within the sensor (Fig. 2.1). For a 100-kPa-rated absolute unit, the diaphragm is fully deflected with standard atmospheric pressure. Application of a vacuum restores the diaphragm to its undeflected (flat) position. The result is a high-level output with no vacuum applied and a low-level signal at full vacuum unless the zero is established at the full-scale deflection of the diaphragm. Pressure can also be applied to absolute units with appropriately designed diaphragms to withstand the additional applied stress. Absolute pressure is frequently indicated by psia.

2.1.3 Differential Pressure Measurements

Differential or Delta-P measurements are also shown in Fig. 2.1. The higher pressure is applied to the top of the diaphragm and the lower pressure, possibly a reference pressure, is applied to the opposite side. The diaphragm's deflection is a result of the pressure difference.

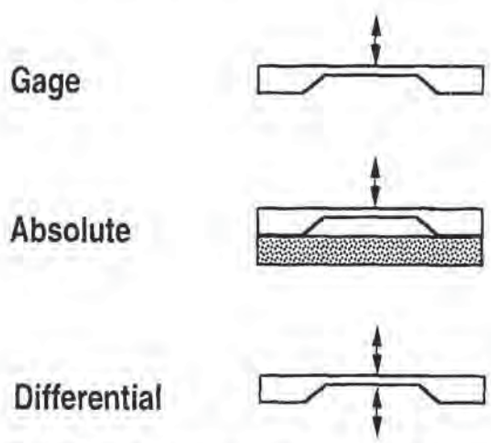


FIGURE 2.1 Types of pressure measurements: (*a*) gage, (*b*) absolute, and (*c*) differential.

PETITIONER'S EXHIBIT 1002
US PATENT NO. 6,581,565

Typically, the pressure differential is only a small percentage of the total line pressure and a system fault can expose one side of the sensor to the full line pressure. This must be taken into account when choosing the sensor and determining the rated pressure range that will be required. Differential pressure is frequently indicated by psid.

2.1.4 Liquid Level Measurements

The height of a column of liquid can be measured by a pressure sensor. The term *head* is frequently used in hydraulics to denote pressure. Measurements of inches or feet of water and centimeters of mercury are direct indications of the effect of pressure on liquid level. Other liquid levels are dependent on their specific weight and can be calculated by $h = (P_L - P_H)/w$, where $(P_L - P_L)$ is the pressure differential caused by the height of the fluid column and w is the specific weight of the liquid. The vapor pressure in a sealed enclosure will have an effect on the measurement of liquid height. Returning the reference side of a differential pressure sensor to the top of the enclosure will compensate for vapor pressure.

2.1.5 Pressure Switch

A pressure switch is typically achieved by mounting an electric contact on a diaphragm (rubber or any elastic material). The application of sufficient pressure (or vacuum) on one side of the diaphragm causes the movable contact to meet a stationary contact and close the circuit.

A pressure switch can also be achieved by any of the previously described techniques merely by establishing a reference threshold voltage that is calibrated to indicate the point that the pressure changes from an acceptable to unacceptable (or low to high) level. Once the threshold voltage is achieved, additional electronic circuits can be used to produce an electronic switch that can control loads such as an indicator lamp.

2.2 AUTOMOTIVE APPLICATIONS FOR PRESSURE SENSORS

Automotive requirements for pressure measurements range from the basic—oil pressure—to the sophisticated—air pressure differential from one side of the vehicle to the other. This section elaborates on the various possibilities for pressure measurements that exist either in the development, laboratory, or pilot phases of the vehicle, to actual volume production. Table 2.2 lists a number of potential pressure measurements versus vehicle systems and provides an indication of the pressure range and type of measurement.

Automotive specification and testing guidelines have been developed and published by the Society of Automotive Engineers (SAE) specifically for manifold absolute pressure (MAP) sensors. These documents are intended to assist in establishing test methods and specifications for other sensors. Other SAE documents that may apply to sensors are summarized in Table 2.3.

The packaging and testing requirements for automotive sensors can represent 50 to 80 percent of the sensor cost and over 90 percent of the warranty and in-service problems. The pressure-sensing applications that are presented in the following sections will include packaging requirements that are of particular concern.

2.2.1 Existing Applications for Pressure Sensors

A late twentieth century production vehicle is likely to have a number of pressure sensors for measurements such as manifold pressure and engine oil pressure, and has the potential for

PETITIONER'S EXHIBIT 1002
US PATENT NO. 6,581,565

TABLE 2.2 Pressure Sensing Requirements for Various Vehicle Systems

System	Parameter	Pressure range	Type
Engine control	Manifold absolute pressure	100 kPa	Absolute
	Turbo boost pressure	200 kPa	Absolute
	Barometric pressure (altitude)	100 kPa	Absolute
	EGR pressure	7.5 psi	Gage
	Fuel pressure	15 psi—450 kPa	Gage
	Fuel vapor pressure	15 in H_2O	Gage
	Mass air flow		Differential
	Combustion pressure	100 Bar, 16.7 Mpa	Differential
	Exhaust gas pressure	100 kPa	Gage
	Secondary air pressure	100 kPa	Gage
Elect transmission (continuously variable transmission)	Transmission oil pressure	80 psi	Gage
	Vacuum modulation	100 kPa	Absolute
Idle speed control	AC clutch sensor/switch	300–500 psi	Absolute*
	Power steering pressure	500 psi	Absolute*
Elect power steering (also elect assisted)	Hydraulic pressure	500 psi	Absolute*
Antiskid brakes/ traction control	Brake pressure	500 psi	Absolute*
	Fluid level	12 in H_2O	Gage
Air bags	Bag pressure	7.5 psi	Gage
Suspension	Pneumatic spring pressure	1 MPa	Absolute*
Security/keyless entry	Passenger compartment pressure	100 kPa	Absolute
HVAC (climate control)	Air flow (PC) Compressor pressure	300–500 psi	Absolute*
Driver information	Oil pressure	80 psi	Gage
	Fuel level	15 in H_2O	Gage
	Oil level	15 in H_2O	Gage
	Coolant pressure	200 kPa	Gage
	Coolant level	24 in H_2O	Gage
	Windshield washer level	12 in H_2O	Gage
	Transmission oil level	12 in H_2O	Gage
	Tire pressure	50 psi	Gage/absolute
	Battery fluid level	1–2 in below	Optical
Memory seat	Lumbar pressure	7.5 psi	Gage
Multiplex/diagnostics	Multiple usage of sensors		

* *Gage measurement but absolute sensors used for failsafe*

TABLE 2.3 SAE Specifications That Effect Pressure Sensors

Recommended environmental practices for electronic equipment design	SAE J1211
Performance levels and methods of measurement of electromagnetic radiation from vehicles and devices	SAEJ551
Performance levels and methods of measurement of EMR from vehicles and devices (narrowband RF)	SAEJ1816
Electromagnetic susceptibility procedures for vehicle components (except aircraft)	SAE J1113
Vehicle electromagnetic radiated susceptibility testing using a large TEM cell	SAE J1407
Open-field whole-vehicle radiated susceptibility 10 kHz–18 GHz, electric field	SAE J1338
Class B data communication network interface	SAE J1850
Diagnostic acronyms, terms, and definitions for electrical/electronic components	SAE J1930
Failure mode severity classification	SAE J1812
Guide to manifold absolute pressure transducer representative test method	SAE J1346
Guide to manifold absolute pressure transducer representative specification	SAE J1347

PETITIONER'S EXHIBIT 1002
US PATENT NO. 6,581,565

several other pressure measurements. Tighter emissions control and improved efficiency may necessitate further sensor use in future systems.

Manifold, Barometric and Turbo Boost Pressure. Manifold absolute pressure (MAP) is used as an input to fuel and ignition control in internal combustion engine control systems. The speed-density system that uses the MAP sensor has been preferred over mass air flow (MAF) control because it's less expensive, but stricter emission standards are causing more manufacturers to use mass air flow for future models.

Higher resolution from 32-bit engine controllers, with greater analog-to-digital (A/D) conversion capability and higher operating frequencies, will provide greater accuracy for a given MAP sensor during the critical transitions of the engine cycle. As shown in Fig. 2.2, previous changes from 8-bit to 16-bit controllers have resulted in a two-time improvement in resolution in the digital conversion for the intake manifold pressure. The 8-bit control unit performed the A/D conversion on a 4-ms timer interrupt in order to maintain a balance with other controls, with the resulting 1.1-ms lag time (worst case) during periods of overlapping interrupts. The 16-bit microcontroller performs the A/D conversion every 2 ms, which reduces the lag time to 0.3 ms. The actual system improvements that can result from using the higher performing microcontrol units is a result of other factors such as more precise and faster control of fuel injectors and sparkplugs, and additional and/or more accurate sensors and control algorithms.

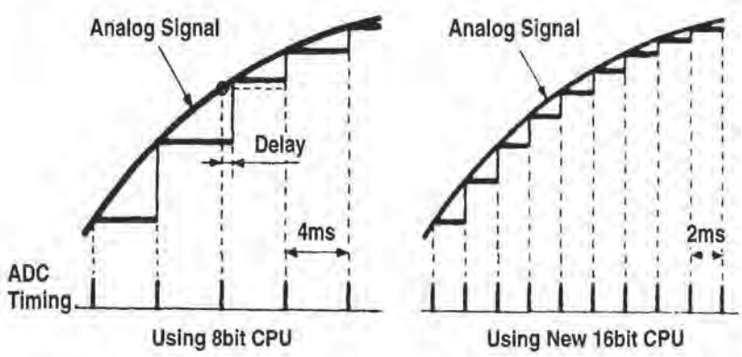


FIGURE 2.2 Effect of A-D on pressure measurements.

The MAP error band is also being tightened with a goal of 1 percent accuracy over the entire automotive temperature range. Existing specifications allow tolerances to increase as shown by the bowtie specification in Fig. 2.3 with associated multiplier(s).

The need for barometric pressure is often desirable in MAF systems to provide altitude information to the engine control computer. The barometric pressure range is typically from 60 to 115 kpA with accuracy on the order of 1.5 percent over the operating pressure range. The error band tolerance increases by a temperature multiplier of up to 2× outside the 0 to 85 °C range. MAP and barometric pressure sensors are frequently mounted inside control modules making the mounting technique a key consideration for manufacturability. The increased usage of surface mount technology, and the need to reduce space so that additional features can be included in control modules are factors that will affect next-generation sensor designs.

A typical turbocharger can provide boost pressure in the range of 80 kPa over the naturally aspirated internal combustion engine. This increases the maximum rating for the sensor to 200 kPa absolute, but other requirements are scaled appropriately.

PETITIONER'S EXHIBIT 1002
US PATENT NO. 6,581,565

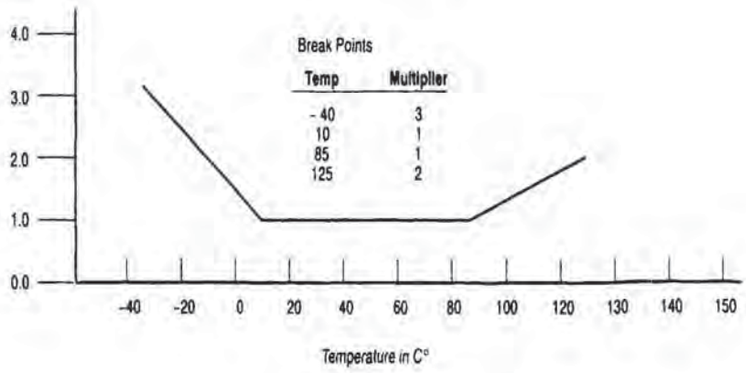
MPX4100 • MPX4101 SERIES

Transfer Function

Nominal Transfer Value: $V_{out} = V_S (0.01059 \times P - 0.1518)$
$+/-$ (Pressure Error x Temp. Mult. x $0.01059 \times V_S$)
$V_S = 5.1\ V \pm 5\%$ P_{in} kPa

Temperature Error Multiplier

MPX4100 Series



Pressure Error Band

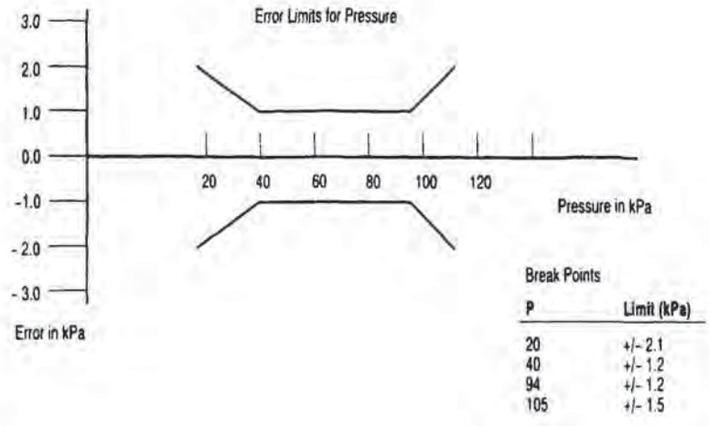


FIGURE 2.3 Error band for MAP sensor.

Oil Pressure. Oil pressure on automobiles has traditionally been measured by the deflection of a rubber diaphragm which closes a set of contacts (switch) providing a lamp indication with low oil pressure or moves a potentiometer to provide an analog signal for a gage.

A replacement for the conventional electromechanical oil pressure sending unit is an electronic device such as the one designed by Chrysler's Acustar Division. In addition to a silicon

PETITIONER'S EXHIBIT 1002
US PATENT NO. 6,581,565

piezoresistive pressure sensor, the unit contains transient protection circuitry, signal amplification for the sensor output, and output drivers for both an electromagnetic gauge and a fuel pump. The FET output drivers are capable of handling 10 A based on the heat dissipated though a heatsink that is integral to the sensor package.

The unit utilizes a supply voltage from 9 to 16 V and operates over a media temperature range of –40 to +150 °C. The overall accuracy is ±3.25 percent with linearity ≤ ±0.25 percent over the entire operating pressure range of 200 psi. The switch point for the low pressure indication is 4 psi ± 1.5 psi.

The sensor package was specially designed for easy assembly. The housing interfaces to the sensor with an extremely reliable O-ring seal that can withstand a burst pressure over 400 psi. Special materials were used for both the package and the protective gel that covers the sensor, which allow it to survive qualification tests with over 1 million pressure cycles, including portions conducted at high temperatures. This exceeds the number of cycles that can be achieved with traditional diaphragm-driven potentiometers that have been used for providing the indication of oil pressure. The sensor has been designed for a 10-year/100,000-mile life that could be required for future vehicle warranties.

Media Compatibility in Automotive Measurements. Pressure sensors frequently have to interface with an environment that is more demanding than other electronic components. For example, the measurement of engine oil pressure, transmission oil pressure, fuel pressure, and so on, or fluid level (oil, gas, coolant, etc.) requires the sensor package to be exposed to one or more fluids that are detrimental to the operation of semiconductor circuitry. Each of these media interface problems is addressed separately, depending on the application. Automotive cost requirements usually limit the usage of stainless steel as the isolation technique. Instead, more cost-effective protective polymers and chemically tolerant plastic and rubber materials have been developed for sensor packages.

2.2.2 New Applications for Pressure Sensing

The list of potential applications for sensing pressure in the automobile includes several new applications. These measurements are frequently made during the development of new vehicle systems. Their actual use on the vehicle is determined by factors such as cost, legislated requirements, need for diagnostics, and value added to the system. Applications in this section will identify areas of concern, range of pressure measurement, and factors that affect the usage of a pressure sensor.

Transmission Oil Pressure and Brake Pressure. Transmission pressure is required as an input in computer-controlled transmission shift points. This pressure can be measured with sensors similar to those developed for engine oil pressure.

Pressure in a hydraulic system, such as the master cylinder of an antilock brake system (ABS), is much higher than transmission oil pressure typically requiring a sensor with minimum rating of 500 psig. Pressures in other locations in the ABS system can be lower. The dynamic pressures in brake tubing can be of interest during the development phase of passenger vehicles and may be of interest in heavy duty commercial vehicles. These pressures can be below 150 psig.

The ABS system controls front and rear tire slip. Tradeoffs that exist in developing an ABS system for a particular vehicle include stopping deceleration to achieve the shortest possible stopping distance versus more steering control. Increased yaw stability can be obtained by reducing the deceleration rate of the rear wheels. The addition of traction control to the system improves stability during acceleration and provides independent control of each wheel during a variety of driving maneuvers for improved vehicle performance.

Passenger vehicles may have a single pressure sensor to monitor the pressure in the hydraulic system. One system, General Motors' ABS-VI, provides information on the brake pressure by detecting the current going to motors in the system. For the ABS-VI system, a pres-

PETITIONER'S EXHIBIT 1002
US PATENT NO. 6,581,565

sure sensor is not required to provide optimum brake pressure at each wheel. However, other systems rely on the rate of brake application and release to control lockup. Commercial vehicles may have several sensors for sensing brake pressures. Sensors close to brake cylinders report the actual pressure, which is compared to the reference value stored in the control unit.

Tire Pressure. The continuous monitoring of tire pressure offers increased fuel economy and safety to passenger cars or commercial vehicles. Underinflated tires create excessive rolling friction and therefore decrease fuel economy. Overinflated tires have excessive stress that can result in failure during operation. Improperly inflated, either over- or underinflated, tires have uneven wear patterns which decrease tire life. Available tire pressure systems consist of a tire pressure sensor (or switch) at each wheel, wheel speed indicator, temperature sensor, a radio frequency transmitter, electronic receiver/controller, and a display unit. The dashboard display provides an indication to the driver that the tires are improperly inflated. Tire pressure increases with temperature approximately 1.5 psi for every 10 °C of tire air temperature rise, so the system must provide correction for this effect. Abrupt increases in temperature and pressure can be sensed by these systems and provide a warning of eminent tire failure providing an additional safety factor.

Another tire pressure system utilizes a separate hand-held reader to easily verify the proper tire inflation when the vehicle is stationary. Yet another commercial vehicle system for trucks with dual tires operates while the vehicle is stationary and employs a visual indication for the driver that adequate pressure exists. This system provides a single fill point for the dual tires, maintains equal pressure under normal conditions, and provides an isolation valve in the event that a blowout or slow leak develops in one tire.

EGR Pressure. EGR (exhaust gas recirculation) back pressure and a pressure differential exist across the EGR valve used to control NO_x emissions in the engine control system. The valve is modulated by a vacuum which lifts a pintle from its seated position to allow exhaust gas to be recirculated. A change in vacuum pressure from 50 to 90 mm Hg is sufficient to fully open the valve, and a pressure differential across the valve of 200 mm Hg is typical. Pressure measurements are made during the development phase to determine system operating characteristics. However, a position sensor is typically used to measure the EGR valve's position and control NO_x emissions during normal vehicle operation.

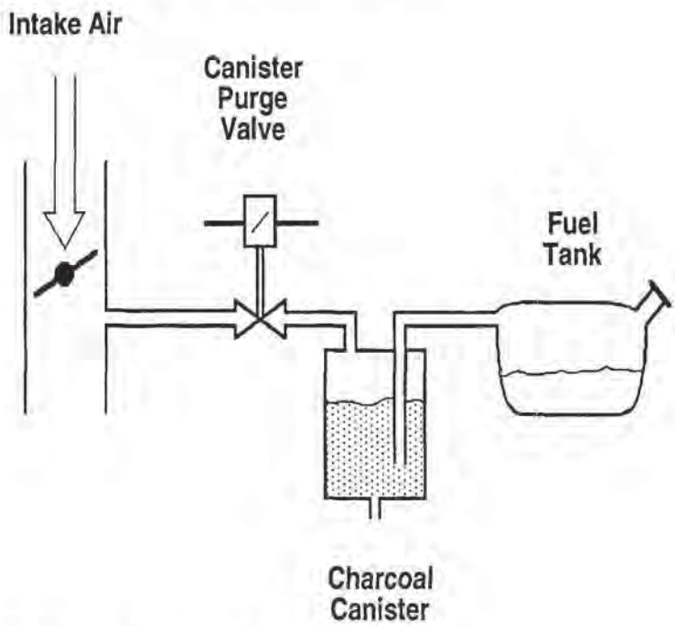


FIGURE 2.4 Canister purge system.

PETITIONER'S EXHIBIT 1002
US PATENT NO. 6,581,565

Fuel Rail and Vapor Pressure. Evaporative emissions that occur when the engine is off are currently stored in an activated charcoal canister of about 850 to 1500 cc until the engine is running, as shown in Fig. 2.4. The vapors are then consumed by the combustion chamber and catalytic converter. One implementation of on-board vapor containment of refueling hydrocarbons (on-board refueling vapor recovery or ORVR) would require refueling canisters on the vehicle that could be three to four times the volume of existing canisters. If leaks need to be detected in this system, a diagnostic pressure sensor may be required.

One approach to fuel routing, employed in the 5.9-liter Dodge Magnum engine, is to mount the fuel filter and pressure regulator at the fuel tank. The fuel pump is mounted inside the tank. Therefore, since only a fuel supply line to the fuel rail and a line to the evaporative canister are necessary, the fuel return line is eliminated. This system maintains lower fuel tank temperatures, resulting in lower evaporative emissions.

Monitors required for on-board diagnostic (OBD) systems per California Air Resources Board's (CARB's) OBDII legislation were originally targeted to be phased in between model year 1994 and model year 1996. A Bosch fuel injection system with on-board diagnostics is shown in Fig. 2.5 that identifies a differential air pressure sensor for tank vapor pressure.

Overpressure Occurrences. Fuel supply pressures in automobile fuel injection systems normally operate at pressures below 75 psi; however, fuel pumps develop pressures up to 3200 psi to open injectors. Pressure spikes can be reflected back through the fuel supply system that measure up to 300 psi during each fuel injection pulse.

Overpressure created by backfire can also apply a positive pressure of 75 psi and higher to the intake manifold absolute pressure sensor. Techniques used to prevent failure from over-

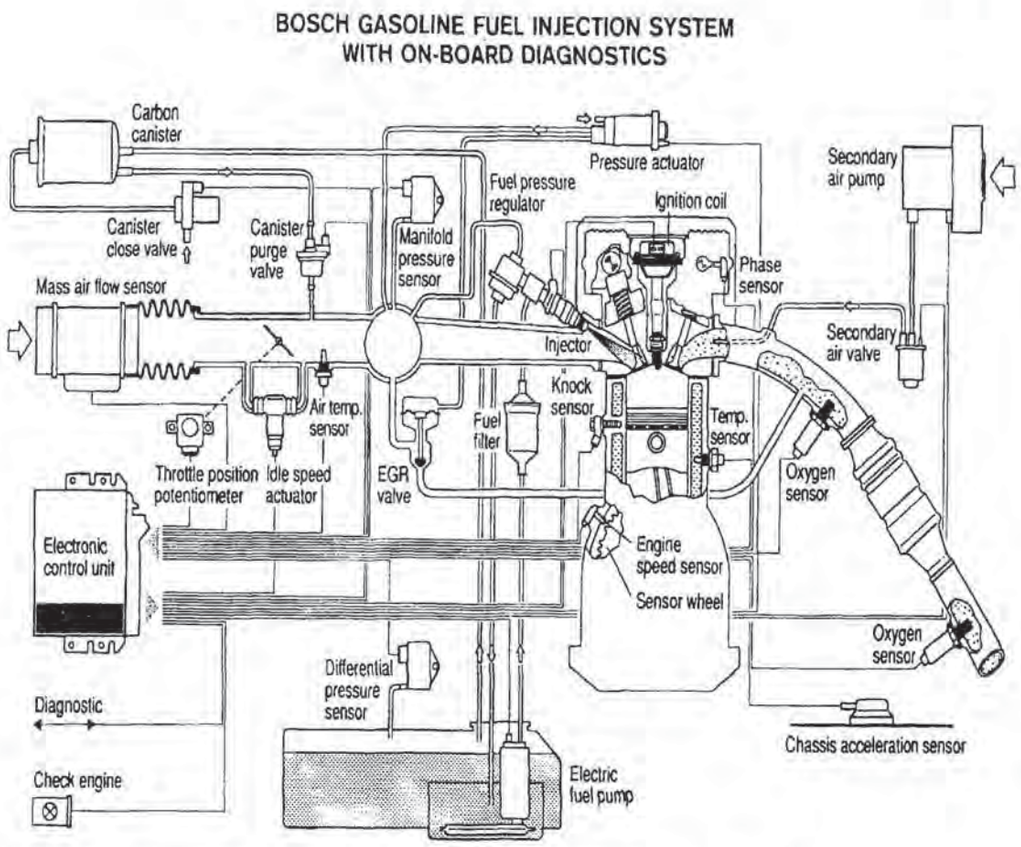


FIGURE 2.5 Fuel vapor control in electronic fuel injection system. *(Courtesy Robert Bosch, GMBh)*

PETITIONER'S EXHIBIT 1002
US PATENT NO. 6,581,565

pressure include overpressure stop built into the transducer, mechanical pulse filtering, and a sensor designed to operate within the overpressure range.

Mechanical stops have been a traditional protection technique for mechanical pressure sensors. This is possible where the amount of diaphragm deflection is large. Silicon pressure sensors have a modulus of elasticity that is the same as steel (30×10^6 psi) and a yield strength (180,000 to 300,000 psi) that is higher than steel, allowing high overpressure without diaphragm damage. However, the sensor package itself must be designed to handle the maximum pressure safely.

Snubbing, or mechanical filtering, is commonly used for static pressure measurements. A small diameter tube reduces the dynamic variation in applied pressure. If dynamic measurements are desired, the ac component of the desired signal may also be attenuated.

Increasing the diaphragm thickness of the sensor to safely handle the full range of pressure within normal operating range will also result in a lower sensitivity.

Alternate Fuel and Alternate Engine Implications to Pressure. Legislation that requires a percentage of the vehicles sold in California to be LEV (low emissions vehicles) and even ZEV (zero emissions vehicles) is increasing the demand for alternate fuel and electric vehicles. Among the alternate fuel vehicles, CNG (compressed natural gas) and hydrogen cells most likely would require sensors for pressure measurements. CNG is pressurized at 3000 psi and the distribution system includes pressure regulators, a transducer, valves, and idle air solenoids. Before the natural gas enters the engine, a regulator reduces the fuel pressure to near atmospheric pressure. Sensing may be required in both low- and high-pressure portions of the system. Development of alternative engines, such as the two-stroke engine for vehicle applications, will utilize electronics for control functions similar to four-cycle engines. However, the range and necessity for pressure measurements will differ from four-cycle engines. The pressure range for direct fuel injection is considerably higher for a two-stroke engine. The need to control the oil pump may necessitate pressure sensing in two-stroke systems as well.

Hydrogen fuel cells are another potential source of energy for use in electric vehicles. In one design, the proton-exchange membrane (PEM) design, a turbocompressor is used to pressurize the system and maintain hydration of the membrane. A pressure of at least three atmospheres (0.3 MPa) is required to remove the water. This pressure or the pressure drop across the membrane may need to be monitored during operation.

2.2.3 Other Applications for Pressure Sensors

Pressure sensors can be used on vehicles for measuring flow through pressure differential, or delta-P, measurements and for determining liquid level.

Delta-P (Flow-Sensing) Measurements. Applications on the vehicle for flow sensing include mass air flow; heating compartment flow; oil, fuel, and cooling liquid flow; and vehicle flow in an air stream. Mass air flow is typically accomplished by hot-wire anemometer or Karman vortex flow meters which do not use pressure-sensing techniques. Other vehicle flow requirements, including the pressure drop across the air filter, could be sensed and monitored by a differential pressure sensor. In addition to requirements such as media compatibility (Sec. 2.2.1), the lower-level signals require higher-sensitivity pressure sensors and/or additional amplification and must tolerate faults that could apply full line pressure to only one side of the sensor.

One of the more interesting applications of differential pressure measurements applied to flow analysis is the flow of the vehicle itself relative to crosswinds. A rear-wheel steering system developed by Daimler-Benz uses two pressure sensors to measure the pressure caused by wind on the vehicle's sides. An electronic control unit analyzes the pressure difference and inputs from other sensors, and alters the rear-wheel setting according to the wind strength. The system that measures the crosswinds directly is faster than yaw sensors, which are reactive and measure the change in attitude and direction of the vehicle.

PETITIONER'S EXHIBIT 1002
US PATENT NO. 6,581,565

Other laboratory measurements of airflow and crosswind force have also been made by Daimler-Benz that utilize 10 differential pressure gages with a range of ±3700 kPa. All pressure sensors were connected to a single pressure vessel to have a common reference. The reference pressure was measured by a 100-kPa absolute pressure sensor. The measurements were used to determine aerodynamic forces and moments and to compensate for wind effects in an active steering system.

Fluid Level Sensing. Various liquid levels can be measured in a vehicle, as shown in Table 2.4. All of these requirements, except fuel level, could be satisfied by a switch that simply detects that a predefined minimum level of liquid has been reached so that a driver indication can be provided. This can be accomplished by directly illuminating a dash lamp or through a microcontroller in a body computer which activates an output driver.

TABLE 2.4 Liquid Level Measurements

Level	Type	Range
Engine oil	Switch	38.1 cm of water
Transmission oil	Switch	30.5 cm of water
Coolant	Switch	61 cm of water
Windshield washer fluid	Switch	30.5 cm of water
Battery	Refraction switch	5.1 cm below reference
Power steering fluid	Switch	7.6 cm below reference
Brake fluid	Switch	30.5 cm of water
Fuel	Sensor and switch	38.1 cm of water

Sensing the fuel level has traditionally been performed by a float to sense the fluid level and a variable resistor with the wiper arm connected to the float. Configuration for the sensor depends upon the specific tank for which it was designed, necessitating a unique sensor for each vehicle. Manufacturers with several different vehicle models have the additional impetus to replace the existing techniques with a nonwearing, more accurate, self-calibrating electronic alternative. However, media compatibility for fuel level is among the harshest requirements for a pressure sensor. In addition to gasoline, oxygenated fuels containing ethanol, methanol, benzene, MTBE, engine additives, and even sour gas must be tolerated by the sensor. Nonintrusive differential sensors isolate the liquid from the sensor interface but must still tolerate fuel vapors. Also, the sloshing of the fuel in a vehicle's tank requires a time amplitude filter to smooth out the indication provided to the driver.

2.2.4 Combustion Pressure

The direct measurement of combustion pressure is being investigated for detecting misfire to meet CARB OBDII requirements. The high pressure (≥16 MPa) and temperature ranges combined with other environment factors make the design of a pressure sensor for this application extremely expensive. As a result, other techniques are being developed as alternatives to direct pressure measurement. These technologies include optical, fiberoptics measuring luminous emissions from combustion, and noncontact torque sensors. Section 2.3.7 explains a fiber optic technique.

The operation of the reciprocating-piston, internal combustion engine is represented by a constant volume process and the engine power cycle is analyzed by using pressure-versus-volume and pressure-versus-crank angle diagrams. To obtain these measurements in a laboratory environment a number of techniques have been developed. Direct (in-cylinder) pressure measurements have been performed with small diameter piezoresistive sensors placed in (or near) the sparkplug and piezoelectric washers placed under the spark plug. A high natural fre-

PETITIONER'S EXHIBIT 1002
US PATENT NO. 6,581,565

quency is required for these sensors based on the dynamic measurement involved in the combustion process. Indirect measurements with shaft torque and optical phase shift are additional possibilities. The need to determine misfire due to component failure during vehicle operation is part of OBDII requirements. A sensor used on production vehicles will be required to survive the high pressure and temperature environment for the life of the vehicle, which could be 100,000 miles and 10 years. It must also have no need for periodic zeroing or calibration and be available at a low cost.

2.2.5 Other Pressure Measurements

An adaptive suspension system (see Chap. 17) can be accomplished with an air pressure controlled shock absorber damping, such as Mitsubishi's Active-ECS (Electronically Controlled Suspension). This system has two air pumps and nine solenoids that regulate air pressure based on inputs from sensors including an air pressure sensor in the rear of the vehicle that measures the passenger and cargo load. The driver can select soft, medium, or hard suspension. Another system utilizes an air reservoir charged to a pressure of 1 Mpa by a compressor. A pressure switch monitors when the pressure drops below 760 kPa to recharge the reservoir. Air springs operate at 300 kPa unloaded and at 600 kPa in the rear when fully loaded.

HVAC (heating, ventilating, and air conditioning) changes are occurring as manufacturers are required to convert from refrigerant CFC-12 to alternatives such as HFC-134a. The theoretical performance of these two refrigerants will mean about a 6 percent loss in efficiency, compressor discharge pressure that is 175 kPa higher, and a discharge temperature that is about 8 °C lower. Measuring the compressor discharge pressure (almost 1900 kPa for the HFC-134a system) is desirable for electric load control as vehicles add more requirements to the 12-V charging system. Also, the effect on engine performance and fuel economy when the A/C is used could make the refrigerant pressure sensor a standard vehicle sensor in the future. An absolute sensor used to measure gage pressure of the refrigerant provides a deadhead effect to prevent refrigerant loss in the event of a sensing diaphragm failure.

The measurement of the pressure developed when the air bag is inflated is part of the evaluation, qualification, and lot acceptance criteria of air bag inflating techniques. Time-to-peak pressure and peak tank pressure measurements require measurements in the tens of milliseconds range. Inflated bag pressures are in the range of 100 kPa or less. Hybrid inflators use a stored inert gas, such as argon, in place of sodium-azide propellant that requires a squib for ignition. The hybrid uses a pressure sensor to monitor the status of the stored gas.

Special heavy duty/commercial truck measurements require pressure measurements that are quite different from those made on passenger cars. Accumulator-type fuel injection systems for direct injection diesel engines have fuel pressurized to 20 to 100 MPa in the accumulator by a high-pressure pump. The accumulator pressure is monitored in this approach to reduce particulates. Another method to reduce diesel particulates utilizes a ceramic fiber as a filter in a canister. A pressure sensor monitors the backpressure and allows the full filter to be regenerated by burning off the accumulated particulates in the filter. A heater element in the trap has power supplied from the power-switching module. A temperature approaching 1300 °F (700 °C) is reached inside the filter cartridge to incinerate the particles.

Lumbar support systems utilize a pressurized system with a pressure sensor ($\leq$7.5 psig) as the feedback element controlling the air pump to provide additional support to the driver's lower back in luxury vehicles. Pressure-sensitive grids have been used in the development process to automatically measure up to 3600 contact points for visual display and weight distribution analysis.

2.2.6 Partial Pressure Measurements

The oxygen (or lambda-) sensor in engine control systems is a chemical sensor that utilizes partial pressures to provide a feedback signal for the closed-loop control system. Lambda is

PETITIONER'S EXHIBIT 1002
US PATENT NO. 6,581,565

defined as the actual air/fuel ratio divided by the stoichiometric (14.6) fuel ratio. The operation of the oxygen sensor is defined by the Nernst equation: $U_L = RT/4F \cdot 1n(P_{O2}''/P_{O2}')$, where U_L is the unloaded output voltage of the sensor, R is the universal gas constant, T is the absolute temperature, F is the Faraday constant, P_{O2}'' is the oxygen partial pressure of the air (about 2.9 psi), and P_{O2}' is the equilibrium partial pressure of the oxygen in the exhaust gases. Equilibrium occurs due to the catalytic activity of the platinum electrodes used to coat the inside and outside of the Y_2O_3 stabilized ZrO_2 ceramic electrode. The oxygen partial pressure changes by a factor of 10^7 at 900°C (or 10^{19} at 500°C) when the exhaust gas changes from a reducing environment (lambda = 0.999) to an oxidizing environment (lambda = 1.001).

2.3 TECHNOLOGIES FOR SENSING PRESSURE

A number of technologies have been used for on-vehicle measurements of static and dynamic pressure: diaphragm-potentiometer, linear variable differential transformer (LVDT), aneroid, silicon or ceramic capacitive, piezoresistive strain gage, piezoelectric ceramic or film, and optical phase shift (combustion pressure). Recent advances in sensing have focused on transducers that provide an electric signal easily interfaced to microcontrollers. Mechanical devices are frequently used in the laboratory for calibration and component development or on the vehicle during the development phase of the vehicle systems. Common mechanical devices include the Bourdon tube, bellows, diaphragms, deadweight gage, and manometer.

The Bourdon tube is a curved or twisted, flattened tube with one end closed that acts as a force collector. When pressure is applied at the open end, the tube tends to straighten and the resulting motion is used as an indication of the applied pressure.

The bellows, or pressure capsule, is a chamber that expands with applied pressure. Absolute pressure can be measured by sealing a reference pressure (e.g., vacuum) inside a closed unit and applying pressure to the outside. The movement of the chamber is proportional to the applied pressure.

Diaphragms are the most common force collector used in modern pressure sensors. The diaphragm material can be rubber, elastomer, stainless steel, silicon, ceramic, or even sapphire. Diaphragm shapes are circular or square and can be supported or clamped around their periphery.

A deadweight tester or piston gage can withstand extreme pressure changes and high overpressure occurrences. The piston is sealed in a cylinder using O-ring or Teflon seals. Pressure on the piston causes a deflection that can be measured by position-sensing techniques. Precision weights allow calibration for high-accuracy measurements. The deadweight tester is one of the few pressure-sensing techniques that measures pressure in terms of its fundamental units—force and area. Errors associated with the measurement are air-bouyancy corrections, gravity error, surface tension, fluidhead, and thermal expansivity. These errors are normally small but should be taken into account when high accuracy is required.

The manometer is used both as a pressure-measuring instrument and a standard for calibrating other instruments. Its simplicity and inherent accuracy result from it being the measurement of the height(s) of a column of liquid. Three basic types of manometers are the U-tube, well (cistern), and slant-tube.

Other measurement devices including McLeod, Pirani, Alphatron, and thermocouple gages which can measure vacuum in the range of 10^{-5} mm Hg.

Sensing techniques that provide a transducer for conversion from mechanical to electrical units include resistive, LVDT, capacitive, piezoresistive, and piezoelectric.

2.3.1 Potentiometric Pressure Sensors

Prior to electronic engine control systems, carburetor dashpots and distributor vacuum advance units used the distance that a rubber diaphragm traveled when pressure was applied

PETITIONER'S EXHIBIT 1002
US PATENT NO. 6,581,565

as a mechanical indication of pressure. A diaphragm which moves a potentiometer (resistor with a sliding element or wiper) provides an electric signal that can be applied to a remote gage such as an oil pressure gage. Potentiometric sensors inherently have some level of noise and wear associated with their operation due to the contact of the wiper to the resistive element. Stiction or static friction is also a potential concern with these devices, especially if control of ≤0.5 percent of the total resistance is required. The finite resolution of wirewound potentiometers is overcome by the use of newer thin-film plastic resistor designs.

2.3.2 Linear Variable Differential Transformer

One of the earliest pressure inputs for engine control systems was provided by the LVDT pressure sensor. The principle of operation is demonstrated in Fig. 2.6. An LVDT pressure sensor consists of a primary winding and two secondary windings positioned on a movable cylindrical core. The core is attached to a force collector which provides differential coupling from the primary to the secondaries resulting in a position output that is proportional to pressure.

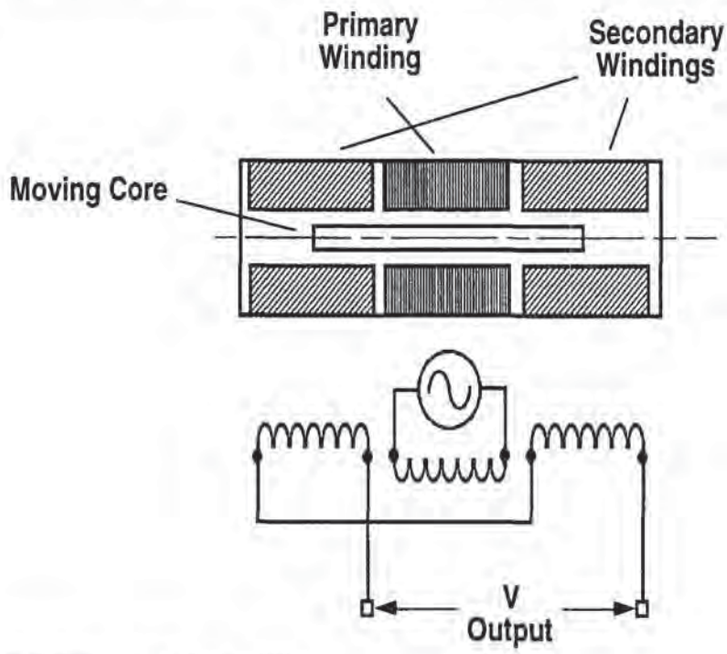


FIGURE 2.6 LVDT pressure sensor.

An alternating current is used to energize the primary winding, which results in a voltage being induced in each of the secondary windings. The windings are connected in series opposing, so the equal but opposite output of each winding tends to cancel (except for a small residual voltage called the null voltage). A pressure applied to a Bourdon tube or diaphragm causes the core to be displaced from its null position and the coupling between the primary and each of the secondaries is no longer equal. The resulting output varies linearly within the design range of the transducer and has a phase change of 180° from one side of the null position to the other. Since the core and coil structures are not in physical contact, essentially frictionless movement occurs.

Electronic devices necessary to signal condition the output of an LVDT consist of an oscillator for the supply voltage, circuitry to transform the constant voltage to a constant current, an amplifier with high input impedance for the output, a synchronous demodulator, and a filter with characteristics designed for quasistatic or dynamic measurements.

PETITIONER'S EXHIBIT 1002
US PATENT NO. 6,581,565

2.3.3 Aneroid Diaphragms

Another early design for sensing automotive manifold pressure consisted of dual sealed aneroid diaphragms. The diaphragms were bonded and sealed with a vacuum inside each unit to a metallized conductive ring on opposite sides of a ceramic substrate. The substrate served as the fixed plates of two separate capacitors. Manifold vacuum was applied to one chamber and the second served as a reference for compensating and signal conditioning that minimized common mode errors due to vibration and shock.

2.3.4 Capacitive Pressure Sensors

Capacitive pressure sensors have one plate that is connected to a force collector (usually a diaphragm), and the distance between the plates varies as a result of the applied pressure. The nominal capacitance is $C = Ae/d$, where A is the area of the plate, e is the permittivity, and d is the distance between the plates. Two common capacitive pressure sensors used in automotive applications are based on silicon and ceramic capacitors.

Silicon. A silicon capacitive absolute pressure (SCAP)-sensing element is shown in Fig. 2.7. The micromachined silicon diaphragm with controlled cavity depth is anodically bonded to a Pyrex® glass substrate. Feedthrough holes are drilled in the glass to provide a precise connection to the capacitor plates inside the unit. The glass substrate is metallized using thin-film deposition techniques. Photolithography is used to define the electrode configuration. After attaching the top silicon wafer to the glass substrate, the drilled holes are solder-sealed under vacuum to provide a capacitive-sensing element with an internal vacuum reference and solder bumps for direct mounting to a circuit board or ceramic substrate. The value of the capacitor changes linearly from approximately 32 to 39 pF with applied pressure from 17 to 105 kPa. The capacitive element is 6.7 mm × 6.7 mm and has a low-temperature coefficient of capacitance (–30 to 80 ppm/°C), good linearity (≈1.4 percent), fast response time (≈1 ms), and no

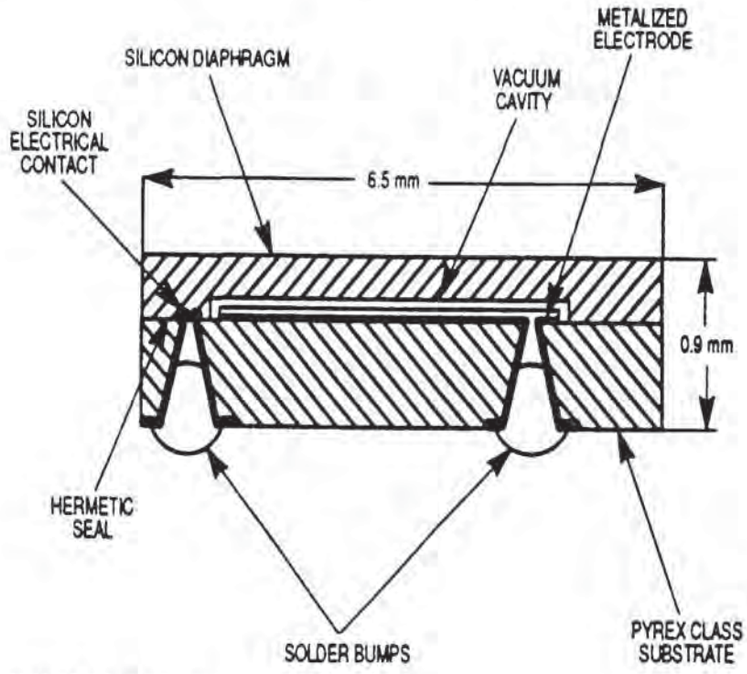


FIGURE 2.7 SCAP sensor.

PETITIONER'S EXHIBIT 1002
US PATENT NO. 6,581,565

exposed bond wires. The output of the sensor is typically signal-conditioned to provide a frequency variation with applied pressure for easy interface to microcontrollers.

Surface micromachining and bulk micromachined silicon-on-silicon techniques (see Sec. 2.3.5) have also been used to build silicon capacitive pressure sensors. These approaches also address the addition of signal-conditioning electronics on the same silicon structure.

Ceramic. The ability to make thin diaphragms from ceramic material combined with thin-film deposition to provide metal plates and connections has been used to manufacture ceramic pressure sensors. Their operation and signal-conditioning requirements are similar to the silicon capacitive sensor described in Sec. 2.3.4.

2.3.5 Piezoresistive Strain Gage

Strain-gage pressure sensors convert the change in resistance in four (sometimes in two) arms of a Wheatstone bridge. The change in the resistance of a material when it is mechanically stressed is called piezoresistivity.

The open-circuit voltage of an unbalanced Wheatstone bridge is given by $V_O = \mathbf{E}[(R1*R3 - R2*R4)/(R1 + R2)(R3 + R4)]$, where V_O is the output voltage, **E** is the applied voltage, and $R1$ through $R4$ are the resistive elements of the bridge. Additional variable resistive elements are typically added to adjust for zero-offset and sensitivity, and to provide temperature compensation.

Different approaches to piezoresistive strain gages range from traditional bonded and unbonded to the newest integrated silicon pressure sensors.

Bonded and Unbonded Strain Gages. The bonded resistance strain-gage pressure sensor consists of a filament-wire or foil, metallic or semiconductor, bulk material or deposited film bonded to the surface of a diaphragm. Pressure applied to the diaphragm produces a change in the dimension of the diaphragm and, consequently, in the length of the gage, and, therefore, a change in its resistance ($R = \rho\, L/A$). The change per unit length is called strain. The sensitivity of a strain gage is indicated by gage factor

$$GF = \Delta R/R \div \Delta L/L = 1 + 2\mu + \Delta\rho/\rho \div \Delta L/L \tag{2.1}$$

Foil strain gages have a negligible piezoresistive effect and their gage factor is usually between 2 and 3.

When a pressure sensor is used for measuring an applied force it is called a load cell.

Integrated Silicon Pressure Sensors. The GF for a strain gage is improved considerably (to about 150) by using a silicon strain gage. In addition to the conventional Wheatstone bridge, silicon processing techniques, and the relative size of piezoresistive elements in silicon enable the design of a unique piezoresistive sensor. The sensor signal can be provided from a single piezoresistive element located at a 45° angle in the center of the edge of a square diaphragm which provides an extremely linear measurement. The offset voltage and full scale span of the basic sensing element vary with temperature, but in a highly predictable manner. In addition to the basic sensing element, an interactively laser-trimmed four-stage network has also been integrated into a single monolithic structure (Fig. 2.8). The size of the silicon die, including the diaphragm, sensing element, and signal-conditioning electronics, is only 0.135 in by 0.145 in. The die is attached to the six-terminal package through the use of a stress-isolating layer of RTV (room temperature vulcanizing) silicone. This approach allows a minimum of external components for amplification to provide a usable output signal.

Two silicon wafers are used to produce the absolute piezoresistive silicon pressure sensor (Fig. 2.9). The top wafer is etched until a thin, square diaphragm, approximately one mil in thickness, is achieved. The square area is extremely reproducible as is the 54.7° angle of the cavity wall based on the characteristics of bulk micromachined silicon. The top wafer is

PETITIONER'S EXHIBIT 1002
US PATENT NO. 6,581,565



FIGURE 2.8 Silicon pressure sensor with integrated electronics. *(Courtesy Motorola, Inc.)*

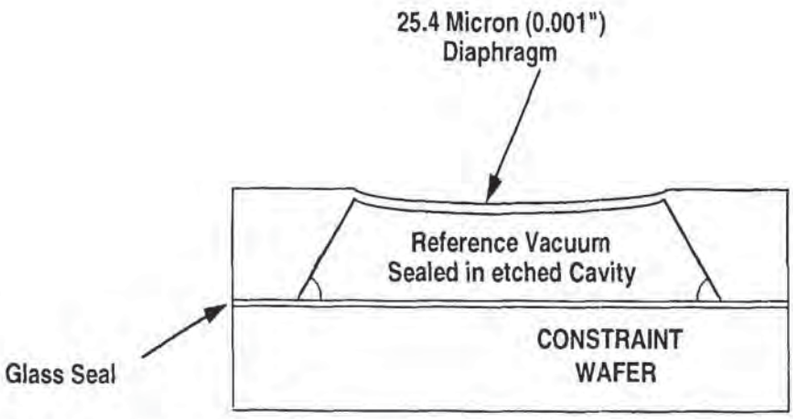


FIGURE 2.9 Cross section of piezoresistive silicon pressure sensor for measuring absolute pressure.

PETITIONER'S EXHIBIT 1002
US PATENT NO. 6,581,565

attached to a support wafer by a glass frit to provide a structure which is isolated from mounting stresses.

The bulk micromachining process used to form the diaphragm and the etched cavity in the majority of silicon pressure sensors is a chemical etching process that allows a thin (0.001-in) mechanical structure—the diaphragm—to be precisely etched from a silicon wafer that is approximately 0.015 in thick. Hundreds of sensors can be formed simultaneously on a 4-in (100-mm) diameter silicon wafer, and several wafers can be batch-processed to yield thousands of sensors in a single lot. Silicon pressure sensors can also be achieved by using surface micromachining techniques. In these sensors, a layer of sacrificial material (usually an oxide) is grown on top of a silicon wafer, and material such as polysilicon is then deposited on the sacrificial layer and patterned to achieve a particular structure. The sacrificial material is removed by a chemical etchant. Both bulk and surface micromachining techniques can be combined with semiconductor processing techniques to provide additional circuitry on the same monolithic structure. A number of new terms are used relative to silicon pressure sensors that are defined in the glossary to this section.

Both bulk and surface micromachining, discussed previously, are performed at the wafer level. A polysilicon thin-film sensor that consists of a thin film of silicon that is doped with boron and vapor-deposited over a stainless steel diaphragm is shown in Fig. 2.10. A thin deposited layer of silicon dioxide insulates the silicon from the stainless steel diaphragm. Silicon nitride is used to cover the strain-sensitive elements. Silicon-on-insulated-stainless-steel (SOISS) sensors are not formed using silicon wafer techniques, but they use batch-processing techniques and are inherently suited for harsh environments.

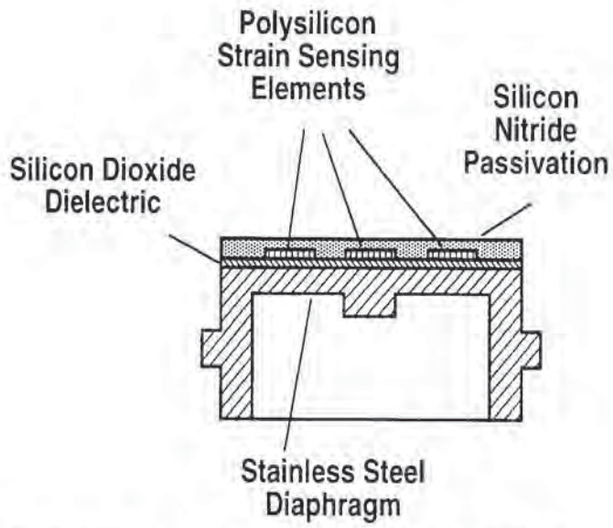


FIGURE 2.10 Polysilicon pressure sensor on stainless steel diaphragm.

2.3.6 Piezoelectric Pressure Sensors

A piezoelectric sensor produces a change in electric charge when a force is applied across the face of a crystal or piezoelectric film. The inherent ability to sense vibration and the necessity for high-impedance circuitry are taken into account in the design of modern piezocrystal sensors. Transducers are constructed with rigid multiple plates and a cultured-quartz sensing element, which contains an integral accelerometer to minimize vibration sensitivity and suppress resonances. A typical unit also contains a built-in microelectronic amplifier to transform the high-impedance electrostatic charge output from the crystals into a low-impedance voltage signal. Units made in stainless steel housings have an invar diaphragm laser welded to seal the

PETITIONER'S EXHIBIT 1002
US PATENT NO. 6,581,565

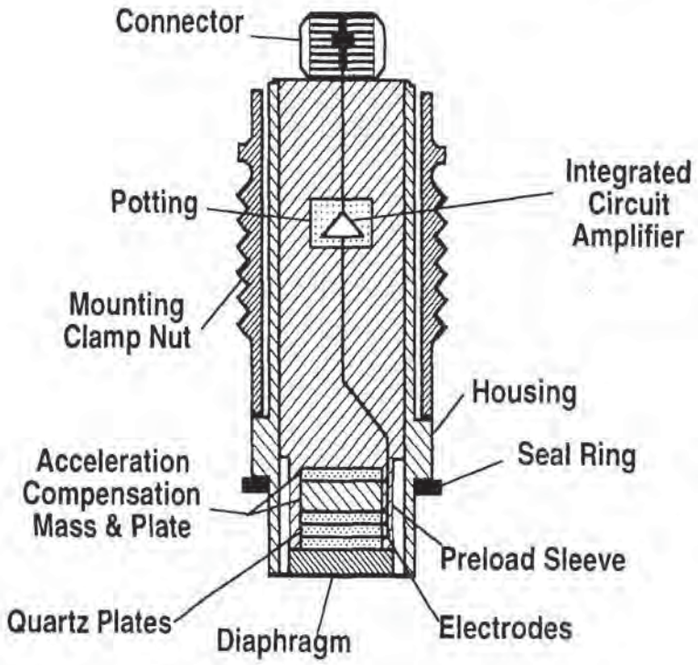


FIGURE 2.11 Piezoelectric pressure sensor.

sensing elements inside the package. Figure 2.11 shows the cross section of a piezoelectric pressure sensor.

More recently, piezo film sensors, which produce an output voltage when they are deflected, provide a very inexpensive method for pressure measurements. One approach has the piezo film cemented to a metallic dimple substrate with the dimple pointed toward the high-pressure source. As the pressure rises, a point is reached when the dimple snaps in the opposite direction and the movement is sufficient for the piezo film to generate a transient voltage.

Surface micromachining techniques have also been combined with piezoelectric thin-film materials, such as zinc oxide, to produce a semiconductor piezoelectric pressure sensor.

2.3.7 Fiber Optic Combustion Pressure Sensor

For extremely high pressure, or pressure measurements at high temperatures, different pressure measurement techniques are used. Figure 2.12 shows an alternative to traditional pressure-sensing techniques that is being developed to sense production vehicles' combustion

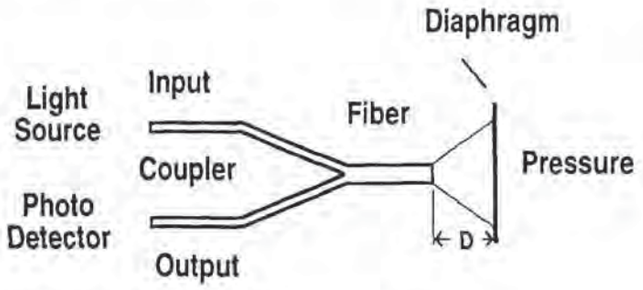


FIGURE 2.12 Fiber optic combustion pressure sensor.

PETITIONER'S EXHIBIT 1002
US PATENT NO. 6,581,565

pressure. The fiber optic pressure sensor can withstand temperatures (up to 550 °C) that are well above the normal range for piezoelectric sensors. Furthermore, the design has a normal pressure range of 0 to 1000 psi and overrange capability of 3000 psi.

The sensor's operation is the result of a light source input to an optical fiber coupler and a photodetector at the receiving end of the coupler. Light exits the optical fiber as a diverging cone which illuminates a diaphragm. The maximum angle is determined by an aperture. The amount of light that is returned to the sensor fiber after it is reflected from the diaphragm depends upon the gap D between the fiber and the diaphragm. The diaphragm can be sized to allow the sensor to be integrated into a spark plug for easy access to the combustion pressure of each cylinder. Accuracy within 5 percent has been demonstrated within the 550 °C operating temperature range.

2.3.8 Pressure Switch

A pressure switch can be simpler and more cost effective than a pressure sensor for an application that only requires detecting a single pressure level. Sufficient motion of the force-collecting diaphragm (e.g., elastomer, Kapton®, fluorosilicon) allows a spring to be compressed and a set of contacts to be closed in a traditional mechanical switch. The design of the contacts may allow several amperes to be switched.

Converting the output of any of the electric sensors in Sec. 2.3 to a threshold-sensing level requires additional circuits, including an electronic switch, such as a power FET, to conduct the current. The sensor can have multiple switch points depending on the amount of additional circuitry that is provided.

2.3.9 Pressure Valves/Regulators

Pressure is frequently controlled in automotive applications by pressure regulators or valves. The actuation of these mechanisms can be a result of applied pressure to a mechanical structure such as an integral piston or relief valve held closed by a spring force, or an electric signal generated from a sensor and subsequent activation of a solenoid, which opens a valve or moves a pintle in an orifice to change the pressure. The thermostat in the engine cooling system allows flow based on a minimum temperature being achieved. It must operate independently of the pressure variations in the cooling system. A common solution is an expansion-element thermostat which actuates a valve to redirect the flow of coolant into a radiator bypass line when the control temperature is reached.

Extremely small and precise silicon-based regulators, and even pumps, are possible using micromachining techniques. Figure 2.13 shows a silicon Fluistor™ (or fluidic transistor) microvalve that is approximately 5.5 mm by 6.5 mm by 2 mm. The valve is actually a thermopneumatic actuator which accepts an electric input. The cavity is etched in the middle silicon chip by bulk micromachining described in Sec. 2.3.4 and filled with a control liquid. When the liquid is heated, the silicon diaphragm moves outward over the valve seat. This approach has demonstrated a dynamic range of 100,000:1 controlling gas flows from 4 μlpm to 4 lpm at a pressure of 20 psid.

The microvalve combined with a pressure sensor and electronic feedback loop provides a solid state pressure regulator. It has potential for usage in both gas and liquid flow control applications on future vehicles. The integration of EGR and idle-air control (IAC) has already been accomplished in a somewhat conventional (patented) manner. A feedback-controlled valve with two inlets and a single outlet orifice eliminate stepper motor programming in the engine controller and only one calibration curve is needed for both EGR and IAC functions. The combination of this approach to control systems and newly developed technologies, such as the silicon microvalve, will allow additional advances in vehicle performance, efficiency, and control.

PETITIONER'S EXHIBIT 1002
US PATENT NO. 6,581,565

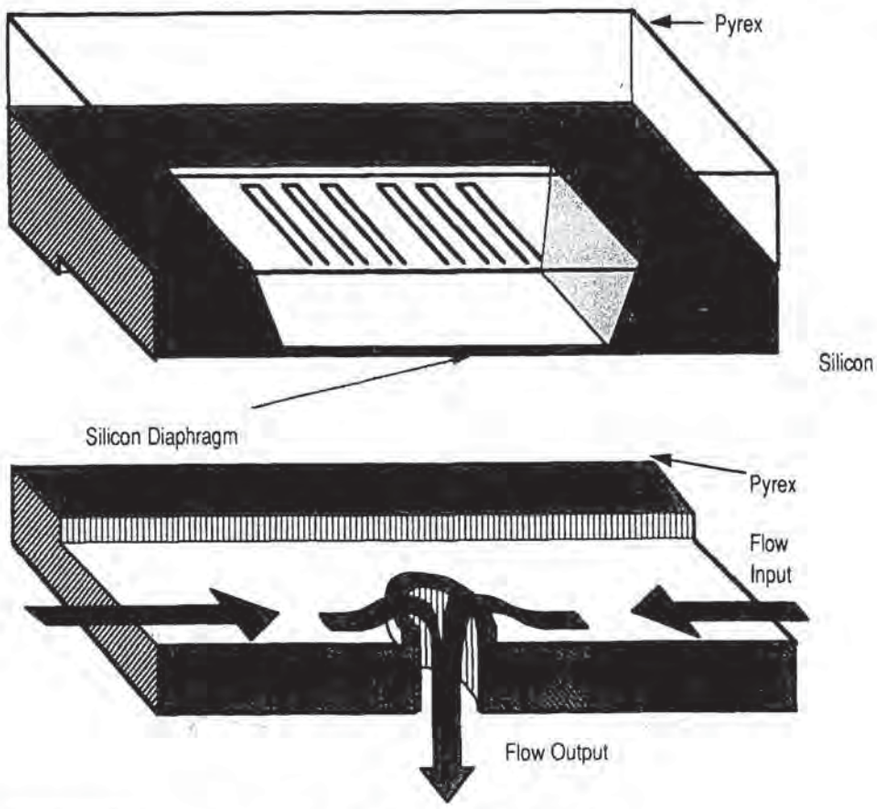


FIGURE 2.13 Silicon microvalve. *(Courtesy of Redwood MicroSystems, Inc.)*

2.4 FUTURE PRESSURE-SENSING DEVELOPMENTS

The different types of pressure measurements, different technologies for measuring pressure, and potential pressure measurements in automotive applications have been explained in this chapter. In addition, alternatives to making pressure measurements, such as indirect sensing and the use of pressure regulators, have been discussed. The use of semiconductor technology applied to sensing applications is producing sensors with inherently more decision and diagnostic capability that can communicate bidirectionally with host microcomputers in complex systems. The desire to directly produce a signal that is compatible with microcomputers rather than requiring analog signals to be converted to digital format through A/D converters is spurring development activity that could affect future automobile systems. Furthermore, recently developed fuzzy logic and neural network approaches to control systems and multiplexing of sensor outputs for use in several systems will make previously cost-prohibitive sensing applications a reality.

Increased and recently initiated sensing activity from industrial organizations such as SAE, the American National Standards Institute (ANSI), and the Institute of Electrical and Electronics Engineers (IEEE) should provide a greater level of understanding, common terminology, and improved specifications and test procedures for the numerous approaches that can be taken to sense pressure in automotive applications.

All trademarks are the property of their respective owners.

PETITIONER'S EXHIBIT 1002
US PATENT NO. 6,581,565

GLOSSARY

Altimetric pressure transducer A barometric pressure transducer used to determine altitude from the pressure-altitude profile.

Diaphragm The membrane of material that remains after etching a cavity into the silicon sensing chip. Changes in input pressure cause the diaphragm to deflect.

Error band The band of maximum deviations of the output values from a specified reference line or curve due to those causes attributable to the sensor. Usually expressed as "±% of full-scale output." The error band should be specified as applicable over at least two calibration cycles so as to include repeatability and verified accordingly.

Linearity error The maximum deviation of the output from a straight-line relationship with pressure over the operating pressure range. The type of straight-line relationship (end-point, least-square approximation, etc.) should be specified.

Operating pressure range The range of pressures between minimum and maximum pressures at which the output will meet the specified operating characteristics.

Overpressure The maximum specified pressure that may be applied to the sensing element of a sensor without causing a permanent change in the output characteristics.

Piezoresistance A resistive element that changes resistance relative to the applied stress it experiences (e.g., strain gauge).

Pressure error The maximum difference between the true pressure and the pressure inferred from the output for any pressure in the operating pressure range.

Pressure sensor A device that converts an input pressure into an electric output.

Ratiometric (ratiometricity error) At a given supply voltage, sensor output is a proportion of that supply voltage. Ratiometricity error is the change in this proportion resulting from any change to the supply voltage. Usually expressed as a percent of full-scale output.

Response time The time required for the incremental change in the output to go from 10 to 90 percent of its final value when subjected to a specified step change in pressure.

Temperature error The maximum change in output at any pressure in the operating pressure range when the temperature is changed over a specified temperature range.

BIBLIOGRAPHY

"Acustar Electronic Oil Pressure Sensor," *Automotive Industries,* March 1993, pp. 26–29.

Budd, John W., "A Look at Pressure Transducers," *Sensors,* July 1990, pp. 10–15.

Doeblin, Ernest O., *Measurement Systems Application and Design,* McGraw-Hill, New York, 1975.

He, Gang, and Marek T. Wlodarczyk, "Spark Plug-Integrated Fiber Optic Combustion Pressure Sensor," *Proceedings of Sensors Expo,* Chicago, Sept. 29–Oct. 1, 1992, pp. 211–216.

Holt, Daniel J., "ABS Testing," *Automotive Engineering,* March 1993, pp. 26–29.

Keebler, Jack, "Automakers, gas refiners debate vapor control units," *Automotive News,* Oct. 14, 1991, p. 39.

Lynch, Terrence, "Integrated Valve Meters EGR and Idle Air," *Design News,* Feb. 22, 1993, pp. 159–160.

Motorola Pressure Sensor Device Data Book, Q1/93, Phoenix, Ariz.

Norton, Harry N., "Transducers and Sensors," *Electronic Handbook,* McGraw-Hill, New York.

PETITIONER'S EXHIBIT 1002
US PATENT NO. 6,581,565

PCB Electronics, Inc., comments in "Piezoelectric Pressure Transducers," *Measurements & Control,* Oct. 1990, pp. 20–222.

Sawyer, Christopher A., "On-Board Diagnostics," *Automotive Industries,* May 1992, p. 57.

Siuru, Jr., William D., "Sensing Tire Pressure on the Move," *Sensors,* July 1990, pp. 16–19.

Tran, Van Truan, "Wind Forces and Moments," *Automotive Engineering,* April 1990, pp. 35–38.

ABOUT THE AUTHOR

Randy Frank is a Technical Marketing Manager for Motorola's Semiconductor Products Sector in Phoenix, Arizona. He has a BSEE, MSEE, and MBA from Wayne State University in Detroit, Michigan, and over 25 years' experience in automotive and control systems engineering. For the past 10 years he has been involved with semiconductor sensors, power transistors, and smart power ICs.

PETITIONER'S EXHIBIT 1002
US PATENT NO. 6,581,565

PETITIONER'S EXHIBIT 1002
US PATENT NO. 6,581,565

CHAPTER 3
LINEAR AND ANGLE POSITION SENSORS

Paul Nickson
Product Line Manager
Analog Devices, Inc.,
Transport & Industrial Products Division

3.1 INTRODUCTION

Position sensors of one form or another are an integral and necessary part of the modern automobile. Position sensors range in technology from the ubiquitous microswitch warning to the driver of a door ajar to linear variable differential transformers (LVDTs) used in sophisticated active suspension systems. Whether as monitors or as critical parts of safety systems, market and legislative pressures for longer warranties and lower emissions are opening avenues for a wide range of sensing technologies to find a place in the modern automobile.

The automotive systems designer must take into account many factors when choosing the appropriate technology for an application. Each sensor type has its own vocabulary, and it is important when making comparisons to understand how a figure of merit for one sensor relates to that of another. It is equally important to understand how the choice of output signal format, whether digital or analog, can affect the resolution of measurement and subsequently the performance or stability of an automotive system.

The purpose of this chapter is to give an overview of position sensor technologies currently used and available for use in automobiles and to compare their characteristics and suitability for particular applications. Consideration is given to the interfacing requirements of each type of sensor with an emphasis on the advantages and disadvantages of each method as they apply in the automotive environment. Where appropriate, descriptions of applications of the various sensor types in automobile applications are given. Other available technologies and technologies in development which have desirable characteristics for automotive applications are also discussed.

3.2 CLASSIFICATION OF SENSORS

Sensors may be classified in many different ways. From the perspective of a system designer, the basic questions are: What kind of information does the sensor provide and how is the sensor used? For the purposes of this discussion, a position sensor is defined as an electromechanical device that translates position information into electric signals. Sensors can be grouped into two basic categories.

PETITIONER'S EXHIBIT 1002
US PATENT NO. 6,581,565

3.2.1 Incremental or Absolute

Position information can be presented in two different ways. Incremental position sensors measure position as the distance from an arbitrary index or zero. Alternatively, position information may be provided that gives an unambiguous or absolute measure of the distance from a well-defined index.

Incremental sensors usually rely on some method of pulse counting. One pulse in the sequence is designed to be wider or of opposite polarity than the others so that it may be used as a nominal zero. A typical optical angle encoder consists of a glass disk marked with a number of equally spaced radial opaque lines and transparent gaps. The disk is illuminated on one side and a light sensor and associated electronics on the other side detect the passage of dark lines and gaps and generate corresponding electric pulses. Dedicated electronics built into the sensor or a remote microcontroller can be used to count the pulses. A zero is established by detecting the wider pulse, known as *North Marker* in optical encoder terminology, and then resetting the pulse counter. The advantage of this data format is that few wires are required to carry the information. Typically, four or five wires would be required depending on the exact details of the format (see Sec. 3.3.2). The biggest disadvantage of incremental sensors is that at power-up the system has no position information and requires a mechanical indexing cycle to find the marker pulse. Another disadvantage is that the system is prone to the effects of noise, which may lead to erroneous counts.

In contrast, absolute position sensors produce an unambiguous output at power-up. Each position or angle has a unique value. The output may be a voltage or frequency or other analog of the input position. Potentiometers are often used in applications requiring this characteristic. Many absolute position sensors have binary digital outputs. The digital formats vary depending on the construction of the sensor. Some optical encoders use Gray code to avoid ambiguities at code transitions. Other sensors, such as resolvers, do not directly produce a digital output but are almost always used with an analog-to-digital converter that may output in parallel or serial form one of the common formats—for example, two's complement or offset binary.

3.2.2 Contact or Proximity

Position sensors are designed to detect the position of components of mechanical systems by either being directly coupled by some shaft or linkage, as in the case of potentiometers or optical encoders, or by some noncontact or proximity means. Environmental issues are often a key influence in the choice of sensor for a given application. High levels of vibration, particularly in small engine applications, may cause rapid wear of the conductive track of a throttle-position-measuring potentiometer. Dirt and dust usually exclude optical sensors from underhood applications due to rapid degradation of the optical path.

The most common form of proximity sensors are based on various methods of magnetic field detection. A device based on magnetic field sensing principles may be more easily isolated from the destructive effects of the harsh environment encountered in many automotive applications.

3.3 POSITION SENSOR TECHNOLOGIES

3.3.1 Microswitches

The simplest form of contact sensor is a switch. Contact position sensors may be as simple as the microswitches that operate anything from brake lights to courtesy lights in the automobile. Many applications of microswitches in position sensing are as limit switches, usually

PETITIONER'S EXHIBIT 1002
US PATENT NO. 6,581,565

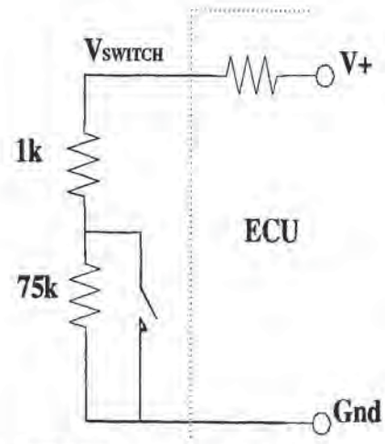


FIGURE 3.1 Diagnosable switch.

wired to limit or warn of the extent of travel of a mechanical component by disconnecting power to an electric motor or by operating an indicator lamp. In some cases, for safety reasons, it is desirable to be able to detect fault conditions that would make the switch inoperable. In some applications, it is possible to connect the switch as shown in Fig. 3.1. In this case, a diagnostic circuit measuring the voltage, V_{SWITCH}, can differentiate between the normal conditions of switch open or closed and can also determine if the switch is disconnected or if V_{SWITCH} is shorted to either power supply.

An undesirable characteristic of switches is that the contacts may bounce on closing. If it is important in the application that the first switching edge is detected, then a simple switch-debouncing logic that rejects noisy signals can be used. If a microcontroller is used to monitor the switch output, then debouncing can be accomplished by software means. This may be a better solution in applications subject to shock or heavy vibration, which may cause occasional false switching. In these cases, a microcontroller can be configured to poll the switch over some period of time and report switch closure only if a number of consecutive readings are the same.

3.3.2 Optical

Optical angle encoders for incremental shaft angular position measurement are constructed of a disk with a series of transparent and opaque equally spaced sectors. The disk can be made of glass for precision applications. Mylar film and metal disks offer high and medium resolutions, respectively, at low cost. The encoder disk is illuminated on one side and light sensors on the other side detect the passage of light and dark sectors as the disk is rotated. (Low-resolution versions such as the Hewlett-Packard HRPG series use an alternative reflective technology.) Most encoders have two sets of light sources and detectors offset by half the width of a sector. Figure 3.2 shows the relationship between the outputs of the light sensors as the encoder is rotated. This format is often referred to as "A quad B," since the signals are in quadrature. The passage of one pair of light and dark sectors over a detector is referred to variously as one cycle, one count, one line or 360 electrical degrees (°e). Encoder resolutions range from around 16 counts per revolution (CPR) for low-cost applications to over 6000 CPR for precision position control systems. Most encoders also include a third signal for use as an index or reference pulse. The index, or North marker as it is sometimes called, occurs once per revolution. The pulse width is usually equal to 90 °e.[1]

Four separate states, each of 90 °e, can be derived from the A and B outputs using integrated circuits available from a number of vendors. This allows a resolution of four times the number of lines on the encoder disk to be achieved. These ICs also determine the direction of rotation of the encoder by observing which output leads the other. By convention for clockwise rotation, the low-to-high transition of A leads the low-to-high transition of B. Control circuitry can be added to improve noise immunity by only allowing valid next states to be counted.

Incremental angle encoder accuracy specifications fall into two categories. The angular position accuracy is the difference between the actual shaft angle and the angle indicated by the encoder. This error is normally expressed in degrees or minutes of arc. The second category includes specifications for the symmetry and repeatability of individual cycles; these are usually

PETITIONER'S EXHIBIT 1002
US PATENT NO. 6,581,565

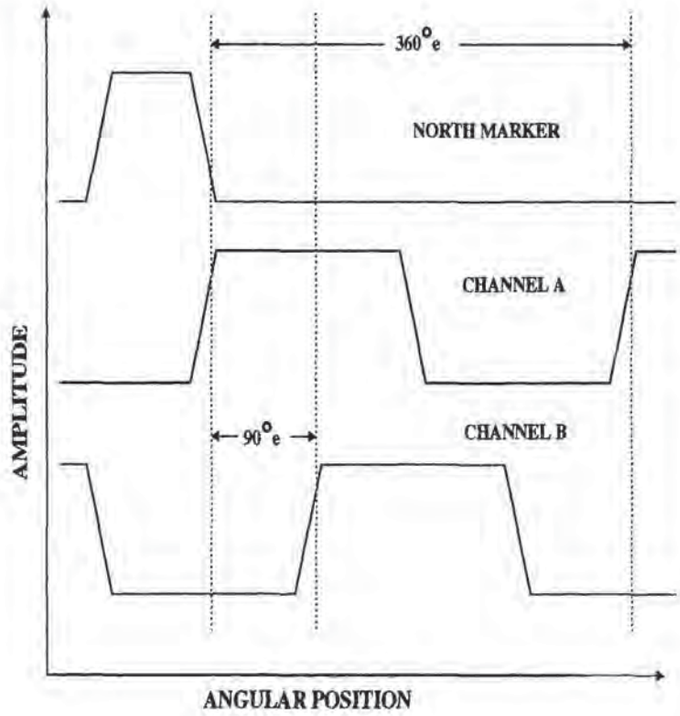


FIGURE 3.2 Encoder outputs.

expressed in electrical degrees. Typical characteristics are detailed in Fig. 3.3 and Table 3.1 Errors are caused by eccentricity and axial play of the code wheel and manufacturing defects in the lithography or etching of the code wheel. Modular encoders consisting of a light source and sensor head are available which use a collimated light source and an array of integrated photodiodes to minimize the effects of these error sources. Differential connection of the photodiodes ensures insensitivity to errors caused by light source variability due to environmental or other factors. A further source of error can occur if the encoder is rotated at high enough speeds that the rise and fall time of the digital outputs significantly affects the pulse width. The light sensor bandwidth usually determines the maximum rotational speed of the sensor. Typical bandwidths are below 100 kHz, which would limit the speed of a 100-CPR encoder to 1000 rpm.

Linear incremental optical encoders are available from many vendors. These allow direct measurement of linear motion. Modular sensor/emitter heads are available that can be used in these applications. The technology is basically the same as incremental angle encoders and the terminology used to describe specifications is the same as for angle encoders. Linear encoders are described in terms of their count density or resolution in counts per mm or mm

TABLE 3.1 Incremental Encoder Specifications

	Minimum	Typical	Maximum	Units
Position error		10	40	min of arc
Cycle error		3	10	°e
Pulse-width error		7	30	°e
Phase error		2	15	°e
State-width error		5	30	°e
Index pulse width	60	90	120	°e

PETITIONER'S EXHIBIT 1002
US PATENT NO. 6,581,565

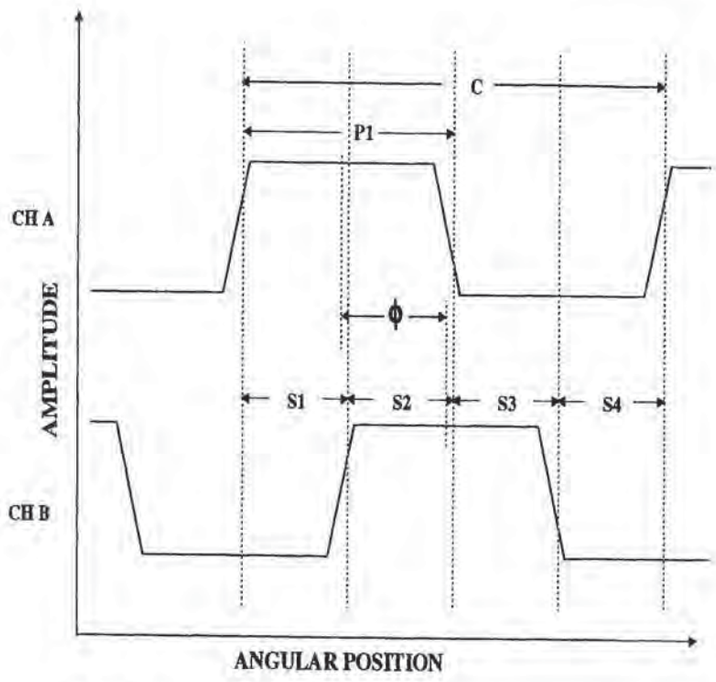


FIGURE 3.3 Encoder definitions.

per count. Line counts range up to approximately 8 per mm, allowing an ultimate linear resolution of around 30 μm.

If it is important to have an unambiguous measure of position as soon as power is applied to a system, then an absolute encoder must be used. Absolute optical encoders are manufactured with resolutions from one part in 2^6 to one part in 2^{16}. The data format can be binary, binary-coded decimal (BCD), or Gray code. An absolute angle encoder is divided into equal sectors which are arranged so that adjacent sectors contain consecutive digital words. The binary bits of each word form N concentric tracks on the encoder disk, where N is the digital word length. N sets of light sources and photodiodes detect the parallel word representing the input shaft angle.

Absolute optical encoders often use Gray code to eliminate code transition errors. In a natural binary sequence between zero and full scale on the disk, all the bits of the digital word change state together. Any misalignment of the code wheel and the light sensors, or sensor-to-sensor misalignment, will cause false codes to be generated. This could be disastrous for a position control system since a misread code could indicate an angle up to 180° away from the correct angle. Gray coding eliminates this problem. Gray code is a unit distance code; consecutive codes differ by only one binary bit. If a code transition is misread, the largest error will be one least significant bit of the digital word.

.3.3 Potentiometric

Potentiometers are widely used as position sensors in automotive applications such as throttle and accelerator pedal position measurement. The automotive industry increasingly

PETITIONER'S EXHIBIT 1002
US PATENT NO. 6,581,565

demands low-cost mechanically and electrically rugged sensors to provide control or measurement of position in the modern automobile. This has resulted in the development of potentiometers that are capable of operational life far in excess of the life of the average car, and in some cases capable of continuous rotational speeds of above 1000 rpm for more than 1000 hours.[2]

Potentiometers can be constructed using a wire-wound track. The resolution of these potentiometers is determined by the number of turns of wire used to wind the track. The resolution of rotary wire-wound potentiometers is often quoted as the number of turns per degree and can be anywhere between 1 (1° per turn) and 7 (8.5 arcmin per turn). The track resistance is proportional to the number of turns used and can be in the range of 10 ohms to 100 kilohms, with a tolerance of approximately 5 percent. Wire-wound potentiometers have advantages where low-value variable resistors are required but do not excel in linearity, resolution, or rotational life which can be as low as 10^5 revolutions. Potentiometers for position-sensing applications are constructed using a resistive track of conductive material, usually a graphite and carbon black doped plastic, and a collector track molded on some supporting substrate. A drive shaft or pushrod draws precious metal multifingered wipers along the tracks. Wiper damping is usually included to make the potentiometer insensitive to vibration. Potentiometers of this type are manufactured with a range of resistance from around 500 ohms to 20 kilohms with a tolerance of 10 to 20 percent (Table 3.2). Potentiometers of this type are capable of excellent linearity and very high resolution.

TABLE 3.2 Potentiometer Specifications

Parameter	Minimum	Maximum
Electrical travel	90°, 10 mm	360, 3000
Nominal resistance	500 ohms	20 kilohms
Resistance tolerance	10%	20%
Resistance temperature coefficient (TC)		500 ppm/°C
TC of V_{out} in voltage divider mode		5 ppm/°C
Linearity error	0.01%	1%

Potentiometric sensors are used as voltage dividers. A reference voltage is applied across the resistive element and the wiper voltage is used as an absolute measure of the position of the actuator. Linear potentiometers are available in a wide range of lengths from 10 mm to 300 cm. Rotary potentiometers are usually restricted to 355° of useful range due to the dead band created by the track-end contacts. Some versions are available with true 360° operation. These use multiple wipers and dedicated electronics to eliminate the dead band.

All potentiometers are ratiometric sensors. That is, the wiper voltage at a given position is some fraction of the reference voltage applied across the resistive track. If the reference voltage is varied, the potentiometer output remains in the same ratio to the reference voltage. Sensor potentiometers, when properly terminated, maintain ratiometric operation over a wide range of temperatures with temperature coefficients typically less than 5 parts per million (ppm) per degree centigrade. Without special signal processing, ratiometricity is compromised at the end of the electrical travel of a potentiometer by the change in resistivity of the track as it joins the end contact and by any parasitic external resistance in series with the track. Figure 3.4 shows the effective limitations on the potentiometer at its endpoints.

Ratiometricity is a very desirable characteristic for a sensor that is used with comparators or analog-to-digital converters. For example, if the same reference voltage that powers the sensor is used as the reference for an analog-to-digital converter, then the measurement system will be insensitive to the absolute value of the reference voltage. A given shaft angle will always be reported as the same digital code. In most automotive control systems, analog-to-digital converters (usually on board a microcontroller) use the regulated 5-V engine controller

PETITIONER'S EXHIBIT 1002
US PATENT NO. 6,581,565

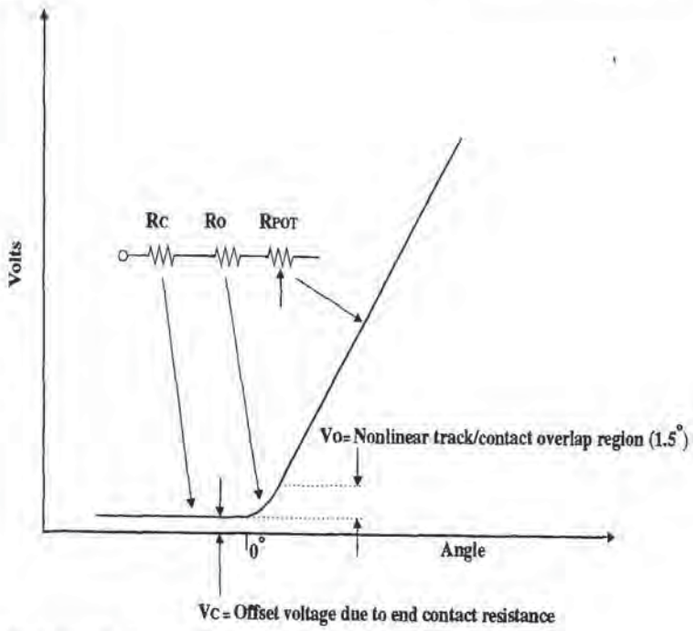


FIGURE 3.4 Potentiometer endpoint nonlinearity.

(ECU) power supply as reference to avoid the additional cost of a separate voltage reference chip. It is desirable that the same voltage, perhaps buffered to isolate the control module from accidental shorts, is used as reference by any ratiometric sensors in the automobile.

Potentiometers are subject to a number of sources of error, of which linearity is the most important. The linearity error is the difference between the actual transfer function of the potentiometer and the ideal transfer function (output voltage change versus mechanical travel) as a percentage of the applied reference voltage. Linearity specifications between 0.03 and 1 percent are available, with sensor cost inversely proportional to linearity. Microlinearity can be an important indicator of the suitability of the potentiometer for use in accurate control systems where large changes in the local gradient of the transfer function may cause instability. Ratiometricity, linearity, and offset errors can be caused by improperly loading the wiper of the potentiometer. The maximum error is at the center of travel of the wiper. If the load is a constant current, such as the input current of a buffer amplifier, a voltage will be developed across R_{EXT} that will cause an offset error at the extremes of travel of the wiper and an additional linearity error at the center of travel. Sensor potentiometers are usually specified with some maximum wiper current (100 nA, typically) to eliminate these errors. Plastic track potentiometers are capable of resolutions better than 0.001 percent of travel. This is primarily limited by the homogeneity of the resistive track material and hysteresis caused by limitations in the mechanical construction of the potentiometer related to bearings, wiper stiffness, and coefficient of friction of the track.

Plastic track sensor potentiometers are capable of operational life in excess of 10^7 revolutions for a rotary sensor or 10^7 strokes for a linear sensor. Unfortunately, no universal standards are available defining test conditions, and these may vary from vendor to vendor. Generally, two types of test are carried out. Dither testing simulates conditions which may exist in control applications or areas with high levels of vibration. The wiper is moved over a small proportion of the travel, say 1 or 2°, at a test frequency of 100 Hz. Information about contact resistance and local gradient changes in the potentiometer transfer function can be gathered rapidly using this technique. A change in gradient (ohms/percent of travel) relative to the mean gradient of the potentiometer can be equated to a change in loop gain in a con-

PETITIONER'S EXHIBIT 1002
US PATENT NO. 6,581,565

trol system. Sensitive systems may become unstable at worn points in the potentiometer track due to relative gradient errors.

A second method of potentiometer reliability testing is to repeatedly move the wiper at around 10 Hz over a large proportion of the available range. An excursion from 0 to 50 percent of the available travel will result in the maximum change in linearity error over a large number of cycles, since only one-half of the track is subject to wear. The criteria for failure of a potentiometer will be very application-specific and may, for example, be a doubling in linearity error. It is important to work with the potentiometer vendors to understand how their specifications can be extrapolated to make a prediction of operational life.

3.3.4 Magnetic

By far the largest category of position sensors relies on electromagnetic induction principles. This group of sensors can be broken into subgroups depending on the details of the employment of the phenomenon. Other sensors in this category rely on materials with magnetoresistive or magnetostrictive properties. Electromagnetic sensors have a number of advantages over other technologies. In general, this class of sensors measures or responds to changes in the relative position of components in a magnetic circuit. The components are always separated by an air gap and are not subject to friction wear. In many cases, it is possible to construct rugged sensors that are insensitive to the harshest automotive environments.

Variable Reluctance. The reluctance of a magnetic circuit determines the magnetomotive force (amp turns) required to produce a flux of a given value.[3] Variable reluctance devices operate by sensing changes in the reluctance within a magnetic circuit. In most cases, the reluctance change is caused by a change in the length of an air gap. The change in reluctance causes a change in the magnetic flux which induces a voltage in an output signal coil. The voltage induced is typically a bipolar pulse shape whose amplitude is proportional to the rate of change of flux (Faraday's law).

$$V = \left(\frac{d\Phi}{dt} \right) \tag{3.1}$$

This sensor technology cannot be used at zero speed since, if the rate of change of flux is zero, then the output will be zero.

In automotive applications, variable reluctance sensors are used to detect the position and speed of rotating toothed or slotted wheels in crank-, cam-, and wheel-monitoring applications. An easily magnetized or "soft" magnetic core or bobbin wound with a sense coil is magnetized by a strong permanent magnet such as samarium cobalt (Sm_2Co_{17}). The sense end of the core is placed in close proximity to a toothed gear wheel. The flux change that occurs when a tooth edge passes the sensor causes a voltage to be induced in the coil. Remote signal-conditioning electronics associated with the ECU are used to amplify the signal and produce a signal that a microcontroller can interpret as a position increment. An alternative construction[4] uses a coaxial pole piece to improve the magnetic circuit. This construction is particularly suited to sensing holes or apertures in a sense wheel. Sensors that detect slots and are positioned in close proximity to the target with a small air gap work at low reluctance and are less likely to be disturbed by interfering fields than sensors configured to detect teeth at a low mark space ratio.

Variable reluctance sensors are prone to a number of sources of error. Vibrations or resonance sometimes exacerbated by the attractive forces between the sensor and the target can seriously degrade the signal-to-noise ratio of the device. The sensors' target is usually a rotating ferromagnetic wheel or gear. Eddy currents will be generated by the movement of the wheel in the magnetic field of the sensor. This may lead to false readings from the sensor. In some refinements of variable reluctance sensors, the holes or apertures in the wheel are filled with an electrically conductive nonmagnetic material to homogenize eddy currents.[4]

PETITIONER'S EXHIBIT 1002
US PATENT NO. 6,581,565

Significant advantages of variable reluctance sensors in the automotive environment are their simple rugged construction and low cost. Additionally, they have a wide operating temperature range and require only two wires for operation. Variable reluctance sensors can also be used as variable inductance sensors by exciting the sense coil with alternating current and employing inductance-measuring means in the signal-conditioning electronics.

Hall Effect. Electric current is carried through the motion of electric charge. If a conductor is moved through a magnetic field with velocity v, the charges in the conductor will experience a force (Lorentz force) in a direction perpendicular to both the direction of motion and the magnetic field. This gives rise to an electric field of strength:

$$\mathbf{E} = v\mathbf{B} \tag{3.2}$$

The charges will move and a surface charge will develop on the conductor until an electrostatic field forms which counterbalances the electric field due to motion, $v\mathbf{B}$. A voltage due to the movement of charge can be detected with a voltmeter. The voltage is proportional to the field **B** and the velocity and length of the conductor. The result of this effect in thin films of material was first described by Hall over 100 years ago. When he passed current through a rectangle of gold foil in the presence of a magnetic field perpendicular to the plane of the foil, a voltage could be measured across the other axis of the foil.

Devices can be constructed using semiconductor materials which can utilize this effect to detect the strength of magnetic fields. Figure 3.5 illustrates the construction and operation of a silicon Hall effect device. A voltage is amplified across one axis of a thin block of high-resistivity n-type epitaxial material. In the presence of the field **B**, charges move in the direction of the arrow. A voltage directly proportional to **B**, the current density in the silicon and the Hall coefficient (scattering factor) can be measured at the point shown. The sensitivity is low and amplification is required to render a useful signal. For example, with a current of 10 mA flowing in an n-type silicon epitaxial layer 1 μm thick with a doping level of $10^{15}/cm^3$ and a field of 100 mT, a voltage difference of approximately 30 mV will be measured at 25 °C. Offsets caused by resistivity gradients, piezoelectric effects from packaging stress, and contact misalignment can amount to 10 mT or more. Layout techniques, such as cross-coupled structures to minimize the effects of resistivity gradients, can significantly improve offsets. Careful alignment of the Hall cell layout with crystal axes can mitigate piezoelectric effects. Silicon Hall effect devices are insensitive to magnetoresistive effects as the field strengths encountered in most applications have good linearity with errors of <0.1 percent for fields from 0 to >100 mT.[5]

The Hall voltage is strongly temperature dependent and, with constant current bias, is proportional to the magnetic field, the bias current, the carrier concentration, the scattering factor, and a constant G, which is a function of the geometry of the device.

$$VH = GI\mathbf{B}\left(\frac{r}{\text{qnt}}\right) \tag{3.3}$$

A typical silicon Hall device will exhibit a temperature coefficient of the Hall voltage of approximately 1000 ppm/°C under these bias conditions. The temperature dependence can be reduced with a current source, the temperature coefficient of which is designed to compensate for the Hall voltage TC. In this way, the sensitivity of a Hall effect device can be controlled within 1 or 2 percent over the range of temperatures normally encountered in automotive wheel position and speed applications. The temperature coefficient of the compensated device can be matched to the magnetic circuit if necessary; a typical requirement might be to provide a residual TC of 200 ppm/°C to compensate for the TC of a Sm_2Co_{17} magnet.

Hall effect devices can be constructed from semiconductor materials other than silicon—for example, gallium arsenide (GaAs). GaAs offers higher carrier mobility and some promise for higher temperature operation than silicon. Silicon has the advantage of low cost and the availability of integrated circuit processing techniques that can be used to integrate Hall effect devices with sophisticated signal conditioning. Dielectrically isolated silicon processes,

PETITIONER'S EXHIBIT 1002
US PATENT NO. 6,581,565

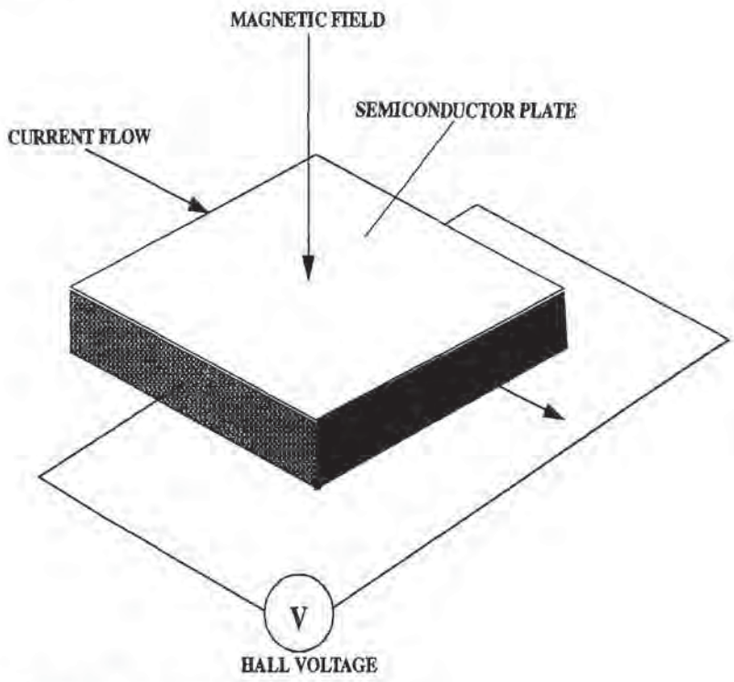


FIGURE 3.5 Hall effect device.

combining integrated circuit techniques with low leakage device isolation, can equal or better the high temperature performance of GaAs.

Hall effect integrated circuits are best categorized in terms of their output characteristics. Analog output devices are usually designed to provide a voltage output that is proportional to the applied magnetic field and also to the power supply voltage. An output ratiometric to the supply allows the device to be easily interfaced to analog-to-digital converters. Analog output devices can be used to construct noncontact absolute position transducers, where the Hall effect device measures a varying field which is designed to be proportional to an angle or linear position. Sensors such as these have no wearing parts other than bearings and can have significant reliability advantages over potentiometers in applications such as throttle-position measurement applications.

Digital output devices are used to construct limit switches or incremental position sensors. The Hall device can be designed to detect homopolar or bipolar fields. Important specifications for digital output devices are operate and release points and the differential between them. The operate point is the maximum field that must be applied to turn the output ON; where ON may be a current-sourcing or current-sinking function. The release point is the minimum field that will guarantee that the sensor is OFF. The differential is the difference between the actual operate and release points. The differential is built in to provide some hysteresis or noise margin to prevent false triggering, particularly at low rates of change of field. The differential may be considerably smaller than the difference between the specified operate and release points. Unipolar devices are specified with operate and release points of the same sign. Bipolar devices are specified with a positive operate point and a negative release point. A caution here is that some devices specified as bipolar do not always require a change of phase of field to operate and release; truly bipolar devices always do.

High-performance Hall effect ICs employ various circuit techniques to improve sensitivity.[6,7] Differential Hall sensors designed for use as gear wheel position sensors use two Hall cells ideally separated by half the gear tooth pitch. This kind of sensor is capable of detecting small changes in unipolar fields. Differential sensors produce an output pulse whose width

PETITIONER'S EXHIBIT 1002
US PATENT NO. 6,581,565

depends on the rate at which the gear tooth passes the sensor. At very low and very high speeds a very small mark space ratio output results. At high speeds, the timing of the output will be delayed from the mechanical event by a significant proportion of the tooth pitch. A second method is to use a filter circuit to determine the average value of an alternating field and then detect variations from the average value. This method also eliminates any offset that the sensor may have. This method more accurately tracks the mechanical stimulus. A disadvantage is that the filtering function imposes a lower limit on the speed that can be tracked. The devices detailed in Refs. 6 and 7 have lower limits of around 4 Hz. An additional limitation is that the sensor may fail to operate with a high mark space ratio stimulus since the average value of the input will be close to the value of the longest part of the cycle.

A typical Hall sensor application is shown in Fig. 3.6. The Hall device is assembled into a probe with a biasing magnet. The Hall device orientation will depend on its mode of operation, whether unipolar or bipolar. In all cases, the device is sensitive to fields perpendicular to the plane of the silicon surface. Figure 3.6 also compares output waveforms of the Hall sensor configurations discussed earlier as they would appear in this application.

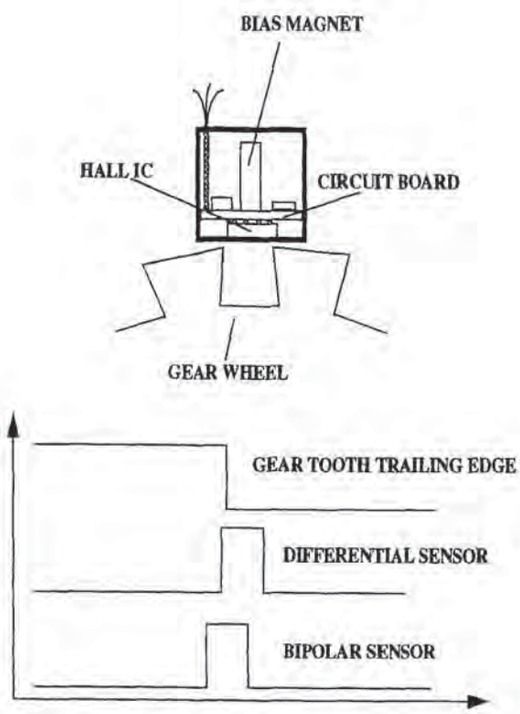


FIGURE 3.6 Hall probe gear position sensor.

Inductive Angle Transducers. Synchro resolvers, or simply resolvers, are absolute angle transducers. Due mainly to their construction, modern brushless resolvers offer the most rugged, reliable, and highest-resolution solution to angle sensing. Resolvers are often considered a high-cost transducer for automotive applications due to the high labor content in the production of most variants. Some designs[8] provide a cost-effective solution by employing sensing and output windings that can be produced on conventional armature-winding machines. Resolvers can be obtained either fully enclosed or as "pancake" devices, with the stator and rotor supplied separated to facilitate over shaft mounting. Resolvers are often referred to by their size. This is the diameter of the case of the device in inches, rounded up to the nearest 10th, and multiplied by 10. For example, a size 11 resolver will be a fraction less than 1.1 in in diameter. Resolver accuracies are specified in arc min. Typical values for

PETITIONER'S EXHIBIT 1002
US PATENT NO. 6,581,565

accuracy lie in the range 7 arcmin, with more or less accurate versions available from some vendors.[9]

Resolvers are basically rotating transformers. The construction of a typical device and the output waveforms for a 360° rotation are shown in Fig. 3.7. An alternating voltage connected to the reference input provides primary excitation. The range of frequencies used can be 400 to 20 kHz depending on the construction of the resolver; most resolvers are optimized for the 2 to 5 kHz frequency range. The reference signal is coupled to the rotor via a transformer mounted at one end of the rotor shaft. A second rotor winding couples to two orthogonally oriented stator windings. The stator coils are wound so that as the rotor shaft rotates, the amplitudes of the outputs of the stator windings vary as sine and cosine of the shaft angle relative to some zero.

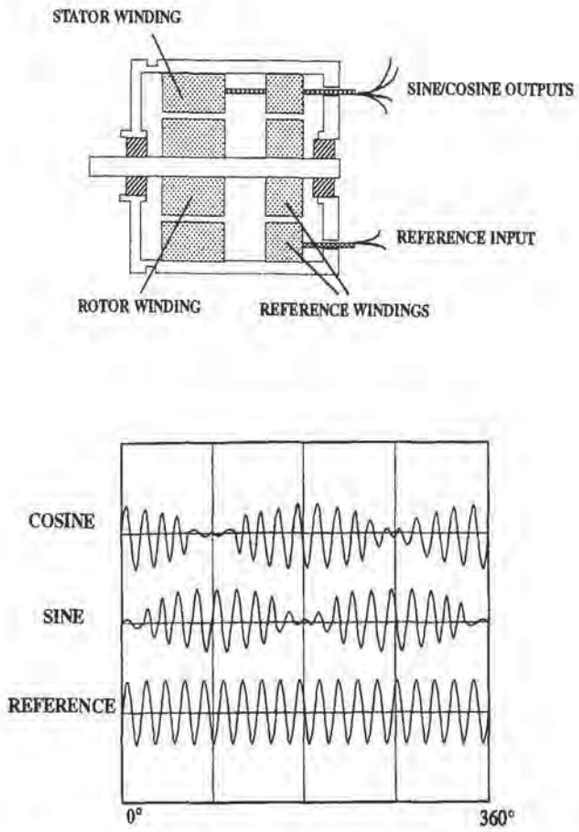


FIGURE 3.7 Resolver construction and output format.

By far, the most economical way of decoding the output of a resolver is to use an IC resolver-to-digital converter (R to D). A functional block diagram of a typical converter is shown in Fig. 3.8. The sine and cosine amplitude-modulated input signals from the resolver representing a shaft angle θ are multiplied by the cosine and sine, respectively, of the current value ϕ of the up/down counter. The resulting signals are subtracted giving:

$$VE = A \sin(\omega t) \sin(\theta - \phi) \tag{3.4}$$

where $A \sin(\omega t)$ represents the reference carrier.

This signal is synchronously demodulated and an integrator and voltage-controlled oscillator form a closed loop with the counter/multiplier, which seeks to null $\sin(\theta - \phi)$. When the

PETITIONER'S EXHIBIT 1002
US PATENT NO. 6,581,565

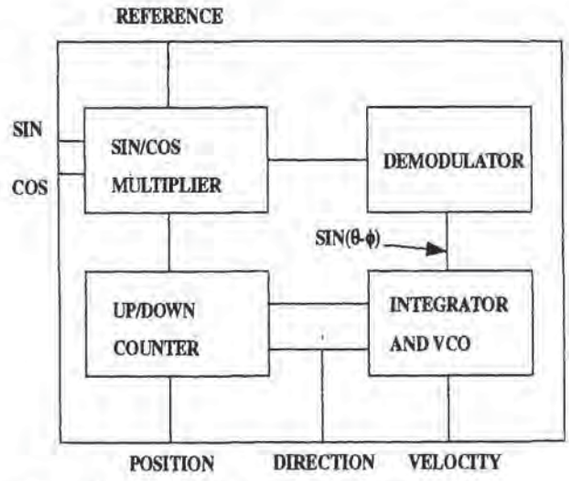


FIGURE 3.8 Tracking resolver-to-digital converter.

null is achieved, the counter value represents the resolver shaft angle within the rated accuracy of the converter. IC R-to-D converters are available that provide parallel or serial digital outputs with resolutions of from 10 to 16 bits and accuracies from 2 to 30 arcmin. Versions are available[10] that emulate standard optical encoder outputs for applications where absolute position measurement is not required but the environment is too harsh for an optical encoder. The system described is a type 2 servo loop which is characterized by zero position and velocity error (not including the limitations of the amplifiers in the IC). R-to-D converters of this type also provide a signal proportional to the angular speed of the resolver from zero to some upper limit, typically 1000 s of rpm, depending on the converter characteristics.

Inductive potential dividers are another class of transducers that are available in many variants.[11,12] A good example is the *rotary variable transformer* or ROVAT.[12] This device comprises a single coil wound on a circular ferromagnetic stator with a number of teeth wound as alternate polarity poles. The stator is excited with an AC signal of around 20 kHz. A rotor with a semicircular conductive screen on its inside surface encircles the stator. The screen reduces the flux linkage between the rotor and stator and the inductance of the screened portion of the stator is reduced, reducing the voltage drop across this portion of the stator. The voltage measured at a central tap on the stator is linearly proportional to the angle of the rotor. Further taps at 90° and 270° from the nominal zero allow a waveform to be measured with amplitude in quadrature with the signal measured at the center point. This allows a 360° absolute angle transducer to be realized, using decoding techniques similar to those which will be described later for the LVDT.

Inductive Linear Displacement Sensors. Shading ring or short-circuit ring sensors are absolute displacement sensors consisting of an E-shaped core with a winding on the central leg of the E. The winding is excited with high-frequency alternating current. An electrically conductive ring of Al or Cu is allowed to slide, maintaining an air gap along the central leg. The ring is attached to the mechanical component, whose position is to be measured. The ring is equivalent to a short-circuited secondary turn in a transformer. The ring has a shading effect, preventing any flux coupling between the legs of the core from its position along the central leg of the core to the open ends of the core (Fig. 3.9).[13] An inductance change can be measured at the terminals of the excitation coil. These sensors are usually used in a potential divider configuration with a reference inductance of similar construction to the main sensor connected in series with the main sensor. A reference alternating voltage is applied across the series-connected reference and sensor inductances, forming an inductive potential divider. The output is then proportional to the ratio of the inductances. This renders the sensor insensitive to tem-

PETITIONER'S EXHIBIT 1002
US PATENT NO. 6,581,565

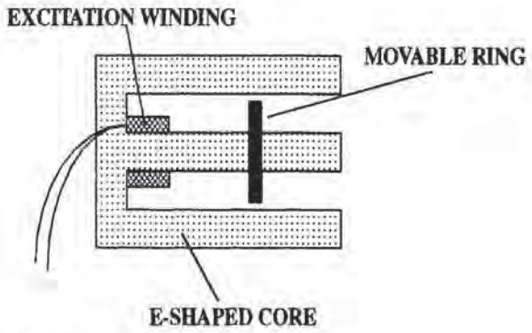


FIGURE 3.9 SCR sensor construction.

perature variations and allows easy adjustment of offsets. Signal-processing electronics can be used to rectify and filter the output and transmit the result to a remote control unit. An alternative construction is to replace the movable ring with an angled channel which can move, relative to the E-shaped core, in a plane perpendicular to the core. Again, the inductance of the sensor is proportional to the linear movement of the angled channel.

Another form of absolute linear displacement sensor is the linear variable differential transformer or LVDT.[14] LVDTs are rugged and reliable and capable of working in harsh environments. Suitable automotive applications include mounting inside hydraulic cylinders in suspension control systems.

LVDTs are constructed from a primary excitation coil positioned centrally on a cylindrical hollow former. Two identical secondary coils are positioned on either side of the primary. The coils have a common core which is free to move within the cylindrical former (Fig. 3.10). The secondaries are normally connected in series, with opposing phases such that with the core centrally positioned and coupling equally to each secondary, the voltage at the node common to both coils will be zero. With this connection, as the core is moved from one extreme of travel through the center to the other extreme, the output signal will vary from a maximum value in phase with the excitation through zero to a maximum value in antiphase with the excitation.

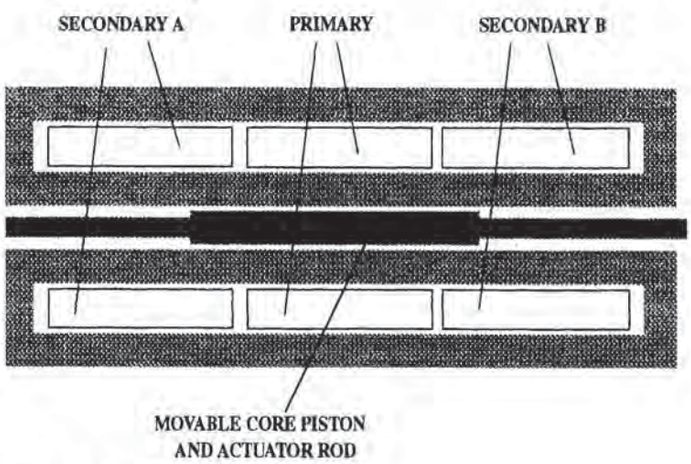


FIGURE 3.10 LVDT construction.

PETITIONER'S EXHIBIT 1002
US PATENT NO. 6,581,565

LVDTs are designed to give a linear output within some tolerance, typically ±0.25 percent, over a specified proportion of the available stroke length. The distribution of turns on the secondary coils is carefully arranged to maximize linearity over the widest possible range. LVDTs are available that maintain good linearity with stroke lengths from ±0.05 to ±10 in.

LVDTs operate with effective transformer ratios of between 10:1 to 2:1. The range of primary excitation frequencies can be from 20 Hz to 20 kHz, depending on the construction of the device. Most LVDTs are optimized for the 2- to 5-kHz frequency range. The output signal from an LVDT can be decoded in several different ways and a number of analog and digital integrated circuit solutions exist for this purpose.[15] An example of a typical connection scheme using an LVDT-to-digital converter is shown in Fig. 3.11. In this example, it is assumed that the sum of the voltages across the series-connected secondaries $V_A + V_B$ is a constant over the range of displacements of interest. The majority of LVDTs in production meet this criterion; for those that do not, an additional nonlinearity will result. The IC decodes the function $(V_A - V_B)/(V_A + V_B)$ over the range $[(V_A - V_B)] \leq (V_A + V_B)/2$ into a 13-bit digital word that can be accessed via a three-wire serial interface. Additional bits indicate null and over or under range for signals outside the linear range. The ratiometric decoding scheme described here is insensitive to primary-to-secondary phase shifts, temperature, and any residual null voltage that the transducer may have due to stray capacitive coupling.

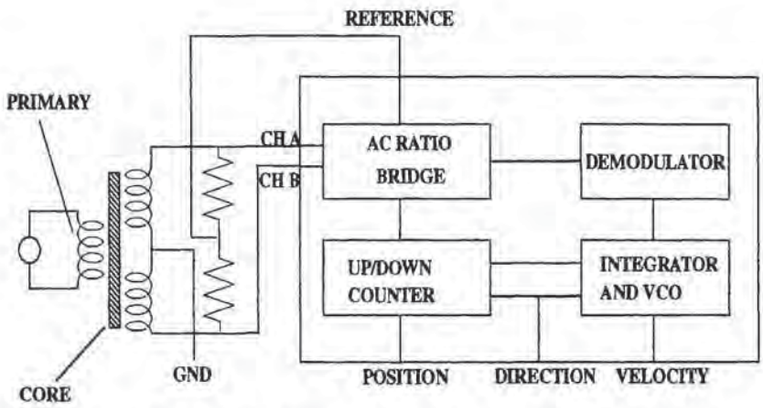


FIGURE 3.11 Tracking LVDT-to-digital converter.

Analog methods of decoding utilize the same basic algorithm as the converter already described. An analog decoder senses the secondary output voltages and evaluates the ratiometric function introduced earlier. The decoder output is filtered and amplified to produce an output voltage proportional to the position of the movable core.

Magnetoresistive. An interesting group of sensors utilize the property of some FeNi alloys such that their resistivity is strongly affected by the presence of a magnetic field. The magnetoresistive effects of one of the useful alloys, Permalloy, which is 81 percent nickel and 19 percent iron, enables sensitive magnetic field sensors with full-scale fields of 5 mT to be built. The variation in resistance is around 2.5 percent for a field of this magnitude. The resistance decreases with increasing field strength; the relationship between field strength and resistance is very nonlinear, approximating a cosine-squared function. Using thin films of Permalloy deposited on a silicon substrate allows signal-conditioning electronics to be integrated with the sensor. Despite the nonlinearity of the phenomenon, accurate linear sensors can be constructed by using the sensor in a bridge arrangement together with flux nulling means, such as a servo-driven coil surrounding the sensor, to effectively operate the sensor at constant resistance. An alternative construction uses opposing "barber pole" thin-film elements.[16] An element is composed of a rectangular thin film of Permalloy overlaid with a series of shorting

PETITIONER'S EXHIBIT 1002
US PATENT NO. 6,581,565

stripes of aluminum at 45° to the long axis. Two series-connected elements, which are mirror images of each other (reflected about the long axis), form a potential divider. Magnetoresistive sensors generally exhibit high sensitivity, but this leaves them prone to interference from unwanted fields and, therefore, they are unsuitable for some applications.

Magnetostrictive. Magnetostriction is a property of materials that respond to a change of magnetic flux by developing an elastic deformation of their crystal structure. Magnetostrictive linear displacement sensors utilize this phenomenon by launching a compression wave down a cylindrical waveguide using electromagnetic means, usually a current pulse. The waveguide passes through a movable permanent magnet ring at some distance from a receiver site. The compression wave generated at the magnet position travels to the receiver site at approximately 2800 m/s where it causes a change of flux and generates a voltage pulse in a sense coil. The time of flight of the pulse can be measured to determine the distance of the movable ring magnet down the wire. Transducers with stroke lengths in excess of 7.5 m are available that use this technique.

3.3.5 Other Technologies

A number of other technologies can be applied to position-sensing problems, limited only by engineering ingenuity. Some, like capacitive-sensing techniques, are not tolerant of the automotive environment due to sensitivity to humidity, vibration, or temperature or pressure extremes. Others, like resolvers of traditional construction, are sufficiently rugged but prohibitively expensive unless low-cost manufacturing techniques can be found. Occasionally, a nonobvious method finds a niche. An example is a fuel-level sensor disclosed by workers at Bosch,[17] which, in principle, could be applied as a position sensor. The device operates by exciting a metal rod with acoustic waves such that it resonates. One end of the rod is immersed in the fuel. The resonant frequency is a function of the depth of immersion and the fuel level can be determined by suitable electronics.

A significant influence in the selection of technologies for automotive use is the mandatory inclusion of safety systems. Microwave or laser-ranging techniques can be applied to anticollision systems to anticipate obstacles at nighttime or in poor-visibility driving conditions. These will be a ubiquitous component of automobiles in years to come.

3.4 INTERFACING SENSORS TO CONTROL SYSTEMS

All sensors, whether they have digital or analog outputs, provide measurement of real-world phenomena that are then interpreted by another system to either indicate a value, a warning, or close a control loop. It is vitally important that the integrity of the data is maintained by the proper choice of interface.

Cost and reliability in automotive systems are primary drivers in the choice of interface. For a given performance, the sensor that requires the fewer connections will always be selected. In some cases, such as LVDTs where the basic sensor requires 5 or 6 wires, it may be advantageous to locate the signal-conditioning electronics with the sensor and communicate the processed data to a remote controller via a simple serial interface. Interfacing incremental or serial binary data to a microcontroller is straightforward. In the case of incremental data, typically the mechanical system being monitored is moved until some limit or index is detected. Knowledge of the absolute position of the mechanical component is then known. A counter or register can be set to an initial nonzero value or reset to zero. As the motion is detected, pulses from the incremental sensor can be counted and stored as a measure of position. The indexing cycle must be performed each time power is applied. Binary serial data can be read into a register and used directly with no further processing.

PETITIONER'S EXHIBIT 1002
US PATENT NO. 6,581,565

Analog-to-digital converters (ADCs) require some special considerations to optimize performance. Not least of these is grounding. In most applications, chassis ground returns cannot be used. Modern automobiles may have voltage drops of 1 V or more between the chassis at the ECU and the sensor site, due to return currents from electric equipment. This voltage is likely to be noisy with many transients and will certainly upset all but the crudest sensors.

Previous sections have discussed the advantages of ratiometric sensors that can use the same reference as the converter. The advantage is that a least-significant bit of the ADC is always a fixed percentage of the sensor span. This eliminates gain, offset, and temperature errors that may occur if separate references are used. Resolution and gain accuracy of a system can be further optimized by making certain that the span of the sensor output uses all of the available input span of the converter. Many ADCs include on board a microcontroller and use switch capacitor techniques to acquire the analog input values. These present a transient load to the sensor once or twice per conversion cycle. Some sensor outputs, particularly sensors with buffer amplifiers, require isolation from this transient to achieve rated accuracy. A simple technique is to use a simple RC filter on the output of the sensor. This limits the transient current that the sensor output sees and shunts the ADC input with a capacitor.

GLOSSARY

Absolute output sensor The sensor output is an unambiguous measure of position and is valid when power is applied.

Arcminute An angular measure. There are 60 arcminutes in 1 degree of arc.

Incremental sensor The sensor indicates changes in position. An additional position reference, such as a limit switch, is often used with this type of sensor.

Linearity error The amount by which the sensor output differs from an ideal characteristic. Usually expressed in percent.

Ratiometric output sensor An input stimulus causes the output to be a fraction of a reference voltage.

REFERENCES

1. Hewlett-Packard, *Optoelectronics Designers Guide,* San Jose, Calif., 1991–1992.
2. Novatechnik Position Sensor Data, Ostfildern, Germany, 1992.
3. P. Hammond, *Electromagnetism for Engineers,* Pergamon Press Ltd., Oxford, England, 1965.
4. Roland K. Kolter, European Patent Application EP 0 019 530 A1, Applicant Bendix, 1980.
5. Henry P. Baltes, and Popovic, Radivoje S., "Integrated magnetic field sensors," *Proceedings of the IEEE* vol. 74, no. 8, Aug. 1986, pp. 1107–1132.
6. Hartmut Jasberg, "Differential Hall IC for gear-tooth sensing," *Sensors and Actuators,* A21–A23, 1990, pp. 737–742.
7. AD22150 Data Sheet, Analog Devices, Norwood, Mass.
8. Charles S. Smith, U.S. Patent 4 962 331, Assigned to Servo-Tek Products Co. Inc., Hawthorne, N.J., 1990.
9. Clifton Precision, Analog Components Data, Clifton Heights, Pa.
10. AD2S90 Data Sheet, Analog Devices, Norwood, Mass.
11. Novatechnik Angle Sensor Data, Ostfildern, Germany, 1993.

PETITIONER'S EXHIBIT 1002
US PATENT NO. 6,581,565

12. Donald L. Hore, and Flowerdew, Peter M., "Developments in inductive analog transducers for 360° rotation or tilt and for linear displacement," *IEE International Conference,* No. 285, 1988.
13. E. Zabler, and Heintz, F., "Shading-ring sensors as versatile position and angle sensors in motor vehicles," *Sensors and Actuators* **3**, 1982/3, pp. 315–326.
14. *Schaevitz Linear and Angular Displacement Transducers Catalog,* Pennsauken, N.J.
15. AD2S93 and AD598 Data Sheets, Analog Devices, Norwood, Mass.
16. F. Heintz and Zabler, E., "Application possibilities and future chances of 'smart' sensors in the motor vehicle," *SAE Technical Paper Series* #890304.
17. E. Zabler, "Universal low-cost fuel-level sensor," Robert Bosch GmbH, Ettingen, Germany.

ABOUT THE AUTHOR

Paul Nickson is product line manager for Analog Devices' Sensor and Automotive Group in Wilmington, Mass. He has BSc Honours in Electronic and Electrical Engineering from the University of Birmingham, England and 16 years' experience in integrated circuit design. For the past five years, he has focused on silicon sensors and sensor signal conditioning.

PETITIONER'S EXHIBIT 1002
US PATENT NO. 6,581,565

CHAPTER 4
FLOW SENSORS

Robert E. Bicking
Senior Engineering Fellow
Honeywell, Micro Switch Division

4.1 INTRODUCTION

Measurement of flow rate is important to optimize the performance of several key engine control subsystems. Mass air flow sensors are replacing the indirect calculation of intake mass air flow for improved performance, driveability, and economy. New requirements for on-board diagnostics are opening new applications for flow sensing in the automobile.

If the parameter to be measured is a gaseous mass flow as opposed to a volume flow, this further focuses the sensing technology selection since only a few technologies inherently measure mass flow. For liquid flow, either a mass flow or volumetric flow approach may be used since the density of a liquid changes only a small amount with atmospheric pressure and temperature.

This chapter is intended to give the reader an understanding of where and why flow sensors are being specified for use in engine control systems and an understanding of the trade-offs among alternative technologies in particular applications.

4.2 AUTOMOTIVE APPLICATIONS OF FLOW SENSORS

4.2.1 Intake Air Mass Flow

Electronic fuel injection has almost universally replaced the carburetor in the auto engine. This is because it provides better performance and is the only way to meet government mandated emissions standards. To do fuel injection, the mass flow rate of air going into the engine must be determined. There are two competing approaches to determining the mass air flow rate. The first, *speed density*, calculates the mass flow rate by measuring engine speed (RPM), intake air temperature (T_a) and intake manifold pressure (P). The per-cylinder nominal displacement (V) is known, as is the gas constant of air (R_a). The engine's volumetric efficiency (η) may be modeled as a function of speed. Then, the mass flow rate ($\dot{m}_a$) is calculated as follows:

$$\dot{m}_a = \frac{(\mathrm{RPM}\, V \eta\, P)}{(R_a T_a)} \tag{4.1}$$

PETITIONER'S EXHIBIT 1002
US PATENT NO. 6,581,565

By using a mass flow sensor, this calculation is eliminated and $\dot{m}_a$ is measured directly. The advantages of using a direct measurement include better accuracy under dynamic conditions because the manifold pressure changes more slowly than the mass flow rate. Also, no assumptions are made about engine displacement or volumetric efficiency, both of which affect the speed density calculation. Volumetric efficiency can change as the intake system becomes contaminated. Mass air flow sensors are presently being used on roughly 20 percent of the cars sold in the United States. They are not more widely used because they cost more than the pressure sensor needed to do the speed-density calculation. The largest drawback to using a mass flow sensor is that a wide dynamic range sensor is needed since the mass flow rate can change over a 100-to-1 range from idle to full throttle, whereas the manifold pressure only changes over a 5-to-1 range. Other important factors in sensor selection include resistance to contamination and particulate damage, accuracy, ability to measure reverse flow, and sensitivity to upstream and downstream ducting.

Fuel is injected to each cylinder on a sequential basis for optimum performance. This requires using the crankshaft sensor and camshaft sensor outputs to time the injection of fuel into the intake manifold at the proper point on the intake stroke. The fuel injector is fed with a constant pressure and is pulse-width modulated to control the amount of fuel injected. The calculation of the mass rate ($\dot{m}_f$) of fuel injected follows:

$$\dot{m}_f = \dot{m}_a \lambda \tag{4.2}$$

where $\dot{m}_a$ = mass air flow rate
λ = stoichiometric air/fuel ratio

4.2.2 Potential or Future Applications of Flow Sensors

Fuel Flow for Gas Mileage Measurement. Driver information systems that predict range and gas mileage need to know the amount of fuel flow. As seen from the preceding discussion of mass air flow measurement, the fuel flow is calculated from the air flow so that this data is already in the engine control computer. By simply summing the injector "on" time over a revolution or multiple revolutions, the fuel flow is known.

Alternatively, the fuel flow can be measured by taking the difference between the fuel coming into the fuel rail and that being returned. This approach could be subject to substantial error, however, due to the fact that these flows are purposely much larger than the net flow into the engine so that the fuel rail will be maintained at a constant pressure. Future fuel-handling systems may simplify the measurement by eliminating the return line and simply modulating the fuel pressure pump to maintain constant pressure. Then, the measured flow would be simply that flow going into the engine.

Exhaust Gas Recirculation Flow. Exhaust gas recirculation (EGR) is performed to reduce the emission of nitrous oxides (NO_x) by cooling the combustion process. If the EGR valve begins to clog or only partially opens, its flow will be reduced and emissions will increase. In the near future, OBDII legislation will require cars to have on-board diagnostics capable of determining when an emissions-related failure (such as that just described) occurs. Measurement of the flow is one way to diagnose a faulty EGR valve. Another way would be the use of an NO_x sensor to measure the emissions. However, no low-cost NO_x sensors have yet been developed.

Secondary Air Pump Flow. The secondary air pump is used to reduce the emissions of carbon monoxide (CO) and hydrocarbons (HC). Measurement of its flow rate is an approach to verifying that it is operating properly and doing its part to reduce emissions. Another way, of course, would be to directly measure the emissions of HC and CO in the exhaust. To date, however, there is no low-cost real-time means to do that. A way to verify air pump operation

PETITIONER'S EXHIBIT 1002
US PATENT NO. 6,581,565

without using any additional sensors is to command the air pump full-on when the fuel injection is slightly rich of stoichiometry. The oxygen sensor output should switch from rich to lean if the air pump is operating properly.

Fuel Flow for Fuel-Air Ratio Feedback Control. Present engine control systems treat the fuel flow as a dependent variable, measuring the intake air flow and then operating the fuel injectors to meter the proper amount of fuel into the engine. This tacitly assumes that each of the injectors is precisely calibrated so that a given "on" time provides a given amount of fuel. Fuel injectors typically use a needle valve in an orifice to meter the fuel. The orifice area is proportional to the square of the diameter so that the fuel flow error will be proportional to two times the diameter tolerance. By measuring the fuel flow, the accuracy of fuel injection could be improved. Table 4.1 summarizes the performance requirements by application.

TABLE 4.1

Application	Measurement type	Range, kg/h	Accuracy, %
Intake air	Mass	10–1000	±4
Fuel flow	Mass/vol.	1–66	±10
EGR flow	Mass	30–100	±10
Air pump flow	Vol.	50	±20
Fuel flow	Mass/vol.	1–66	±4

4.3 BASIC CLASSIFICATION OF FLOW SENSORS

4.3.1 Energy Additive or Energy Extractive

Flowing fluid possesses energy, both potential and kinetic. One approach to flow measurement extracts energy from the flow. Alternately, energy may be added to the flow and its effect observed. The energy-additive approach typically is nonintrusive, so the act of measuring doesn't affect the flow. As might be expected, flowmeter selection involves a number of factors, as will be discussed later.

4.3.2 Measurement of Mass Flow or Volume Flow

Intake air measurement requires that the mass of air flowing into the engine be measured. This favors a mass-flow approach, since, otherwise, pressure and air temperature must be measured to calculate the mass flow from the volume flow. The mass flow rate ($\dot{m}_a$) is calculated as follows:

$$\dot{m}_a = \dot{V}_a \rho \tag{4.3}$$

where ρ = air density
$\dot{V}_a$ = volumetric flow rate

The density, in turn, is calculated as follows:

$$\rho = \frac{P}{ZR_aT_a} \tag{4.4}$$

where P = air pressure
Z = compressibility factor
R_a = gas constant for air
T_a = air temperature

PETITIONER'S EXHIBIT 1002
US PATENT NO. 6,581,565

4.4 APPLICABLE FLOW MEASUREMENT TECHNOLOGIES

4.4.1 Gaseous Flow

Vane. The vane simply consists of a vane or paddle which is located in the flow duct and is restrained by a spring so that it blocks the duct with no flow. The deflection of the vane is thus proportional to flow. This deflection is read out by a potentiometer. The largest drawback of a vane sensor is that it increases the pressure drop in the intake tract, reducing the volumetric efficiency of the engine. This approach was used in the earliest engine control systems and is being replaced by technologies such as hot-wire air flow sensors which offer much lower pressure drop.

Thermal. This is the favored approach and is used in all engines currently being manufactured that employ direct measurement of the intake air mass. Depending on design details, it provides a nearly direct measurement of the mass flow and thus simplifies the engine control strategy. A variety of designs exists, from the straightforward hot-wire air flow sensor to more complex schemes. The basic idea is to heat a fine wire, and then as the gas flows past the wire, convection removes heat. The amount of heat removed can be measured with an electronic circuit and is proportional to mass air flow rate as the following equation shows:

$$\Delta P \cong \Delta T\,[C_t + (2\pi d C_v \dot{m}_a)^{1/2}]^* \tag{4.5}$$

where ΔP = change in electric power due to a given flow rate
ΔT = temperature difference between air and sensor
C_t = thermal conductivity of air
d = diameter of hot wire
C_v = thermal capacity of air
$\dot{m}_a$ = mass flow rate of air

Note that the first term of the equation isn't proportional to flow rate. Either this needs to be modeled and removed or the change in ambient air temperature needs to be minimized to accurately measure mass flow rate. A hot-wire air flow sensor and its control circuit is shown in Fig. 4.1. Control circuits typically either supply constant power to the heated element or

* From Joseph P. DeCarlo, *Fundamentals of Flow Measurement*, Instrument Society of America, 1984, pp. 173 and 176.

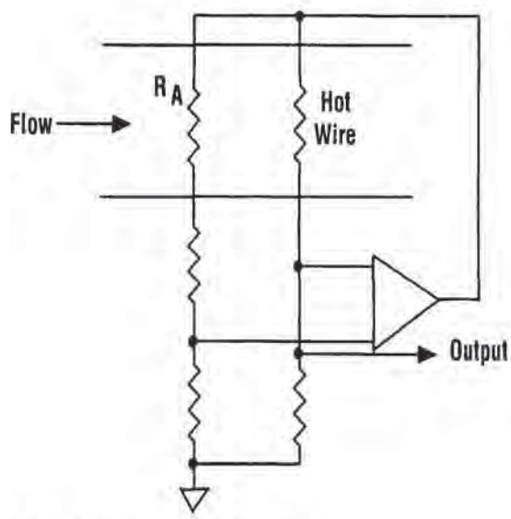


FIGURE 4.1 Hot-wire air flow sensor.

PETITIONER'S EXHIBIT 1002
US PATENT NO. 6,581,565

operate it at a constant temperature delta above the ambient temperature. The latter is shown in Fig. 4.2 and is preferred because it simplifies temperature compensation.

One of the problems with the hot-wire sensor is that fine dust particles may pass through the air filter and, under full-throttle conditions, can impact the hot wire with sufficient force to break it. Particulate build-up is also a source of error and has been alleviated by placing the heated element in a bypass channel or by incorporating a burn-off cycle at power-on. Most of the development in hot-wire sensors has been to ruggedize them to withstand the automotive environment and to desensitize them to upstream and downstream flow anomalies. Figure 4.2 is an example of a bypass design for a hot-element mass air flow sensor. It uses a platinum wire wound on a ceramic mandrel and coated with glass as the sensing element. It is located in a bypass channel away from the main flow to reduce the likelihood of particulate contamination. The bypass exits into the main channel through slots which are intended to desensitize it to backflows and backfires.

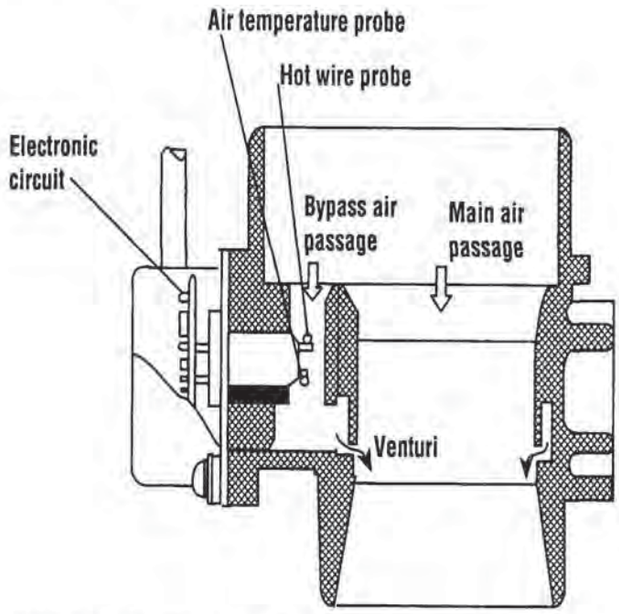


FIGURE 4.2 Bypass hot-wire air flow sensor. *(U.S. Patent 4,264,961)*

Backflow can occur in engines with four or fewer cylinders at low speed. It is most desirable for the sensor to measure the backflow, but most either don't measure it at all or rectify it, which makes the measured flow appear larger than it really is. This error is compensated by measuring the backflow on an engine and then using software to remove the nominal error. One of the issues with bypass designs is that upstream ducting of the air may affect measurement accuracy. A bend just ahead of the sensor will cause the air to move toward the outside of the bend and, depending on where the bypass is located, it may read either too low or too high. This effect is minimized by placing a screen or honeycomb in the sensor to straighten the flow.

Micromachined air flow sensors have been available commercially for several years and efforts are underway to adapt them to automotive applications. Their primary advantages include the low cost of the sensing element due to batch fabrication; excellent performance over temperature due to the close proximity of the heated and reference elements; the ability to measure reverse flows; low operating power due to the small size of the heated element; and fast response, again due to the small size of the heated element. Because of the use of integrated circuit manufacturing techniques, it is no more difficult to include additional resistors on the sensor chip than to simply replicate a hot wire. A calorimetric flow sensor may be constructed by separating the heater and sensor functions as shown in Fig. 4.3. The advantage

PETITIONER'S EXHIBIT 1002
US PATENT NO. 6,581,565

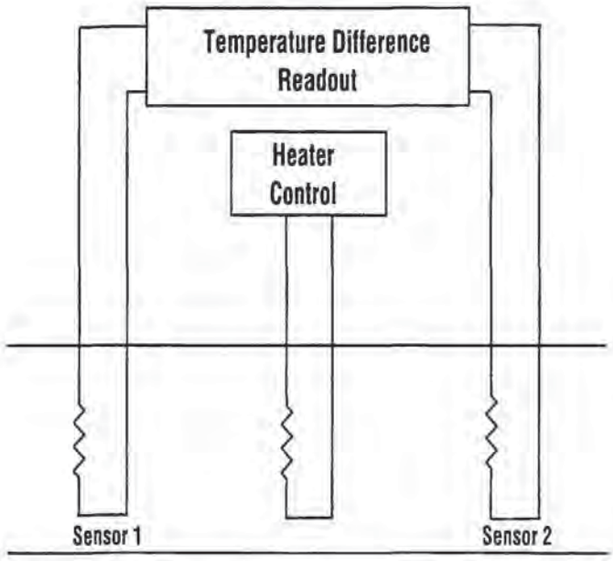


FIGURE 4.3 Calorimetric flow sensor.

of a calorimetric flow sensor is that it does measure the mass flow rate as the following equation shows:

$$\Delta P = \dot{m}_a C_p \Delta T^* \tag{4.6}$$

where ΔP = change in power due to a given mass flow rate
$\dot{m}_a$ = mass air flow rate
C_p = thermal capacity of air
ΔT = temperature difference between air and sensor

One of the issues with microstructure sensors is protection from damage due to particle impact and preventing build-up of contamination. This requires clever packaging.

Table 4.2 compares the main types of thermal mass air flow sensors.

Differential Pressure. A simple way to measure volumetric flow is to place an obstruction in a flow channel and measure the differential pressure drop across it. The flow is proportional to the square root of the differential pressure. This only works well for narrow flow ranges because to operate over a given flow range, the pressure sensor must operate over the square of that range. For the automotive intake flow range of 100 to 1, a pressure sensor with a range of 10,000 to 1 is required, which is not achievable except at high cost. An important advantage of this approach is that it is resistant to contamination, since the pressure sensor merely needs

* From "Fundamentals of Flow Measurement," Joseph P. Decarlo, Instrument Society of America, 1984, pp. 173 and 176.

TABLE 4.2

Type	Effect of contamination	Meas. rev. flow	Affected by ducting	Power used
Hot Wire	High*	Rectifies	Low	Medium
Hot RTD Bypass	Low	Ignores	High	High
Micro RTD	Low	Yes	Low	Low

* Burn-off cycle used to alleviate.

PETITIONER'S EXHIBIT 1002
US PATENT NO. 6,581,565

to sense the pressure difference across the flow restriction (in the case of an orifice plate or venturi). The differential pressure approach could be suitable for some low-accuracy or low dynamic range applications such as EGR valve flow. Venturis (Fig. 4.4), flow restrictions (Fig. 4.5), and pitot tubes (Fig. 4.6) all operate on the same principle.

4.4.2 Liquid Flow

Differential Pressure. The preceding discussion on differential pressure sensing applies equally to liquid flows.

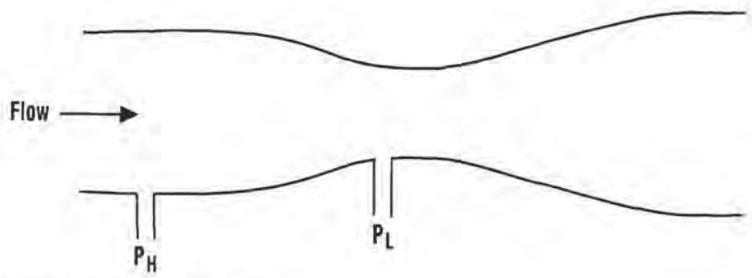


FIGURE 4.4 Venturi flow sensor.

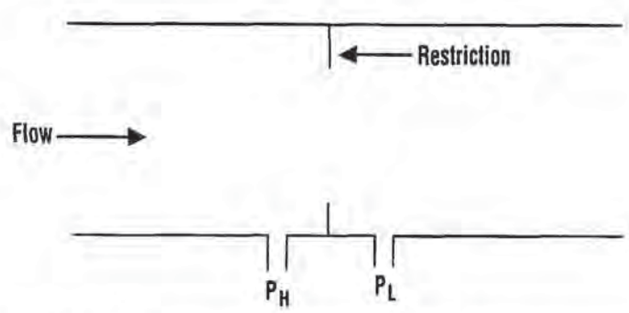


FIGURE 4.5 Flow sensor using a restriction to develop a differential pressure.

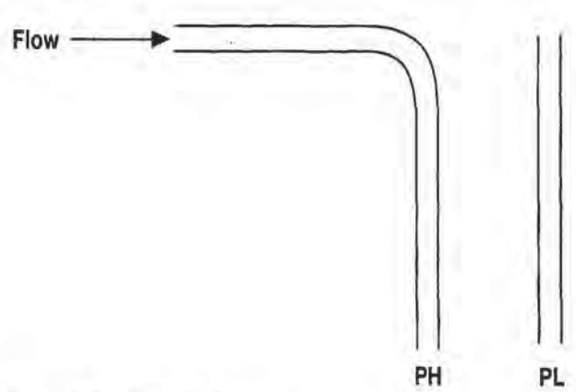


FIGURE 4.6 Pitot tube flow sensor.

PETITIONER'S EXHIBIT 1002
US PATENT NO. 6,581,565

Turbine. A turbine blade placed in a flow channel can offer low restriction to flow, and by counting the speed of rotation it can also measure flow. It is analogous to the vane described previously except that it is more subject to wear since it is revolving, not merely deflecting. Use of a noncontacting means of counting revolutions (such as a Hall effect sensor) is recommended. This approach is well-suited to measurement of fuel flow.

Vortex Shedding. Oscillations may be induced in a fluid by placing an obstruction in the flow stream. The oscillations may be measured thermally, by pressure changes or using ultrasonics. This approach doesn't work well at low flow rates due to instability in the vortex shedding mechanism, so it is not suited to wide dynamic range applications such as intake air measurement. An example of a vortex shedding flow sensor is shown in Fig. 4.7.

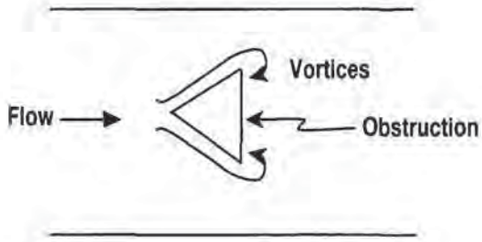


FIGURE 4.7 Vortex shedding flow sensor.

Other Technologies. There are a number of other technologies which are not well-suited to automotive applications, primarily due to cost considerations. A variety of flow sensors has been developed for industrial applications where performance is paramount and cost is secondary. These include the use of ultrasonics, gyroscopic effects, ionization of gases, and so on. These will not be discussed herein. Information on these technologies is given in the books by DeCarlo and Norton. See the list of suggestions for further reading.

GLOSSARY

Backflow The flow of air out of the intake system of an engine. This occurs at low speeds in engines containing only a few cylinders when all intake valves are closed at once.

Exhaust gas recirculation A process in which exhaust gases (containing primarily nitrogen) are returned to the intake system to reduce emissions by lowering the combustion temperature.

Micromachining Formation of very small three-dimensional structures in a semiconductor material.

Speed density A method of calculating the intake mass air flow rate by measuring engine speed and air density.

Stoichiometry The air-to-fuel ratio at which all the oxygen is consumed during combustion.

Volumetric efficiency The volume flow rate of air into the intake system divided by the volume rate of piston displacement.

PETITIONER'S EXHIBIT 1002
US PATENT NO. 6,581,565

BIBLIOGRAPHY

Adler, Ulrich, *Automobile Electric/Electronic Systems,* Robert Bosch, Stuttgart, 1988.

DeCarlo, Joseph P., *Fundamentals of Flow Measurement,* Instrument Society of America, Research Triangle Park, 1984.

Heywood, John B., *Internal Combustion Engine Fundamentals,* McGraw-Hill, New York, 1988.

Norton, Harry N., *Handbook of Transducers,* Prentice Hall, Englewood Cliffs, N.J., 1989.

ABOUT THE AUTHOR

Robert E. Bicking received the B.E.E. and M.S.E.E. degrees from the University of Minnesota and has been involved with sensors nearly all of his 32 years in engineering. He is currently involved with the development of new automotive sensors at the Micro Switch division of Honeywell. He has been awarded three U.S. patents and is the author of over 24 technical papers. He is a member of the I.S.A., I.E.E.E., and S.A.E.

PETITIONER'S EXHIBIT 1002
US PATENT NO. 6,581,565

PETITIONER'S EXHIBIT 1002
US PATENT NO. 6,581,565

CHAPTER 5

TEMPERATURE, HEAT, AND HUMIDITY SENSORS

Randy Frank
Motorola Semiconductor Products

5.1 TEMPERATURE, HEAT, AND HUMIDITY

Temperature sensing and taking into account the effect of temperature on the performance and reliability of automotive components, and therefore the systems that contain these components, is one of the more important aspects of vehicle design. The heat sources that are present on modern automobiles range from the engine itself to catalytic converters, losses in power conversion (e.g. the alternator), and specific heat-generating devices such as heated windshields, seats, and mirrors. Humidity adds to the effect that temperature has on the reliability of components and also impacts vehicle performance and passenger comfort.

5.1.1 Temperature—the Effect of Heat

The temperature of a body or substance is (1) its potential of heat flow, (2) a measure of the mean kinetic energy of its molecules, and (3) its thermal state with reference to its ability to transfer heat to other bodies or substances.

Temperature affects every aspect of automobiles, from the performance of the engine and various vehicle systems to the comfort of the driver and passengers. The wide range of worldwide vehicle operating temperatures (from –60° to +57 °C) and the subsequent localized electronic module temperature ambients underhood (from –40 to +125 °C) and in the passenger compartments (from –40 to +85 °C) affect both the performance and reliability of electronic components. The viscosity of lubricating and cooling fluids is also affected by the wide temperature variations that must be tolerated. Even paint, fabric, plastics, rubber, and other organic and inorganic materials must be designed to survive the environmental extremes of temperature and humidity. Sensing the temperature of these components is essential during vehicle development.

5.1.2 Conduction, Convection, and Radiation

Heat energy is transferred with corresponding temperature changes by conduction, convection, and/or radiation. Conduction occurs by diffusion through solid material or in stationary liquids or gases; convection involves the movement of a liquid or gas between two points, and radiation occurs through electromagnetic waves.

PETITIONER'S EXHIBIT 1002
US PATENT NO. 6,581,565

5.1.3 Heat Sources in Vehicles

In addition to the temperature rise that can be generated by sunlight on the metal and glass that form the body of the vehicle, there are several heat-generating devices in a vehicle as shown in Table 5.1. The foremost heat source is the engine in internal combustion engine equipped vehicles. This causes the engine compartment to generally be classified as a +125 °C ambient for electronic components, although considerably higher temperatures are reached within the combustion chamber (≥1000 °C) or on the engine block.

The catalytic converter used to reduce unburnt hydrocarbons and carbon monoxide emissions has a peak catalyst efficiency around 450 °C, minimum operating temperature around 350 °C, and high temperature operation in the area of 1000 °C.

Tire flexure and friction generated between the tires and the road surface are major sources of heat. Moreover, heat is generated by friction between any moving components of a vehicle. Gears and bearings in transmissions, rear axle, and pumps are most notable for generating a significant temperature rise. Brake surfaces also create high temperatures when the brakes are applied.

Even though they do not generate heat, in the process of reducing the temperature of other components, heat exchangers—such as coolant or transmission radiators for the passenger compartment heater and their associated plumbing and electronic heat sinks—have considerably higher than ambient temperatures.

Electric heating elements, including heated back light, windshield, windshield wiper, mirrors, and seats, increase the temperature to improve visibility and driver comfort. Heated windshield wipers can be maintained at 15 °C even when outside temperatures are around −40 °C. In some cases, temperatures in the area of 350 °C are produced by supplemental heating elements for components such as the catalytic converter, the oxygen sensor, and some advanced electric vehicle batteries.

The windings of electric components such as the starter motor, heater motor, alternator, and solenoids are a source of heat and high temperatures, especially in continuously moving, heavily loaded units like the alternator. The resistance in the windings as well as resistance in semiconductor components like alternator rectifiers and power transistors creates a power loss proportional to the square of the current being conducted ($P = I^2R$). In semiconductors, the change in temperature is related to the power dissipated through the thermal resistance.

$$\Delta T = R_\theta P \tag{5.1}$$

where R_θ = thermal resistance in °C/W
ΔT = temperature difference in °C (frequently $T_{junction} - T_{case}$)
P = power in watts

TABLE 5.1 Heat Sources in Vehicles

General category	Example	Max. temperature °C
Engine	Combustion/ignition process	>1000
Catalytic converter	Chemical reaction	>1000
Road/tire friction	Tires	<100
Brakes	Disk/drum	250
Mechanical motion (gears, bearings)	Transmission/rear axle/air pump/power steering pump	200
Heat exchangers	Radiator (coolant, transmission), heater, heatsink	>175
Electric heaters	Windshield, backlight, seats, mirrors	Ta + 25
Electric windings	Motors, alternator, solenoids	<155 (Class F)
Resistors	Ballast resistor	150
Lamps	Headlamps, tail lamps, dash lamps	125
Power transistors	Ignition driver, voltage regulator	Up to 200
Electric vehicle battery	Sodium sulfur	300

PETITIONER'S EXHIBIT 1002
US PATENT NO. 6,581,565

Lamps have a significant inrush current (10 · steady state) and a high steady state value which generate high temperatures as well.

Temperature at various locations in the vehicle are shown in Table 5.2.

TABLE 5.2 Temperature at Various Vehicle Locations

Location	Temperature, °C		Slew Rate	Humidity		Frost
	Low	High		High	Low	
Underhood—Engine						
Exhaust manifold	–40	+649	–7 °C/min	95% at 38 °C	0	Yes
Intake manifold	–40	+121	–7 °C/min	95% at 38 °C	0	Yes
Underhood—Dash Panel						
Normal	–40	+121	Open	95% at 38 °C		
Extreme	–40	+141	Open	80% at 66 °C		
Chassis						
Isolated	–40	+85	NA	98% at 38 °C	0	Yes
Near heat source	–40	+121	NA	80% at 66 °C	0	Yes
At drive train temperature	–40	+177	NA	80% at 66 °C	0	Yes

5.1.4 Effect of Humidity

Humidity affects the comfort of the drivers and the passengers as well as the performance of the engine and impacts the reliability of vehicle components. The primary measurement for humidity is relative humidity RH, the ratio of water partial pressure to saturation pressure. Other measurements include dew point (temperature); specific humidity (mixing ratio); the mass of water per unit mass of dry gas; and volume ratio, the parts of water vapor per million parts of air. The dew point is a direct measure of vapor pressure and absolute humidity. Humidity is the water vapor in gas. Water in a solid or liquid is called moisture. High humidity and low dew point can lead to increased moisture content which can affect the operation of vehicle fluids such as fuel and brake fluid and impact solid surfaces like the windshield or brake linings.

5.1.5 Reliability Implications to Electronic Components

The effect of temperature on electronic components was recognized as "one of the most severe environments generally encountered on the automobile." Warm-up time of engine liquids and local ambient temperatures are as high as several tens of minutes, especially in cold weather. A recommended practice, SAE J1211, was published in November 1978 that still serves as a guideline to developing environmental design goals for electronic equipment, especially in the area of temperature variations within various vehicle locations.

Temperature affects the performance and expected life of electronic components. Mechanical stress created by different coefficients of thermal expansion can cause failures in thermal cycling test (air-to-air) or thermal shock (water-to-water) transitions.

The failure of electronic components also occurs because the mechanical durability, solder strength, or glass transition of plastic mold compound is exceeded. Electrical properties including thermal runaway in bipolar transistors and loss of gate control in MOS-gated (Sec. 5.4.6) devices also directly cause failure due to temperature extremes.

The typical failure rate for a semiconductor component can be expressed by the Arhennius equation:

$$\lambda = A \cdot \exp \frac{\theta}{kT} \tag{5.2}$$

PETITIONER'S EXHIBIT 1002
US PATENT NO. 6,581,565

where λ = failure rate
A = constant
exp = 2.72
θ = activation energy
k = Boltzmann's constant
$8.62 \cdot 10^{-5}$ eV/°K
T = temperature in °K

The failure rate of semiconductor components typically doubles for every 10 to 15 °C increase in operating temperature. However, increased testing and design improvements have minimized the failures due to specific failure mechanisms. Semiconductor components manufactured in the 90s are orders of magnitude more reliable than those first used in vehicles in the 60s. However, their response time is considerably faster than vehicle liquids and local ambients. For example, the transient thermal response, $r(t)\ R\theta_{JC}$, which is a reduced level of the thermal resistance (Sec. 5.1.4) based on the transistor operating in a switching mode and being off for a period of time, approaches the dc level within a second. Excessive temperatures can be generated quickly and must be detected within milliseconds to prevent failure.

Accelerated life testing is performed at elevated temperatures to determine the reliability of electronic components and obtain the maximum amount of information in the minimum amount of time. The actual failure mechanisms are a result of the component design and environment in which they operate. Life testing seeks to identify areas that are vulnerable in a particular design and provides minimum acceptable criteria for qualification.

The activation energy is directly proportional to the degree of influence that temperature has on the chemical reaction rate. Temperature acceleration factors for a particular failure mechanism can be expressed as the ratio of the failure rates at two different levels of stress:

$$F_a = \exp\left(\frac{\theta}{k}\right) \cdot \frac{1}{T_r - 1/T_l} \tag{5.3}$$

where F_a = acceleration factor
θ = activation energy
k = Boltzmann's constant, $8.62 \cdot 10^{-5}$ eV/°K
T_r = junction temperature in °K at the rated ambient temperature
T_l = junction temperature in °K at the life test ambient temperature

To determine a component's ability to withstand the adverse effects of temperature and humidity extremes to which the vehicle is exposed, a number of reliability stress tests are included in the qualification procedure. These tests include:

- *High-temperature Storage Life* is performed to accelerate failure mechanisms which are thermally activated through extreme temperatures.

  Typical test conditions: T_a = 70 to 200 °C, no bias, time = 24 to 5000 h
- *Temperature Cycling* (air-to-air) evaluates the ability of a device to withstand both exposure to temperature extremes and transition between temperature extremes. This test also exposes excessive thermal mismatch between materials.

  Typical test conditions: T_a = –65 to 200 °C, cycle = 10 to 4000 (1000 most common)
- *Thermal Shock* (liquid-to-liquid) testing evaluates the ability of the device to withstand both exposure to extreme temperature and sudden transitions between temperature extremes. This testing also exposes extreme thermal mismatch between materials.

  Typical test conditions: T_a = 0 to 100 °C, cycle = 20 to 300 (100 most common)
- *H^3TRB* (high-humidity, high-temperature reverse bias) is an environmental test designed to measure the moisture resistance of plastic encapsulated devices. A bias is applied to accelerate corrosive effects on internal components of semiconductors.

  Typical test conditions: T_a = 85 to 95 °C, RH = 85 to 95%, bias = 80 to 100% of max rating, time = 96 to 1750 h

PETITIONER'S EXHIBIT 1002
US PATENT NO. 6,581,565

- *Autoclave* (or pressure cooker) testing is performed to measure device resistance to moisture penetration and resulting galvanic corrosion. This is a highly accelerated and destructive test.
  Typical test conditions: T_a = 121 °C, RH = 100%, p = 1 atmosphere, time = 24 to 96 h
- *Moisture Resistance* testing evaluates the moisture resistance of components under tropical environments.
  Typical test conditions: T_a = −10 to 65 °C, RH = 80 to 98%, time = 24 h/cycle, cycle = 10

In addition, a number of high-temperature tests under different biasing conditions are also performed for semiconductor devices, including high-temperature forward bias, high-temperature reverse bias, and high-temperature gate bias.

5.2 AUTOMOTIVE TEMPERATURE MEASUREMENTS

Numerous temperature measurements are made during the development of the vehicle to ensure the proper operation of systems and components. Some measurements are included in the control system strategy or as diagnostics for production vehicles. A list of the potential temperature and humidity measurements that can be made and may be incorporated in future systems is shown in Table 5.3. The technique used to measure temperature may vary from development to production mode, from one vehicle manufacturer to another and even from system to system within a given vehicle manufacturer. The choice in technology for production sensors depends upon performance, reliability, and cost. For development vehicles, cost is not a major concern, but availability of test probes, compatibility with readout equipment, and ease of use are additional factors that should be taken into consideration.

Common vehicle temperature measurements will be explained in the remainder of this section.

5.2.1 Measuring Liquid Temperatures

A number of liquid temperatures are measured during vehicle development, especially under high vehicle ambient temperatures and severe driving conditions, such as trailer towing up steep grades and stop-and-go Phoenix traffic during summer months. These include coolant, engine oil, transmission oil, fuel, power steering, brake, and battery electrolyte. Monitoring coolant temperature is common in engine control systems in production vehicles. Engine and transmission oil temperature are being evaluated for future monitoring. Racing vehicles frequently monitor oil and fuel temperature in addition to coolant temperature to achieve peak performance. Sensing fuel temperature may be required to meet future emissions standards. A latent heat cooling system has been developed that uses a temperature sensor to control the engine under various operating conditions. The system employs control valves that control the flow of vaporized coolant based on temperature in a manifold connected to the top of the combustion chamber.

Mounting location, fluid contacting the sensor, and packaging are critical concerns for liquid temperature sensors. Upper temperature limits are typically around 150 to 200 °C and operation down to −40 °C is usually required.

Battery temperature measurements in vehicle development use glass thermometers or glass-shielded thermocouple probes to protect the sensor from the corrosive electrolyte.

5.2.2 Battery Temperature

Maintaining the proper state of charge in the vehicle's battery is essential for obtaining adequate cranking rpm during starting and for ensuring optimum battery life. The charge accep-

PETITIONER'S EXHIBIT 1002
US PATENT NO. 6,581,565

TABLE 5.3 Sensing Requirements versus Vehicle Systems

System	Parameter
Engine control	Air charge (intake air) temperature Engine coolant temperature Intake air humidity Ambient temperature Fuel temperature
HVAC (climate control)	Humidity in passenger compartment (PC) Temperature (PC) Outside air temperature
Electronic transmission (continuously variable transmission)	Transmission oil temperature
Driver information (body computer inputs)	Coolant temperature Ambient air temperature Temperature (PC) Tire surface temperature Rain sensor Windshield moisture Sun sensor Battery temperature
Multiplex/diagnostics Cruise control Idle speed control Memory seat Navigation	Multiple usage of sensors
Antiskid brakes	Brake fluid temperature
Traction control/ABS	Brake moisture sensor
Air bags	
Suspension	
Electronic power steering	Power steering fluid temperature (also electric assisted)
Four-wheel steering Security and keyless entry	

tance curves of lead-acid batteries require that the charging voltage be modified for temperature. A higher voltage is required at lower temperatures. Cold temperatures also place the most difficult requirements on the battery because the viscosity of engine oil is low and the load on the cranking system is very high.

Compensation circuitry in the voltage regulator in the charging system is designed to provide a voltage that is within an acceptable range over the entire vehicle operating temperature range as shown in Fig. 5.1. Semiconductor sensing techniques (Sec. 5.4.6) are used in this approach. The most desirable location for the voltage regulator is close to the battery. However, some systems integrate the regulator inside the alternator and provide a temperature environment that can be considerably different from the battery. The temperature of the battery can also vary by several degrees from cells closest to the engine to those further away from the engine. The overall mass of the battery prevents these temperatures from changing very quickly. However, a failed voltage regulator that applies full voltage to the alternator can easily cause excessive battery temperatures to be generated.

PETITIONER'S EXHIBIT 1002
US PATENT NO. 6,581,565

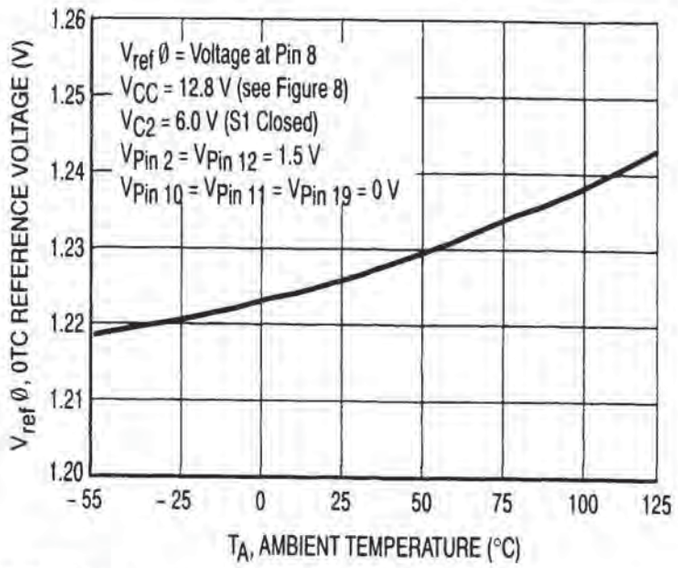


FIGURE 5.1 Temperature compensation in voltage regulator.

Batteries for electric vehicles (EVs) may require maintaining a specified high-temperature operating range. Sodium sulfur cells can store four times the energy of lead acid cells, but the battery's operating temperature must be kept within 300 to 350 °C. Solid oxide fuel cells operate at 1000 °C. If higher-temperature batteries are adopted for use in EV systems, sensing the battery temperature could be part of the diagnostic and fault detection.

5.2.3 Air Temperature Measurements

Air is measured for ambient temperature, passenger compartment temperature, and inlet air on production vehicles. For development purposes, a number of location ambients are always evaluated as potential mounting locations for electronic components. Upper temperature ranges are lower than liquid measurements, with 85 or 125 °C being common upper limits.

5.2.4 Catalyst Temperature

Measuring catalyst temperature during vehicle development has been performed since the earliest implementation of these devices. Concern for excessive temperatures in nearby vehicle locations meant that a number of measurements were made. However, the converter must be at a minimum temperature, usually above 350 °C, to be effective. Tougher exhaust emission standards are spurring manufacturers to utilize the converter sooner after the vehicle is started. Techniques are being pursued that would decrease the warm-up time for the catalyst to increase its effectiveness in controlling emissions. One technique involves heating the catalyst briefly by igniting a measured mixture of fuel and air in an afterburner ahead of the catalyst. Another technique utilizes electric heating to reduce the warm-up time. The power required for this approach would require an excessive power drain from the vehicle's power system. A linear temperature sensor has been developed to measure the temperature across the catalyst. A thermistor (see Sec. 5.4.1) is inserted diagonally inside the converter. A range of resistance has been evaluated and a time constant of about 2 s has been achieved. For fault condition monitoring, the sensor is able to detect a localized hot spot inside the catalyst and may prove to be able to detect misfire as part of future on-board diagnostic equipment required by the California Air Resources Board or the federal Environmental Protection Agency.

PETITIONER'S EXHIBIT 1002
US PATENT NO. 6,581,565

The temperature of exhaust gases increases rapidly under severe operating conditions such as continuous high speed or insufficient octane rating. One company has monitored their efforts at controlling the engine's operating temperature by locating a temperature sensor in the exhaust manifold. If the sensor detects an exhaust gas temperature rise above an established limit, a computer sends a command to inject extra fuel into the combustion chamber to cool the engine. Since exhaust gas temperatures can reach 1000 °C, a specially designed magnesium oxide thermocouple in a metal tube is used to sense the temperature (see Sec. 5.4.2). This approach may also be used in the future to reduce catalyst warm-up time.

5.2.5 Oxygen Sensor

The oxygen sensor used as the feedback element in closed-loop engine control systems generates a signal based on the difference in the oxygen concentration from inside the exhaust gas and ambient. As shown in the Nernst equation:

$$V_S = RT/4F \ln (P_a/P_g) \tag{5.4}$$

where V_S = the generated output voltage
P_a = oxygen partial pressure of the air
P_g = oxygen equilibrium pressure
R = gas constant
F = Faraday's constant
T = absolute temperature of the sensor

In addition to being affected by temperature, the oxygen sensor requires a minimum temperature to operate properly and provide a closed-loop control system. Typically, this minimum temperature is ≥450 °C. To reduce the oxygen sensor's warm-up time, heaters are added. A heated oxygen sensor achieves operating temperature much sooner than an unheated unit and allows closed-loop operation to be initiated. Monitoring temperature during engine and vehicle development is part of control strategy and component development.

5.2.6 Tire Temperature Sensing

Sensing the temperature within the tire is part of the pressure measurement and fault detection provided by tire pressure measuring and automatic adjustment systems. In a system like the one developed by Michelin (Fig. 5.2) that is used on Peugot's experimental sports car, the Proxima, both a pressure and temperature sensor are located on each wheel. A circular antenna and a transceiver allow these signals to be sent to an electronic processing module. An air compressor attempts to maintain desired tire pressure under normal conditions. If the pressure-temperature indications go above 85 °C, the system recommends speeds be held below 240 km/h (148 m/h). For temperatures above 90 °C, the limit is 160 km/h and for 95 °C, the limit is 80 km/h. For temperatures in excess of 100 °C, the system recommends stopping the vehicle.

5.2.7 Fault Detection for Electronic Components

As indicated in Sec. 5.1.6, temperature can cause reliability failures from several mechanisms in electronic systems. Therefore, detecting excessive temperature and designing system strategies to account for excessive temperatures can minimize improper operation and catastrophic failures.

Sensing for fault conditions, like a short circuit, is an integral part of power ICs or smart power transistors. The ability to obtain temperature sensors in mixed Bipolar-CMOS-DMOS semiconductor processes provides protection and diagnostics as part of the features of smart power ICs, like Motorola's SMARTMOS™ products. The primary function of the power IC is to provide a microcontroller-to-load interface for solenoids, lamps, and motors. It is a definite

PETITIONER'S EXHIBIT 1002
US PATENT NO. 6,581,565

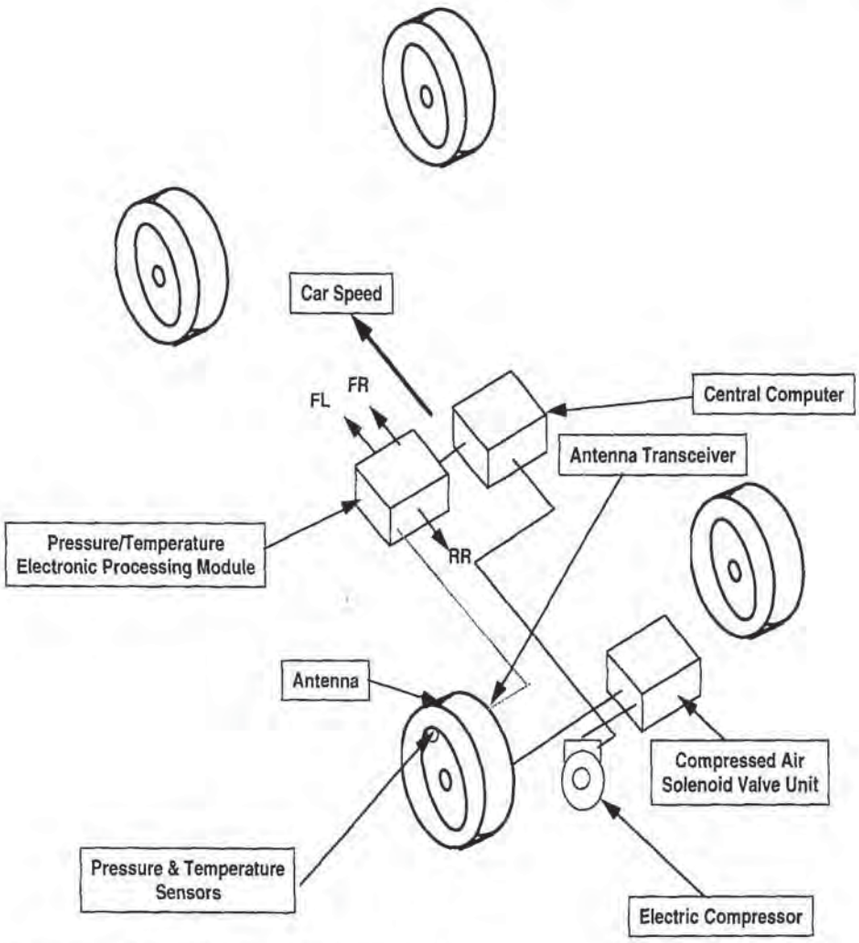


FIGURE 5.2 Temperature sensing in tire pressure control.

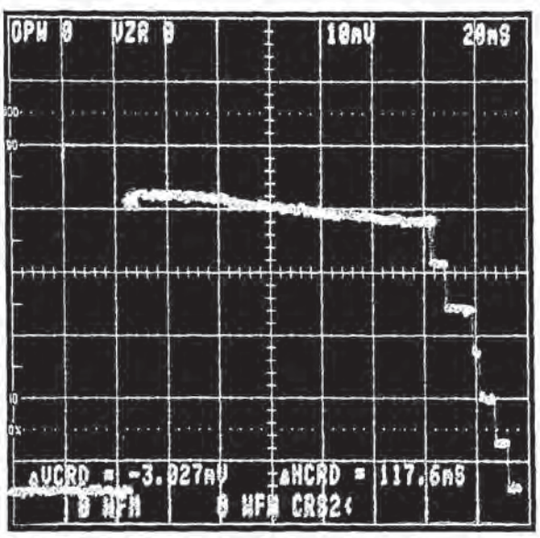


FIGURE 5.3 Thermal shutdown of six outputs of smart power IC.

PETITIONER'S EXHIBIT 1002
US PATENT NO. 6,581,565

advantage in multiple-output devices, to sense the junction temperature of each device, provide status input to the microcontroller and, if necessary, shut down a particular unit that has a fault condition. The sequential independent shutdown of six output drivers with a short applied across each unit's load is shown in Fig. 5.3. The action that is taken based on sensing a fault condition can vary depending on the control system. Sensing excessive temperature in a power device may mean that the device can turn itself off to prevent failure in one case and in another situation, a fault signal provides a warning but no action is taken. The remaining portion of the system is allowed to function normally. With the fault conditions supplied to the MCU, an orderly system shutdown can be implemented.

5.2.8 Mass Air Flow Sensor

The generalized model of a transducer is shown in Fig. 5.4. In addition to the desired input, undesired environment effects, like temperature and, to a lesser extent, humidity, are factors that affect the performance and accuracy of the transducer and must be taken into account during the design of the transducer.

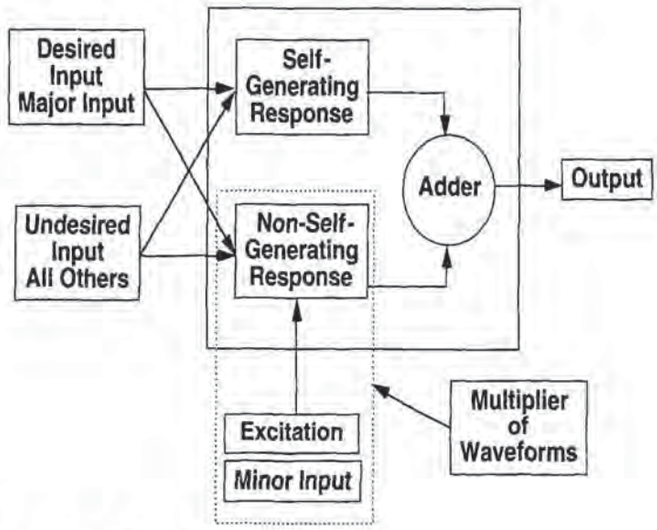


FIGURE 5.4 Generalized model of a transducer.

In the case of mass air flow sensing, temperature effects are used as part of the measurement process. A typical approach for mass air flow involves a hot-wire anemometer with a platinum wire as the sense elements, as shown in Fig. 5.5. The air temperature probe detects the temperature of the air flowing into the combustion process. The hot-wire probe is heated by current supplied from a power transistor. The difference in temperature between the probes is detected as a difference in electrical resistance. The electronic circuitry regulates the heating current to the hot-wire probe to keep the temperature difference constant at any flow rate (Fig. 5.6). The current required is proportional to the air flow rate. One of the main issues in this type of sensor is the response time. Improvements which reduce the response time from 50 to 30 ms have been made in recently developed units.

A microbridge silicon mass air flow sensor has been developed that utilizes temperature-resistive films laminated within a thick film of dielectric material and micromachined cavity as shown in Fig. 5.7. The resistors are suspended over the etched cavity, which also provides thermal isolation for the heater and sensing resistor. Heat is transferred from one resistor to the other as the result of flow. The imbalance in the resistance caused by the heat transfer

PETITIONER'S EXHIBIT 1002
US PATENT NO. 6,581,565

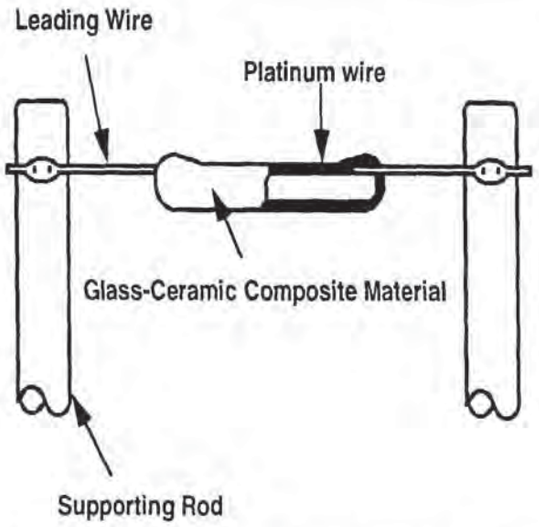


FIGURE 5.5 Probe for hot-wire anemometer mass air flow sensor.

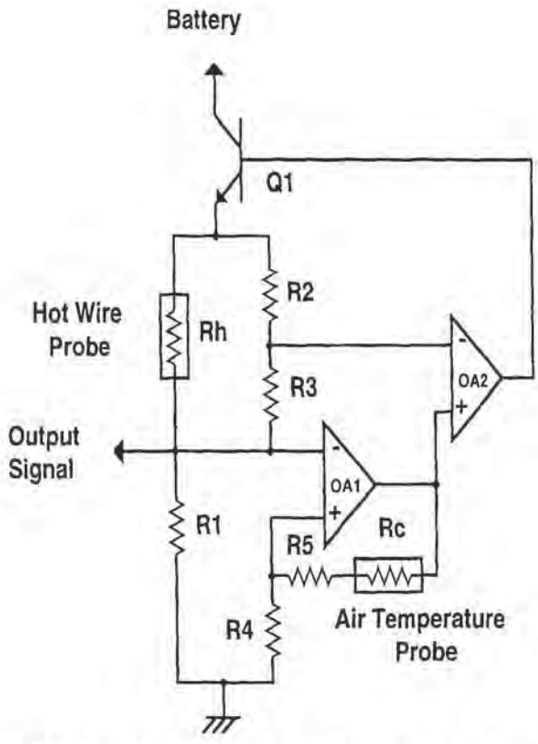


FIGURE 5.6 Circuit for hot-wire anemometer mass air flow sensor.

PETITIONER'S EXHIBIT 1002
US PATENT NO. 6,581,565

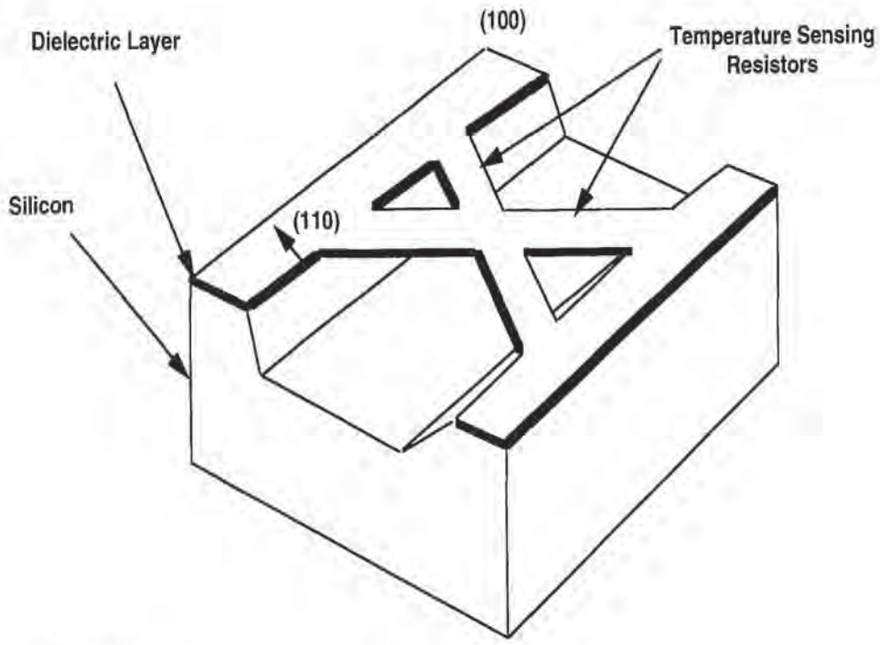


FIGURE 5.7 Temperature sensor in microbridge mass air flow sensor.

is directly proportional to the flow. The small size of the resistors allows fast response time (≤3 ms) and high sensitivity to flow. The device has also been found to be useful as a differential or absolute temperature sensor.

5.2.9 Temperature Measurements in New Systems

As new vehicle systems are developed or existing systems are modified to provide improved performance, or meet legislated or customer demands, new applications for temperature sensors will occur. An example of two systems, air bags and thermo accumulator, is provided.

In inflatable restraint systems, the air bag is inflated based on the ignition of a gas generant. In this system, an igniter receives an electric impulse, passes it through to a heating filament, and actuates a small pyrotechnic charge to ignite the gas generant, which produces nearly pure nitrogen gas to inflate the bag. The initial temperature is high but the nitrogen gas cools rapidly, so a fully deployed bag is only slightly above room temperature. Measuring the temperatures that occur during this event is part of the development activity.

A heat battery, or thermoaccumulator, can store the latent heat from a previously driven vehicle for up to three days at an ambient temperature of –29 °C. The accumulator is made of salt-based crystals which change from solid to liquid form above 78 °C. Heat provided by this device has proven to reduce the emissions which are generated during the first 20 s of the federal emissions test procedure. The unit also has potential application in passenger compartment heating.

5.3 HUMIDITY SENSING AND VEHICLE PERFORMANCE

Correlation of a number of vehicle tests requires that the humidity be monitored. Variations in humidity can explain variations that occur in test results.

PETITIONER'S EXHIBIT 1002
US PATENT NO. 6,581,565

Significant, repeatable, and controllable results may lead to humidity sensing being part of future engine control systems and passenger compartment comfort control systems.

Some sensors, such as rain (and/or windshield moisture) or sun sensors, are already being used on some vehicles to control wiper blade and fan controls.

5.3.1 Engine Performance

Injecting water to cool the intake charge and prevent premature detonation is a technique that has been used in high-compression (≥10:1) engines. The cooling effect from evaporation reduces the operating temperature.

An increase in inlet air humidity has been shown to reduce the nitric oxide emissions. Condensation in the gas tank can add a considerable amount of moisture to the fuel. Measuring the actual amount of humidity or moisture present during development tests is useful to identify all variables that can affect performance.

5.3.2 Passenger Compartment Comfort

A traditional passenger temperature control system shown in Fig. 5.8 uses only temperature as the indication for the system to open or close blend doors in the HVAC (heater, ventilating, and air conditioning) system. Laboratory evaluations monitor the HVAC systems' effectiveness under known and controlled humidity conditions. A fuzzy logic system combining temperature and humidity sensing has been investigated by researchers for home use. In this case, additional humidity is available to speed up the effect of adding heat. In a vehicle application, the blower speed could be adjusted based on the presence of humidity or an alternate strategy could be developed which uses less energy from the vehicle to make the driver and passengers comfortable.

The development of new test techniques frequently involves either the development of new sensors or novel use of existing sensors. A sweat impulse test developed at Volkswagen AG allows researchers to evaluate the ability of a seat to direct sweat away from its surface.

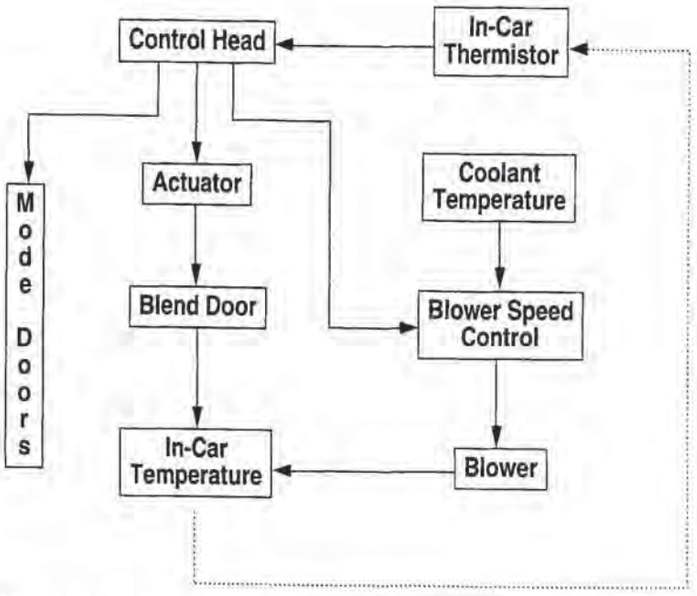


FIGURE 5.8 Automatic temperature control diagram.

PETITIONER'S EXHIBIT 1002
US PATENT NO. 6,581,565

As part of the measurement process, a platinum RTD (Sec. 5.4.5) and a capacitive humidity sensor provide data. In excessive sweating situations, the fabric is unable to absorb sufficient moisture, so it is passed to the surrounding environment as increased humidity.

5.3.3 Brake Moisture Sensing

Brake fluids are hygroscopic and, therefore, absorb moisture. Sufficient moisture lowers the boiling point of the brake fluid, and eventually vaporizes the fluid resulting in loss of stopping power. A meter has been developed that can be inserted into the master cylinder reservoir and measure the boiling point of the brake fluid. A heating element boils a sample of the brake fluid. A microcontroller calculates the actual boiling point by the initial temperature reading, temperature drop, and time between cooling and boiling. This approach may be applicable to other vehicle fluids that can be checked during maintenance procedures.

5.4 SENSORS FOR TEMPERATURE

Several different sensing techniques are used in production vehicles and during vehicle development to provide the temperature measurements. Table 5.4 shows a list of these techniques and the temperature range that is typical for this approach. Characteristics of temperature-sensing devices that allow a designer to determine if the approach will meet development or production requirements are explored in this section. In addition to the operating temperature range, linearity, response time, packaging, reliability, and cost are factors that must be considered. Temperature sensors can be as simple as thermal expansion devices, such as mercury or alcohol thermometers, or as complex as infrared sensors used in night vision systems. Common sensors and some recent additions to temperature sensing are covered in this section. Other sensor techniques, including the temperature-generating characteristics of quartz and temperature-sensing reed switches, are also possible but not covered.

5.4.1 Thermistors

Thermistors have found broad application acceptance in several vehicle systems that require temperature sensing from the coolant system to control the engine. The thermistor is a special

TABLE 5.4 Temperature Sensing Techniques versus Operating Range

Sensing technique	Temperature range, °C	Usage: Production (P) Development (D) Future (F)
Thermistor	0 to 500	P
Thermocouple	−200 to +3000	D
Bimetallic switch	−50 to +400 (650)	P
Potentiometer temperature sensor	−40 to +125	P
Platinum wire resistor (RTD)	−200 to +850 (−40 to +200)	D (P)
Semiconductor (junction)	−40 to +200	P
Thermostat (pressure spring)	−50 to +500	P
Fiber optic temperature sensor	+1800	D/F
Temperature indicator	+40 to +1350	D
Infrared	>Ta	F
Liquid thermometer	−200 to +1000	D

PETITIONER'S EXHIBIT 1002
US PATENT NO. 6,581,565